# OXIDATION OF SILICON AND GERMANIUM BY ATOMIC AND MOLECULAR OXYGEN

by

Maja Kisa

Dipl. Ing. Inorganic Chemical Engineering, University of Belgrade, 1998

M.S. in Materials Science and Engineering, University of Pittsburgh, 2004

Submitted to the Graduate Faculty of

The School of Engineering in partial fulfillment

of the requirements for the degree of

Doctor of Philosophy

University of Pittsburgh

2007

UNIVERSITY OF PITTSBURGH

SCHOOL OF ENGINEERING

This dissertation was presented

by

Maja Kisa

It was defended on

January 5, 2007

and approved by

Dr. Gerald H. Meier, Professor, Materials Science and Engineering

Dr. John P. Leonard, Assistant Professor, Materials Science and Engineering

Dr. Jörg M.K. Wiezorek, Associate Professor, Materials Science and Engineering

Dr. Ian K. Robinson, Professor, London Centre for Nanotechnology, UK

Dr. Judith C. Yang, Associate Professor, Materials Science and Engineering
Dissertation Director

# OXIDATION OF SILICON AND GERMANIUM BY ATOMIC AND MOLECULAR OXYGEN

Maja Kisa, PhD

University of Pittsburgh, 2007

Space vehicles residing in the low Earth orbit (LEO) are exposed to a harsh environment that rapidly degrades their materials. The LEO ranges from 200-700km in altitude from the Earth's surface, and the temperature varies between 200 and 400K. The most hazardous species in LEO is atomic oxygen (AO) containing 5eV kinetic energy due to the high velocity of the spacecrafts (8km/s).

The goal of this research is the elucidation of the fundamental mechanisms of semiconductor degradation and passivation in LEO conditions by comparing the structural differences in the oxide films created by exposure to AO and molecular oxygen (MO). Silicon is the base material for solar cells used in LEO whereas Ge and $SiO_x$ films are common coatings to protect polymer materials that are used as structural materials in spacecrafts.

Hyperthermal AO was created by the laser detonation of MO within a high vacuum (HV) chamber, that produces a high flux of AO. A variety of nano-characterization techniques, including high resolution transmission electron microscopy (HREM), and electron energy loss spectroscopy (EELS) were used to determine the microstructure and local chemistry of the oxide and the oxide/semiconductor interface.

For Si, the amorphous silica formed by AO was nearly twice as thick, more ordered, and more homogeneous in composition, than the oxide formed by MO. The $Si/SiO_x$ interface formed by AO was atomically abrupt, with no suboxides detected near the interface or throughout the oxide.

The oxide scale formed by MO on Si(100) consisted of transitional oxidation states. The oxide film formed on Ge(100) due to exposure to 5eV AO, is 2-3 times thicker and similarly to the Si/$SiO_x$ interfaces, the Ge/$GeO_x$ interface was found to be atomically abrupt.

The oxidation kinetics of Si and Ge were monitored *in situ* using a research quartz crystal microbalance (RQCM) that was incorporated into the AO source. The oxidation kinetics in hyperthermal AO did not follow the standard linear to parabolic Deal-Grove kinetics. A novel oxidation model, based on the oxide structure continually changing during AO exposure, is proposed to explain the unusual power law oxidation kinetics.

## TABLE OF CONTENTS

1.0 INTRODUCTION ........................................................................................................ 1

2.0 BACKGROUND ........................................................................................................ 3

2.1 Low Earth Orbit (LEO) environment ........................................................................3

2.2 Materials protection from atomic oxygen (AO) attack ............................................5

2.3 Silicon oxidation by AO and molecular oxygen (MO)-an overview and comparison .............8

2.3.1 Effects of hyperthermal AO on Si oxidation-previous MS research ..................................13

2.4 $SiO_2$ surface roughness and thickness. $Si/SiO_2$ interface thickness........................................14

2.4.1 Investigation of $Si/SiO_2$ interface and oxidation states.......................................................17

2.5 Increased ordering in the Si-oxide caused by energetic AO ..................................................20

2.6 Germanium oxidation by AO and MO-an overview and comparison ....................................24

2.7 Oxidation process.......................................................................................................28

2.7.1 The initial oxide formation ........................................................................................29

2.7.1.1 Thermionic emission effect............................................................................ 30

2.7.1.2 Thermal spiking effect ................................................................................... 33

2.7.1.3 The Cabrera-Mott model................................................................................ 34

2.7.2 Later stages of oxidation process and Deal –Grove model.................................................37

2.7.2.1......Difficulties in modeling ultra-thin oxide growth and limitations of Deal-Grove model ........................................................................................................................ 41

2.7.2.2 Deal-Grove model modifications........................................................................ 45

3.0 MOTIVATION AND HYPOTHESES ......................................................................... 57

4.0 RESEARCH OBJECTIVES ........................................................................................ 62

5.0 EXPERIMENTAL PROCEDURE ................................................................................ 64

5.1 AO sources ..... 64
5.1.1 Fast atom sample tester (FAST ™) laser detonation source (LDS) ..... 64
5.2 Modifications of the FAST ™ laser detonation AO source ..... 68
5.3 Si single-crystal oxidation by 5eV and 9eV AO ..... 70
5.3.1 Native oxide removal procedure prior to oxidation and oxidation conditions ..... 70
5.4 Si single-crystal oxidation by MO ..... 72
5.4.1 Native oxide removal procedure prior to oxidation and oxidation conditions ..... 72
5.5 Ge single-crystal oxidation by 5eV, 9eV and 15eV AO ..... 73
5.5.1 Native oxide removal procedure prior to oxidation and oxidation conditions ..... 73
5.6 Ge single-crystal oxidation by MO ..... 75
5.6.1 Native oxide removal procedure prior to oxidation and oxidation condition ..... 75
5.7 Characterization methods ..... 77
5.7.1 Transmission electron microscopy (TEM) techniques ..... 77
5.7.2 Dark field imaging ..... 78
5.7.3 Selected area electron diffraction (SAED) ..... 79
5.7.4 Radial distribution function (RDF) ..... 82
5.7.5 Fluctuation electron microscopy (FEM) ..... 85
5.7.6 High-resolution transmission electron microscopy (HRTEM) ..... 87
5.7.7 Electron energy loss spectroscopy (EELS) ..... 89
5.7.8 Scanning Transmission Electron Microscopy (STEM) Spectrum Imaging (SI) ..... 89
5.7.9 Electron Energy Loss Spectrum ..... 90
5.7.10 Electron loss near edge fine structure (ELNES) ..... 93
5.7.11 EELS spectra processing ..... 95
5.7.12 EELS Acquisition Conditions and Spectra Processing-Experimental ..... 97
5.7.13 X-ray photoelectron spectroscopy (XPS) ..... 99

5.7.14 Atomic force microscopy (AFM) ....................100
5.8 Stopping range of ions in matter (SRIM) simulation....................101
5.9 Kinetic study of energetic AO reaction with Si and Ge in research quartz crystal microbalance (RQCM) - principle....................103
5.9.1 Si and Ge coatings deposition on standard crystals....................105
5.9.2 Oxidation of Si and Ge by 5eV AO in QCM....................106
5.9.3 Oxidation of Si and Ge by 9eV AO in QCM....................107
6.0 RESULTS AND DISCUSSION .................... 108
6.1 Effects of hyperthermal AO on silicon oxidation....................110
6.1.1 $SiO_2$ thickness....................110
6.1.2 Investigation of $Si/SiO_2$ interface and oxidation states....................111
6.1.3 Increased order in the Si oxide caused by energetic AO ....................113
6.2 Effects of energetic AO and temperature on germanium oxidation ....................119
6.2.1 $GeO_2$ increase in thickness due to increase in AO kinetic energy....................120
6.2.2 Investigation of $Ge/GeO_2$ interface and oxidation states....................123
6.2.3 $GeO_2$ surface roughness....................125
6.3 Kinetics of Si and Ge oxidation by AO species....................129
6.3.1 Oxidation curves obtained during 5eV and 9eV AO exposure of Si and Ge in QCM ......130
6.3.2 Oxide thickness dependency on the AO kinetic energy ....................134
6.3.3 The Deal-Grove model fit to the kinetic data ....................139
6.3.4 Reisman model and power law....................142
6.3.5 Oxygen efficiency to form Si-O and Ge-O bonds ....................149
7.0 DISCUSSION OF THE OXIDATION MECHANISMS BY HYPERTHERMAL AO ON SEMICONDUCTORS .................... 154
8.0 CONCLUDING REMARKS.................... 172

9.0 FUTURE WORK ..... 177
APPENDIX A ..... 180
APPENDIX B ..... 190
APPENDIX C ..... 200
BIBLIOGRAPHY ..... 204

## LIST OF TABLES

Table 1 Crystal structures of $SiO_2$ and $GeO_2$ phases [25, 26]. ........................................................ 21

Table 2 The species in the AO beam of the LDS (determined by mass spectroscopy) [16]. ............. 67

Table 3 Experimental conditions ........................................................................................... 76

Table 4 Summary of the mean square roughness (RMS) of the oxide surface formed by energetic AO on Ge substrate........................................................................................................ 125

Table 5 Statistic analyses and goodness of fit parameters of the least squares fit procedure........... 143

Table 6 *a* and *b* coefficients calculated from QCM and XPS-Tagawa [18] kinetic data at T=297K. .......................................................................................................................... 145

Table 7 Determination of the rate-limiting mechanism of the oxidation process (interface reaction or diffusion-limited). Coefficients *b* and *a* were calculated from QCM and XPS (Tagawa) [18] kinetic data at T=297K; *b*~1 for the oxidation process which is interface reaction-limited; *b*≤0.5 for diffusion-limited process.......................................................................................... 164

Table A III- 1 Thermodynamical and electronic properties of Si, Ge, $SiO_2$ and $GeO_2$................... 203

Table A III- 2 Thermodynamic properties of $SiO_2$ and $GeO_2$ phase transformations [130, 131]. ... 203

## LIST OF FIGURES

Figure 1 Cross-sectional view of a typical blanket assembly [14]. .................................................... 7

Figure 2 Adsorption probabilities for AO and MO (a) for zero oxygen coverages as a function of substrate temperature, the translational energies were 4kcal/mole for O and 2 and 14kcal/mole for $O_2$ (as indicated on the graph), with incident angle 75$^o$ in both cases, and (b) for different oxygen coverages on different substrate temperatures. The translational energies were 16kcal/mole for O and 5kcal/mole for $O_2$. (Engstrom et al. XPS) [15]....................................... 8

Figure 3 Coverage dependence on exposure for AO and MO on Si(100) substrate at 300K (XPS, Engstrom et al.) [17]. ...................................................................................................... 10

Figure 4 Oxide thickness versus fluence for AO oxidation of H-terminated Si(100) at 297K . The hyperthermal AO beam had three different translation energies: 1.6eV, 3.6eV and 4.6eV (XPS, Tagawa et al.) [18]. ........................................................................................................ 11

Figure 5 Cross-sectional HRTEM micrographs of the silicon oxide layer formed on Si(100) oxidized by a) 5 eV AO b) MO at 220$^o$C [5, 21]......................................................................... 14

Figure 6 Intensity profiles obtained from cross-sectional HRTEM micrographs of the silicon oxide layer formed on Si(100) oxidized by 5 eV AO at 220$^o$C [5, 21]. ............................................. 15

Figure 7 Intensity profiles obtained from cross-sectional HRTEM micrographs of the silicon oxide layer formed on Si(100) oxidized by MO at 220$^o$C [5, 21]. ..................................................... 16

Figure 8 AFM image of Si(100) oxidized at 220$^o$C a) by 5eV AO, RMS≅1.54±0.21nm b) by MO, RMS≅0.83±0.13nm.......................................................................................................... 17

Figure 9 Characteristic core-loss ionization for Si(100) oxidized by 5eV AO a) Si $L_{2,3}$ edge b) O K edge acquired on JEM 2010F [5, 21]........................................................................... 18

Figure 10 Characteristic core-loss ionization for Si(100) oxidized by MO a) Si $L_{2,3}$ edge b) O K edge acquired on JEM 2010F [5, 21]........................................................................... 18

Figure 11 $SiO_2$ phase stability regions [24]. ........................................................................... 20

Figure 12 (a) Plan-view HRTEM micrographs and corresponding SAED pattern of the silicon oxide layer formed on Si(100) oxidized by 5eV AO (b) MO [5, 21]. ............................................... 23

Figure 13 Oxide thickness as a function of oxidation time a), b) thermal oxidation c), d) ECR plasma oxidation at +60V bias. Solid lines-total thickness; filled symbols-interface thickness. a) and c) were obtained from SWE measurements and using single layer model, while b) and d) obtained by SE using the two layer model (ellipsometry, Wang et al.) [30]........................................... 25

Figure 14 Ge oxide thickness as a function of VUV exposure time at different temperatures. Vacuum ultraviolet radiation was emitted by a Xe silent discharge lamp, and film thicknesses were measured by SWE (Craciun) [31]. 27

Figure 15 Schematic representation of fluxes for thermionic emission model [47]. 30

Figure 16 Schematic of the ion removal from the metal surface [41]. 34

Figure 17 Model for silicon oxidation [48]. 38

Figure 18 a) Representation of the depth -dependent $O_2$ diffusivity and b) schematic of the oxide growth, $SiO_2$ is stoichiometric oxide having diffusivity of bulk, denoted by $D_{frac}$ ('fractal'), $SiO_2/SiO_x$ is interface sublayer with intermediate diffusivity, while $SiO_x/Si$ is interface sublayer with low diffusivity. Si is crystalline substrate (very low diffusivity) Verdi and Kelly [58]. 44

Figure 19 Oxygen transport to the $Si/SiO_2$ interface via pores or channels 46

Figure 20 Compressive stress at the $Si/SiO_2$ interface [35]. 48

Figure 21 Schematic of the thin epitaxial oxide layer ($SiO_x^{I}$) of thickness $x_I$ and viscosity $\eta_{I.}$ (time - independent). Growing oxide layer is marked as $SiO_x^{II}$ , with the thickness $x_{II}$ and viscosity $\eta_{II.}$ (time -dependent). A= the oxide surface area. Due to the increasing thickness of the oxide II with time, the average viscosity changes with time. If the bulk oxide viscosity is greater than the viscosity of the thin epitaxial oxide, then the average viscosity increases with time, which slows down the oxidation and oxide growth, leading to b<1. $\eta_{II} > \eta_{I,}$ and b<1, reaction is slower than for the reaction rate-limited process (b=1). 51

Figure 22 a) Schematic b) actual dimensions c) image of the laser detonation AO source at the University of Pittsburgh 66

Figure 23 UHV heating stage, (Boraelectric heater used), incorporated in the laser detonation AO source 68

Figure 24 Schematic diagram of rays in TEM a) BF image formation from direct beam b) DF image formed from off-axis scattered beam c) DF image formed from on-axis scattered beam [77]. 78

Figure 25 Ewald sphere construction [79]. 80

Figure 26 The relationship of the atomic arrangement and density function ρ(r) for an "amorphous" material [76]. The 1st and 2nd peaks in ρ(r) correspond to the first and second shell of atoms, respectively. 84

Figure 27 Variance sensitivity to MRO [83, 85]. 86

Figure 28 STEM analyses with Spectrum Imaging (SI). 90

Figure 29 Characteristic EELS spectrum of $SiO_2$ as-acquired containing the most intense zero-loss peak, low-loss and high-loss region characterized with core-loss edges. Si $L_{2,3}$ edge onset is visible around 100eV.[5]. ........ 92

Figure 30 As - recorded EELS spectrum and background fitting to $SiL_{2,3}$ edge [5]........ 98

Figure 31 (a) Quartz crystal with the electrode pattern shown on both sides - dotted electrode is located at the bottom side of the crystal (b) Schematic of the transfer wave propagating through a quartz crystal, film deposit and electrodes........ 103

Figure 32 Cross-sectional HRTEM micrograph of the silicon oxide layer formed on Si(100) oxidized by 9 eV AO at 200°C. ........ 110

Figure 33 (a) HAADF image of cross-sectional TEM sample ([110] zone axis). (b) Background subtracted $SiL_{2,3}$ spectrum image of Si(100) oxidized by 5eV AO (MSU) at 220°C (total AO fluence =$8.1x10^{19}$ at/$cm^2$), acquired on a $C_s$-corrected VG HB501 STEM-step size~1.4Å..... 112

Figure 34 Reduced RDF plots obtained from Si(100) oxidized by atomic (5eV) and MO. First six peaks correspond to the Si-O, O-O, Si-Si, Si-2$^{nd}$ O, O-2$^{nd}$ O, and Si-2$^{nd}$ Si distances........ 114

Figure 35 Variance V(*k*) plots obtained from Si(100) oxidized by atomic (5eV) and MO........ 115

Figure 36 Si(100) oxidized by 5eV AO (a) Annular dark field image (b) $SiL_{2,3}$ background stripped edge recorded in Si bulk, Si/$SiO_2$ interface and oxide bulk........ 116

Figure 37 ELNES comparison of $SiL_{2,3}$ edges of Si oxidized by 5eV AO with results of Garvie et al. (data acquired on $C_s$ corrected VG-HB501 STEM)........ 117

Figure 38 Cross-sectional HRTEM micrographs of the Ge oxide layer formed on Ge(100) oxidized by a) 5eV AO b) MO at 200°C, where the oxide thickness doubled due to AO exposure (2-3nm) as compared to MO (~1nm)........ 120

Figure 39 Cross-sectional HRTEM micrograph of the 2-3nm Ge oxide layer formed on Ge(100) oxidized by 5eV AO at room temperature........ 121

Figure 40 Cross-sectional HRTEM micrograph of the Ge oxide layer formed on Ge(100) oxidized by a) 9eV AO at 200°C (3-4nm) b) 15eV AO at 200°C (5nm)........ 122

Figure 41 Background subtracted $GeL_{2,3}$ and $GeL_1$ spectrum image of Ge(100) oxidized by 5eV AO, acquired on Philips Tecnai STEM (CMU). ........ 123

Figure 42 AFM images of Ge(100) oxidized by a) 5eV AO at 200°C (RMS=2.26nm) b) MO at 200°C (RMS= 1.49nm) c) 5eV AO at 25°C (RMS=1.93nm), d) native oxide (RMS= 0.48nm), e) 9eV AO at 200°C (RMS=2.37nm) and f) 15eV AO at 200°C (RMS=5.25nm) ........ 126

Figure 43 Kinetic curves from QCM obtained for oxidation of amorphous Si and Ge by 9eV AO (Pitt) at T=297K and AO flux=$1.88x10^{13}$ at/$cm^2$sec. a) Oxide mass gain vs. oxidation time. b)

Oxide thickness (calculated from the mass gain) vs. AO fluence. Error bars are not visible since they are smaller than the symbols used in the data points. ..................................................... 131

Figure 44 Kinetic curves from QCM obtained for oxidation of amorphous Si and Ge by 5eV AO (Pitt) at T=297K and AO flux=$1.75x10^{14}$ at/$cm^2$sec. a) Oxide mass gain vs. oxidation time. b) Oxide thickness (calculated from the mass gain) vs. AO fluence. Error bars are not visible since they are smaller than the symbols used in the data points. ..................................................... 132

Figure 45 Kinetic curves for the oxidation of H-terminated Si(100) by 1.6, 3.6, 4.6eV [18] AO (flux=$1.45x10^{15}$at/$cm^2$ sec), and oxidation curve for amorphous Si (native oxide covered) oxidized by 9eV AO (Pitt) (flux=$1.88x10^{13}$at/$cm^2$ sec), at T=297K. ..................................... 134

Figure 46 Si and Ge oxide thickness dependence on the AO energy; combined data from X-TEM and XPS techniques from ref. 16. ................................................................................. 137

Figure 47 The Deal-Grove linear-parabolic law model fit (solid curves) through the oxidation data points (symbols) for a) Si single-crystal oxidized by 1.6, 3.6 and 4.6eV AO at T=297K (Tagawa, XPS), AO flux=$1.4x10^{15}$ at/$cm^2$sec, b) amorphous Si and Ge oxidized by 9eV AO (QCM, Pitt), AO flux=$1.88x10^{13}$ at/$cm^2$sec, at T=297K. Error bars for QCM PITT data are within the symbols for the data points. ........................................................................ 141

Figure 48 Power law model fit (solid curves) through the oxidation data points (symbols) for Si and Ge oxidized by a) 9eV AO (Pitt) at T=297K, AO flux=$1.88x10^{13}$ at/$cm^2$sec and b) 5eV AO (Pitt) at T=297K, AO flux=$1.75x10^{14}$ at/$cm^2$sec. Two sets of coefficients for one curve indicate break in the AO kinetics. .................................................................................... 147

Figure 49 Power law fit (dotted lines) through the oxidation data points (symbols) for Si oxidized by 1.6, 3.6 and 4.6eV AO at T=297K, AO flux=$1.4x10^{15}$ at/$cm^2$sec (Tagawa's data, taken with XPS) [18]. ..................................................................................................... 149

Figure 50 Atomic oxygen efficiency (%) to form Si-O and G-O bonds; 9eV AO on Si and Ge (Pitt), flux=$1.88x10^{13}$ at/$cm^2$sec and 1.6, 3.6 and 4.6eV AO on Si, from [18], flux=$1.4x10^{15}$ at/$cm^2$sec ......................................................................................................................... 150

Figure 51 Atomic oxygen beam efficiency (%) to form a) Si-O bond (1.6, 3.6 and 4.6eV AO) and b) Si-O and Ge-O bonds with 9eV AO ......................................................................... 151

Figure 52 Average AO efficiency for (1.6, 3.6 and 4.6eV AO) to form Si-O bond, and for 9eV AO to form Si-O and Ge-O bond.......................................................................................... 152

Figure 53 Comparison of initial oxidation steps of Si(100) surface by MO and AO. ..................... 154

Figure 54 The interface reaction controlled oxidation process....................................................... 160

Figure 55 Modified Reisman model –diffusion controlled oxidation process. $SiO_x$ is a growing oxide layer, with thickness x. The diffusion coefficient of oxygen, D(t), is time –dependent, due to the oxide structure changing with time. The thermal spike is brief (decays within 1ps) and localized

(~6Å from the site of impact) but allows for structural re-arrangement of the oxide towards the more thermodynamically stable ordered quartz structure. ...... 163

Figure A I- 1 Boraelectric heating stage elements [126, 127] ...... 182

Figure A I- 2AutoCAD drawings of the heating stage elements a) heater housing b) heater mount c) block-connector and d) rod-support ...... 184

Figure A I- 3 Hardware of Research QCM (Maxtek Inc) system [105] ...... 185

Figure A I- 4 The view of the QCM unit inside the AO chamber (right), and the outside of the chamber (left). ...... 186

Figure A I- 5 Image and machine drawing of the RQCM unit (with the mounting flange) ...... 186

Figure A I- 6 Top flange modification ...... 188

Figure A I- 7 Deuterium VUV source specifications and drawings (from Resonance Limited) ...... 189

Figure A II- 1 SRIM simulation of 5eV AO impact (100 000 incident atoms) onto 5Å thick $SiO_2$ layer-no transmitted atoms. ...... 191

Figure A II- 2 SRIM simulation of 5eV AO impact (1 000 000 incident atoms) onto 3Å thick $SiO_2$ layer-0.94% transmitted atoms ...... 192

Figure A II- 3 SRIM simulation of 5eV AO impact (100 000 incident atoms) onto 4Å thick $SiO_2$ layer-0.11% transmitted atoms ...... 194

Figure A II- 4 SRIM simulation of 9eV AO impact (100 000 incident atoms) onto 5Å thick $SiO_2$ layer-0.3% transmitted atoms ...... 195

Figure A II- 5 SRIM simulation of 15eV AO impact (100 000 incident atoms) onto 5Å thick $SiO_2$ layer-2% transmitted atoms ...... 196

Figure A II- 6 SRIM simulation of 5eV AO impact (100 000 incident atoms) onto 5Å thick $GeO_2$ layer-no transmitted atoms ...... 197

Figure A II- 7 SRIM simulation of 9eV AO impact (100 000 incident atoms) onto 5Å thick $GeO_2$ layer-0.006% transmitted atoms. ...... 198

Figure A II- 8 SRIM simulation of 15eV AO impact (100 000 incident atoms) onto 5Å thick $GeO_2$ layer-0.3% transmitted atoms. ...... 199

Figure A III-1 Si-O phase diagram [128, 129] ...... 200

Figure A III-2 Ge-O phase diagram [128, 129] ...... 201

Figure A III-3 Oxidation of Si in dry $O_2$ [44] ...... 202

## ACKNOWLEDGEMENTS

I would like to begin by thanking my advisor, Professor Judith C. Yang, for her guidance and support throughout my academic career at the University of Pittsburgh. I would also like to thank the members of my thesis committee for their suggestions and input regarding this work. The specimens were oxidized at the Montana State University in the laboratory of Prof. T. Minton, Chemistry Department, and MSE Department at the University of Pittsburgh. High-resolution transmission electron microscopy and electron energy loss spectroscopy were performed at the Materials Research Laboratory (MRL)-University of Illinois at Urbana-Champaign (UIUC) which is supported by the U.S. Department of Energy (#DEFG02-96-ER45439), and also at CMU.

The help from the following people is greatly appreciated: Tim Minton –(MSU), Ray Twesten, -Materials Research Laboratory, (UIUC), Tom Nuhfer (CMU), Xidong Chen (Argonne National Lab), Paul Voyles, Bill Stratton (University of Wisconsin), Steve Pennycook and Klaus Van Benthem (ORNL). Thanks to Dr. John Leonard (MSE Department, University of Pittsburgh) and Dr. Ian Robinson (UIUC) for invaluable help about the heating stage design.Thanks to the faculty, staff, and students of the Materials Science and Engineering Department.  Finally, thanks to my family, here and back home, for constant support and encouragment. Financial support from the AFOSR-MURI is gratefully acknowledged.

# 1.0 INTRODUCTION

Satellites and space vehicles residing in the low Earth orbit (LEO) are subjected to a harsh environment that can increase their failure rate. The LEO ranges from 200 to 700km in altitude, with average surface temperatures that vary between 200 and 400K [1]. Atomic oxygen (AO) is considered the most hazardous factor causing corrosion and degradation of spacecraft materials, acting either alone or in synergy with other components, such as debris impacts, vacuum ultraviolet (VUV) radiation, solar irradiation, electron and proton exposures and fluctuations in temperature, in this environment. The surfaces of the materials present in LEO are exposed to constant temperature cycling from 200-400K, which introduces stress and cracking of the materials.

Kapton and fluoroethylene-propylene (FEP) Teflon polymers are commonly used as structural components of the spacecraft. Unprotected polymers will erode rapidly in the LEO environment [2]. Current approaches to protecting polymers from erosion in LEO involve coating the polymer with $SiO_x$ or Ge [2, 3] or incorporating Si into a polymer structure so that a passivating $SiO_x$ layer will be formed upon AO exposure [4]. Germanium coating provides a barrier to AO attack and Ge is also used as a structural component which lowers the solar cell operating temperature. Germanium also helps to dissipate charge build-up.

This study focuses on the passivation of semiconductors, particularly germanium and silicon by hyperthermal AO. Background information is presented to provide an overview of Si and Ge oxidation by atomic and molecular oxygen (MO). There is a lot more information

available in the literature about the oxidation of Si than about Ge oxidation both by atomic and molecular oxygen. Since Ge and Si have the same crystal structure, available literature data and the previous results of my Master's thesis work on Si oxidation provided critical insights into the possible effects of AO on Ge oxidation [5]. The results of my MS work on Si oxidation by AO are presented in the background section in order to give the insight of the AO reaction with Si. There were still some open questions regarding the oxidation of Si in energetic AO, and one of them is the effect of AO kinetic energy on the oxide thickness and structure. The experiments in which the kinetic energy was altered were conducted within this PhD thesis to address these issues. The research objective followed by the experimental results (including kinetics data) on Si and Ge oxidation is presented in the following chapters. These results are then discussed and compared with the corresponding data available in the in order to gain more complete understanding of energetic AO effects on Si and Ge oxidation.

# 2.0 BACKGROUND

This section presents the environmental conditions in LEO, as well as issues about the materials protection from AO attack. An overview of the Si and Ge oxidation by AO and MO will be given in this chapter, including available literature data and results of my MS work. Various oxidation models for Si oxidation will then be presented, starting with generally accepted Deal-Grove model. Of particular importance, Reisman's et al. model of changing viscosity during oxidation will be described, since it is the only paper that describes the deviations from purely linear or parabolic kinetics.

## 2.1 LOW EARTH ORBIT (LEO) ENVIRONMENT

Among the most noticeable effects of the space environment on spacecrafts is the continual bombardment by AO (created by the photo-dissociation of $O_2$ by the solar photons, where the pressure in LEO is too low to permit rapid re-combination) [6]. The AO flux incident on the spacecraft's surface is very high ($10^{14}$ atoms $cm^{-2}sec^{-1}$). As a direct consequence of high velocity of orbiting spacecrafts (8km/sec at 250km altitude), AO has kinetic energy of about 5eV. The number density of AO at approximately 250km altitude is $10^9$ atoms $cm^{-3}$, where the vacuum at this altitude is $10^{-7}$ Torr [1]. Therefore, a high concentration of AO exists, which decreases with increasing altitude. The flux of the AO and thermal cycling depends on the altitude, the time, and the season. Thermal cycling, VUV radiation, charged species, such as

electrons, X-rays from solar bursts and debris impacts additionally act synergistically with AO to rapidly hasten failure of materials in LEO. As mentioned before, temperature oscillates from 200-400K in LEO atmospheres and this induces stresses and cracking of materials; therefore, my experiments were designed in this temperature range.

Although there are several methods such as $O_2$ dissociation in radio frequency (RF) plasma ashers [7] or in electron cyclotron resonance (ECR) plasma sources [28] to produce thermal or low energy AO, hyperthermal (especially 5 eV) AO is quite challenging to produce within a ground-based laboratory. A relatively recent method based on the laser detonation of $O_2$, has been developed that produces a large flux of hyperthermal AO with very low concentration of ionic O or other charged species, that best simulates the LEO environment [8, 9]. This type of AO source was used to oxidize both Ge and Si and compare to the same samples oxidized in $O_2$.

## 2.2 MATERIALS PROTECTION FROM ATOMIC OXYGEN (AO) ATTACK

Many devices based on semiconductors are present in space and exposed to harsh LEO atmosphere. Protection of solar cells is currently achieved by glass covers which add weight to the satellites. Si-based materials are also used as detectors for radiation in space and they need suitable, light-weight protection as well. Here we focus on the application of the protective coatings on materials used as structural components of the spacecrafts.

The exterior surface of the spacecraft is covered with a thermal blanket consisting of bare polymeric materials. These lightweight materials are heavily used in LEO environment because of their specific functional properties, such as solar absorptance and thermal emittance. Polymeric materials such as Kapton or FEP Teflon are readily oxidized when exposed to the LEO atomic oxygen. The reduction in thickness and change in thermal blanket functional properties occur when polymers are in contact with AO. Extensive mass loss and morphology change into the "carpet-like" structure of polymeric film are evident under the AO exposure [10].

Kapton will show 1.2 mm thickness loss after 15 years of exposure in the LEO, which is more than the desired solar array blanket thickness of 0.05mm. The majority of past and present efforts have been in alternative protective coatings than toward the replacement of Kapton [10].

Protective coatings are required to be lightweight and flexible, durable in the presence of AO as well as sufficiently thick to prevent oxidation of underlying material since oxide must form a diffusion barrier to AO. On the other hand, the coating must be thin enough not to affect functional properties of the underlying material–solar absorptance and thermal emittance.

Optically transparent inorganic materials are used as overlay protective coatings. Various types of protective coatings, such as tin dioxide ($SnO_2$), silicon dioxide ($SiO_2$), and indium tin

oxide have been used [10]. Metal coatings, such as Al are also commonly used and special attention has been paid to the perfection of the coating. Oxide coating homogeneity is critical since small pinholes and imperfections in the coating lead to the erosion of the underlying material due to its direct contact with AO [11, 12]. The reasons for the imperfections forming in the protective coatings could be due to contamination of the surface prior to the thin film deposition, microscopic undulations on the polyamide surface, abrasion during handling or processing, micrometeoroid and debris impact while in orbit. Currently, 600-1300Å thick $SiO_x$ ($1.9 < x < 2.0$) sputter-deposited coatings are used for thermal blanket protection from the AO. This type of coating shows good adhesion to the substrate as well as a small number of defects and imperfections [12]. Si, $SiO_x$, Ge and $GeO_x$ coatings all show good resistance to AO attack.

Beside resistance of the protective coating to AO attack, the following requirements must be satisfied:

-the coating must be thin, lightweight, and strongly adherent,

-the barrier must be flexible and abrasion resistant,

-the barrier must be tolerant but not alter the substrate's optical properties,

-the coating should have high enough surface conductivity in order to prevent the charge buildup [13]. The exterior coating is subjected to both natural and induced electrical environments that can produce the charge buildup on the spacecraft surfaces. This charge buildup is especially large in the case of nonconductive materials such as Kapton and Teflon.

The electrostatic charging is an extremely hazardous factor caused by the Van Allen belts and solar wind (in geostationary orbit), and can cause loss of the whole spacecraft [13]. Solar blanket assembly cross section is given in Figure 1.

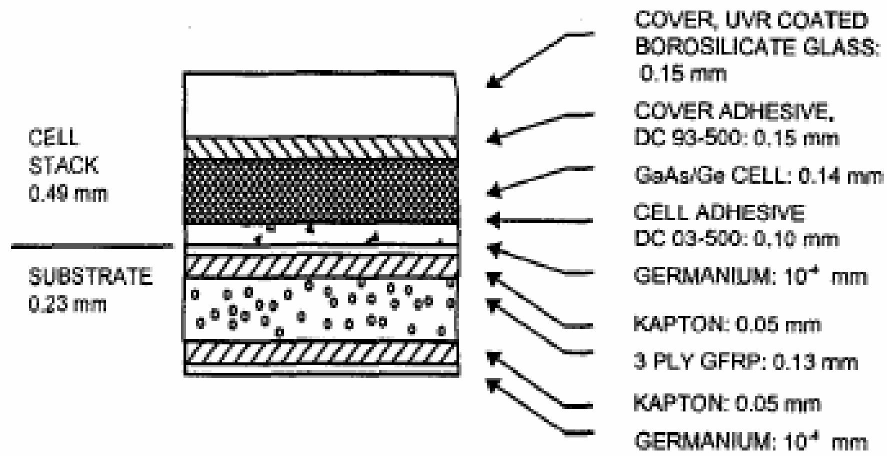


**Figure 1** Cross-sectional view of a typical blanket assembly [14].

It can be seen that Kapton is coated with Ge on its outer surfaces, and this coating is grounded to prevent build-up of electrostatic charges. Coated polymers dissipate their surface charge quite rapidly, and this decay is fast for semiconductors, such as Si and Ge.

## 2.3 SILICON OXIDATION BY AO AND MOLECULAR OXYGEN (MO)-AN OVERVIEW AND COMPARISON

Kinetics of adsorption of atomic oxygen on Si(100) was investigated by Engstrom et al. using X-ray photoelectron spectroscopy (XPS) and probability of adsorption of atomic oxygen as a function of substrate temperature, coverage and beam translation energy [15]. Figure 2 shows the adsorption probability of AO and MO on the Si(100) substrate.

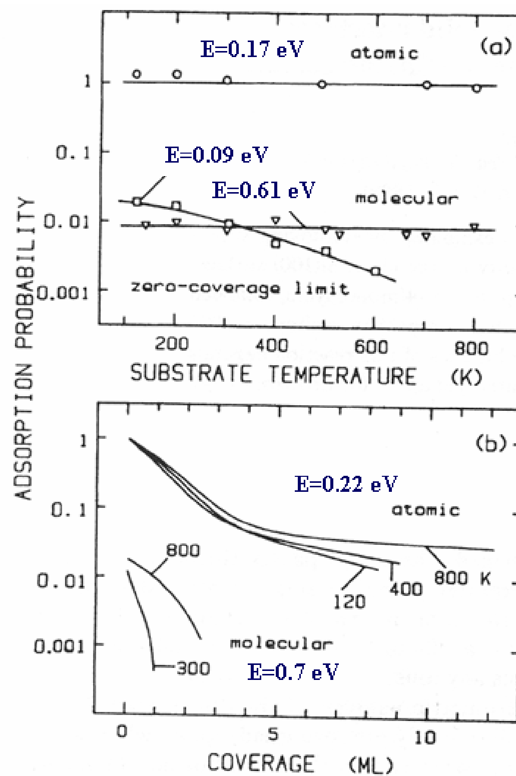


**Figure 2** Adsorption probabilities for AO and MO (a) for zero oxygen coverages as a function of substrate temperature, the translational energies were 4kcal/mole for O and 2 and 14kcal/mole for $O_2$ (as indicated on the graph), with incident angle $75^o$ in both cases, and (b) for different oxygen coverages on different substrate temperatures. The translational energies were 16kcal/mole for O and 5kcal/mole for $O_2$. (Engstrom et al. XPS) [15]

Adsorption probability of MO is dependent on both incident beam energy and substrate temperature, and ranges from 0.002-0.04. In contrast, AO adsorption probability is not affected by the substrate temperature, angle of incidence and incident beam energy, it is 1.00 (for the substrate temperature 120-800K) as can be seen in Figure 2-a. This finding indicates a facile, direct adsorption of AO on the exposed material. Therefore, it could be generally assumed that the oxide formed during AO exposure is due to AO only. This is an important observation since some fraction of O2 is commonly present in AO sources. For example, a significant amount of O2 (almost 20%) exists in the beam of the FASTTM atomic oxygen source at the University of Pittsburgh [16]. The fractions of the species present in the AO beam of the LDS source are given in Table 2 section 5.1.1

The oxygen coverage of the substrate plays a significant role in the adsorption probability of AO and MO. This is shown in Figure 2-b [15]. It can be seen that the adsorption probability for AO is much greater than that for MO for all coverages. For AO, there is a rapid decrease in adsorption probability as the coverage increases to 3-4 monolayers (ML) (1ML=6.8x1014 atoms cm-2). After this coverage is reached, there is slower adsorption of AO and the rate of oxidation begins to be dependent on the substrate temperature; e.g., it increases as the temperature rises.

This point at 3-4ML is defined as the “break” in the AO kinetics. For MO there are also two stages of adsorption, but the transition occurs near 1ML. Figure 3 shows the coverage (ML) that can be achieved by atomic and MO oxidation as a function of exposure (ML) to these oxidizing species.

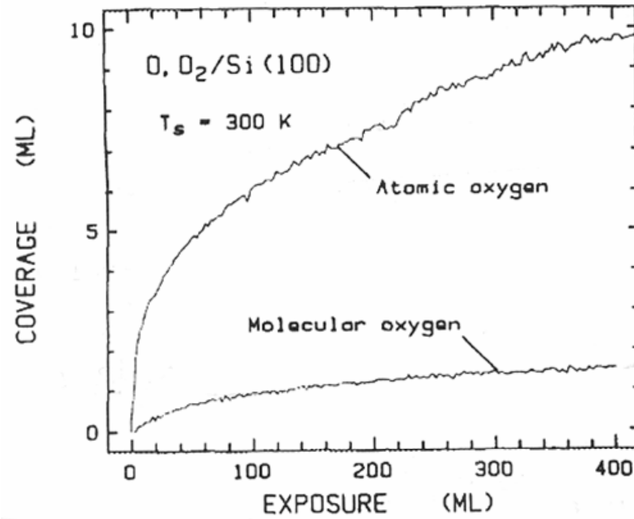


**Figure 3** Coverage dependence on exposure for AO and MO on Si(100) substrate at 300K (XPS, Engstrom et al.) [17].

MO shows a two step reaction, with initial, fast step that reaches its completion around 1ML. On the other hand, for AO the fast step of adsorption reaches its completion near 3-4ML and it is followed by the slower step, which does not saturate, even at 10ML and greater. This two-stage oxidation by AO shows similarities with the well-known Deal-Grove oxidation model which is applied to thick oxide growth. [17]. The oxide thickness dependence on the AO fluence and energy is shown in Figure 4. Hyperthermal AO beams with average kinetic energies of 1.6, 3.6, and 4.6eV were obtained by changing the laser timing, and Tagawa et al. measured the oxide thickness by XPS.

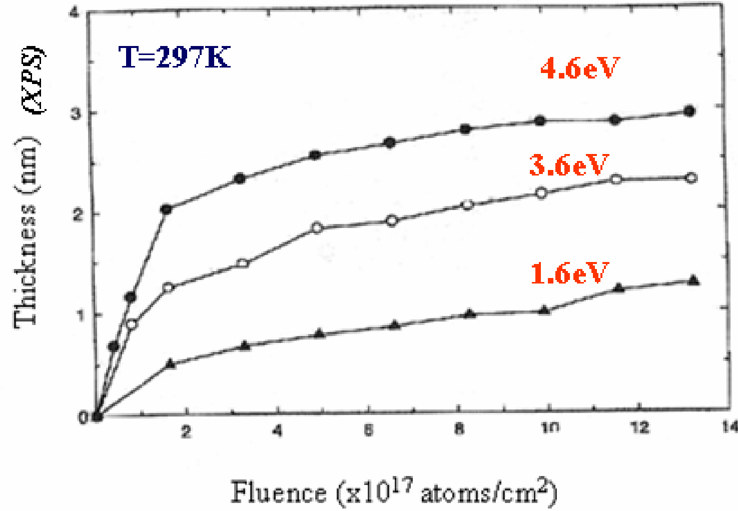


**Figure 4** Oxide thickness versus fluence for AO oxidation of H-terminated Si(100) at 297K . The hyperthermal AO beam had three different translation energies: 1.6eV, 3.6eV and 4.6eV (XPS, Tagawa et al.) [18].

One intriguing observation, from Figure 4, is that H-terminated Si(100) surface can be oxidized by AO even at the temperatures as low as room temperature. Previous studies have shown that HF-cleaned Si surface (Si surface with H-termination) oxidation does not proceed quickly even at 400$^{o}$C, as compared to the clean surface with dangling bonds [19]. As mentioned before, two step processes are characteristic for the oxidation by AO for all three oxidation curves shown in Figure 4. Tagawa et al. found using XPS that the transition from the fast to slow oxidation stage is at the oxide thickness of one or two atomic layers (~2nm) [18]. Oxidation with dangling bonds at the surface region as well as backbond oxidation is the mechanism of the initial rapid oxidation by AO [18]. Similarly to the previous investigators, they found that the slower secondary stage involves transportation of oxidants through the $SiO_2$ layer. These investigators also found that 5eV AO produces stoichiometric, bulk-like $SiO_2$, and mainly the presence of the $Si^{4+}$ oxidation state with only a few percent of suboxides [18]. Engstrom et al. reported that oxidation of Si(100) by energetic AO, but only of 0.16eV, kinetic energy, produced

a large amount of suboxides which in XPS showed that the $SiO_2$ bulk signal was not the major peak in the analyses [20]. Based on previous research, it can be concluded that formation of bulk-like, stoichiometric silica can be directly associated with the high kinetic energies of the AO.

While Engstrom and Tagawa both studied oxidation of Si by XPS, Rosencher studied thermal oxidation of Si in dry oxygen using $^{18}O$ as the tracer [123]. $SiO_2$ layers first grown in oxygen were further grown in highly $^{18}O$- enriched oxygen for 8.5hrs, at 930$^{o}$C. Since the major part (93%) of the $^{18}O$ was accumulated near the Si/$SiO_2$ interface, it was inferred that the oxide grows mainly at the Si/$SiO_2$ interface, by the long-range migration of the oxygen through the oxide.

Although 7% of $^{18}O$ atoms were found in the vicinity of the oxide surface, it was concluded that neither the oxygen atoms already fixed into the oxide layer nor the Si atoms are involved in transport mechanism. Costello et al. observed previously by secondary ion mass spectrometry that the bulk of the oxide does not incorporate oxygen during the oxidation and that a new oxide grows at the Si/$SiO_2$ interface [125]. The studies were based on sequential $^{16}O$ and $^{18}O$ oxidation. Nevertheless, these studies also revealed the occurrence of oxygen exchange process at the external $SiO_2$ surface.

### 2.3.1 Effects of hyperthermal AO on Si oxidation-previous MS research

My MS thesis focused on the effect of energetic (5eV) AO on the oxidation of Si-single crystal. Some of the results of this previous study will be presented in this section, since they give the insight in the oxide thickness and surface roughness, and oxide structure comparison for the same samples oxidized in MO. The structural properties of the oxide formed by 5eV AO, and oxidation states in the oxide and across the $Si/SiO_2$ interface were investigated within my MS thesis. The investigation of the energetic AO effect on Si oxidation was continued within the course of this PhD thesis, and new findings are presented in the results section of this document.

## 2.4 $SiO_2$ SURFACE ROUGHNESS AND THICKNESS. SI/$SiO_2$ INTERFACE THICKNESS

The thickness of the oxide formed by 5eV AO and MO oxidation of Si(100) single crystal was determined by high-resolution transmission electron microscopy (HRTEM) and Rutherford backscattering spectrometry (RBS), and this work is a part of my MS thesis [5]. The thickness of the silicon oxide created by 5eV AO on Si(100) is ~5nm, while the passivated layer formed by MO was only 3nm thick (Figure 5).

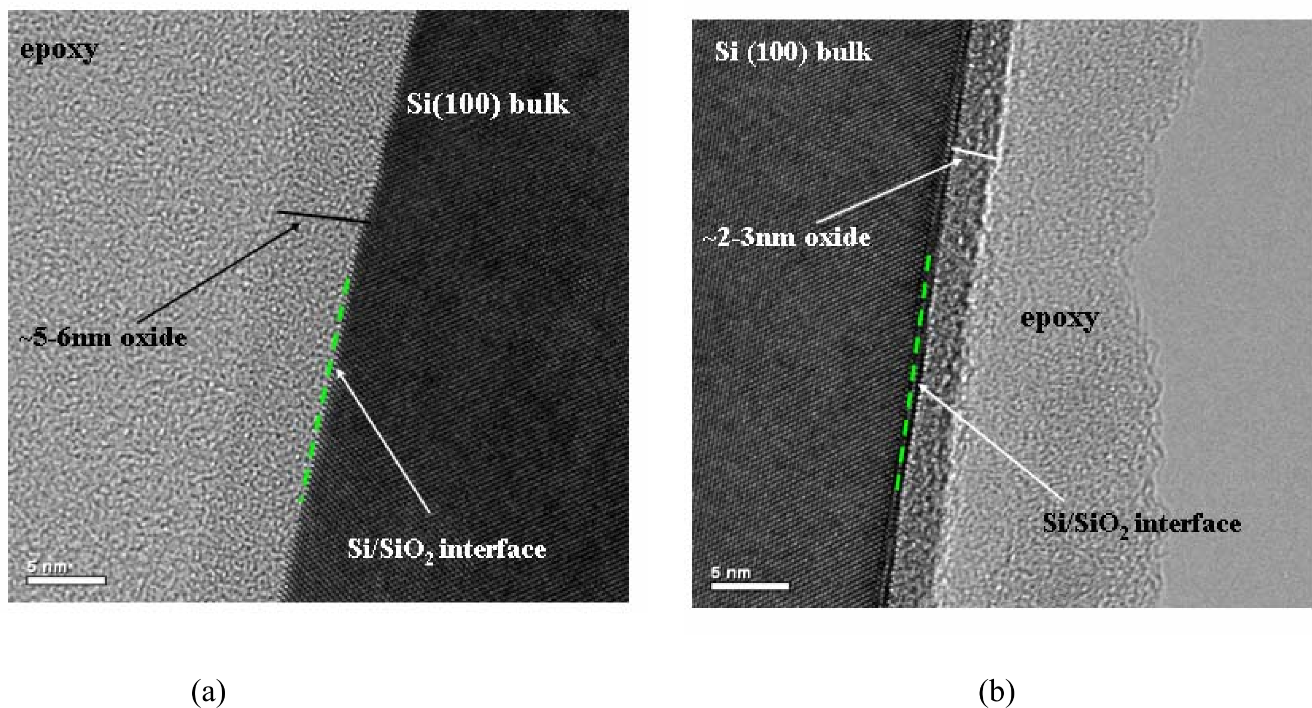


(a) (b)

**Figure 5** Cross-sectional HRTEM micrographs of the silicon oxide layer formed on Si(100) oxidized by a) 5 eV AO b) MO at 220°C [5, 21].

Oxide created with 5eV AO appeared to be more uniform in thickness, as compared to the oxide formed by MO. The Si/$SiO_2$ interface formed by 5eV AO exposure seems to be abrupt, where no clear evidence of secondary phases, cavities or voids exists [21]. In order to determine

the thickness of the transitional interface region, intensity profiling method was used on HREM micrographs as well as high spatial resolution electron energy loss spectroscopy (EELS).

Intensity profiles across the Si/$SiO_2$ interface created by atomic and MO on Si(100) are given in Figure 6 and Figure 7, respectively. Intensity plots were obtained by averaging intensities vertically in the area enclosed by the rectangle. This analysis was carried out using Gatan Digital Micrograph [22, 23].

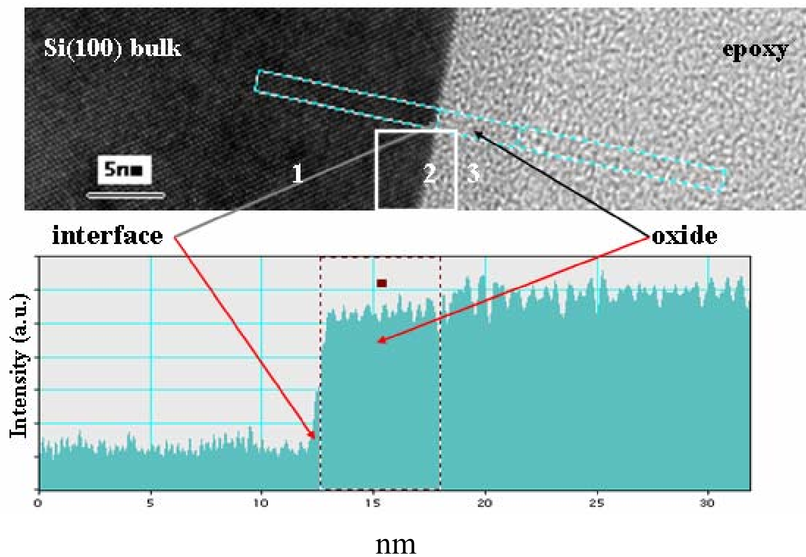


**Figure 6** Intensity profiles obtained from cross-sectional HRTEM micrographs of the silicon oxide layer formed on Si(100) oxidized by 5 eV AO at 220$^oC$ [5, 21].

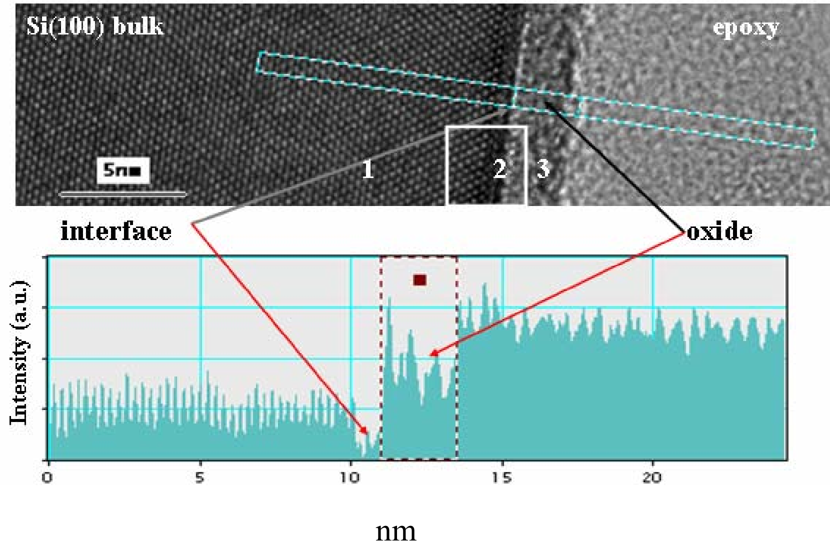


**Figure 7** Intensity profiles obtained from cross-sectional HRTEM micrographs of the silicon oxide layer formed on Si(100) oxidized by MO at 220°C [5, 21].

The intensity profiling across the Si/$SiO_2$ interface suggests that almost no interfacial layer is present for 5eV AO oxidized Si(100) (Figure 6), whereas ~1 nm interfacial layer is found to exist for $O_2$ oxidized Si(100) (Figure 7). Electron energy loss spectra showing an abrupt transition from $Si^{o}$ to $Si^{4+}$, for the AO oxidized sample, are presented later. In contrast, $Si^{o}$ to $Si^{4+}$ transition for the MO oxidized sample was found to be gradual, suggesting a broad interface, as also evidenced by EELS spectrum imaging (shown later in section 2.4.1).

The atomic force microscopy (AFM) investigation was performed on a Dimension 3100 Digital instruments, and AFM images were acquired in the tapping mode. AFM images of Si(100) oxidized by 5eV AO and MO at 220°C are given in Figure 8. The surface roughness of the oxide formed by 5eV AO was nearly twice than that formed by MO. The mean square roughness (RMS) is ~1.54nm (Figure 8-a) for the oxide created by AO, and ~0.83nm (Figure 8-b) for the oxide created by MO.

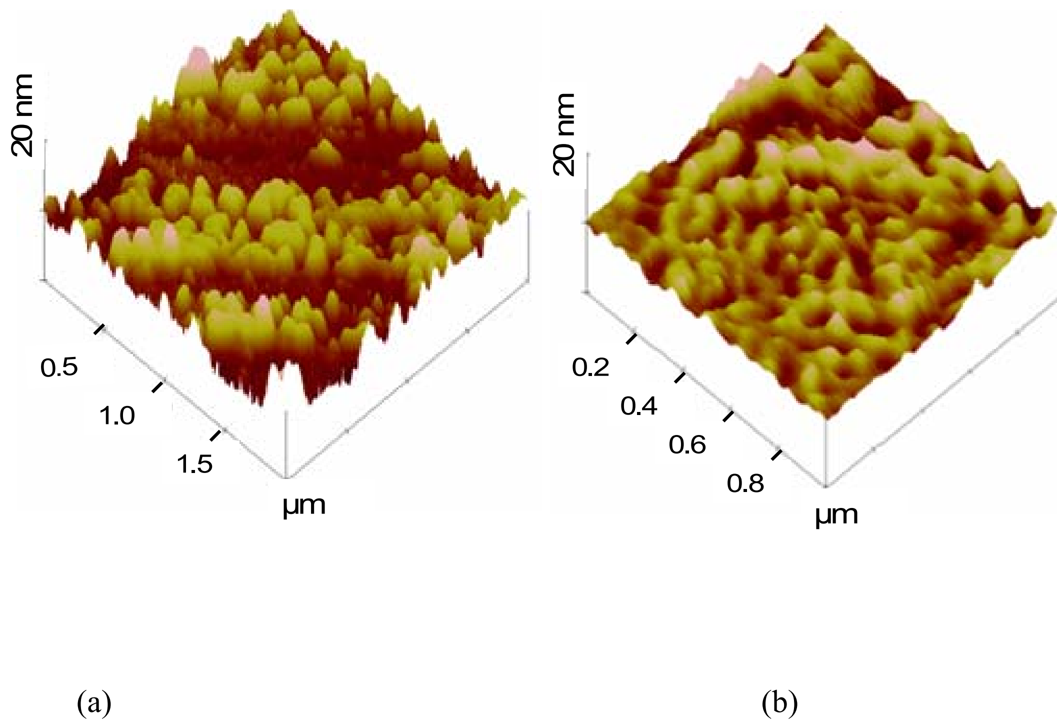


(a) (b)

**Figure 8** AFM image of Si(100) oxidized at 220°C a) by 5eV AO, RMS≅1.54 ± 0.21nm b) by MO, RMS≅0.83 ± 0.13nm.

### 2.4.1 Investigation of Si/$SiO_2$ interface and oxidation states

The EELS technique was used to study and compare properties of the Si/$SiO_2$ interface when formed by energetic (5eV) AO and by thermal MO. Characteristic Si $L_{2,3}$ and O K background subtracted edges obtained from Si(100) single crystal, oxidized at 220°C by 5eV AO, are shown in Figure 9-a and 9-b, respectively. JEM 2010F microscope operating at 200kV, and with the probe size of 1.2nm and 1eV energy resolution was used for the data acquisition.

Basically, background subtraction was done using the Hartree-Slater model embedded in GATAN EELS software, and the background pre-edge window <10eV was used [23]. The length of the scan was 95 Å, and the distance between each spectrum was ~6 Å.

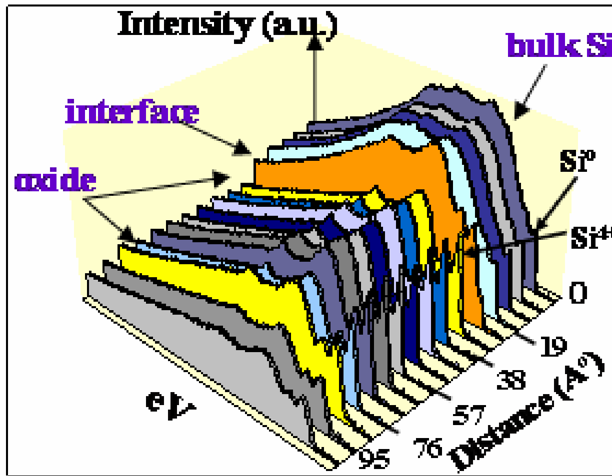


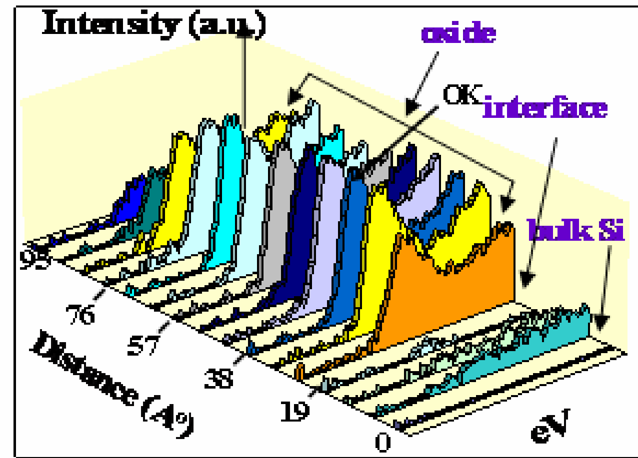


(a) (b)

**Figure 9** Characteristic core-loss ionization for Si(100) oxidized by 5eV AO a) Si $L_{2,3}$ edge b) O K edge acquired on JEM 2010F [5, 21].

Characteristic Si $L_{2,3}$ and O K background subtracted edges obtained from Si(100) single crystal, oxidized at 220°C by MO, are shown in Figure 10-a and 10-b, respectively. The length of this scan was 64 Å, and the distance between each scan was ~3.2 Å.

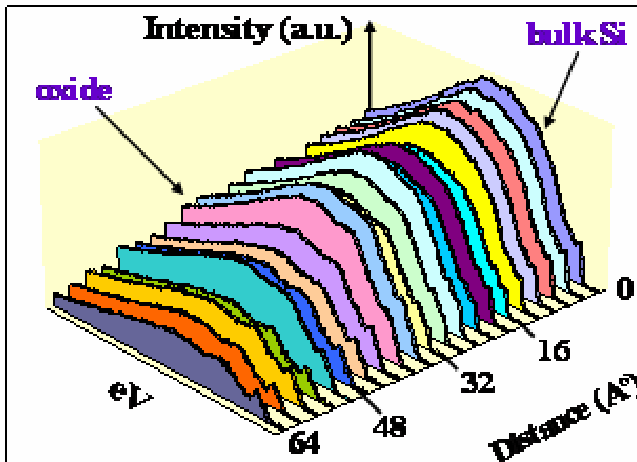


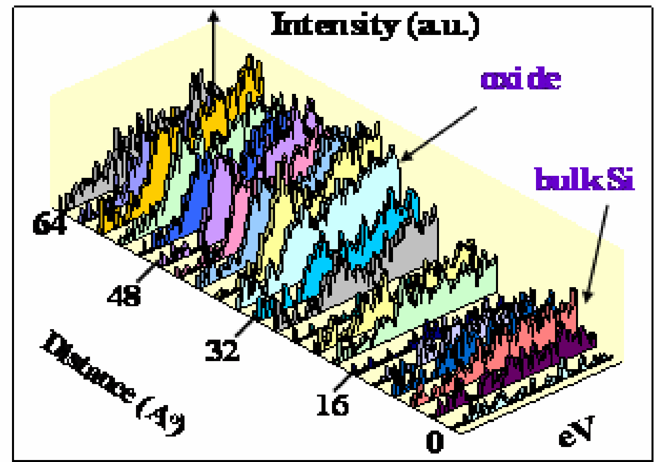


(a) (b)

**Figure 10** Characteristic core-loss ionization for Si(100) oxidized by MO a) Si $L_{2,3}$ edge b) O K edge acquired on JEM 2010F [5, 21].

The evolution of the $SiL_{2,3}$ edge from the bulk silicon ($Si^o$), across the $Si/SiO_2$ interface to the silica bulk oxide ($Si^{4+}$) shows that only peaks corresponding to $Si^o$ and $Si^{4+}$ valence states are present (Figure 9-a). Both $SiL_{2,3}$ and O K ionization edges reveal an abrupt $Si/SiO_2$ interface for the Si(100) sample oxidized by 5eV AO (Figure 9-a and 9-b). The $SiL_{2,3}$ edge onset shift from $Si^o$ (99.5eV) to $Si^{4+}$ (103.5eV) valence state is abrupt, no evidence of suboxides near the interface is present (Figure 9-a). Results from $SiL_{2,3}$ edge of Si(100) oxidized by MO reveal that there is a transition (~1nm) from $Si^o$ to $Si^{4+}$ state, with a number of intermediate states (Figure 10-a and 10-b). These results confirm HRTEM results where intensity profiling showed that there is no interfacial layer present for Si(100) oxidized by 5eV AO (Figure 6), and that ~1nm thick interface layer is present for Si(100) oxidized by MO (Figure 7).

## 2.5 INCREASED ORDERING IN THE SI-OXIDE CAUSED BY ENERGETIC AO

In nature, depending on the pressure and temperature during crystallization of the silica, different minerals can be formed. There are many crystalline forms of $SiO_2$, polymorphs including: α-quartz, β-quartz, α-cristoballite, β-cristoballite, α-tridymite, β- tridymite, coesite, stishovite, lechatelierite and keatite. The alpha phase is stable at room temperature and 1 atm pressure of $O_2$. Creation of β phase requires heat and with cooling, they transform into their alpha phase. Only three polymorphs of $GeO_2$ have been reported, quartz, rutile and cristobalite type [26]. The regions of stability for the $SiO_2$ polymorphs are given in Figure 11 (Si-O and Ge-O phase diagrams are given in Appendix ).

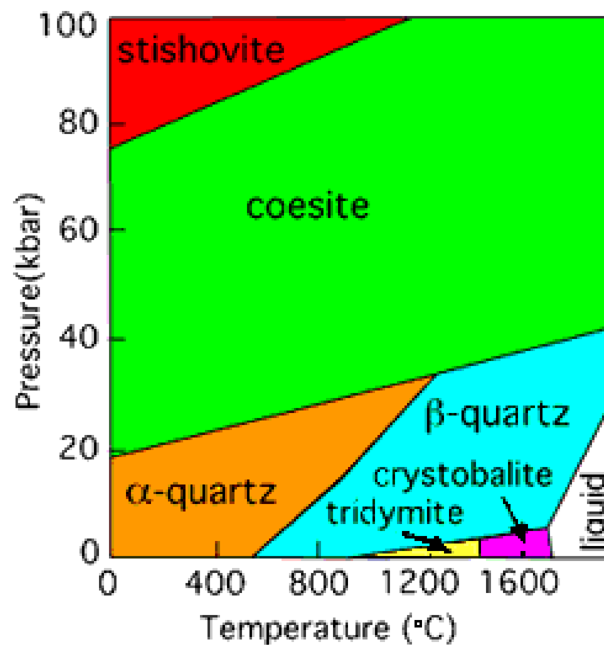


**Figure 11** $SiO_2$ phase stability regions [24].

Silica and germania phases along with their crystal structure and lattice parameters are given in Table 1.

**Table 1** Crystal structures of $SiO_2$ and $GeO_2$ phases [25, 26].

| Mineral | Crystal System | a(nm) | c(nm) | Stable at T ($^oC$) |
|---|---|---|---|---|
| $SiO_2$ α-quartz | Trigonal | 0.49134 | 0.54052 | Room T-573 |
| $SiO_2$ β-quartz | Hexagonal | 0.5020 | 0.5523 | >573 |
| $SiO_2$ α-tridymite | Orthorhombic | | | <870 |
| $SiO_2$ β- tridymite | Hexagonal | 0.5052 | 0.8272 | >870 |
| $SiO_2$ α-cristobalite | Tetragonal | 0.49281 | 0.68217 | <268 |
| $SiO_2$ Coesite | Monoclinic | 0.7137 | 1.2370 | Intense T and pressure (~2.3-7.8GPa) |
| $SiO_2$ Stishovite | Tertragonal | 0.41262 | 0.26896 | Intense T and pressure (~7.8 GPa) |
| $SiO_2$ Lechatelierite | Amorphous | | | |
| $SiO_2$ Keatite | Tetragonal | | | |
| $GeO_2$ α-quartz | Hexagonal | 0.49850 | 0.5648 | >470 at ambient p |
| $GeO_2$ rutile type | Tetragonal | 0.4397 | 0.2863 | Ambient T and p |
| $GeO_2$ cristoballite type | Tetragonal | 0.4985 | 0.7070 | |

Alpha-quartz is the most stable and common form of $SiO_2$, usually found at room temperature. Alpha-tridymite and α-cristobalite do not occur as the stable phases, and can only be found as metastable phases that are converted to the stable forms of $SiO_2$ under certain pressures and temperatures. Only the α-quartz, β-quartz and tridymite can actually exist as a stable phase under room temperature conditions. Coesite, stishovite and lechatelierite are very rare, natural forms of $SiO_2$ that are created under the conditions of extreme temperature and

pressure. They can be found in crater impact sites which possess huge temperature and pressure at the moment when meteorites struck the earth. Keatite is a synthetic $SiO_2$ form. Some fundamental thermodynamic properties for Si and Ge elements and their oxides and for $SiO_2$ and $GeO_2$ phase transformations are given in the Appendix . Electronic properties and bond strengths are also given in the same Appendix.

High–temperature oxidation of metals usually creates polycrystalline oxides, but $SiO_2$ formed by high temperature oxidation is non-crystalline [42]. Low-temperature Si oxidation also forms non-crystalline oxides.

A less random arrangement of atoms in the Si-oxide was formed by energetic AO which is quite different than the random arrangement in the oxide formed by MO species. Plan view high-resolution transmission electron micrographs (HRTEM) of Si(100) oxidized by 5eV AO and MO are shown in Figure 12-a, 12-b respectively, and corresponding selected area electron diffraction (SAED) patterns are given as inserts in the upper left corner of the micrographs.

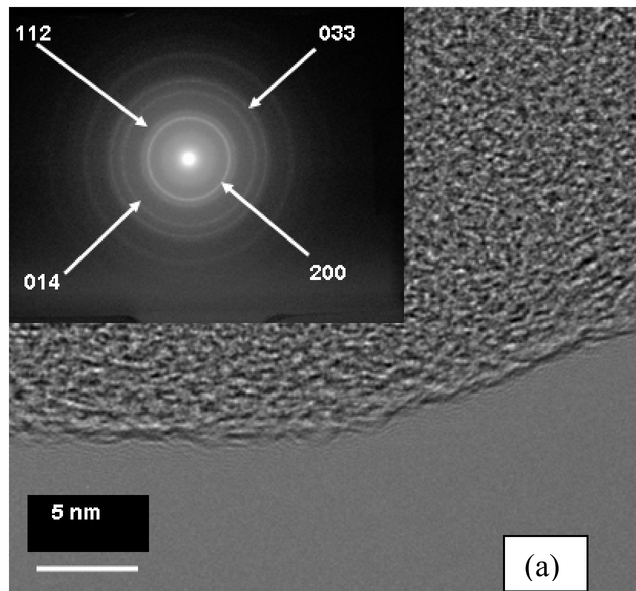

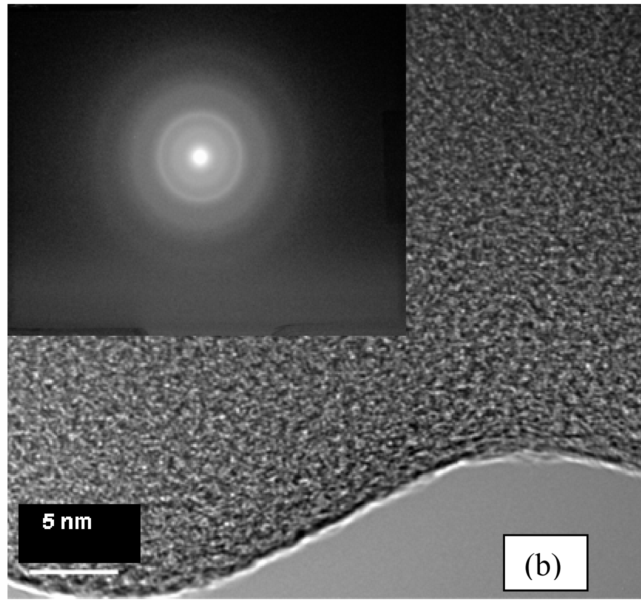


**Figure 12** (a) Plan-view HRTEM micrographs and corresponding SAED pattern of the silicon oxide layer formed on Si(100) oxidized by 5eV AO (b) MO [5, 21].

Selected area diffraction pattern of the Si(100) oxidized by MO showed diffuse haloes rings, characteristic of amorphous materials. In contrast, much sharper diffraction rings are present in the diffraction pattern of Si(100) oxidized by reactive AO species. Due to their sharpness, certain diffraction rings can be identified and indexed. These experimental d-spacings for the oxide created by reactive 5eV AO species ($d_{200}$=2.070Å, $d_{112}$=1.783Å, $d_{014}$=1.282Å and $d_{033}$=1.085Å) correspond to that of alpha-quartz ($d_{200}$=2.1275Å, $d_{112}$=1.8178Å, $d_{014}$=1.2879Å and $d_{033}$=1.1144Å) [24]. The lattice parameters for the oxide created by AO were determined to be $a$ = 4.78 ± 0.1and $c$ = 5.13 ± 0.1 Å, while $a$ = 4.9134 and $c$ = 5.4052 Å for alpha-quartz.

Experimental lattice parameters are smaller than that of alpha-quartz, suggesting that the silica layer created by 5eV AO is under compression [26, 27]. This conclusion is in agreement with the previous Fourier transform infrared spectroscopy (FTIR) results of Tagawa et al., which revealed smaller Si-O-Si bond angles in the oxide film created by AO as compared to those of alpha-quartz, indicating that the $SiO_2$ film is under compression [28].

## 2.6 GERMANIUM OXIDATION BY AO AND MO-AN OVERVIEW AND COMPARISON

Low T oxidation (25-400$^oC$) of clean Ge surfaces in $O_2$ was studied by Ligenza, and the oxidation law was found to change with T and the oxidation time. In this early study (1960), the experiments were carried out with a vacuum microbalance and Ge powder, and the reaction course was followed by measuring the increase in the weight of powder. Ligenza found that the initial oxidation (up to 2 oxide layers) of clean Ge at T below 250$^oC$ follows the logarithmic law, while the subsequent oxidation beyond the second layer obeys Cabrera-Mott inverse logarithmic oxidation law [114]. At the T~250$^oC$, second layer forms in less than 1 min, while the subsequent oxidation rates beyond the second layer are very slow. For example, even at 400$^oC$, only 17.5Å of $GeO_2$ formed in three hours [114].

Past investigators used a variety of surface science methods to directly compare thermal oxidation of Ge to oxidation in more reactive oxygen species. Wang et al. compared thermal oxidation of Ge with the electron cyclotron resonance (ECR) plasma oxidation during the first 20min [30]. They utilized *in situ* single wave ellipsometry (SWE) to monitor the oxide thickness in real time, and *in situ* static spectroscopic ellipsometry (SE) was performed at various times as well to monitor the oxide thickness [30]. Optical modeling, using single and two layer models,

was used to find best fit parameters for ECR and thermal oxidation. Figure 13 shows the progression in the oxide thickness as a function of oxidation time at different temperatures.

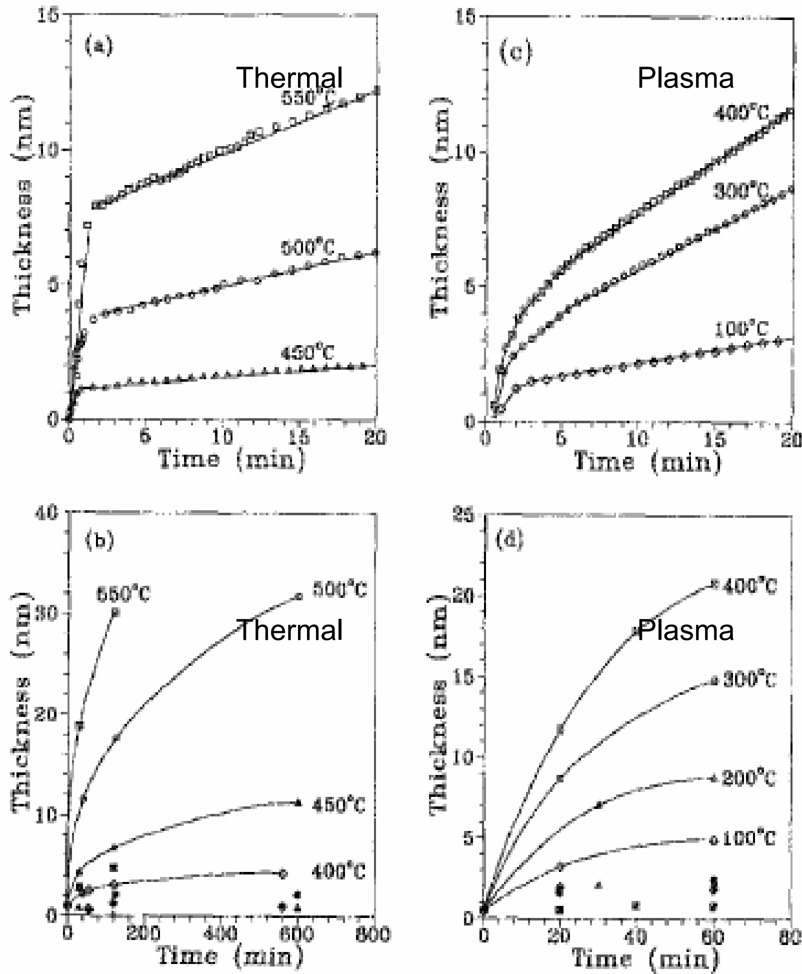


**Figure 13** Oxide thickness as a function of oxidation time a), b) thermal oxidation c), d) ECR plasma oxidation at +60V bias. Solid lines-total thickness; filled symbols-interface thickness. a) and c) were obtained from SWE measurements and using single layer model, while b) and d) obtained by SE using the two layer model (ellipsometry, Wang et al.) [30].

Similar to the kinetics proposed for Si thermal oxidation, linear to parabolic oxidation kinetics was observed for both thermal and ECR plasma oxidation of Ge for longer time (Figure 13-b and d). The oxidation species are MO for thermal oxidation and plasma oxidant species for

ECR plasma oxidation. An initial, faster oxidation regime exists for the initial regime, representing the surface reaction between the substrate and oxidant species, is bias independent for both oxidation methods. The observation that the oxide growth rate does not depend on the bias applied on the substrate means that this initial regime represents the surface reaction between Ge and plasma oxidant species for ECR plasma oxidation and molecular oxygen for thermal oxidation.

The oxidation rate for the case of ECR plasma oxidation is greatly affected by positive substrate bias after the initial regime, when the thicker oxide is formed. It was concluded that negatively charged oxidation species dominate ECR plasma kinetics in the transport-limited regime of oxide growth. Negatively charged O ions are generated by the dissociation of $O_2$ by plasma electrons. Activation energies were determined from the linear Arrhenius plots of the parabolic rate constants for thermal and ECR plasma oxidation. It was found that the activation energy for ECR plasma oxidation is almost one order of magnitude smaller than for thermal oxidation. The main reason for this observation is due to the different oxidizing species, $O^-$ and $O_2$, for plasma and thermal oxidation, respectively.

The effect of VUV irradiation on Ge oxidation is discussed next, since these studies focused on the possibility to form thicker oxide layer in more reactive species than $O_2$. It could be seen from Figure 14 that an initial, rapid linear oxidation step is present for each T in the plot.

Usually, low T oxidation of Ge (without VUV) obeys logarithmic behavior in the initial stage, which is due to the blocking of electron tunneling from the substrate towards the surface by the oxide layer [114]. Once the oxide thickness is too large, electrons can no longer tunnel. 7.2eV photons emitted from Xe lamp can easily induce transition of electrons from Ge valence band into the $GeO_2$ conduction band for much higher oxide thickness than 3nm that effectively

blocks the electrons during normal low T oxidation. These electrons can then chemisorb to $O_2$ at the oxide/$O_2$ interface to produce neutral and charged O species which then can easily transfer through the oxide to the Ge/oxide interface to form $GeO_2$.

This effect of enhanced electronic transfer could be similar to the effect of energetic AO impact on the sample surface. It could be expected that kinetic energy of AO could influence electron transfer from Ge to $GeO_2$, and therefore rapid, linear oxidation step might be observed for the oxidation by energetic AO, similarly to the effect of VUV irradiation.

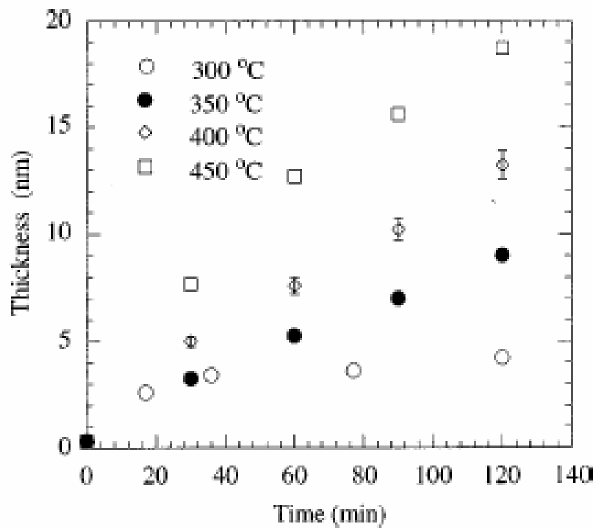


**Figure 14** Ge oxide thickness as a function of VUV exposure time at different temperatures. Vacuum ultraviolet radiation was emitted by a Xe silent discharge lamp, and film thicknesses were measured by SWE (Craciun) [31].

It was also concluded by Craciun et al. [31] that the increase in the oxide thickness as compared to $O_2$ oxidation might be due to the formation of more chemically active species, such as ozone and O atoms formed by the photodecomposition of $O_2$. Therefore, the oxidation in reactive AO is expected to be enhanced as compared to the oxidation in $O_2$ at the same temperature.

## 2.7 OXIDATION PROCESS

There are many factors involved in the composition and defects present in the thin films, and these factors could be surface orientation, reconstruction, surface preparation and impurities [42]. Consequently, these difficulties in controlling Si surface led to many, but not one conclusive model for Si oxidation in low T regime. The progress is made starting from the single-crystal films in order to reduce the influence of the substrate factors. The oxidation of Si and Ge now can be explored in more details, since single-crystals with few defects and well-controlled surfaces are available.

Oxide growth kinetics on Si and Ge can be divided into three steps. First step is the reaction of oxygen with the Si or Ge substrate and initial oxide formation, while the second step is the diffusion of oxygen through the oxide scale formed. The final, third step is the reaction of $O_2$ with Si or Ge, to form the oxide, at the semiconductor/oxide interface. The first and the third step are basically the same denoting the reaction between Si or Ge and $O_2$, the only difference is that the first step takes place at the bare Si surface, while the third step occurs when the oxide is already formed. These steps could be represented as following for the case of Si or Ge (for clarity, only the symbol for Si is used below):

1. $Si + O_2 \rightarrow SiO_2$ initial oxide formation at Si surface
2. $O_2$ (diffusion) $\rightarrow$ to the $Si/SiO_2$ interface $O_2$ transport through the oxide scale
3. $O_2$ (at $Si/SiO_2$ interface) + Si $\rightarrow$ $SiO_2$ reaction of Si and $O_2$ at the $Si/SiO_2$ interface

Each of the basic steps mentioned above will be considered next and different effects which could influence these steps will be commented. For example, the very initial stage (step 1), which represents the initial oxide formation, depends on the electronic transfer. The transfer

of electrons from Si or Ge to the $O_2$ molecule at the oxide/$O_2$ interface facilitates $O_2$ dissociation, and formed ionic and atomic species are transported through the oxide faster than non-dissociated $O_2$. Whether the semiconductor has direct (GaAs, InP) or indirect (Si, Ge) band-gap [43] could play the role in the oxidation kinetics. Possible implications of AO on each of the steps, and how these steps could be altered as compared to the steps for $O_2$, will be discussed in this chapter as well.

### 2.7.1 The initial oxide formation

In the first oxidation stage of Si and Ge, all the trap electrons in the surface states are used and ~ 10 Å of oxide is formed. Surface states containing trapped electrons are not available any more after the initial (native oxide) formation; therefore, the rate of the oxidation process decreases. Further growth of the oxide film in this initial stage is enabled by tunneling of electrons through the initially formed thin oxide, which is temperature independent. The electrons that tunneled through the oxide scale chemisorb to the $O_2$ at the oxide/$O_2$ interface to form $O_2^-$, which can easily dissociate into neutral and charged O species, which are more mobile and therefore easily transported to the semiconductor/oxide interface where they react with Si or Ge to form a new oxide. When the oxide thickness reaches 20Å, electron tunneling becomes very difficult since it is limited by the oxide film thickness. In order to continue the oxidation process a higher temperature must be employed to achieve thermionic emission [46, 47]. It is important to distinguish between these two different mechanisms for the electron transport, tunneling and thermionic emission. An incident electron with the energy below the height of a potential barrier of limited thickness has a finite probability of penetrating the barrier. Particles that have penetrated the barrier in this manner are said to have tunneled through the barrier as

opposed to having been excited over the top of the barrier. A thermionic emission becomes a more likely mechanism for the electron transport when the oxide thickness exceeds 20Å, since electron tunneling is very difficult. The region in the film thickness where electron tunneling and thermionic emission occur simultaneously to an appreciable extent is limited. The tunneling current is extremely large for very thin films, thinner than 20Å, but decreases sharply for larger thickness. The thermionic emission cannot occur easily at low temperatures while tunneling is essentially independent of temperature.

**2.7.1.1 Thermionic emission effect**

Thermionic emission helps electrons to overcome the energy barrier of a band gap and to transfer from the Si to $SiO_2$ conduction band. Figure 15 is a schematic drawing of the fluxes for the thermionic emission model.

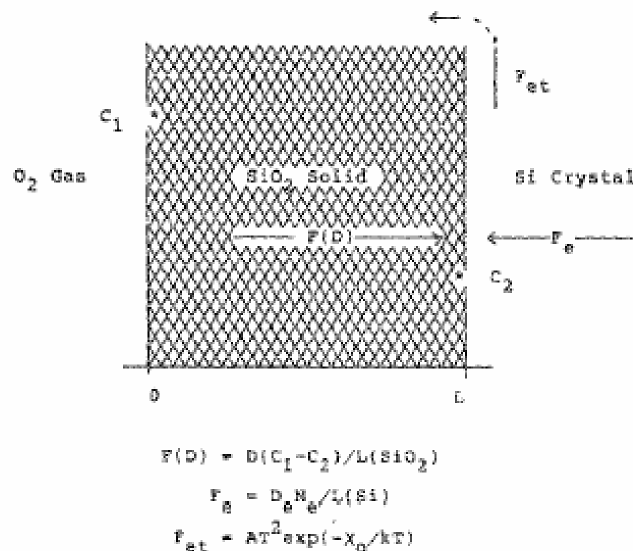


**Figure 15** Schematic representation of fluxes for thermionic emission model [47].

Oxidation steps for the oxidation of Si by $O_2$ in initial stage (linear regime), as determined by Irene et al [46, 47], are:

1. $e^-$ (conduction band of Si) $\rightarrow$ $e^-$ (Si surface)
2. $e^-$ (Si surface) $\rightarrow$ $e^-$ (free in $SiO_2$)
3. $e^-$ (in $SiO_2$) +$O_2$ (from diffusion) $\rightarrow$ $O_2^-$
4. $O_2^-$ $\rightarrow O^-$ + O
5. $Si^+$ (at Si surface) +$O^-$ + O $\rightarrow SiO_2$

Step 1 is the flux of electrons to the Si surface

Step 2 is emission of electrons over the energy barrier-rate limiting

Step 3 is electron attachment to $O_2$

Step 4 is decomposition of $O_2^-$ into neutral and charged species

Step 5 is reaction of atomic and charged species.

Electronic transfer from the Si to $SiO_2$ conduction band by thermionic emission on 220$^o$ C appears to be very sluggish (step 2). Released electrons can combine with the $O_2$ molecule to form $O_2^-$ ion (step 3). The $O_2^-$ ions decompose into the $O^-$ ion and neutral O atom, which are more mobile than $O_2$ (step 4). Therefore, the $O^-$ ions and neutral O atoms will diffuse quickly to the Si/$SiO_2$ interface and react with the $Si^+$ cations to form $SiO_2$ (step 5). Once all of the electrons from the Si conduction band are consumed, the formation of the $O_2^-$ on the $SiO_2$ surface and consequent dissociation to monatomic O species on the $SiO_2$ surface will become very difficult. Consequently, for the oxide to continue to grow, $O_2$ must diffuse through the oxide, which is a very slow process and corresponds to the parabolic growth regime.

The thermionic emission model, as proposed by Irene et al., assumes that the rate-limiting step is the electron flux from Si to $SiO_2$ (step 2) [46, 47]. These authors proposed that the thermionic electron flux from Si to $SiO_2$ is proportional to the oxide growth rate and that the key step in the interface reaction is emission of electrons from Si to $SiO_2$. The electron flux from Si to $SiO_2$ by the thermionic emission is given by the Richardson-Dushman equation:

$$F_{et} = AT^2 \exp(-\chi_0 / kT) \qquad \text{(Equation 1)}$$

where A is Richardson constant, T is temperature in K, $\chi_0$ is barrier height (from the Fermi level to vacuum, for metals). This can be adjusted further for a $Si/SiO_2$ interface, since there are several energy levels on which electrons are available for transfer into the vacuum. If an electron is emitted from the valence band 4.25eV is required, while for emission from the intrinsic Fermi level of Si and from the conduction band 3.7eV and 3.15eV are needed respectively.

A modification of the thermionic emission oxidation model to describe the enhancement in the initial, linear regime is presented below (part of my MS work) [5, 27]. Oxidation by energetic AO at low temperature differs from the oxidation by $O_2$ and following steps were proposed:

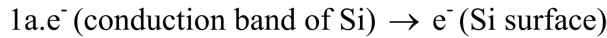
1a. $e^-$ (conduction band of Si) $\rightarrow$ $e^-$ (Si surface)

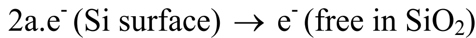
2a. $e^-$ (Si surface) $\rightarrow$ $e^-$ (free in $SiO_2$)

3a. $e^-$ (in $SiO_2$) +1/2$O_2$ (on the surface) $\rightarrow$ $O^-$(chemisorbed)

4a. $Si^+$ (at Si surface) + $O^-$ + O $\rightarrow SiO_2$

Step 1a is the flux of electrons to the Si surface

Step 2a is emission of electrons over the energy barrier

Step 3a is electron attachment to O

Step 4a is reaction of atomic and charged species.

The critical step is step 2, which was rate - limiting for the oxidation by $O_2$. I suggested that this step has become significantly more rapid (step 2a, because of the effect of "thermal spiking", caused by the energy of AO). Also, in step 4 -the decomposition of $O_2^-$ into the neutral and charged species is not present in the mechanism for AO oxidation and this will contribute some to the increased reaction rate. Steps 3a and 4a are modified as compared to the oxidation by $O_2$. The dissociation of $O_2^-$ ions does not occur during exposure to AO, as in the model for oxidation by $O_2$. This could increase the reaction rate in the linear oxidation regime, since atomic species are already present. The "thermal spike" effect is discussed next, since it refers to the energy of AO which can help electrons to overcome the energy barrier in order to transfer to $SiO_2$.

#### 2.7.1.2 Thermal spiking effect

I will refer to thermal spiking as brief T increase which provides local heating of the substrate and crystal lattice vibrations following the impact of hyperthermal atom. This effect is due to the large kinetic energy of AO, part of which is transferred to the neighboring atoms at the site of impact. Hyperthermal Cu deposition was studied by Zhou et. al and they found that athermal diffusion takes place upon the energetic atom impact on the surface [118]. Their MD study revealed that the crystal lattice vibrates which results in defect annihilation and diffusion enhancement. The temperature increase following the hyperthermal atom impact was found to be highly localized and very brief (psec, or $10^{-12}$sec). Although extremely short, this time is still longer than the typical time of electronic transfer (femtosec, or $10^{-15}$sec). As the temperature increases, the thermionic emission is promoted and the number of electrons transferred from Si to $SiO_2$ conduction band increase. Because of the increased number of available electrons to

chemisorb to the $O_2$, and consequent formation of more neutral and negatively charged O species which can react to build the oxide, the oxidation reaction will be enhanced in the linear regime. The Cabrera-Mott model will be discussed next since it assumes motion of charged species due to the electric field established by the tunneling or thermionic emission of the electrons.

#### 2.7.1.3 The Cabrera-Mott model

The Cabrera-Mott model is widely accepted when low-temperature oxidation conditions are considered. The Cabrera-Mott model is described in the following text, since it is commonly used to explain enhanced self-limiting oxidation when not a thermally –driven process which is not explained by classical Deal-Grove model. The Cabrera-Mott model describes an ionic transport mechanism which is enhanced due to the induced E field [41]. As already mentioned, electron tunneling or thermionic emission are possible ways to transfer the electron to the surface of the oxide to chemisorb to O and form O-ion. This induced E field is the driving force for the new oxide formation. The Cabrera-Mott model proposed cation diffusion, represented in Figure 16.

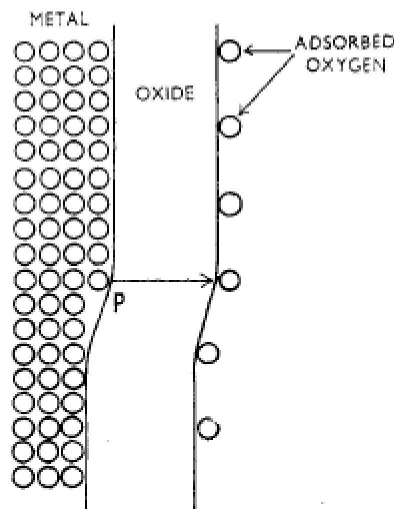


**Figure 16** Schematic of the ion removal from the metal surface [41].

The electric field pulls metal cation across oxide to form the oxide at the surface. The ion is removed from its original position P on the metal surface layer and placed into an interstitial position of the oxide. These two steps are known as the process of solution of the ion in the oxide.The Cabrera-Mott theory assumes that oxygen atoms are adsorbed on the oxide surface and that electronic species can pass rapidly through the oxide scale. This creates anions and thus an electric field which facilitates the transport of ions across the oxide film. Dissolution of anions at the oxide/gas interface or cations at the metal/oxide interface is assumed to be rate determining. An inverse logarithmic growth rate is predicted by the following expression:

$$\frac{x_1}{x} = -\ln\left(\frac{t}{x^2}\right) - \ln(x_1 u) \qquad \text{(Equation 2)}$$

where x is oxide thickness, t is time and *u* is oxide growth rate. Oxide thickness where the energy for thermally driven diffusion equals that for field-driven drift is given by: $x_1 = qaV/kT$, where q is magnitude of charge on an ion, *a* is half the distance separating two adjacent equilibrium ion sites in an oxide, V is voltage, k is Boltzmann constant and T is temperature [39].

Generally, movement of charged species (anions) must be compensated with the movement of the other charged species (electrons) in the opposite direction, so that the electro-neutrality is preserved. During the early oxidation stages, an ion moves across the oxide to reach (neutralize) an opposite charge ion and to react forming oxide, causing the field at the oxide surface to immediately decrease until another ion is created on the surface of the oxide. It is apparent that the other charged species (electrons) must move at the same time through the oxide, just in the opposite direction. Cabrera and Mott [41] proposed that ion –diffusion processes are rate limiting and this was reiterated by Fehlner and Mott [42]. The ionic and electronic currents are present at the same time and electrons and ions can neutralize each other

for certain distances, as given by Cabrera and Mott. Their theory assumes adsorption of oxygen atoms at the surface of the oxide and easy passing of electronic species across the oxide in order to equilibrate metal and absorbed oxygen. Anions are formed and subsequently the electric field, which gives rise to the ions transfer through the oxide film.

Yang et al. worked on the self-limiting passivation of Cu and concluded that the Cabrera-Mott model does not apply to the oxide islands formation [44]. The possibility that the oxidation of Si and Ge by energetic AO occurs via Cabrera-Mott model is considered next. The Cabrera-Mott model might be possible to apply if we had charged oxidizing species (e.g. for ECR plasma oxidation, oxidizing species is negative O atom), which will introduce E field and diffusion of charged species will be dominant process. Atomic oxygen produced in LDS source is neutral, so it might not be possible to have any field across the oxide layer that would enhance the oxidation process. Yates et al. investigated uniform oxide formation, such as on Al substrate, and the idea of the Cabrera-Mott model seemed to apply in this case. These researchers investigated the possible role of surface charging on the oxidation kinetics of Si and Al [122]. They oxidized Si(111) by $O_2$ at 90K and studied the kinetics of the process by XPS. Using 100eV electron bombardment in ultra-high vacuum, the thin oxide layer was electronically excited in the middle of oxidation process. There was no significant change in oxidation kinetics noted. In comparison, the same experiment done on Al showed that the surface charging greatly increased oxidation rate of this metal [122]. It was concluded that the production of the artificial E field across the oxide enhances Cabrera-Mott oxidation mechanism, and thus ionic transport through the oxide film. The enhancement in the oxidation rate due to the charging effect was expected for $Al_2O_3$ since it is ionic solid, but not for $SiO_2$, which is covalently-bonded. Therefore, the Cabrera-Mott model should not be applicable in the case of Si and Ge oxidation by energetic AO species.

The discussion of the generally accepted Deal-Grove model is given below since this model represents the base line in the Si oxidation field. Other effects not considered by Deal and Grove may influence the oxide growth kinetics and this factors are commented later in section 2.7.2.2.

### 2.7.2 Later stages of oxidation process and Deal –Grove model

The basic model describing the thermal oxidation of Si has been developed by Deal and Grove. This model is generally valid between 700-1300$^{o}$C and partial pressures of oxygen between 0.2 and 1 atm, when the oxidation occurs by molecular $O_2$ species [48].The main components of the Deal-Grove model are given by the following equations, already mentioned at the beginning of this section (steps 2 and 3):

2. $O_2$ (diffusion) $\rightarrow$ to the $Si/SiO_2$ interface $O_2$ transport through the oxide scale
3. $O_2$ (at $Si/SiO_2$ interface) + Si $\rightarrow$ $SiO_2$ reaction of Si and $O_2$ at the $Si/SiO_2$ interface

From the application of this model to experimental results, it has been concluded that the applicability of this model is restricted to oxides thicker than 25nm, and the oxidation rates for thinner oxides are significantly higher than those predicted by the Deal-Grove model. These discrepancies led to the introduction of different models which are modifications introduced into the Deal-Grove model in order to explain the “anomalous” thin oxide growth. The Cabrera – Mott model (described in the previous section) was one of the earliest models proposed to account for the initial thin oxide growth.

This chapter is organized in following way: first, the Deal-Grove model will be described, then difficulties in the modeling of the thin films oxidation kinetics will be addressed;

finally, different effects that could account for the enhanced growth rate in the initial regime will be discussed.

The oxidation of Si proceeds by the inward motion of the oxidizing species through the oxide layer. Therefore, the main processes of the kinetics are the transportation of the oxidizing species from the gas to the oxide/gas interface, followed by the diffusion across the oxide layer and finally reaction at the $Si/SiO_2$ interface resulting in the $SiO_2$ layer growth. In their model Deal and Grove assume the above-described mechanism, and in addition to that, after an initial oxide growth, they assume that the steady-sate has been established. The Deal-Grove oxidation model can be explained using Figure 17, where symbols are as follows:

$C_g$ = oxidant molecules concentration in the bulk gas ($O_2$)

$C_s$ = oxidant molecules concentration in the layer immediately adjacent to the oxide surface

$C_o$ = equilibrium oxidant molecules concentration at the oxide surface

$C_i$ = oxidant molecules concentration at the $Si/SiO_2$ interface

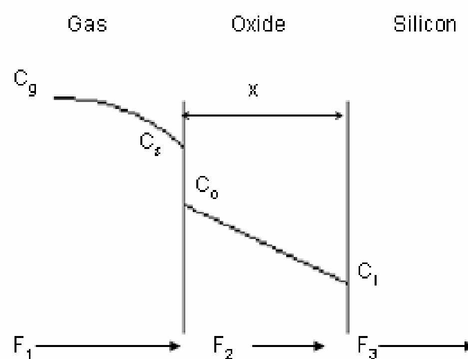


**Figure 17** Model for silicon oxidation [48].

$C_g > C_s$ because the oxidant is depleted on the oxide surface and $C_s > C_o$ due to the oxygen solubility limits in $SiO_2$.

$F_1$= flux of the oxidant species from gas to the gas-oxide interface

$F_2$= flux of the oxidant species from gas-oxide to the oxide-Si interface (or flux through the oxide layer)

$F_3$= flux of the oxidant species to the oxide-Si interface (or oxidant flux consumed by reaction at the Si/$SiO_2$ interface)

Flux is represented as the number of molecules per unit area and unit time, and fluxes are given as:

$$F_1 = h_g (C_g - C_s) \qquad \text{(Equation 3)}$$

where $h_g$=gas phase mass transfer coefficient [cm/sec]

The expression for the flux $F_2$ is known as Fick's law of solid-state diffusion and a concentration gradient is responsible for the flux of oxidant through the oxide.

Using the ideal gas law and Henry's law,

$$C_g = \frac{n}{V} = \frac{p_g}{kT} = \frac{C^*}{H}\left(\frac{1}{kT}\right) \qquad \text{(Equation 4)}$$

where $C^*$ = equilibrium bulk concentration of oxidant in oxide and Henry's law constant.

Similarly, $C_s = \frac{n_s}{V} = \frac{p_s}{kT} = \frac{C_o}{H}\left(\frac{1}{kT}\right)$ (Equation 5)

where $C_o$ = oxidant concentration just inside the oxide surface.

So, $F_1 = h(C^* - C_o)$ (Equation 6)

where $h = \frac{h_g}{HkT}$ (Equation 7)

$$F_2 = -D\frac{dC}{dx} \cong D\frac{(C_o - C_i)}{x} \quad \text{(Equation 8)}$$

where D =the diffusivity of the oxidant molecule in $SiO_2$ [$cm^2$/sec] (diffusion coefficient) and x= oxide thickness

Oxidant reacts with Si following 1st order reaction:

$$F_3 = k_s C_i \quad \text{(Equation 9)}$$

where $k_s$= rate constant of silicon oxidation at Si/$SiO_2$ interface [$cm^2$/sec]

At steady-state, after the initial oxide thickness $x_i$ growth, three fluxes are equal $F_1$=$F_2$ =$F_3$=F resulting in $F = \frac{k_s C^*}{1 + k_s/h + k_s x/D}$ (Equation 10)

The expression for the rate of oxide growth is:

$$\frac{dx}{dt} = \frac{F}{N_1} \quad \text{(Equation 11)}$$

where x = the oxide thickness, $x_i$ = the thickness of the initial oxide layer that is formed by other mechanisms not included in the Deal-Grove model (e.g space charges).$N_1$= number of molecules of oxidant incorporated into a unit volume of the oxide layer.

Helms [49] originally developed a linear-parabolic equation, which is obtained as a solution when x=$x_i$ and t=0:

$$x^2 + Ax = B(t + \tau) \quad \text{(Equation 12)}$$

$$A \cong 2D\left(\frac{1}{k_s} + \frac{1}{h}\right) \quad \text{(Equation 13)}$$

$$B \cong \frac{2DC^*}{N_1} \quad \text{(Equation 14)}$$

$$\tau = \frac{x_i^2 + Ax_i}{B} \quad \text{(Equation 15)}$$

If the oxide thickness or times are small, a linear rate law is found:

$$x \cong \frac{B}{A}(t + \tau) \qquad \text{(Equation 16)}$$

$t << A^2/4B$

and B/A=linear rate constant

This regime is known as reaction-controlled and it is determined by the reaction rate of the oxidant with silicon on the $Si/SiO_2$ interface.

If the oxide thickness or times are larger - a parabolic law is obtained:

$$x^2 \cong Bt \qquad \text{(Equation 17)}$$

where $t >> A^2/4B$ and $t >> \tau$ and B= parabolic rate constant

This regime is known as diffusion-controlled. Again, the main limitation of the Deal-Grove oxidation model, when considering low temperature oxidation by $O_2$, is its validity for shorter oxidation times since it predicts greater oxide thickness than was experimentally found (for $t \to 0$, $x \to 250\,\overset{0}{\mathrm{A}}$).

#### 2.7.2.1 Difficulties in modeling ultra-thin oxide growth and limitations of Deal-Grove model

Although oxidation of Si in the thin regime has been under intensive investigation for the last 50 years, there is no oxidation model generally accepted. The basis for Si oxidation is the Deal-Grove model, which fits kinetic data very well, but only in the high temperature regime, and for the larger oxide thickness (>25nm). All modifications to the Deal-Grove model (oxide structural effect, oxide stress effect, interfacial volume zone, etc.) presented later in this section to account for the enhancement of the oxidation kinetics in the thin film regime have limited success to account for growth-rate enhancement, or have no physical, theoretical or experimental justification [50, 51]. Such phenomena as are outlined above have been strongly doubted by

many authors, and in addition, there is no experimental evidence which would suggest that one of the above-mentioned mechanisms has a determining effect on the Si oxidation. Despite the large number of models proposed to explain oxide growth in the thin regime, none has yet been convincingly accepted as more valid than the others [51].

Investigation of the oxidation of Si in the thin film regime is usually limited by experimental conditions under which the reaction rate was studied. It was shown that successful fit achieved by applying the model on the set of data from one author does not necessarily mean that the same model will fit the data from another research group [50, 51]. The experimental limitations such as Si purity, native oxide removal and Si surface control were some of the factors involved in the reproducibility of the experimental results from one to another research group.

Consequently, this was reflected in a multitude of growth laws obtained such as linear, a parabolic, linear-parabolic, logarithmic and inverse logarithmic. There are many physical explanations included in modifications based on the Deal-Grove model, but none has been clearly correct, therefore, for now, empirical expressions are used. A comprehensive and systematic study is necessary since knowledge of a rate law obtained from the data taken at the limited experimental conditions is not sufficient to determine reaction mechanism. Silicon surface preparation, roughness and impurities (level of dopant) should be very well controlled during the experiments since these factors all significantly impact the oxidation kinetics in the thin film growth regime.

All of the above mentioned modifications of the Deal-Grove model are prone to the same inherent ambiguities of the Deal –Grove model itself in the thin film regime. Some of these issues, such as the meaning of diffusion coefficient and validity of Henry's law in thin films are

discussed next. When employing the Deal-Grove model, there is an issue of the “nature” of diffusion coefficient D in very thin films, which are investigated within this work. Bongiorno et al. proposed variable diffusion coefficients across the oxide films to explain “anomalous” oxide growth [55, 59]. The variation of the diffusion coefficient could be due to the different oxide structure formed close to the Si/$SiO_2$ interface and the bulk oxide. The currently adopted assumption in modern models is that the diffusion rate should decrease as the oxide films become thinner [55, 59]. On the other hand, the results of Monte-Carlo simulations shows that the diffusion rate through thin oxides ($<$20nm) increases for decreasing oxide thickness [55]. On a short-range scale, oxide layer (e.g. amorphous $SiO_2$) is not homogeneous, and the presence of low-barrier pathways accounts for the increase in the rate of diffusion (percolation behavior).

Since this is in clear contrast with experimental observations [55], there should be another mechanism to oppose this behavior leading to an overall lower diffusivity with respect to the bulk conditions. This opposing mechanism might be governed by the presence of higher-density oxide layer near the Si/oxide interface. This dense layer could reduce the diffusivity, which is actually confirmed by X-ray reflectivity experiments [56]. Verdi et al suggested the consideration of the oxygen diffusion in terms of random walk on a percolation cluster characterized by some correlation length [58]. The $SiO_2$ structure can be seen as a granular random network containing preferential diffusion paths, rather than a continuous random network. They proposed the presence of 3 main structural domains for the oxide layer: 1) granular structure with percolative diffusivity of the thick oxide, 2) a reactive layer at the $SiO_x$/Si interface and 3) a stress modified layer at the $SiO_2$/$SiO_x$ interface. Figure 18 explains the positions of the 3 structural domains in the Si/$SiO_2$ system.

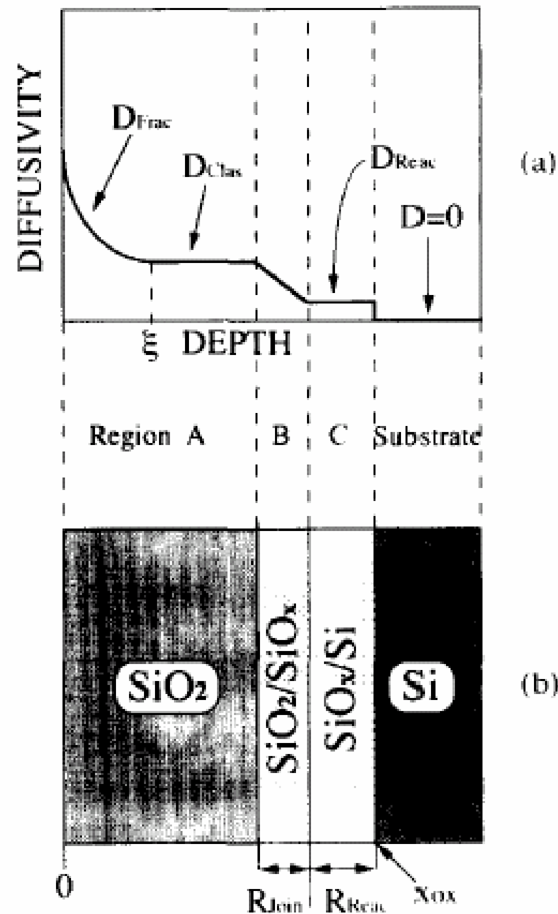


**Figure 18** a) Representation of the depth -dependent $O_2$ diffusivity and b) schematic of the oxide growth, $SiO_2$ is stoichiometric oxide having diffusivity of bulk, denoted by $D_{frac}$ ('fractal'), $SiO_2/SiO_x$ is interface sublayer with intermediate diffusivity, while $SiO_x/Si$ is interface sublayer with low diffusivity. Si is crystalline substrate (very low diffusivity) Verdi and Kelly [58].

It was found that the reaction layer near the interface, with a typical thickness of $R_{reac}$ <5nm (region C), can be characterized by a constant and low diffusivity $D_{reac}$. The physical picture shown in Figure 18 applies to thermally grown oxides on Si, which are characterized by transitional zones with a density gradient. It will be shown later, in the results section, that the oxides formed by AO are homogeneous, similar to the bulk structures, from the Si/oxide

interface through the entire oxide scale. This might be an important issue when considering the nature of diffusion coefficients, although the oxide scales are very thin.

As mentioned previously, the other ambiguity when using the Deal-Grove model to describe thin oxide growth, is Henry's law validity for the thin oxides. According to the Henry's law ($C^*=Hp_g$), the equilibrium concentration C* of the oxidant in the oxide is related to the partial pressure of oxidant species in the gas. This relationship is generally valid in the absence of dissociation or recombination of the oxidant species at the oxide/gas interface and when their chemical potential in the oxide is independent of pressure (dilute case). The constant of proportionality in Henry's law might be increased for the case of thin films, when the oxide thickness is less than the average spacing between the oxygen solute molecules in the oxide. For example, for $C^*=5x10^{16}cm^{-3}$ and $3x10^{19}cm^{-3}$ for dry and wet $O_2$ oxidation, the average spacings are 270 and 32Å, respectively [61]. Since in the reaction-limited regime the oxidation rate is directly proportional to the concentration of the oxidizing species at the $Si/SiO_2$ interface, a higher oxygen solubility in oxide films thinner than 270Å implies a faster oxidation process.

**2.7.2.2 Deal-Grove model modifications**

In the thin oxide regime, for high T oxidation (700-1000$^o$C), the Deal-Grove model is "corrected" to account for an experimentally observed enhancement in the initial oxidation regime. A brief overview of the effects that could possibly influence fluxes in the Deal-Grove model will be presented in this chapter. These effects include: the oxide structural defects, stress, and interface layer. The effects listed above will be presented because hyperthermal AO could alter these mechanisms as compared to MO. Comments regarding the possible influence of the energetic AO on these effects are given in the discussion section.

The viscous flow effect (Reisman's modification of the Deal-Grove model) is also based on the stress effect and will be presented in greater detail than the other models, since this is the only model that provides a physical explanation for kinetics that deviate from the simple linear or parabolic rate, which was observed in my QCM experiments.

**The possible presence of oxide structural defects** was used by Revesz et al. [34] to account for the enhanced oxide growth. The enhanced transport of oxidant through the oxide scale via channels and pores causes the faster diffusion of the oxidant species (step 2 of Si oxidation).

2. $O_2$ (diffusion) $\rightarrow$ to the Si/$SiO_2$ interface $O_2$ transport through the structural defects within the oxide scale

Figure 19 is a schematic diagram illustrating the enhanced transport of oxidant through the oxide scale.

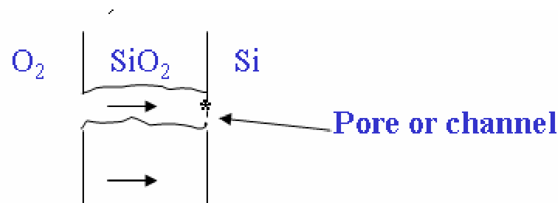


**Figure 19** Oxygen transport to the Si/$SiO_2$ interface via pores or channels

Gas permeability studies indicated the presence of microchannels (diameter < 50Å) in thermally grown $SiO_2$ [31]. Also, it was noticed that etching of oxide films proceeds in a non-homogeneous manner, indicating a non-homogeneous oxide scale [62, 64]. This oxide film is usually amorphous and can contain some structural micro-heterogeneities, such as channels and pin-holes, which can provide high diffusivity paths for the diffusing species [31]. The enhanced

growth rate in the initial oxidation regime may be due to the relatively easy migration of oxygen along channels and pin-holes in the oxide.

Atomic oxygen could affect the evolution of the oxide structure. For example, an oxide scale containing micro-pores or channels could be created by the energetic bombardment of AO. Alternatively, the hyperthermal AO could provide energy for the oxide scale to form a more homogeneous and ordered oxide.

Electron microscopy will be used to investigate the structural homogeneity of the oxide formed by reactive AO and thereby to gain essential insights into the oxidation mechanism by AO.

**The stress effect model** proposes that due to the volume expansion during oxidation an interfacial stress exists. The conversion of Si to $SiO_2$ involves a 2.2-fold increase in molar volume, which causes an intrinsic compressive stress within the oxide. The requirement for extra space can be satisfied only at high temperatures (close to the glass-transition temperature of 1175$^o$C for $SiO_2$, and 527 $^o$C for $GeO_2$), when the oxide network can rearrange by viscous flow. At lower temperatures, the network is not able to rearrange, resulting in residual stress and strain in the oxide film. The stress effects can affect the kinetics of thermal silicon oxidation, particularly in the initial stages. There is a controversy whether the stress affects the interface reaction, or the diffusion process [34]. Stress could change the rate of the reaction at the $Si/SiO_2$ interface (step 3 on pg. 27: $O_2$ (at $Si/SiO_2$ interface) + Si $\rightarrow$ $SiO_2$), since stressed Si-Si bonds are easier to break as compared to the bonds in the unstressed state. The diffusion of the oxidant species might be more altered through the stressed oxide structure (this would affect step 2: $O_2$ (diffusion) $\rightarrow$ to the $Si/SiO_2$ interface). Due to the fact that the oxide is constrained by the substrate surface, the volume required for the oxide to grow must be obtained in the direction

normal to the Si substrate surface. The z-direction in which the oxide viscous flow is possible is represented in Figure 20.

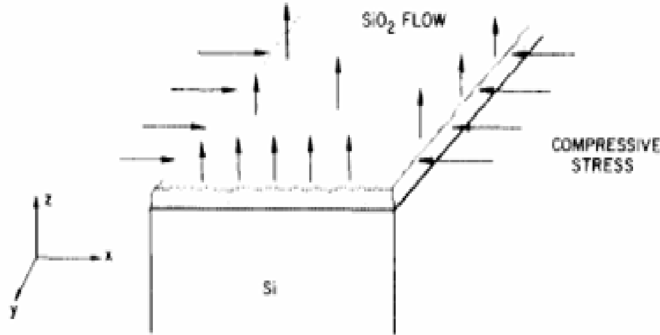


**Figure 20** Compressive stress at the $Si/SiO_2$ interface [35].

If the temperature is below 950$^o$C (T of viscous flow), viscous flow is not possible and the stress that arises as a result of the volume requirement is only partially relieved, causing the oxidation process to slow down [32]. At a high temperature, larger than 950$^o$C (for $SiO_2$), the oxide can easily flow in the direction normal to the substrate surface, and the volume required can be obtained.

Irene proposed that the interface reaction is affected by the stress developed in the oxide during Si oxidation [35]. Due to the lack of viscous flow, the Si atoms available near the interface are screened by the oxide, therefore the reaction is inhibited. Inability of the oxide to obtain the necessary molar volume in the normal direction will screen other Si atoms on the interface from reacting. The effective concentration of Si available for the reaction is controlled by the rate at which the oxide can viscously relax. The behavior predicted by this model has not been confirmed because accurate values for stress at the $Si/SiO_2$ interface, $\sigma_{xy}$, and viscosity of $SiO_2$, $\eta$, as a function of orientation and temperature have not yet been reported [36].

Two other researchers propose models that stress affects the diffusion process, rather than the interfacial reaction. Doremus [37] proposes that the initial linear oxidation rate does not represent the reaction at the interface, but instead arises from the strain in the oxide. The compressive strain in $SiO_2$ films, which is parallel to the Si/oxide interface, decreases linearly from the Si/oxide interface to the oxide/gas interface. The diffusion of the oxidizing species is the only parameter that controls the oxidation rate according to this model. The changes to the linear-parabolic kinetics are due to changes in the diffusion coefficient within the oxide scale.

The other model, given by Fargeix [38], introduces the stress effect directly into the parabolic rate constant (through the diffusion coefficient) of the Deal-Grove model. This model proposed that the diffusion is slower near the Si/$SiO_2$ interface, and that increase in diffusivity across the oxide layer far from the interface is related to the relaxation of the stresses.

Atomic oxygen should alter the oxide structure as compared to MO, therefore changing the stress at the Si/$SiO_2$ interface. Selected area electron diffraction (SAED) method and cross-sectional TEM/STEM will be performed to observe any structural changes as function of distance from the interface. It is possible that different nature of AO as compared to MO species will cause interaction of AO with the oxide network and possible stress relief. QCM will be used to monitor changes in oxidation kinetics. The comparison of in-situ QCM and structural studies will provide critical insights into how structural changes affect oxidation kinetics.

**In the interfacial layer model** Murali and Murarka propose that there is an oxygen – diffused zone (increased oxygen concentration) near the Si/$SiO_2$ interface in the Si [39]. Oxygen diffused zone is a volume zone (rather than only interface region) where oxidation occurs. According to this model, this zone starts from the Si/$SiO_2$ interface and extends into the Si substrate.

The flux of oxidizing species is very high if the film is very thin, thus leading to the formation of an oxygen-enriched-zone in the Si near the interface. Instead of reaction precisely at the interface, the reaction occurs within the oxygen-enriched zone in Si, resulting in enhancement in the oxidation rate. Once the oxide film becomes thick enough, the diffusion through the oxide is reduced and all of the oxidizing species are converted to $SiO_x$ at the interface.

No build-up of oxidants in the Si will occur because of the reduced arrival rate of oxidants to the interface. The thickness of the oxygen-diffused zone depends on the oxide thickness, oxygen diffusivity into Si, oxygen partial pressure, oxygen concentration in Si, temperature and Si crystal orientation. The value of oxygen solubility in silicon at 1000$^o$C is $7x10^{17}$at/cm$^3$ [40]. For comparison, solubility of $O_2$ in $SiO_2$ is $5x10^{16}$ at/cm$^3$ for dry $O_2$, and solubility of $H_2O$ in $SiO_2$ is $3x10^{19}$ at/cm$^3$ for wet oxidation, at 1000$^o$C.

This model assumes that three processes occur during oxidation: diffusion of oxygen through the thin gas film (very thin region close to the oxide surface), diffusion of oxygen through the oxide film and the reaction at the silicon surface. Any of these three processes could be the rate-limiting step.

Atomic oxygen could influence the interfacial layer zone formation, since more O atoms could be transferred into the Si and the zone could be extended into the substrate. An abundance of AO could exist at the Si/$SiO_2$ interface due to the AO energy and high mobility; therefore, a reaction zone layer could form. High-resolution transmission electron microscopy and EELS techniques will be used in order to study the interfacial thickness and the possible existence of this reaction zone.

### Reisman viscous flow effect

A detailed description of this model is given in this section, since this is the only model providing a physical explanation for oxidation kinetics that does not follow a simple linear or/and parabolic rate, but instead follows a power law $X_{ox} = a\,t^{b}$ ($b \neq 1$ or 0.5). Reisman et al. found that the power law relationship proposed by their model where $X_{ox}$=oxide thickness, t=time, a and b are constants for a given set of oxidation conditions fit majority of the existing literature data available between 1968-1988, for the oxide thickness range 4nm-1 µm [65]. Nicollian and Reisman propose that a deviation from the linear growth rate is due to the average viscosity of the oxide changing during oxidation. A schematic representation of the Reisman model in which the oxide growth is always controlled by the reaction at the $Si/SiO_2$ interface is given in Figure 21 below.

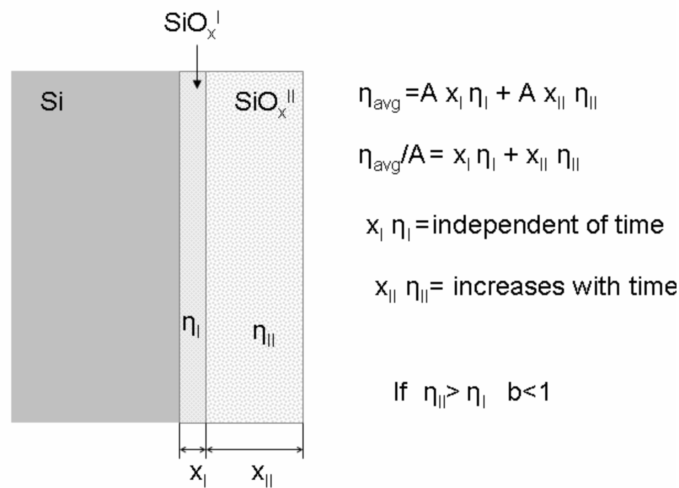


**Figure 21** Schematic of the thin epitaxial oxide layer ($SiO_x^{I}$) of thickness $x_I$ and viscosity $\eta_{I.}$ (time -independent). Growing oxide layer is marked as $SiO_x^{II}$ , with the thickness $x_{II}$ and viscosity $\eta_{II.}$ (time -dependent). A= the oxide surface area. Due to the increasing thickness of the oxide II with time, the average viscosity changes with time. If the bulk oxide viscosity is greater than the viscosity of the thin epitaxial oxide, then the average viscosity increases with time, which slows down the oxidation and oxide growth, leading to b<1. $\eta_{II} > \eta_{I,}$ and b<1, reaction is slower than for the reaction rate-limited process (b=1).

Two essential processes occur during the thermal oxidation of Si:

1) chemical reaction between the Si and $O_2$ at the Si/$SiO_2$ interface –linear step (interface limited)
2) the transport of $O_2$ from the gas phase through the oxide scale to the Si/$SiO_2$ interface, when some initial oxide thickness is already grown –parabolic step (diffusion limited)

If the partial pressure of $O_2$ at the Si/$SiO_2$ interface ($p_r$), is time independent and equal to the input partial $O_2$ pressure (p), the oxidation process is reaction - limited. The linear oxidation rate is then given by the following equation:

$$\frac{dx}{dt} = k_f p^n - k_r p_r^m \qquad \text{(Equation 18)}$$

where x is the oxide thickness, and t is the oxidation time. Two reactions are possible at the Si surface: the forward reaction Si(s)+$O_2$ (g)=$SiO_2$, with the specific reaction rate given by $k_f$ , and a decomposition reaction: $SiO_2$(s) + Si(s) = 2SiO(g), with the reverse reaction rate coefficient $k_r$. The coefficients n and m are the orders of forward and reverse reaction, respectively. Assuming the reverse reaction is negligible for most of the temperatures and oxidation pressures used experimentally, the following expression is obtained by integrating the first term of equation 18, when $k_f$ is assumed to be time - independent:

$$x = k_f p^n t \qquad \text{linear} \qquad \text{(Equation 19)}$$

Another case is when the partial pressure of $O_2$ at the Si/$SiO_2$ interface is less than the input partial $O_2$ pressure, and is a function of time. The oxidation in this case is limited by the mass –transport and if the diffusion coefficient (D) is time independent, the following relation is proposed:

$$x = D^{1/2} t^{1/2} \qquad \text{parabolic} \qquad \text{(Equation 20)}$$

It was noted that neither equation 19 or 20 can be used to fit a wide range of experimental data. The general equation for both equations is given by the power law:

$$x = at^b \qquad \text{(Equation 21)}$$

For the reaction - limited process, b=1, and b=1/2 for the mass - transport limited oxidation process. Coefficient "a" is also time independent and its physical meaning will be explained later in this section (see equation 29). Nicollian and Reisman determined that a power law fits an extensive amount of data reported in the literature, with the values of b varying from 0.24 to 0.90, depending on T and $O_2$ pressure. Low $O_2$ pressures led to low values of b, for example, for pressures < 1atm, b was found to be as low as 0.24. Ideally, b would be 0.5 (for transport - limited processes), or 1 (reaction - rate limited process). However, observation of b values different than 0.5 and 1 implies that either $k_f$ (the reaction – rate constant) or D (diffusion constant) is time dependent. For example, if the diffusion slows down with respect to oxidation time, then the diffusion – constant would be time –dependent as well and alter b to be less than 0.5. Similarly, for the reaction rate limited process, if b<1, could be explained by a time-dependent $k_f$, where the reaction rate slows down with oxidation time. Since Reisman et al. determined 1>b>0.5 in many cases, even for longer oxidation times, they assumed that the oxidation process is reaction - limited, where the transport of mass through the $SiO_2$ scale is fast, which is reasonable since the oxide is an open structure.

Reisman et al. assumed that the Si/$SiO_2$ interface reaction controls the oxidation process at all times, and that volume expansion and the viscous flow of the oxide at the interface control the growth kinetics. All stress models propose that a stress during oxide formation exists due to the 2.2 x increase of volume [34, 42]. Models of stress relaxation by viscous flow were proposed before, and described previously in this section, but it was not recognized by previous

investigators who supported the stress-effect model that the oxidation rate could be entirely reaction limited, with the viscous flow of the oxide identified as the rate limiting mechanism [65].

The average viscosity of the oxide $\eta_{avg}$ is determined by a viscosity of the thin epitaxial layer near $Si/SiO_2$ interface ($\eta_I$), and by the viscosity of the growing oxide layer ($\eta_{II}$) (see Figure 21). At fixed T and pressure, the average viscosity of the bulk oxide (II) increases whereas the thickness of the thin interface oxide (I) stays constant, leading to a time-dependent average viscosity. As the viscosity changes with time, then the ability for new oxide to form changes with time, leading to deviations of b from 1.

For thermal oxidation of Si, the oxide structure should be considered at the microscopic scale in order to explain the lower viscosity in the epitaxial oxide layer near the interface as compared to the high viscosity in the bulk amorphous oxide. The initial, epitaxial oxide structure consist of rings containing on average 4 Si atoms, whereas bulk amorphous silica is characterized mostly by rings containing around 6 Si atoms [62]. When the oxide structure transforms from epitaxial and hence, more ordered to the amorphous oxide, the average viscosity of the oxide increases because atomic movement becomes more difficult as the number of Si atoms in the rings increases, requiring the cooperative movement of larger number neighboring atoms. Hence, the viscosity of the epitaxial oxide is smaller than the bulk oxide. As the oxide thickness increases, the average viscosity increases due to increased amount of the bulk oxide (II) relative to the thin epitaxial oxide (I), which slows down the oxidation with respect to time, giving rise to $b<1$. $b<1$ was observed for all of the Si thermal oxidation data reported in Reisman's paper.

To understand the physical meaning of “a”, let us first consider the oxidation rate:

$$\frac{dx}{dt} = k_f(t, p, T)\, p^n \qquad \text{(Equation 22)}$$

The interfacial reaction rate, $k_f$, which could be time-dependent, is given as follows:

$$k_f(t, p, T) = k_a \exp[-\Delta E_A(t, p, T) / kT] \qquad \text{(Equation 23)}$$

where $k_a$ is the forward specific reaction rate coefficient for $Si(s)+O_2\ (g)=SiO_2$ reaction, k is Boltzmann’s constant, T is absolute temperature, p is the oxygen pressure. $\Delta E_A$ (t,p,T) is the activation energy for the oxidation reaction, which is the sum of the energy required to produce the free volume by viscous flow to accommodate the volume expansion, $\Delta E_V$(t,p,T), and the energy to form Si-O bonds and break Si-Si bonds, $\Delta E_F$ (the Gibbs free energy to form $SiO_2$).

It follows that $\Delta E_A$ (t,p,T) = $\Delta E_V$(t,p,T) + $\Delta E_F$. Now the reaction rate can be expressed as:

$$\frac{dx}{dt} = k_a p^n \exp\{-[\Delta E_V(t, p, T) + \Delta E_F] / kT\} \qquad \text{(Equation 24)}$$

Changes in the average oxide viscosity have been observed experimentally [63] and given by:

$$\eta(t, p, T) = \eta_o \exp[\Delta E_v(t, p, T) / kT] \qquad \text{(Equation 25)}$$

where $\eta_o$ is the average oxide viscosity at “infinite” T. The standard viscosity value for any material is $10^{-4}$ poise for the “infinite” T limit [64].

A viscosity increase means that more energy is needed in order to dislocate atoms and provide the free volume needed to accommodate the volume expansion of the growing oxide. Solving the differential equation 24 and using equation 25 for $\Delta E_V$ one finds that the power - law expression ($X_{ox} = a\, t^{\,b}$) (equation 21) is actually the short form of the equation

$$x = k_a\, p^n \exp(-\Delta E_F / kT)\eta_o G^{-1}(1-\phi)^{-1} t^{1-\phi} \qquad \text{(Equation 26)}$$

where G is a constant and $\phi$ (p, T) determines the shape of η vs t curve according to

$$\eta(T,P,t) = G(t - t_i)^{\phi(p,T)} \quad \text{(Equation 27)}$$

where $t_i$ is the time it takes to form the original ordered structure. By comparing equation 26 with the equation 21 ( $x = at^b$ ), the following expressions for the coefficients b and a are:

$$b(p,T) = 1 - \phi(p,T) \quad \text{(Equation 28)}$$

where $b(p,T)$ represents a measure of the magnitude and rate of increase with time of average oxide viscosity, and

$$a = k_a p^n \exp(-\Delta E_F / kT)\eta_o[Gb(p,T)]^{-1} \quad \text{(Equation 29)}$$

where coefficient a is dependent on b, as can be seen from the above equation. A large b value means a slow increasing rate of the average oxide viscosity, and vice versa. After fitting the power law to many sets of data by Reisman, *b* was found to be less than 1 in all cases, thus it was suggested that the reaction at the Si/$SiO_2$ interface is limited by the availability of free volume only and limited by the increasing average oxide viscosity [65].

It is possible that AO will follow different reaction pathways and might form different oxide structures on semiconductors, as compared to $O_2$, as well as follow kinetics that are not simply linear and/or parabolic. The presented model might be suitable to explain the oxide growth rate by AO, since it provides a physical explanation of oxidation kinetics that deviate from linear kinetics based on a time-dependent property of the oxide. Processes involving energetic AO could lower the overall energy needed for the oxide reaction, formation of the free volume, and creation of Si-O bonds. Since the Reisman model assumes two oxide phases, HREELS would be useful to distinguish between the two zones, and this technique will be used during my experimental work.

# 3.0 MOTIVATION AND HYPOTHESES

The purpose of this thesis work is the fundamental understanding on the oxidation mechanisms of semiconductors by hyperthermal AO, since it is the primary species corroding materials in LEO. Germanium and Si were selected as model semi-conductor systems, since they are used as coating materials, solar cells, and in semiconductor devices. From my MS thesis research, completely different oxide and interface structures were noted for Si oxidation in AO as compared to MO, indicative of markedly different oxidation mechanisms.

The goal of this PhD work is to establish the oxidation model that best describes oxidation of Si by energetic AO, to quantify this model and extend it to Ge. This will contribute to a greater universal model for oxidation of semiconductors that incorporates the effects of hyperthermal AO.

The effect of LEO AO on semiconductor oxidation has not been studied in depth before. The main characterization technique used by NASA researchers to investigate the oxide films formed in LEO by energetic AO was scanning electron microscopy (SEM), which showed pinholes and other defects in the oxide layer and undercutting of the oxide on the micron scale caused by AO [12]. Fundamental mechanisms of the oxidation by AO, occurring at sub-nanometer scale level were not identified, since atomic-scale characterization was necessary.

Recently improved experimental techniques now give the possibility to study the oxidation process in more details.

Semiconductor materials exposed to the AO will form oxides that have properties different than when formed by MO. The extreme reactivity of AO, due to its atomic nature and due to the high translational energy can alter the oxidation kinetics and influence the surface and the oxide formation. Previous investigations of silicon oxidation by the oxygen species other than MO have shown that the oxidation process proceeds by alternate paths, via different transitional states, resulting in structurally different oxides [15-18, 66-69]. The structure of the oxide and interface layer formed on Si(100) and Si(111) at 493K by hyperthermal AO or MO were investigated in my MS thesis work, and compared by a variety of experimental techniques including AFM, RBS, HRTEM, SAED,EELS and XPS. The main results were that the thickness of the oxide layer formed by AO were almost doubled when compared to the MO formed oxide both on Si(100) and Si(111). The $Si/SiO_2$ interface formed by AO on Si(100) in LDS was found to be very abrupt. Also, the presence of suboxide transitional states was greatly reduced. Only the presence of $Si^{4+}$ state was clearly detected by EELS and XPS. This is in good agreement with the previous studies on the Si oxidized by ozone [69]. The oxide created by ozone was etched off and surface roughness measured by scanning tunneling microscopy (STM) [69]. It was determined that the silicon/oxide interface has less than 0.2nm root-mean-squared roughness.

The interface formed was determined to be chemically abrupt. Investigation on Ge done by Wang et.al for thermal and electron cyclotron resonance plasma (ECR) oxidation conditions showed that the interface layer for ECR plasma oxidation is considerably thinner than for thermal oxidation (at $400^oC$, the interface layer thickness was $0.82 \pm 0.08$nm for ECR plasma oxidation, while it was $1.43 \pm 0.51$nm for thermal oxidation) [30]. Therefore, a flat $Ge/GeO_2$ interface was expected to be formed by energetic AO.

The interface formed by MO on Si(100) revealed transitional states. The interface abruptness due to AO oxidation was explained by the ability of AO to equally attack uppermost, first and second backbond layers. An analysis of the possible bond breaking along with the bond energies consideration was given. The oxide scale formed by AO on Si(100) was found to be very homogeneous and uniform, with no fluctuations in the Si and O content from the interface to the oxide surface. This was found to be in excellent agreement with the oxidation of Si by ozone which produced a homogeneous oxide structure. Previous investigators noticed that ozone formed more ordered aluminum oxide on an Al substrate [66]. Si oxidized by ozone showed homogeneous structure from the Si/$SiO_2$ interface to the oxide surface, as implied by the constant etching rate with HF solution through the oxide layer [67]. Since ozone dissociates to AO and MO, it was expected to observe similar behavior for the oxidation of Si and Ge by energetic AO.

The oxide layers formed by AO on both silicon orientations were found to be less random. More ordered structure, similar to that of alpha-quartz, was identified as opposed to the amorphous silica formed by MO. The oxide surface roughness was determined to be 2 times larger for the Si(100) oxidized by AO, as compared to the silica layer formed by MO.

There are still some open questions from my MS work that needed to be answered. One of them is certainly why is the thickness of the oxide scale larger when formed by hyperthermal AO than when created by MO? What is the temperature effect on the thickness of the oxide scale formed? The impact of AO kinetic energy on the thickness, of the oxide formed, and on semiconductors oxidation kinetics needs to be determined as well.

Hyperthermal AO is expected to react differently with the silicon and germanium surface than $O_2$, due to its energy and monoatomic nature. To characterize these differences, a variety of

characterization techniques, including HRTEM, EELS, SAED and AFM was used. Kinetic Quartz crystal microbalance (QCM) studies of the oxidation of Si and Ge by energetic AO was undertaken in order to investigate oxidation kinetics. Different energies of AO were used, therefore enabling the study of the effect of kinetic energy of AO on the oxidation process and on the final oxide thickness.

Another intriguing aspect of this work, of particular interest for the semiconductor industry, is the possibility of producing better gate oxides and interfacial structures using hyperthermal AO. Since Si is the primary electronic material, due to the unique Si/$SiO_2$ interfacial structure and properties, it is very important to characterize the interface created by AO on semiconductors. In Metal-oxide-semiconductor (MOS) devices, the charge carriers (electrons) flow along the channels. The performance of the device is controlled by the width of the channel, which is controlled by the electrode (gate) separated from the channel by a thin insulating oxide layer. This insulating layer prevents current from flowing between the gate and channel. The interface width and uniformity, as well as states and defect densities control the quality of semiconductor devices. Aggressive scaling of electronic devices, introduction of new materials in technology and growing requirements to the device performance have increased a demand in the fundamental knowledge of the materials properties and their interfaces at atomic and nanoscale level. Since physical thickness of gate oxide is being reduced to a few nanometers or less, the quality and characteristics of the thin oxide films and their interfaces are becoming absolutely critical in design of the functional elements. Although the Si/$SiO_2$ interface has been an object of the extensive investigations in the last 40 years, there is still no sufficient knowledge of the Si/$SiO_2$ interface at the atomic scale level, due to the limitations in the resolution of the

characterization techniques used. The interface roughness and defects are related to the inversion layer carrier mobility degradation, gate dielectric reliability and gate leakage current.

It is also of great interest to study Ge, because the mobility of holes in this material is larger than in any other semiconductor. High quality oxide insulator films should be grown on Ge at low temperatures to avoid the interface decomposition of the oxide. The oxide films with promising properties were grown by ECR plasma oxidation on Ge [30]. It can be assumed that AO can create oxide films with similar useful properties. Study of the interface thickness, states, and defects created by AO can provide the knowledge needed for the development of new and more effective semiconductor/oxide interfaces.

# 4.0 RESEARCH OBJECTIVES

The objective of this study is to investigate the oxidation of Si and Ge single crystals by AO and MO, and to understand the differences in the oxidation mechanisms and formed oxide structures. The reaction of hyperthermal AO with the materials can be quite different from the reaction of MO. The oxidation mechanism could be altered and hence, change the oxide structure. Information about the oxidation behavior of AO is limited, although it is the primary reactive species causing rapid degradation of materials exposed in LEO, due to the limited amount of materials that have actually been exposed in the LEO environment. Since Ge and Si have identical crystal structures, the effects of hyperthermal AO on Ge oxidation are expected to be similar to Si oxidation. The structure of the oxides formed by AO on Si and Ge is very likely to differ from the structure of oxides usually formed by thermal oxidation. The goal of this PhD thesis is to develop a model that best describes the oxidation mechanisms of semi-conductors in hyperthermal AO. This study can be divided in five sections:

1. Investigation of the structural properties of the silica layer and the Si/$SiO_2$ interface formed by AO-this is mostly my MS work [5]. It is presented again in this document because of its relevance to Ge oxidation and my overall objective of determining the oxidation kinetics of AO on semi-conductors.
2. Characterization of the nanostructure, including thickness, homogeneities and surface structures of the oxides and interfaces created by the exposure of Si and Ge to hyperthermal AO was done and compared to MO formed structure. Also,

changes in “amorphous” structure of the silicon oxide were investigated. The oxides and interfaces created were characterized by TEM, SAED, HRTEM, EELS, fluctuation electron microscopy (FEM), and AFM techniques, in order to best clarify the effects of AO, temperature and kinetic energy on the nanoscale oxidation processes of semiconductors.

3. Si and Ge-oxide thickness dependence on the AO energy and temperature.
4. Kinetic study of the oxidation of Si and Ge by AO with different kinetic energies using research quartz crystal microbalance (RQCM) incorporated into Fast atom sample tester (FAST)$^{TM}$ AO source was undertaken in order to obtain real-time oxidation curves for 5-9eV AO and to compare them with the existing literature kinetic data for lower energies AO (1.6-4.6eV).
5. Stopping range of ions in matter (SRIM) simulations of energetic O atom impact on $SiO_2$ and $GeO_2$ target materials.

All of the above information will be used to develop a model of semiconductor oxidation at the nanoscale by hyperthermal AO.

# 5.0 EXPERIMENTAL PROCEDURE

## 5.1 AO SOURCES

The production of 5eV neutral AO with a flux similar to that in LEO is critical for ground-based simulation. Currently several different types of AO sources are used based on $O_2$ dissociation in radio frequency (RF) plasma source [32] or in electron cyclotron resonance (ECR) plasma source [33]. These various sources differ in their spreads of AO and the beam fraction of neutral AO. Atomic oxygen with kinetic energy of ~5eV is very difficult to produce; most sources produce at best a few eV, as well as produce a wide range of O species, including ionic species. Since a laser detonation source (LDS) produces neutral AO beam with uniform kinetic energy with a flux that best simulates the LEO environment, this type of source was used to oxidize Si and Ge-single crystals by hyperthermal AO. This type of source exists at very few sites in the world, and one of them is at the University of Pittsburgh. The UHV capabilities and portability of this source are unique.

### 5.1.1 Fast atom sample tester (FAST $^{TM}$) laser detonation source (LDS)

A laser detonation source is used to produce a beam of hyperthermal neutral AO similar to LEO conditions. This AO source uses the laser breakdown of $O_2$ and was originally developed by Physical Sciences Inc (PSI) [8, 9]. A $CO_2$ laser with 7 J/pulse and pulsed supersonic valve (PSV) are used in LDS. Pure oxygen gas is introduced through a pulsed supersonic valve into a

conical Cu nozzle. A laser pulse produced by a $CO_2$ laser with 7 J/pulse, is focused on to the nozzle throat where it ignites an oxygen plasma to over 24000K. The plasma expands rapidly out of the cone and this shock wave dissociates the $O_2$ in front of it to primarily neutral AO. The remaining energy is transferred to kinetic energy of the AO. Hence, the kinetic energy is tunable between 4-20eV by altering the timing between the $O_2$ and laser pulse. The AO beam velocity is measured by two radiometers spaced 7.6cm apart, by observing the differential time-of-arrival of the peak of the electron-ion recombination radiation at 777nm. Since the distance between the 2 radiometers is fixed and known (7.6cm), then by measuring the time between when the radiation is measured by the first radiometer and second radiometer gives the speed, hence, kinetic energy, of the AO beam. Tuning the timing between $O_2$ pulse and $CO_2$ pulse can tune the kinetic energy.

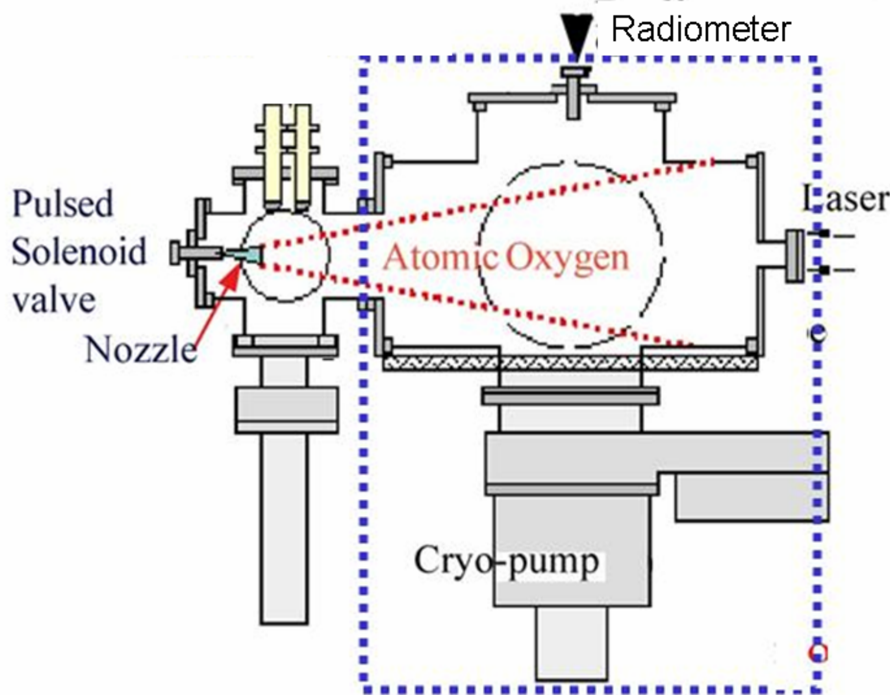


(a)

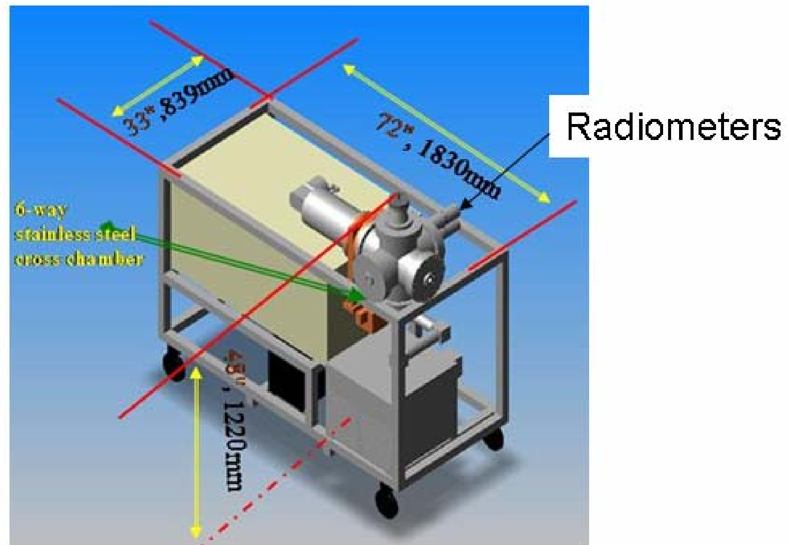


(b)

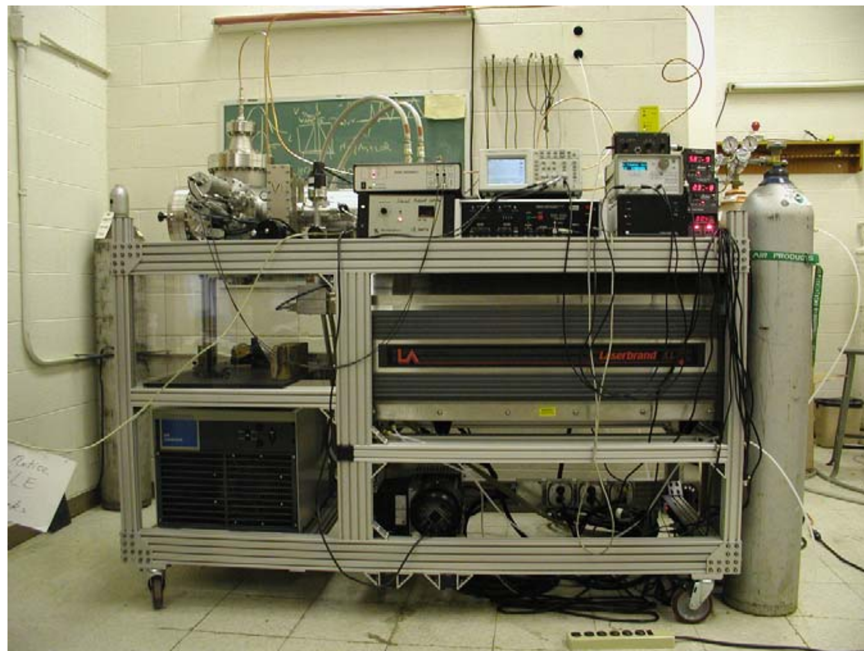

(c)

**Figure 22** a) Schematic b) actual dimensions c) image of the laser detonation AO source at the University of Pittsburgh

This type of AO source can produce both atomic and MO with the $O/O_2$ concentration ratio of 0.5-3. Since the AO beam spreads out (cone-shaped), the arrival flux depends on the distance between the conical nozzle and the sample. By reducing the distance from nozzle to the sample, an AO flux higher than $10^{15}$ atoms $cm^{-2}$ $sec^{-1}$ could be achieved. The beam composition at the velocity of 8 km/sec is given in Table 2.

**Table 2** The species in the AO beam of the LDS (determined by mass spectroscopy) [16].

| Species in the AO beam of the LDS | % |
|---|---|
| Neutral O (atomic) | 80 |
| Metastable O (1D) | 0.25 |
| Ionic oxygen ($O^+$) | 1-2 |
| Molecular $O_2$ | 17.75-18.75 |

More technical details especially about the modifications to the FAST™ AO source, at the University of Pittsburgh, are available in the Appendix .

## 5.2 MODIFICATIONS OF THE FAST ™ LASER DETONATION AO SOURCE

Modifications of the AO source include addition of a research quartz crystal microbalance (RQCM) system, heating stage, and VUV source. Dual-head Research quartz crystal microbalance was added in order to study the kinetics of the reaction of hyperthermal AO with different materials.

In order to examine the effects of temperature on AO oxidation, a UHV -compatible heating stage, with dimensions of ~5 x 6 cm, capable of annealing up to 2000K was designed and built utilizing a Boraelectric heating element. Figure 23 below shows set-up and the position of the heating stage within the chamber of FAST ™ laser detonation AO source.

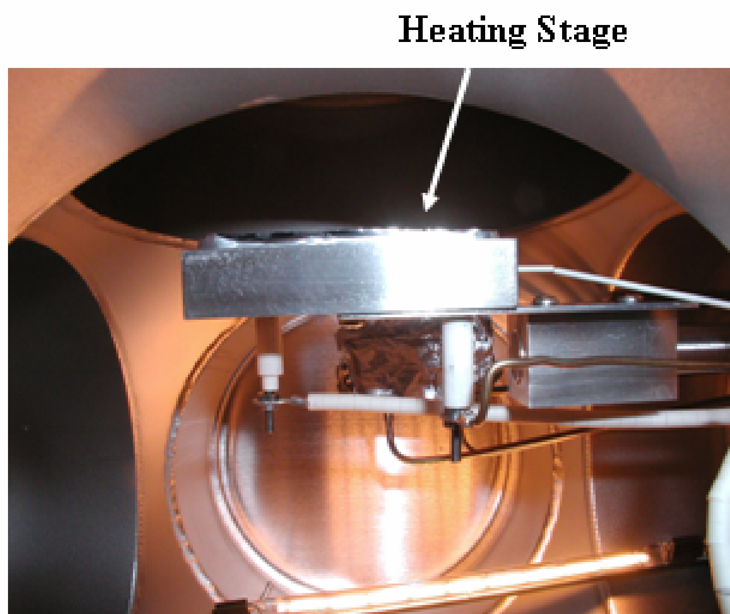


**Figure 23** UHV heating stage, (Boraelectric heater used), incorporated in the laser detonation AO source

VUV source addition is done. This modification will enable simulation of real LEO environment which includes synergistic effect of AO and VUV irradiation on the oxidation of materials. The details of these elements and modifications of FAST$^{TM}$ AO instrument at the University of Pittsburgh can be found in Appendix .

## 5.3 SI SINGLE-CRYSTAL OXIDATION BY 5EV AND 9EV AO

### 5.3.1 Native oxide removal procedure prior to oxidation and oxidation conditions

Single crystal silicon (100) oriented wafers were obtained from MTI Corporation [70]. Samples for AO exposure were cut from double side polished, boron type doped wafers 4 inch in diameter with resistivity 10-50 ohm cm, thickness 0.5mm and average surface roughness 10 Å (by AFM). Prior to AO oxidation, Si samples were cleaned from native $SiO_2$ using hydrofluoric acid (HF) dip. Samples were immersed in 5% aqueous HF for 2min, then rinsed in deionized water (DI) for 1min and finally blown dry with high purity nitrogen. This type of cleaning procedure produces an atomically rough surface with H-terminated Si-dangling bonds which prevents natural oxide formation for about 10 min [64, 66]. In HF cleaning procedures, rinsing in DI water was done in order to decrease organic contamination during dilution of HF as well as to decrease the residual F on the Si surface.

The LDS at Montana State University (MSU) was used for 5.1eV AO oxidation at 493K. The fraction of AO in the beam was 70% with mean energy of the hyperthermal AO approximately 5.1 eV. The erosion amount of Kapton "witness" samples was used to measure AO fluence according to the formula:

AO fluence (atoms/$cm^2$)=[$\Delta$m (g)] / [erosion yield (g/atom) x area ($cm^2$)]    (Equation 30)

where $\Delta$m is the mass change of Kapton sample of particular area due to the oxidation by AO.

A batch of 4 Si samples was loaded in a reaction chamber for the duration of ~7h at 493K and average flux of $3.2 \times 10^{15}$ atoms $cm^{-2}$ $sec^{-1}$ for a total fluence of $8.1 \times 10^{19}$ atoms $cm^{-2}$. A total of 50000 pulses with 2 pulses per second were used. The oxidation of Si(100) by 9eV AO at

473K was done in the LDS source at the University of Pittsburgh. This temperature was used since it is the most extreme temperature found in the LEO environment. The higher energy of the AO beam was achieved by adjusting the laser timing, so that the delay time measured between the 2 radiometers was Δ=7.4 μs, corresponding to a beam velocity of 10.3km/s. Two Si samples, $1cm^2$ each, previously cleaned by HF etch, were loaded in the reaction chamber for ~7hrs at 473K and average flux of $1.79 \times 10^{14}$atoms $cm^{-2}$ $sec^{-1}$ for a total fluence of $4.52 \times 10^{18}$atoms $cm^{-2}$. A total of 50400 pulses with 2 pulses per second were used.

## 5.4 SI SINGLE-CRYSTAL OXIDATION BY MO

### 5.4.1 Native oxide removal procedure prior to oxidation and oxidation conditions

Prior to MO oxidation, Si samples were cleaned using the Radio Corporation of America (RCA) etch. Samples were ultrasonically cleaned first with ethanol for 5min, and then with DI water for an additional 5min. Samples were then dipped into 2% HF solution at room temperature (298K) for 10 sec and dipped into $NH_4OH:H_2O_2$ = 1:1 solution at 353K for 10 min. Additional steps were performed by dipping in DI water for 1 min, 2% HF solution for 10 sec and finally, dipping in DI water for 5 sec. These steps were repeated 3 times. The consequence of the RCA cleaning procedure is H-terminated Si surface causing Si surface passivity and preventing natural oxide formation for about 10 min in $O_2$. Oxidation with MO was performed in a conventional clam-shell, one zone Lybold furnace with a mullite tube controlled by a Eurotherm PID controller. Samples were loaded vertically into the $Al_2O_3$ boats with the Si surface of interest perpendicular to the MO flow. The temperature was ramped to 493K and $P_{O2}$ of 1atm for 48 hrs. A new mullite tube and a new $Al_2O_3$ boat were used in order to ensure the clean conditions within the furnace during the oxidation.

It was shown earlier, within the course of my MS thesis work, that 748 Å thick Si-oxide was grown at 800$^o$C and $P_{O2}$=1 atm for 19 hrs in the same Lybold furnace [5, 21]. The oxide thickness was determined by Rutherford backscattering spectroscopy (RBS) and agrees very well (less than 8% difference) with the oxide thickness estimated from the plot given in Figure A III - 3 in APPENDIX AII of this thesis [48]. Therefore, we can consider that the performances of the furnace used for the oxidation of Si and Ge wafers in MO are good.

## 5.5 GE SINGLE-CRYSTAL OXIDATION BY 5EV, 9EV AND 15EV AO

### 5.5.1 Native oxide removal procedure prior to oxidation and oxidation conditions

Single crystal germanium (100) wafers were obtained from University Wafer Company. [61]. Samples for AO exposure were cut from single-side polished, Sb type doped wafers 2 inch in diameter with resistivity of 6-20 ohm cm, thickness 0.5mm and average surface roughness of 10 Å (as determined by AFM). Ge(100) samples were cleaned just prior to exposure in order to remove native $GeO_2$, using buffered HF method (75g $NH_4F$, 35ml concentrated HF and 250ml $H_2O$). The specimens were then rinsed in deionized water (DI) for 1min and finally blown dry with high purity nitrogen. The Fast Atom Sample Tester (FAST)™ AO source at the University of Pittsburgh was used for AO oxidation. The mean energy of the hyperthermal AO was approximately 5eV. The samples were oxidized for ~7hrs, at 473K, at AO flux of 1.03 x $10^{15}$at/cm$^2$sec for a total fluence of 2.6 x $10^{19}$at/cm$^2$. The delay time measured between the 2 radiometers was $\Delta$=9.5 μs, corresponding to a beam velocity of 8km/s. The erosion amount of Kapton "witness" sample was used to measure the AO fluence.

The oxidation of Ge(100) by 9eV AO at 473K was done in LDS source at the University of Pittsburgh. The higher energy of the AO beam was achieved by adjusting the delay between $O_2$ pulse and laser pulse to $\Delta$=7.4 μs, corresponding to a beam velocity of 10.3km/s. Two Ge samples, 1cm$^2$ each, previously cleaned using HF etching, were loaded in the reaction chamber for the duration of ~7hrs at 473K and average flux of 1.79 x $10^{14}$ atoms cm$^{-2}$ sec$^{-1}$ for a total fluence of 4.52 x $10^{18}$at/cm$^2$. A total of 50400 pulses with 2 pulses per second were used.

Ge samples were also oxidized by 15eV AO at 473K, for total time of 3hrs and 40 min. Delay time between $O_2$ pulse and laser pulse was adjusted to 5.7μs, corresponding to a beam velocity of 13.3km/sec. This set of samples received a total of 13200 pulses with 2 pulses per second, with the average AO flux of of $5.81 \times 10^{14}$ atoms $cm^{-2}$ $sec^{-1}$ for a total fluence of $7.67 \times 10^{18}$at/$cm^2$.

Another set of Ge samples was oxidized at room T (298K), for 7hrs, by 5eV AO. The samples were cleaned prior to oxidation and loaded into the chamber of the LDS. This set of samples received a total of 50400 pulses with 2 pulses per second, with the average AO flux of $9.7 \times 10^{14}$atoms $cm^{-2}$ $sec^{-1}$ for a total fluence of $2.4 \times 10^{19}$at/$cm^2$.

## 5.6 GE SINGLE-CRYSTAL OXIDATION BY MO

### 5.6.1 Native oxide removal procedure prior to oxidation and oxidation condition

Prior to MO oxidation, Ge samples were cleaned using buffered HF procedure. Oxidation with MO was performed in a conventional clam-shell, one zone Lybold furnace with a mullite tube controlled by a Eurotherm PID controller. Samples were loaded vertically into the $Al_2O_3$ boats with the Ge surface of interest perpendicular to the MO flow. The temperature was ramped to 473K and $P_{O2}$ of 1atm for 24 hrs. A new mullite tube and a new $Al_2O_3$ boat were used in order to ensure the clean conditions within the furnace during the oxidation.

Table 3 summarizes all Si and Ge samples, cleaning methods, and oxidation conditions described above. Values for oxide thickness (from the result section), measured by X-TEM, and mean square roughness (RMS) of the oxide surface (by AFM) are also shown.

**Table 3 Experimental conditions**

| Sample | Cleaning method | Oxidizing species and equipment | Exposure time (hrs) | Flux (at/$cm^2$sec) | Fluence * (at/$cm^2$) | T ($^oC$) | Oxide Thickness (Å) | RMS (nm) |
|---|---|---|---|---|---|---|---|---|
| Si(100) p-type | HF | 5.1 eV AO LDS Montana | 7 | $3.2 \times 10^{15}$ | $8.1 \times 10^{19}$ | 220 | 50-60 | 1.54 |
| Si(100) p-type | RCA | $O_2$ furnace | 48 | $4.0 \times 10^{30}$ $p_{O2}$ =1 atm | $7.0 \times 10^{35}$ | 220 | 20-30 | 0.83 |
| Si(100) p-type | HF | 9 eV AO LDS Pitt | 7 | $1.79 \times 10^{14}$ | $4.52 \times 10^{18}$ | 200 | ~50 | 2.61 |
| Ge(100) n-type | Buff HF | 5 eV AO LDS Pitt | 7 | $1.03 \times 10^{15}$ | $2.6 \times 10^{19}$ | 200 | 20-30 | 2.26 |
| Ge(100) n-type | Buff HF | $O_2$ furnace | 24 | $4.0 \times 10^{30}$ $p_{O2}$ =1 atm | $3.5 \times 10^{35}$ | 200 | <10 | 1.49 |
| Ge(100) n-type | Buff HF | 9 eV AO LDS Pitt | 7 | $1.79 \times 10^{14}$ | $4.52 \times 10^{18}$ | 200 | 30-40 | 2.376 |
| Ge(100) n-type | Buff HF | 15 eV AO LDS Pitt | 3hr40min | $5.81 \times 10^{14}$ | $7.67 \times 10^{18}$ | 200 | ~50 | 5.25 |
| Ge(100) n-type | Buff HF | 5 eV AO LDS Pitt | 7 | $9.7 \times 10^{14}$ | $2.4 \times 10^{19}$ | 25 | 20-30 | 1.93 |
| Ge(100) n-type | none | Ambient air (native oxide) | - | - | | 25 | | 0.47 |

* determined by erosion of Kapton witness sample

## 5.7 CHARACTERIZATION METHODS

An overview of the techniques and instrumentation used for the structural characterizations of the oxides and interfaces is given below.

### 5.7.1 Transmission electron microscopy (TEM) techniques

Transmission electron microscopy incorporates very powerful methods that allow microstructural and analytical material characterization. The intensity of the electrons transmitted through the specimen is imaged on a fluorescent screen or a CCD camera. Transmission electron microscope is composed of the following sections: illumination system, imaging system and detection system. The major TEM techniques include bright-field (BF) and dark-field (DF) imaging, selected area electron diffraction (SAED), high-resolution TEM (HRTEM), and electron energy loss spectroscopy (EELS). Many of TEM techniques, including BF, DF, SAED, EELS and ELNES were used to characterize oxides and semiconductor/oxide interfaces formed by AO and MO species.

**Bright field (BF)** image is created by permitting only the transmitted beam (electrons) to pass through the objective aperture.

**Dark field (DF)** image is created by selecting a diffracted electron beam to pass through the objective aperture.

The contrast in BF and DF images is referred to as “diffraction contrast” [78].

### 5.7.2 Dark field imaging

There are two possibilities when forming the image within TEM: bright-field (BF) and dark-field (DF) imaging. SAED pattern contains a bright central spot (transmitted beam) which contains the direct and diffracted electrons. The image in TEM can be formed by choosing which electrons will contribute to the image, and this is done by inserting an aperture into the back focal plane of the objective lens [77]. This aperture will block the majority of the diffraction pattern except the SAED spots that are chosen by the aperture. If the transmitted beam is chosen, BF image is obtained, and selection of diffracted electrons produces DF image.

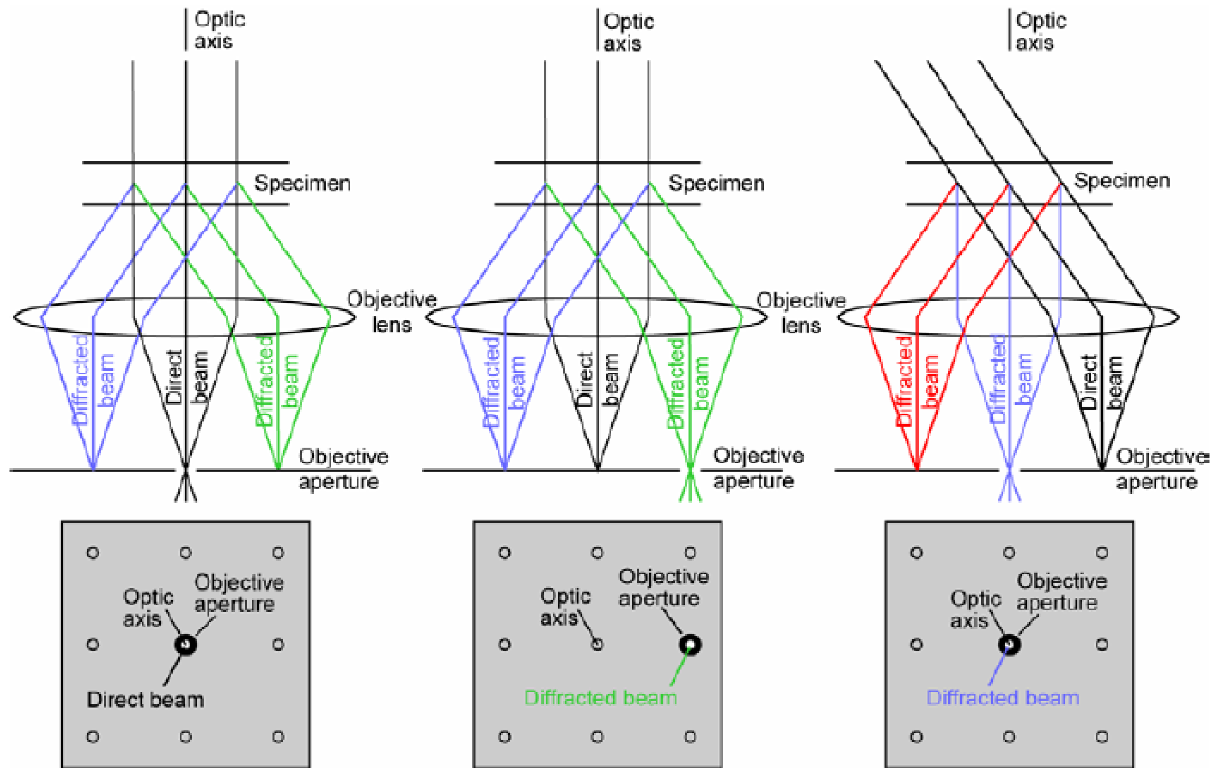


**Figure 24** Schematic diagram of rays in TEM a) BF image formation from direct beam b) DF image formed from off-axis scattered beam c) DF image formed from on-axis scattered beam [77].

In Figure 24–b, DF image is formed from off-axis scattered electrons by displacing the aperture. In order to avoid astigmatism and aberration, the incident beam should be adjusted (tilted) Figure 24-c), so that scattered electrons travel down the optic axis.

Dark field images of the $GeO_2$ plan-view samples were acquired using JEOL 200CX TEM, operating at 200kV, with 0.25 point-to point resolution, at the University of Pittsburgh.

### 5.7.3 Selected area electron diffraction (SAED)

Selected area electron diffraction is used to create a diffraction pattern from a selected area on the specimen. Transmission electron microscope allows observation of both an image, corresponding to information in real space, and electron diffraction giving information in reciprocal space. An intermediate aperture is used to ensure that the signal is coming only from the selected feature of interest. In the case when the incident beam is scattered only once by the sample, kinematical diffraction theory is applicable. On the other hand, electrons can be scattered many times, especially thru thick specimens. Effects of multiple scattering are described by dynamical diffraction theory. Different kinds of diffracted patterns can be created depending on the structure of the sample. Single-crystal, polycrystalline material and amorphous material produce spot, ring and diffuse haloes diffraction patterns, respectively [78, 79].

Diffraction phenomena

Only coherent scattering can lead to diffraction and a precise relationship between the phases of the incident and scattered wave is required. Constructive or destructive interference of the phases from different atoms along different angles in the sample takes place in diffraction. Constructive interference occurs when the path difference is an integer number n of wavelengths

λ, so that Bragg's law, 2dsinθ=nλ, is satisfied. For only certain values of θ will scattering from parallel planes add up in phase resulting in a strong diffracted beam.

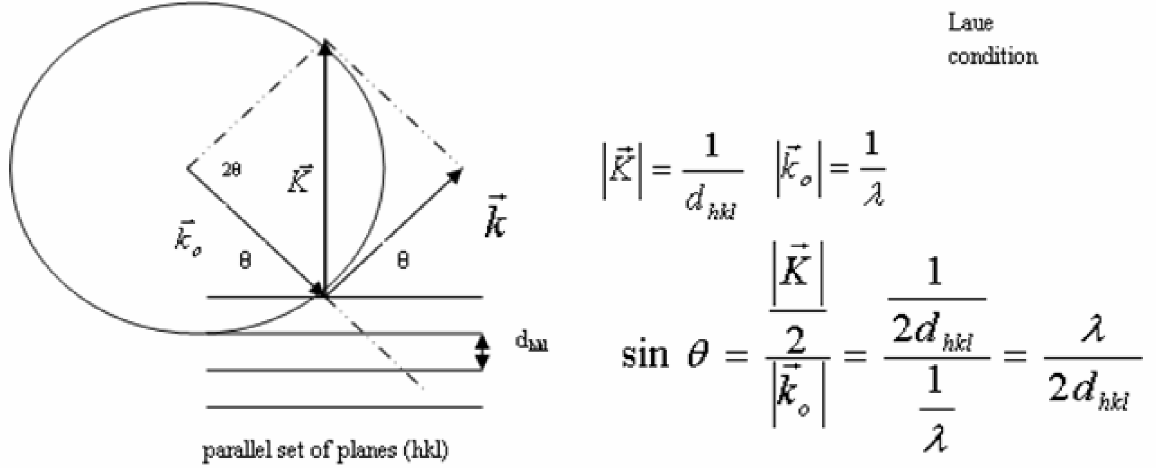


**Figure 25** Ewald sphere construction [79].

Bragg's law $\lambda = 2d_{hkl}\sin\theta$ (Equation 31)

gives the necessary geometric condition for constructive interference (diffraction).

The condition for constructive interference is that the reciprocal lattice point, $\vec{r}^{\,*}_{hkl}$ lies on the Ewald sphere. The center of the Ewald sphere is set at the origin of the incident wavevector.

The total amplitude of electron wavelets scattered coherently from the unit cell is:

(Equation 32)

$$F = A_c = \sum_j \Delta A_j = \sum_{j=1}^{n} f_j e^{2\pi i \Delta\vec{k}\vec{r}_j}$$

where F is called the structure factor. $\Delta A_j$ is amplitude scattered from the j$^{th}$ atom with the fractional coordinates $u_j$, $v_j$ and $w_j$, at the position $r_j$.

$$\Delta A_j = f_j e^{i\phi_j}$$ (Equation 33)

where $\phi_j$ is the phase factor for the j$^{th}$ atom represented as

$$\phi_j = 2\pi\Delta\vec{K} \circ \vec{r}_j \qquad \vec{K} = \vec{k} - \vec{k}_o \qquad \text{(Equation 34)}$$

If $r_j = u_j\vec{a} + v_j\vec{b} + w_j\vec{c}$ (Equation 35)

then the total amplitude scattered by the unit cell is given as:

$$F_{hkl} = \sum_j f_j e^{2\pi i\left(hu_j + kv_j + lw_j\right)} \qquad \text{(Equation 36)}$$

which is the structure factor given by equation 32.

Diffraction itself is a cooperative phenomenon based on phase relationships between the outgoing wavelets scattered coherently by the individual atoms. In the case of crystalline materials, a translationally-periodic arrangement of atoms in a crystal permits strong constructive interference between individual wavelets, creating Bragg diffractions. The electrons are scattered in a predictable manner due to the periodic structure of crystalline solid characterized by the long-range atomic order. Single-crystalline materials generate a pattern of discrete spots, while in poly-crystalline materials the spots converge to form concentric rings. A finer grain size material produces more continuous ring pattern, but the widths of the rings of diffracted intensity become broader and it can be used as an inverse measure of the grain size. When the grain size is larger, the rings might be made of discrete spots (speckle pattern). The diffraction pattern from a poly-crystalline material could be seen as a superposition of a large number of single-crystal diffraction patterns oriented randomly. In amorphous solids, there is no long-range order of the positions of the atoms. Atoms separated by larger distances have a greater variability in their separation, thus the electrons are scattered in less predictive manner in amorphous than in crystalline solids [79]. Consequently, diffused haloes rings are produced and this rings become sharper (similar to the rings for poly-crystalline materials) if the amorphous material orders.

Selected area electron diffraction technique is used to obtain diffraction patterns from the oxide formed by atomic and molecular oxygen. Selected area electron diffraction patterns give structural information about the crystal structure from the particular location of the specimen. These patterns can be used to conclude about the crystallinity and ordering of the analyzed material.

### 5.7.4 Radial distribution function (RDF)

Although amorphous materials are by definition non-crystalline, the structure of many amorphous solids is in fact not completely random arrangement of atoms, at least on certain length scales. For example, in the case of silica, the basic structural building unit is $SiO_4$ tetrahedra. There might be considerable degree of local ordering despite the lack of long-range periodicity, and this can be quantified by the radial distribution function (RDF). The radial distribution function is the probability, per unit element of volume, that an atom will be found at a distance r from another atom [76]. The radial distribution function, J(r), is given by the following expression:

$$J(r) = 4\pi r^2 \rho(r) \qquad \text{(Equation 37)}$$

When this function is plotted against r, the area under the particular peak is proportional to the number of the atoms in that particular shell. The importance of the RDF lies in the fact that the area under a given peak is proportional to the effective coordination number of that particular shell. The position of the $1^{st}$ peak corresponds to the values for the nearest-neighbor bond length (Si-O in silica), position of the $2^{nd}$ peak corresponds to the next-nearest neighbor distance (O-O in silica), etc. The radial distribution function only carries a limited amount of structural

information since it is actually one-dimensional representation of the three-dimensional structure.

The reduced RDF, G(r), is used within this thesis work to characterize the structure of amorphous oxides formed by the oxidation of Si. Reduced RDF is obtained by the direct Fourier transformation of diffraction patterns and it is defined by the following expression:

$$G(r)=4\pi r[\rho(r)-\rho^{o}] \qquad \text{(Equation 38)}$$

where the density function $\rho(r)$ tends to $\rho^{o}$ (average density) at larger r, since the amorphous materials have no long-range order. The term reduced means that the function oscillates around zero instead of being an increasing or decreasing function of r. The reduced RDF curve oscillates about zero since the average density has been subtracted. It is commonly used for data representation since it represents structural variations more clearly than RDF. The relationship between reduced RDF, G(r), and RDF, J(r), is given by the following equation:

$$G(r)=[J(r)/r -4\pi r\rho^{o}] \qquad \text{(Equation 39)}$$

Figure 26 shows the relationship of the density function $\rho(r)$ to the actual atomic arrangement in the structure.

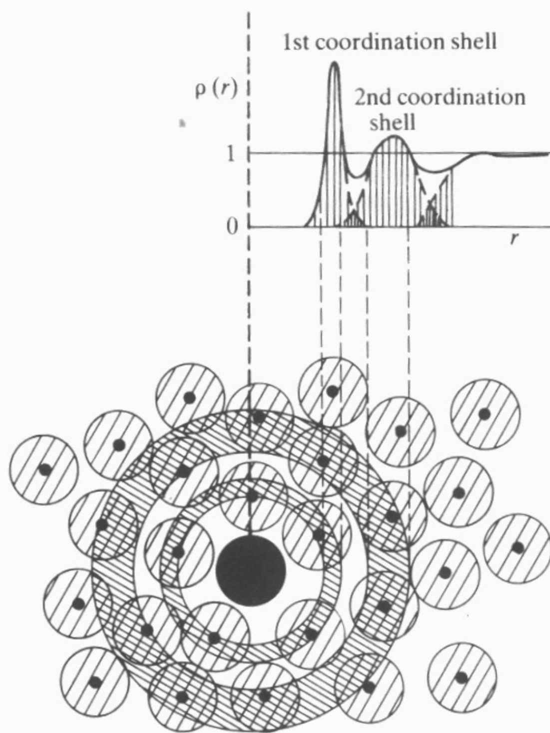


**Figure 26** The relationship of the atomic arrangement and density function ρ(r) for an "amorphous" material [76]. The 1st and 2nd peaks in ρ(r) correspond to the first and second shell of atoms, respectively.

It can be seen from Figure 26 that the density function ρ(r) tends to $\rho^o$ at larger r, since the amorphous materials have no long-range order. Therefore, $[\rho(r)-\rho^o]$ goes to zero for a distances greater than a few primary atomic distances (~6Å).

Two important functions should be mentioned here since they are precursors to obtaining the RDF. These are total scattering intensity, I(k), and reduced scattering intensity, F(k). Total scattering intensity, I(k), is obtained directly from the diffraction patterns after the subtraction of incoherent contributions to the scattering such as Compton scattering. The measured scattered intensity contains contribution from the substrate of the sample (if present), polarization factor contribution and noise. When these contributions are eliminated, the total unnormalized scattered intensity is obtained. These reciprocal space data are converted via Fourier transform into real-

space information, and the scattering vector $\vec{k}$ is given as $\vec{k} = (4\pi\sin\theta)/\lambda$. Reduced scattered intensity curves are obtained using following equation:

$$F = [(\frac{I}{N} - f^2)/f^2]k \qquad \text{(Equation 40)}$$

where N is the total number of atoms in the sample, and f is atomic scattering factor. However, from the examination of correlation curves for F(k) in reciprocal space it is difficult to identify real-space structural correlations simply by the inspection of the curves. Therefore, the reduced scattered intensity, F(k), is converted into the reduced RDF, G(r), using Fourier transform procedure:

$$G(r) = \frac{2}{\pi}\int_0^\infty F(k)\sin krdk. \qquad \text{(Equation 41)}$$

The equation 41 is important since it connects F(k), directly obtained from diffraction experiment, with the reduced RDF, G(r), the function which describes the real-space structure of amorphous material.

Reduced RDF plots for silica formed by 5eV AO and MO are shown in the results section. The SAED patterns taken from plan-view TEM samples were used as the input data for a Digital Micrograph script in order to calculate reduced RDF (Xidong Chen, Cedarville University and Argonne National Lab).

### 5.7.5 Fluctuation electron microscopy (FEM)

Fluctuation electron microscopy provides a statistical measurement of medium range of order (MRO) in material. Medium range of order (MRO) describes the correlations at the 10-20Å range. Fluctuation electron microscopy measures diffraction from nanoscale volumes using annular dark-field transmission electron microscopy. The magnitude of the spatial fluctuations in

diffraction, measured by the normalized variance *V* as a function of scattering vector *k*, gives information about MRO at the length scale of the image resolution. Peaks in variance curve give information about the type of MRO from their position in *k* and the degree of MRO from their height [83, 85].

Variance is given by the following equation:

$$V(k,Q) = \frac{\langle I^2(r,k,Q) \rangle - \langle I(r,k,Q) \rangle^2}{\langle I(r,k,Q) \rangle^2} \quad \text{(Equation 42)}$$

where

I(r,k,Q) = the intensity in the annular dark field (ADF) image as a function of position, r.

k= diffraction vector used for the ADF imaging

Q=radius of the objective aperture in diffraction space (1/Q = proportional to spatial resolution)

V(k,Q) depends on the pair-pair correlations (i.e. three-and four-body correlation) [80].

Figure 27 is a schematic diagram to explain the sensitivity of V to MRO.

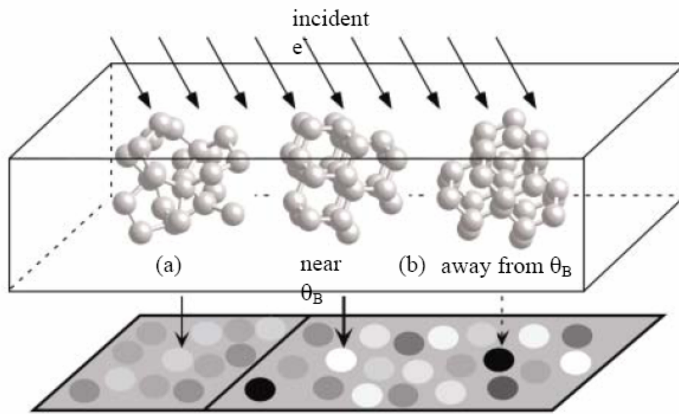


**Figure 27** Variance sensitivity to MRO [83, 85].

If the sample is homogeneous, the diffracted intensity is the same from all of the volumes that contribute, resulting in a low variance map (Figure 27-a). On the other hand, a

heterogeneous sample, with randomly oriented ordered clusters will give a high variance map (Figure 27-b). Clusters oriented near Bragg diffraction condition will diffract strongly, and bright spot will be obtained, while away from $\Theta_B$, diffraction will be weak-dark spot will be obtained. Fluctuation electron microscopy data were acquired on a LEO 912 EFTEM, operating at 120kV, with 1.6 nm spatial resolution (courtesy of W. Stratton and P. Voyles, University of Wisconsin, Madison).

### 5.7.6 High-resolution transmission electron microscopy (HRTEM)

The high-resolution technique uses phase-contrast imaging to form images of columns of atoms. The phase of the diffracted electron wave is preserved and interferes constructively or destructively with the phase of transmitted wave. This type of imaging is based on coherent elastic scattering. HRTEM image represents an interference pattern between the forward-scattered and diffracted electron waves from the sample. If $\psi_o$ and $\psi_g$ represent amplitude of the forward scattered and diffracted beams respectively, then the resulting image amplitude obtained by the superposition of the two waves in the image plane will be given as:

$$\Psi = \psi_o + \psi_g e^{-iW(\theta_g)} \qquad \text{(Equation 43)}$$

where $W(\theta_g)$ is the wave aberration in the diffracted beam , or instrumental phase shift (distortion) which depends on the spherical aberration and focus of the objective lens [78] . The magnitude of $W(\theta_g)$ is the largest for the waves that are bent further from the optical axis. Recently, spatial (point) TEM resolution reached 1.5 $A^o$, and this limit has recently decreased below 1.35 $A^o$ using spherical aberration constant $C_s$ corrected objective lens [86]. Distribution of the atoms in the material is determined by the scattering factor distribution, $\rho(r)$.The diffracted

wave is the Fourier transform of the scattering factor distribution, ρ(r). The expression for the Fourier transform of ρ(r) of the atoms distribution within the sample is:

$$F(\rho(r)) = \frac{1}{\sqrt{2\pi}} \int_{-\infty}^{+\infty} \rho(r) e^{-i\Delta k \cdot r} d^3 r \qquad \text{(Equation 44)}$$

where $\Delta k = k_o - k$ is a diffraction vector and has units Å$^{-1}$, and therefore, represents atom periodicities in the material [79]. This means that short periodicities of ρ(r) are associated with a Fourier transform having large vectors $\Delta k$ .High-resolution images are affected by focus and specimen thickness. Also, instrumental conditions such as high electronic stability of acceleration voltage and lens currents, vibrational-free mechanical stability, high-gun brightness, already mentioned low spherical aberration constant $C_s$, etc. influence HRTEM. HRTEM was used to precisely determine silicon and germanium oxide thickness, as well as characterize the oxide microstructures and the $Si/SiO_2$ and $Ge/GeO_2$ interfaces. A JEOL 2010 FEG microscope operating at 200kV, with a point -to - point resolution of 0.194nm, was used to acquire HRTEM data on Si (Frederick Seitz Materials Research Lab (MRL), user facility at the University of Illinois at Urbana Champaign (UIUC)). High-resolution TEM data on Ge were acquired on a Phillips Tecnai operating at 200 kV (point - to - point resolution of 0.24nm) TEM at Carnegie Mellon University (CMU).

### 5.7.7 Electron energy loss spectroscopy (EELS)

The electron energy loss spectroscopy technique measures the energy loss of the electrons that interact with the specimen. It measures the energy transfer between the electrons in the incident beam and atomic electrons. Information regarding the local environment of the atomic electrons and nearest neighbor atoms can be obtained.

After interacting and passing through the sample, the electrons travel down the microscope column and reach the EELS spectrometer which is mounted after the projector lens. The magnetic prism is the main component of the spectrometer and it is used to resolve the energies of the electrons. When electrons enter the magnetic prism spectrometer, they are deflected by the magnetic field. The amount of deflection is determined by the energy loss that the electrons experienced and the greater the energy loss of the electron, the further is the deflection. There are two basic designs of the EELS spectrometers, serial and parallel. The parallel method is characterized by much shorter spectra acquisition time and it is the preferable method in EELS analyses. Acquiring the EELS spectrum includes checking the width of the zero-loss peak since it gives a direct estimate of the energy dispersion of the spectrometer [87]. A Gatan Imaging Filter (GIF) possesses both imaging and spectral possibilities. Instruments at CMU and UIUC all contained a GIF.

### 5.7.8 Scanning Transmission Electron Microscopy (STEM) Spectrum Imaging (SI)

Changes in composition of the materials can take place at the nanometer level; therefore it is important to determine accurately the chemical distribution on such a small scale. The spatial resolution of EELS Spectrum Imaging is approximately 1nm. Acquiring a spectrum image requires using Scanning Transmission Electron Microscope (STEM) and a parallel

recording detector. A nanoscale probe is produced at particular point (x,y) on the sample. The probe is scanned across a predefined region and the EELS spectrum is acquired and stored within a pixel at each of the probe positions. The electron intensity within a 3-D volume (x,y and E) is recorded, as represented in Figure 28. For example, if the size of the image is 20x20 pixels, it will contain 400 acquired spectra [56, 58].

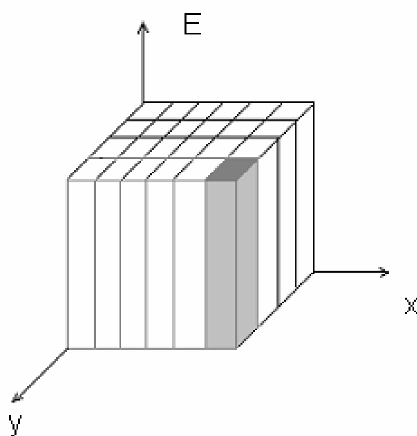


**Figure 28** STEM analyses with Spectrum Imaging (SI).

It is also possible to create a background subtracted spectrum image and follow the progression at a particular edge over a range of probe positions.

### 5.7.9 Electron Energy Loss Spectrum

In Electron Energy Loss Spectroscopy, electrons which experienced inelastic interaction with the sample are analyzed. Not all of the beam electrons have interacted with the specimen inelastically – the EELS spectrum contains information about both elastically and inelastically scattered electrons. All features except zero-loss peak result from the inelastic scattering of the incident electron beam. The term elastic means that there is no change in energy, but there is the change in the deflection angle. Inelastic scattering refers to the beam electrons that are scattered

by the inner or outer shell atomic electrons. Inelastic interactions carry information about the nature of the atoms, their electronic structure and bonding with surrounding atoms. Different energies are involved in inner and outer-shell scattering; therefore, these losses occupy different parts of the EELS spectrum [23, 77]. Regions of the EELS spectrum are:

***Zero - loss peak*** is the most intense feature in the spectrum and contains the elastic forward-scattered electrons that experienced very small energy losses. Therefore, these electrons have approximately the same energy as the incoming electron beam.

***Low-Loss spectrum*** appears adjacent to the zero-loss peak and is much less intense. It contains electrons that interacted with the weakly bound outer shell electrons of the sample resulting in low energy losses (up to ~50eV).

***High-Loss*** spectrum contains electrons that interacted inelastically with tightly bound inner-shell (core) electrons and it appears above 50 eV. The energy needed for the ionization process is transferred from the incoming electron to a core- shell electron in the atom. Hence, the amount of energy lost by the incoming electron is equal to the ionization energy. Since the ionization process is characteristic of the atom, the high-loss spectrum provides chemical information. The K shell is the lowest energy state and, hence, requires the highest energy to be ionized. Therefore, a feature that corresponds to the removal of an electron from the K shell will appear at the highest energies in the EELS spectrum. Ionization of L, M, N and O shells requires much less energy since these are higher energy states corresponding to quantum numbers $n = 2$, 3, 4 and 5, respectively. A limit of EELS is typically around 1000eV, so this technique is more sensitive to higher level shells and low atomic number elements. Figure 29 is an example of an EELS spectrum taken from the Si-oxide formed by 5eV atomic oxygen on Si.

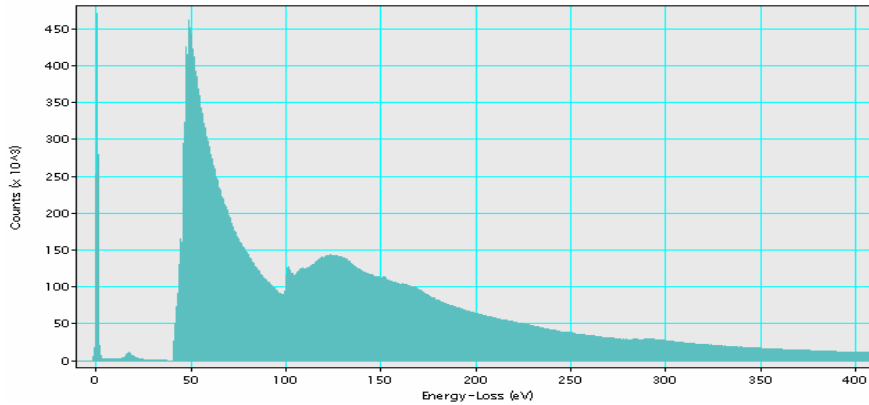


**Figure 29** Characteristic EELS spectrum of $SiO_2$ as-acquired containing the most intense zero-loss peak, low-loss and high-loss region characterized with core-loss edges. Si $L_{2,3}$ edge onset is visible around 100eV.[5].

A sharp rise appears at the ionization threshold and the energy loss corresponds to the binding energy of the Si -$L_{2,3}$ atomic shell. The presence of certain elements can be determined from the appearance of the edges in the spectrum.

The ratio of the background to ionization edges will increase if the sample is not thin enough making these edges difficult to resolve. Generally, specimens thinner than 50nm should be used in EELS experiments. Effects of plural and multiple scattering can distort the shape of the EELS spectrum; therefore, great care has to be taken in the specimen preparation step. Plural (more than 1 scattering event) and multiple scattering (more than 20 scattering events) arise when the specimen thickness is more than the mean free path of the inelastic scattering phenomena. The term mean free path refers to the average distance between scattering events. If the intensity of the plasmon peak is less than 10% of the intensity of the zero-loss peak, then the specimen is adequate for EELS analyses.

Superimposed on the monotonically decreasing background are ionization edges characterized by their fine structure. By the comparison of the experimental edges fine structure with the EELS Atlas database or other standard EELS spectrum, it is possible to determine the

particular element as well as their oxidation states [88]. This fine structure changes for the element when it undergoes phase transition or changes valence state. A change in valence state of the element reflects the change in the energy levels of molecular orbitals (e.g. due to the bonding in compounds). The distribution of the electrons is also changed, which is reflected in the changed peaks positions and shapes in the EELS spectrum. Therefore, EELS spectra must be processed and the near edge fine structure revealed in order to asses these subtle changes. .

### 5.7.10 Electron loss near edge fine structure (ELNES)

Electron loss near edge fine structure corresponds to fine peaks around core-loss edges (<50eV). It is very sensitive to the chemical and structural surrounding around the particular excited atom. This technique probes the electronic structure and the density of states (DOS). An electron can be excited into any of the unfilled states, but the excitation probability is not equal for all of the energy states. Since EELS measures transitions, it probes unoccupied density of states. Density of states depends on the chemical binding, such as oxidation state. It is extremelly difficult to model electron-atom interaction. Density of states gives a “fingerprint” of the element in the particular oxidation state.

A chemical shift of the ionization threshold can accompany the ELNES where this shift originates from the changes in chemical bonding. For the particular case of the $SiO_2$ compound, a molecular orbital diagram is useful in explaining the origin of the Si $L_{2,3}$ edge shift from 99.5eV in bulk silicon to 103.5eV in silica.

In pure silicon, four $sp^3$ orbitals are formed by hybridization of the Si s and p orbitals. Pure silicon can be visualized as a central Si atom which is $sp^3$ hybridized bonded with 4 other Si atoms, and, consequently, forming two kinds of molecular orbitals. Antibonding molecular

orbitals have higher energy levels than atomic orbitals and therefore do not contribute to bonding. On the other hand, the energy of bonding molecular orbitals is lower than that of atomic orbitals. These bonding-molecular orbitals are filled with electrons which contribute to bonding. Since all four Si atoms surrounding the central Si atom are identical, there will only be a small decrease in the energy level due to the formation of molecular orbitals. In the case of $SiO_2$, the Si atom is bonded to four O atoms, which are electronegative and have lower atomic orbital energies as compared to Si. The overlap of the hybridized $sp^3$ orbitals of Si with 2p orbitals of O produces σ bonds [94]. Therefore, $SiO_2$ molecular orbitals will have lower energy when compared to the bonding orbitals of pure silicon. The $SiL_{2,3}$ edge represents the transition of an electron from the 2p core state to the 3d and 4s unoccupied states, respectively. The SiL near-edge structure (ELNES) depends on the neighboring chemical environment of the silicon atom. Changes in the ionization threshold energy and edge profile are observed by ELNES. These changes result from the bond-induced changes in the valence shell electronic structure [90, 95-97]. The electronic structure is changed since the energy levels of the molecular orbitals shifted due to bonding, thus influencing the electron distribution. The "fingerprint method" is particularly useful to determine the atom surroundings and its valence. It was found that electronegativity and type of bonding directly influence the core loss edge shape, therefore giving rise to the unique features that are recognizable as a fingerprint of the material. For example, ELNES of $SiL_{2,3}$ and SiK edge of quartz is quite different from ELNES of stishovite, which is characterized by Si bonded with 6 other atoms [98] .

### 5.7.11 EELS spectra processing

In order to extract either qualitative or quantitative data, the acquired EELS spectrum must be processed. The signal to background ratio becomes very small if the specimen is too thick and the spectra obtained from such specimens must first be deconvoluted. Generally, deconvolution should be avoided since one can easily introduce many artifacts and obtain a spectrum that is a worse representation of the data than the one originally collected. The steps to extract the EELS signal are as follows:

Input the experimental conditions, such as beam energy [keV], convergence and collection semi-angles [mrad].

Calibration of the energy scale is usually done using a known edge position.

Removal of the large, monotonically decreasing background signal to determine ELNES spectrum and quantify the core-loss signal $I_{k.}$

$$I_k = I_t - I_b \quad \text{(Equation 45)}$$

where $I_t$ is the total integrated intensity over the core-loss integration range and $I_b$ is background contribution to the total intensity. This background intensity has to be removed since it originates from valence-electron excitations, plural inelastic scattering and the tails of preceding core-loss edges and it is often comparable or even greater than the core-loss signal of interest. In order to minimize the effect of plural scattering, very thin specimens should be used for EELS studies, and their thickness should be significantly less than the inelastic mean free path, λ, of the material of interest [56].

There are several models available in the EELS package for background extrapolation and one should choose the model that provides the most accurate fit. A simple energy-loss

function, I(E), is fitted to a background region immediately before the edge of interest. Generally, a 50eV offset should be used not to lose information from the pre-edge region. A polynomial, log-polynomial or power-law models can be used for this operation [23, 88]. An inverse power-law is the most commonly one applied and produces the most satisfactory results in a broad range of analyses. The integration window over the edge should be such that $E_{finish}$ ~1.5 $E_{start}$, since fit parameters A and r in the power law function are valid and constant over ~100eV.

Depending on the shell type, different models should be used to calculate the cross-section. Egerton's SIGMAK and SIGMAL computer programs are used only for modeling K and L shells, and they are provided with the GATAN EELS software [23, 88]. SIGMAL and SIGMAK use the hydrogenic model to calculate the generalized oscillator strengths (GOS) and ionization cross-sections. This model is the simplest one since it assumes an isolated hydrogen atom, neglecting outer shell electrons, so it is best for K shell electrons. It gives a very good fit to the experimentally observed edge, but it also neglects near -and post -edge fine structure since it does not take into account any other electrons. Beside the hydrogenic model, the Hartree-Slater model can also be used. This model assumes that the elements are in atomic form and can be treated as single-electron inner-shell wave functions undergoing transitions to a final state. This model is much more complicated than the hydrogenic model and better for L and M edges and generally can be applied for any edge that is beyond the range of SIGMAL.

#### 5.7.12 EELS Acquisition Conditions and Spectra Processing-Experimental

1. Calibration of the energy scale was done using known carbon K edge position at 284 eV. The major source of carbon is the epoxy used for the preparation of cross –sectional TEM samples. Generally, C edge is an undesired feature in the spectrum, but on the other hand, it is very useful to calibrate the energy scale.

2. Background removal was done using power-law. The power law profile is fitted in the pre-edge region and extrapolated to the post edge region and subtracted. Fitting was done in a chosen background window (<50eV in width) in the pre-edge region. Since the Si L edge ionization energy is low (~99 eV), the background fitting window was very small while it was larger for O K edge which appears at 532eV. The background is subtracted when both the sharp rise in the edge intensity and the best fit in the pre-edge region were achieved during the fitting procedure. Figure 30 shows an EELS spectrum as acquired from Si(100) and the background fitting using a power law revealing Si $L_{2,3}$ edge fine structure and C K edge at ~284eV.

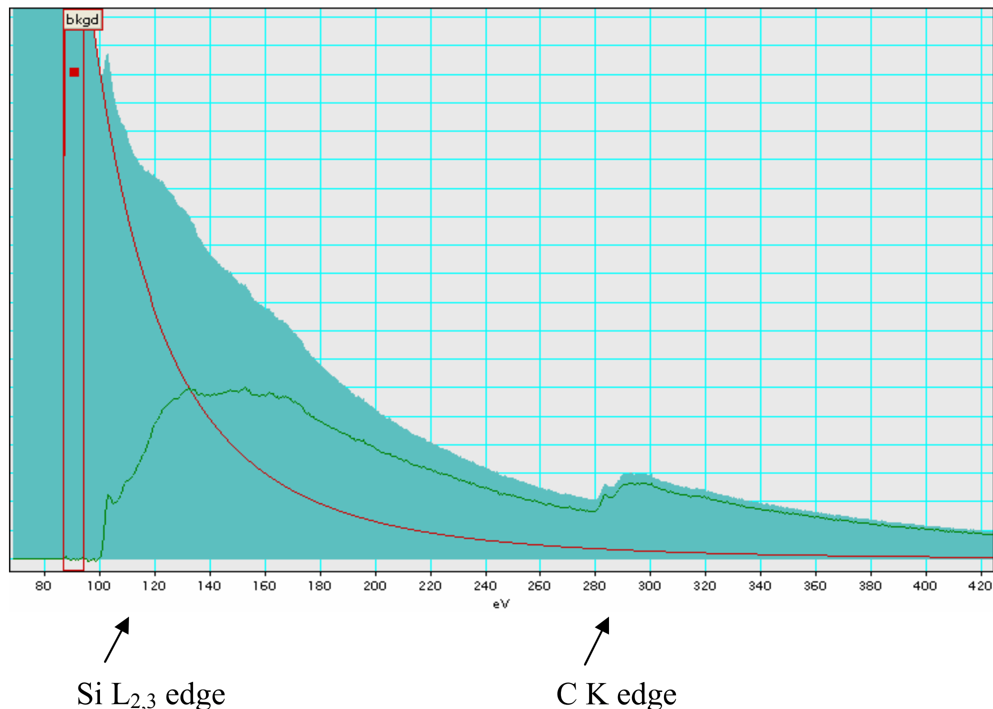


Figure 30 **As - recorded EELS spectrum and background fitting to Si$L_{2,3}$ edge [5].**

Partial ionization cross-section was calculated using Hartree-Slater model both for SiL and GeL edges since it seemed to be very good approximation of the experimentally observed edges [23, 88].

The EELS technique enables determination of valence states of the analyzed element. Chemical shift of the characteristic ionization edge reflects the change in the oxidation state of the particular element. We used this method to get information about the oxidation states of Si and Ge within the bulk oxide and at the semiconductori/oxide interface. This technique also allows determination of the stoichiometry of the formed oxide. The fingerprint method was used to determine the oxide structure.

JEOL 2010FEG microscope operating at 200kV and with the probe size of 1.2nm was used initially, (UIUC) on Si/$SiO_2$ specimens. High spatial resolution electron energy loss spectroscopy (EELS) data were acquired with a parallel electron energy-loss spectrometer

attached to an $C_s$ aberration-corrected VG HB501 dedicated scanning transmission electron microscope (STEM), operating at 100kV. This microscope is capable of achieving an energy resolution better than 0.5 eV, with a spatial resolution below 0.1nm (Klaus van Benthem, Steve Pennycook, Oak Ridge National Laboratory (ORNL)) due to the addition of a NION $C_s$-corrector. It is equipped with a Gatan Enfina parallel detection electron energy loss spectrometer and a cathodoluminescence detection system. EELS data on $Ge/GeO_2$ were acquired on a Phillips Tecnai, operating at 200kV (spatial resolution 0.2nm, energy resolution 1eV), at CMU.

### 5.7.13 X-ray photoelectron spectroscopy (XPS)

X-ray photoelectron spectroscopy characterization method is not used within this thesis experimental work, but a brief overview of this technique is given since I compare my QCM results with XPS data available from the literature [16]. X-ray photoelectron spectroscopy (XPS) is widely used in surface science to study chemical properties of materials. The principle of XPS is that photons with certain energy are absorbed by a system and core electrons are emitted. The most commonly employed X-ray sources are those giving rise to Mg $K_a$ radiation ($h\nu$ = 1253.6 eV), and Al $K_a$ radiation ($h\nu$ = 1486.6 eV). Therefore, the emitted photoelectrons have kinetic energies in the range of 0 - 1250 eV or 0 - 1480 eV [91].

The electron is excited from the core state, but it can escape only from the top atomic layers due to the low energy of the emitted photoelectrons. Consequently this is a surface-sensitive technique. Incident photon of energy $h\nu$ causes an electron to be ejected from the material with kinetic energy $E_k$. This process can be described by the formula:

$$E_k = h\nu - E_b \quad \text{(Equation 46)}$$

where $E_b$ defines binding energy of electron in the particular core state.

The binding energy represents the amount of energy needed to remove an electron from the nucleus [99].

In contrast to the EELS, the electrons in the final states in XPS are free of nuclei attraction. An energy analyzer measures the kinetic energy of these electrons. The measured kinetic energy of the emitted electron depends on the binding energy and the work function of the spectrometer. Peaks in the XPS spectrum correspond to the occupied energy levels in atoms, while EELS probes unoccupied states. Intensity of the peaks depends on the number of atoms present. Knowing that the binding energy of core electrons is determined by the chemical environment, it is possible to determine the composition of the sample or the valence state of a certain element. By measuring chemical shifts, determination of the coordination number of an element is possible. The surface depth limit (~100 Å) and large probe size (10μm-2mm) are two basic limitations of XPS as compared to the EELS technique [92].

### 5.7.14 Atomic force microscopy (AFM)

Atomic force microscopy is used to determine the oxide surface roughness. **Tapping mode** is particularly suitable for the delicate samples that are easy to damage or alter in other modes [100]. A Dimension 3100 Digital instruments AFM (University of Pittsburgh, MSE Department), was used in this study. Atomic force microscopy can be classified in three categories according to the interaction between the tip and the surface of the sample. **Contact mode** is based on the repulsive force while noncontact mode uses attractive force. In the contact mode, the tip scans across the sample in close contact with the surface and the magnitude of the repulsive force is $10^{-9}$ N. The measured cantilever deflection is converted into the height of the features on the sample surface. The problem with this kind of mode can be seen particularly in

insulators and semiconductors that can trap electrostatic charge and consequently create large attractive forces between the probe tip and the sample surface. **Non-contact mode** utilizes the tip that scans 50-150A$^o$ above the surface of the specimen. Attractive Van der Waals forces between the probe tip and the sample surface are measured, along with the change in amplitude, frequency or phase of the cantilever [100]. The probe tip is placed on the specimen surface to obtain high resolution surface morphology and then lifted from the surface in order not to damage it by dragging. The cantilever oscillates until it touches the surface; the oscillations then decrease due to the physical contact of the tip to the surface. The AFM was used to determine the surface roughness of the $SiO_2$ and $GeO_2$ formed by atomic and molecular oxygen.

It was found by the X-ray diffraction studies, done by Brügemann et al. on Si, that the oxidation process by $O_2$ has only a small influence on the micro-roughness of Si surface [102]. Since the oxidation of Si occurs in layer-by layer fashion, a smooth oxide surface is expected as well [102, 103]. The effect of energetic AO on Si should be different from the effect of $O_2$, and the oxide surface roughness will be investigated using AFM.

## 5.8 STOPPING RANGE OF IONS IN MATTER (SRIM) SIMULATION

In the AO oxidation of Ge and Si, one can assume that the oxidation reaction stops when there is no more available oxygen atoms at the semiconductor/oxide interface. Availability of the O atoms at the interface depends mainly on the ability of AO to travel through the already formed oxide layer. Hence, to understand the possible effect of the kinetic energy of the AO on the transport of oxygen and oxidation mechanisms, SRIM simulations were performed to know "how far" into the target the moving AO carrying a certain amount of energy can reach. Many interactions between the incident atoms and oxide layer (target) will contribute to the final

transport process. SRIM is used as an additional method to estimate the stopping range of energetic AO in the oxide layers. The compilation of several programs included in SRIM provides calculation of stopping range of ions in the material. SRIM is based on Monte Carlo method and on the full quantum mechanical treatment of the incident atom interaction with the target atoms [101]. The best accuracy is achieved for the energies of ions or atoms in the range of 10eV-2GeV, and it can be used for targets up to eight layers. SRIM simulations account for every collision between the incident and target atom, including exchange and correlation interactions between the overlapping electron shells. The moving atom can create plasmons and electron excitations within the target. A 3D distribution of atoms can be calculated, as well as the kinetic phenomena associated with the incident atom's energy loss, such as sputtering, target damage and ionization. Besides the calculation for 15eV AO, we used it in our calculation for lower energies AO, 5eV and 9eV, in order to obtain estimate for the fraction of transmitted AO atoms and their energies after they penetrate through the certain oxide layer thickness. The results of the SRIM calculations are given in the APPENDIX AI of this thesis. While SRIM software is a useful tool in prediction of the range of atoms in matter, and the energy loss of the incident atom, it has some limitations. For example, it uses Bragg's rule that the stopping power of a compound in the target may be estimated by the linear combination of the stopping powers of individual elements contained within the target material [104]. This rule is reasonably accurate, and the measured stopping of ions in compounds usually deviates less than 20% from that predicted by Bragg's rule. On the other hand, the accuracy of Bragg's rule is limited because the energy loss to the electrons in any material depends on the detailed orbital and excitation structure of the matter. Therefore, any differences between elemental materials and the same atoms in compounds will cause Bragg's rule to become inaccurate.

## 5.9 KINETIC STUDY OF ENERGETIC AO REACTION WITH SI AND GE IN RESEARCH QUARTZ CRYSTAL MICROBALANCE (RQCM) - PRINCIPLE

When electrodes are placed on a quartz crystal, and a periodic voltage is applied, the crystal will vibrate at its resonant frequency. A particular mode of vibration dominates when the crystal is cut in a certain way. The AT-cut is most commonly used since the mode of vibration for this cut is in the thickness-shear mode and is most responsive to mass change, and is somewhat insensitive to temperature changes near room temperature [105, 106]. An electrical potential is applied across electrodes, resulting in mechanical shear deformation (piezoelectric effect). When the potential is alternated, the crystal oscillates producing an acoustic wave. This wave propagates through the thickness of the crystal, as shown in Figure 31-b.

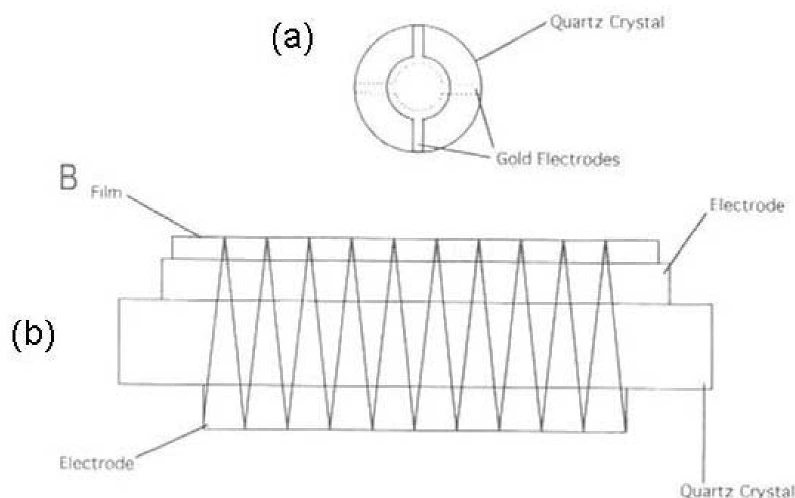


**Figure 31** (a) Quartz crystal with the electrode pattern shown on both sides - dotted electrode is located at the bottom side of the crystal (b) Schematic of the transfer wave propagating through a quartz crystal, film deposit and electrodes.

The following relationship holds between the thickness of the quartz crystal and the resonance wavelength:

$$t_q = 1/2\ \lambda_q \qquad \text{(Equation 47)}$$

where $t_q$ is the thickness of the quartz crystal, and $\lambda_q$ is the wavelength of the acoustic wave in quartz. If this relationship is expressed in terms of the resonant frequency of quartz ($f_o$), and the acoustic wave velocity in quartz ($v_q$), and since $\lambda_q f_o = v_q$ , the following equation is obtained:

$$f_o t_q = 1/2 v_q \quad \text{(Equation 48)}$$

It can be seen that a change in the thickness results in a change in the resonant frequency, which is given by the Saurebrey relationship:

$$\Delta f = -\frac{2 f_o^{\,2} \Delta m}{A(\mu_q \rho_q)^{1/2}} \quad \text{(Equation 49)}$$

where $\Delta m/A$ (g/cm$^2$) is a mass change per unit area and $\Delta f$ is the observed frequency change in Hz; $f_o$ is the resonant frequency of the quartz crystal (Hz), typically, about 6 MHz, $\rho_q$ is the density of the quartz (2.648g/cm$^3$), $\mu_q$ is the shear modulus of AT-cut quartz (2.947x10$^{11}$ dyne/cm$^2$) [106]. Since $f_o$, $\mu_q$ and $\rho_q$ are physical constants of quartz, the equation above can be expressed as

$$\Delta f = -C_f \, \Delta m \quad \text{(Equation 50)}$$

where $C_f$ is defined as the mass sensitivity of the particular quartz crystal.

The oxidation behavior of Si and Ge in energetic AO was investigated using a dual-head RQCM instrument (Maxtek corporation) incorporated into the UHV FAST AO source at the University of Pittsburgh [105]. The QCM unit is designed so that it can measure sensor crystal frequency for up to 2 crystals simultaneously (through channels 1 and 2). There are 2 electrodes on the crystal, one is on the front side (sensing electrode), while the contact electrode is on the rear side of the crystal. Silicon and Ge films (~1000Å thick) were deposited onto the quartz

crystal. As the Si or Ge are exposed to AO, they oxidize and the mass of the sensing crystal increases, thus reducing the oscillating frequency of the crystal. The mass change per unit area at the QCM electrode surface is related to the observed change in oscillation frequency of the crystal by the Sauerbrey equation. The software available with the Maxtek RQCM automatically converts these resonant crystal frequency changes to various physical parameters such as mass gain (in $\mu g/cm^2$). The mass gain is proportional to the thickness of the growing oxide, which is a common parameter used for kinetic measurements.

A high performance phase -lock oscillator (PLO) uses an internal oscilattor to drive the crystal. A PLO circuit provides superior stability of the measurements for a wide frequency range (3.8 to 6.06 MHz). The frequency resolution for the QCM at University of Pittsburgh is 0.03Hz at 6MHz, which corresponds to a mass resolution of $<0.4 ng/cm^2$. Sauerbrey's expression is valid for only very small changes in frequency (less than 3% shift).

### 5.9.1 Si and Ge coatings deposition on standard crystals

The sensing crystal is an essential part of the QCM system. Maxtek crystals are available in a variety of surface finishes, such as Au, Pt, Ag, Al and Ti [105]. The thickness of the crystal is about 0.013inch. A Si and Ge amorphous film, approximatelly 100nm thick, was prepared on an Al-coated quartz crystal, 1/2 inch in diameter by sputter deposition. This was done within the MRL at University at Illinois at Urbana-Champaign (UIUC) (courtesy of Tony Banks), where the AJA sputter system was used. The base vacuum was held at $10^{-7}$ Torr in the chamber, and the deposition rate was 0.6-1.0 Å/sec and 1.0-1.1Å/sec for Si and Ge films, respectively. Argon gas (5mT pressure) was used as a protective atmosphere to prevent any oxide formation during the thin film growth. It is very important to carefully handle both the crystal and crystal holder in

order to ensure accuracy of the measurements. Nevertherless, due to air exposure during transport from UIUC to the University of Pittsburgh, Si and Ge coatings contained a native oxide. The native oxide was not removed prior to placing them into the AO chamber since etchants (containing HF) would etch the quartz surface, and possibly corrode the electrode material too.

### 5.9.2 Oxidation of Si and Ge by 5eV AO in QCM

One Si and one Ge sample were loaded to each QCM head for simultaneous measurements during AO exposure. These samples were exposed to AO with an average flux of 1.75 $x10^{14}$ atoms $cm^{-2}$ $sec^{-1}$ and kinetic energy of either 5 or 9eV. A total of 108000 pulses with 3 pulses per second were used. The frequency of the oscillating crystal was measured every 10s with a frequency resolution of 0.03Hz, corresponding to a mass resolution of $<0.4ng/cm^2$. At the onset of AO exposure, immediate mass gain did not occur; there was an anomalous regime that might be due to outgassing and the stabilization of the AO source. Contaminants that are present on any film surface usually cause the appearance of the anomalous frequency reduction and subsequent recovery. The total data collection time for this run was 10 hrs, but only the portion from 6 to 10 hrs is used for quantitative data analysis since the data acquired for t<6hrs did not show significant mass gain. Contamination of the sample surface is the most probable reason for this unusual observation at the beginning of the oxidation process where the AO is reacting with the carbon build-up to form gaseous carbon oxides. The experiment was done at room temperature, and the mean energy of the hyperthermal AO was approximately 5 or 9eV. The erosion rate of Kapton “witness” sample was used to calculate the AO fluence.

### 5.9.3 Oxidation of Si and Ge by 9eV AO in QCM

One Si and one Ge sample were loaded into the sample holder (using 2 channels for data acquisition), at the average flux 1.88 $x10^{13}$ atoms $cm^{-2}$ $sec^{-1}$. A total of 75600 pulses with 3 pulses per second were used. The mass increase for this run occurred earlier than for 5eV AO experiment, and the data were collected for 7hrs of oxidation time. The mass loss during the initial period was probably due to surface contamination and since inconclusive, is not presented in results section. A high energy (9eV) beam of AO was obtained by adjusting the delay time to 7.4μs between the two radiometers. Consequently, the velocity of AO beam was 10.3km/s, since the distance between the radiometers is 7.6cm. The experiment was done at room temperature. The erosion rate of a Kapton "witness" sample was used to measure the AO fluence.

# 6.0 RESULTS AND DISCUSSION

The highlights of my MS thesis results on Si oxidation with AO and MO species were presented in the background section to provide insights into the oxidation processes by energetic AO. Nevertheless, the research on Si oxidation was continued within this PhD work and these results are presented in the following chapters. High-resolution transmission electron microscopy studies of cross-sectional (X-TEM) samples of Si oxidized by 9eV AO were performed in order to determine the effect of kinetic energy of the AO on the oxide thickness. Electron energy loss spectroscopy investigation was performed on a $C_s$ corrected VG HB501 STEM at Oak Ridge National Lab, for higher energy and spatial resolution of the Si/$SiO_2$ interface. Also, kinetic QCM studies were performed and the $SiO_2$ thickness was monitored in-situ for 2 different energies of AO, 5eV and 9eV. The kinetic energy of 5eV was used since the performances of the source are optimized at this value, and 9eV (rather than 15eV) was used to explore higher energy AO effect on Si and Ge oxidation. 9eV AO energy was chosen over 15eV since the performances of the AO source are optimized at 5eV, and so the performance of the source at 9eV should be closer to its optimal performance at 5eV, as compared to 15eV.

After a more complete investigation of Si oxidation by hyperthermal AO species, I investigated the effects of AO on Ge oxidation. The results obtained on Si served as a reference point and provided a guideline for the experiments on Ge oxidation, since both are semiconductors, and have diamond cubic crystal structures. The lattice parameters are 5.4309

and 5.6576 Å for Si and Ge, respectively, and Si has a larger band gap (1.11eV, indirect) as compared to Ge (0.67eV, indirect) [26, 43].

As described in the experimental part, some of the exposures to energetic AO were done at Montana State University (MSU), one of seven sites in the world where FAST™ AO source was available. The other sites where this type of AO source is presently available are: Japan (2 instruments), PSI (2 instruments), France, Netherlands and now at the University of Pittsburgh. Since the apparatus was not readily available, the exposure of the samples in this unique source represent original, for the first time done experiment. Fortunately, FAST™ AO source has arrived at the University of Pittsburgh, at the MSE Department. Every exposure is unique since depends on many factors in this complex apparatus composed of UHV and the laser components. The experimental constraints and difficulties in the samples production consequently led us to use many characterization methods for every sample to extract as much information as possible. Since the exposed area of the samples (oxidized at MSU) was small ($1cm^2$), non-destructive characterization techniques were used first, before the samples were cut to prepare TEM specimens. AFM, HRTEM, SAED, RDF, FEM and EELS characterization methods were all used on the available samples.

## 6.1 EFFECTS OF HYPERTHERMAL AO ON SILICON OXIDATION

### 6.1.1 $SiO_2$ thickness

My previous MS research focussed on the room temperature ex-situ oxidation of Si by 5eV AO. Here I used AO of higher energy, 9eV, in order to determine kinetic energy effects on the oxide formation. Figure 32 is a HRTEM micrograph taken from the X-TEM sample of Si oxidized by 9eV AO at 200$^{o}$C. In order to clearly distinguish between the amorphous oxide and epoxy (also amorphous) used in sample preparation, a Au capping layer was deposited on the oxide surface by sputtering at room T (MEMS lab, at the University of Pittsburgh, courtesy of Sandy Hu).

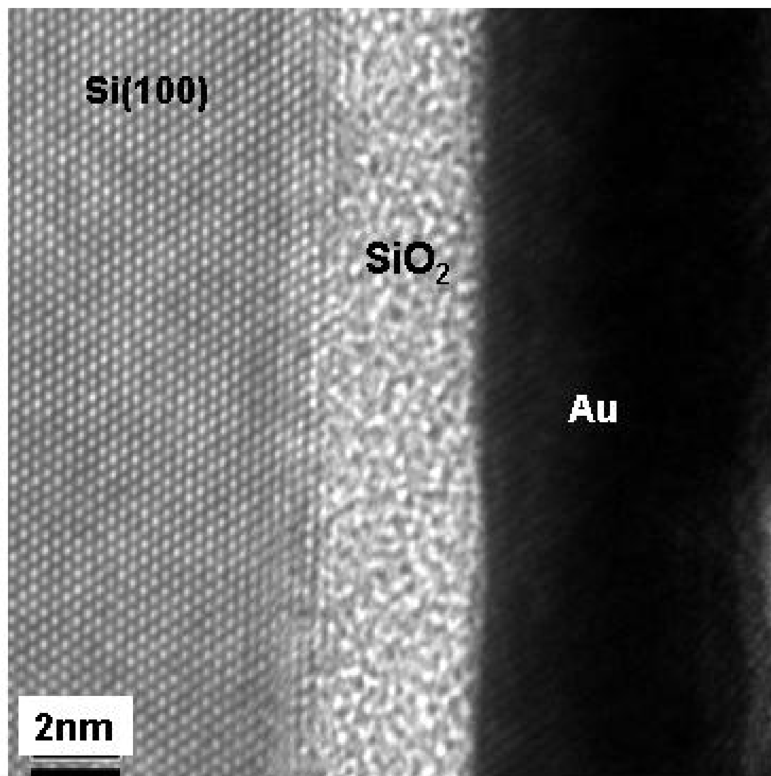


**Figure 32** Cross-sectional HRTEM micrograph of the silicon oxide layer formed on Si(100) oxidized by 9 eV AO at 200$^{o}$C.

The oxide layer formed by 9eV AO was observed to be ~5nm thick, which is similar to my observations of 5eV which also formed 5-6nm thick layer on the same substrate and temperature, as presented in the background section (Figure 5-a). This might be assigned to the one order of magnitude higher flux used for 5eV AO oxidation ($3.2 \times 10^{15}$ at/cm$^2$sec), as compared to the flux used for 9eV AO oxidation ($1.79 \times 10^{14}$ at/cm$^2$sec). In order to obtain fully comparable data on the oxide thickness, all parameters including AO flux, sample temperature, and cleaning process should be the same. Some discrepancies are possible, since the results for 5eV AO oxidation shown in the background (Figure 5-a) were obtained from the AO source in Montana, and the result presented in Figure 32 is obtained from the source at the University of Pittsburgh. The flux within the AO source depends on the distance from the nozzle to the sample stage, and this distance is different within two sources.

### 6.1.2 Investigation of Si/$SiO_2$ interface and oxidation states

Since the probe size used to acquire the spectrum shown in Figure 9 and Figure 10 was 1.2 nm, high spatial resolution EELS was performed to determine whether the Si/$SiO_2$ interface formed by 5eV AO was atomically abrupt. $C_s$ corrected VG-HB5O1 STEM at Oak Ridge National Laboratory (ORNL), with energy resolution better than 0.5eV, and spatial resolution below 0.1nm, was used to determine that the change from $Si^{o}$ to $Si^{4+}$ was within 2 ML.

Figure 33-a is the HAADF image of the Si/$SiO_2$ interface where the (110) Si lattice with 2.71Å spacing, can clearly be seen. Figure 33-b represents the $SiL_{2,3}$ edge progression across the Si/silica interface. The position of the spectrum image is shown at the high angle annular dark field (HAADF) image of cross-sectional TEM sample, in Figure 33-a.

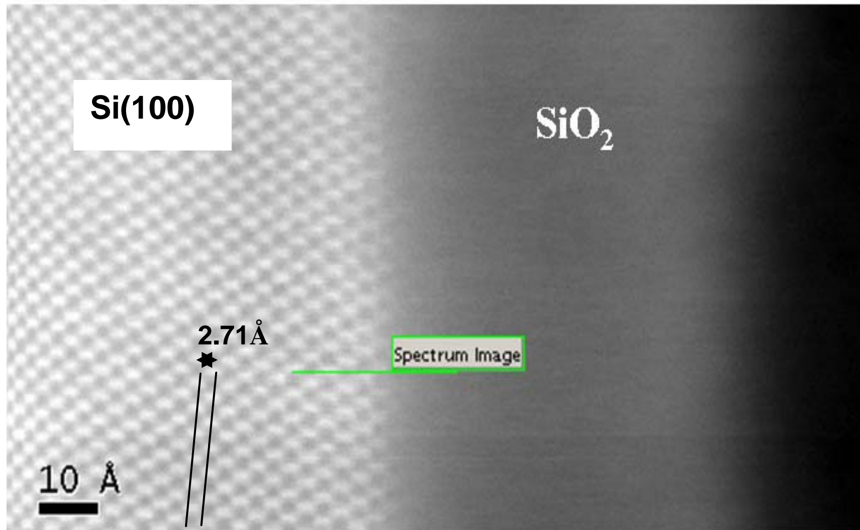


(a)

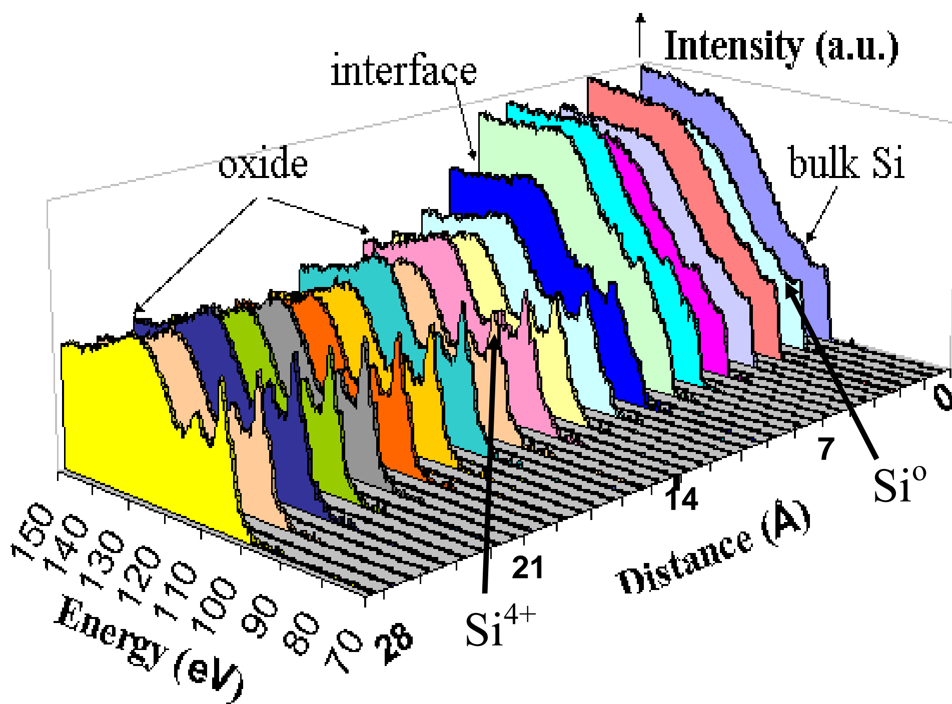


(b)

**Figure 33** (a) HAADF image of cross-sectional TEM sample ([110] zone axis). (b) Background subtracted $SiL_{2,3}$ spectrum image of Si(100) oxidized by 5eV AO (MSU) at 220$^o$C (total AO fluence =$8.1x10^{19}$ at/cm$^2$), acquired on a $C_s$-corrected VG HB501 STEM-step size~1.4Å.

Only $Si^0$ (99.8eV), in the Si, and $Si^{4+}$ (103.5eV) oxidation states, in the oxide were detected, where a transition zone of <2ML was noted. The spacing between each spectrum was 1.4Å.

It should be noted that this sample was oxidized in the LDS source at MSU, with the total AO fluence of $8.1x10^{19}$ at/cm$^2$. The run for the same energy (5eV) was not repeated within the AO source at the University of Pittsburgh. A more direct comparison of kinetic energy effect would be if all of the samples were exposed using same AO source. Generally, the samples at the University of Pittsburgh were not exposed to as much AO as at MSU (e.g. for the case of Ge oxidized by 5eV AO at the University of Pittsburgh, total fluence was $2.4x10^{19}$ at/cm$^2$). It will be shown later that the Ge -oxide thickness depended on the AO energy (see Figures 38 and 40), and similarly to that, AO energy should affect Si oxidation as well.

### 6.1.3 Increased order in the Si oxide caused by energetic AO

A further analysis of SAED patterns is done by calculating Radial distribution functions (RDF) [87]. This function measures the short range order (SRO), and describes 1$^{st}$ coordination sphere and nearest neighbors on the length scale < 10Å. Selected area electron diffraction (SAED) patterns taken from the plan-view TEM sample of Si oxidized by 5eV AO and by MO were used as the input data for a Gatan Digital micrograph script (written by Xidong Chen, Cedarville University and ANL) [82]. This script is basically a code that calculates RDF, J(r), and reduced RDF, G(r), from the reduced scattered intensity, F(k), as described in section 5.7.4.

The reduced RDF's, obtained directly by Fourier transformation of diffraction patterns, are shown in Figure 34.

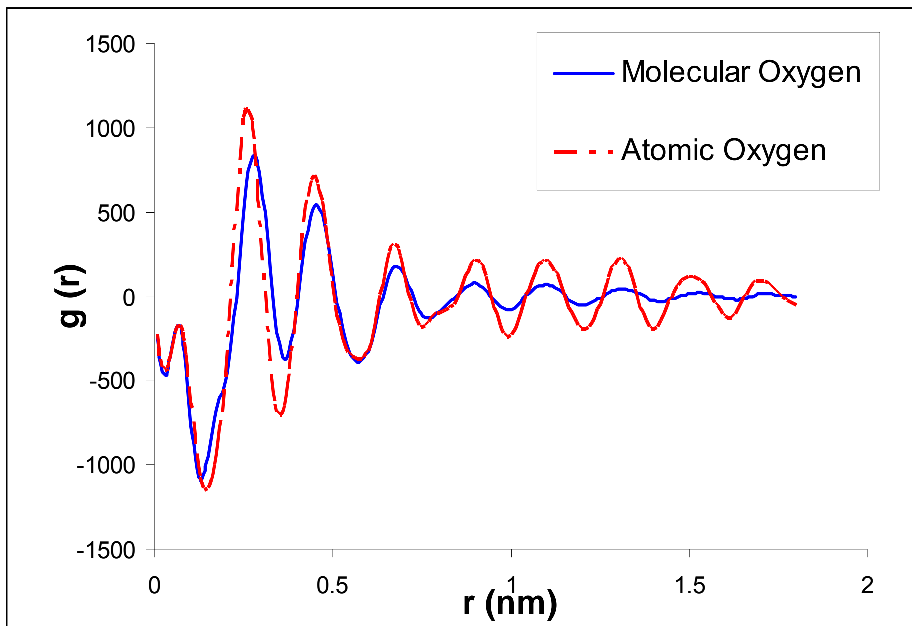


**Figure 34** Reduced RDF plots obtained from Si(100) oxidized by atomic (5eV) and MO. First six peaks correspond to the Si-O, O-O, Si-Si, Si-2nd O, O-2nd O, and Si-2nd Si distances.

These functions oscillate about zero since the average density, the $r^2$ dependency of the radial distribution function, has been removed [107]. The peaks in the reduced RDF for Si sample oxidized by 5eV AO and by MO are at the same positions, as seen from Figure 34.

The analyses of the area under the peaks showed that 45% larger area is obtained for 5eV AO oxidized Si, as compared to the MO oxidized sample. This result may suggest that the oxide structure formed by AO is denser than the oxide structure formed by the MO. This is in agreement with the fact that AO forms more ordered oxide (similar to alpha-quartz), as presented by the EELS results shown later (Figure 37). The density of the quartz is higher ($2.65 g/cm^3$) as compared to the density of amorphous $SiO_2$ ($2.27 g/cm^3$), supporting the RDF result that the denser oxide structure is formed by AO.

The 1st peak corresponds to the Si-O distance, and the 2nd peak corresponds to the O-O distance in the reduced RDF plot in Figure 34. The higher peaks present in the reduced RDF

curve for the AO oxidized sample might indicate a more ordered oxide is formed by 5eV AO. However, the difference in the peaks height is not big enough to be considered as a clear indication of a difference in short-range order (SRO) between these two samples. Therefore, fluctuation electron microscopy (FEM) technique is used to characterize medium range order (MRO), as discussed next.

The RDF provides information on the SRO, but is not useful for obtaining information on the MRO [86]. Therefore, we employed variable coherence FEM to obtain a variance curve for both samples, as shown in Figure 35 [83, 85].

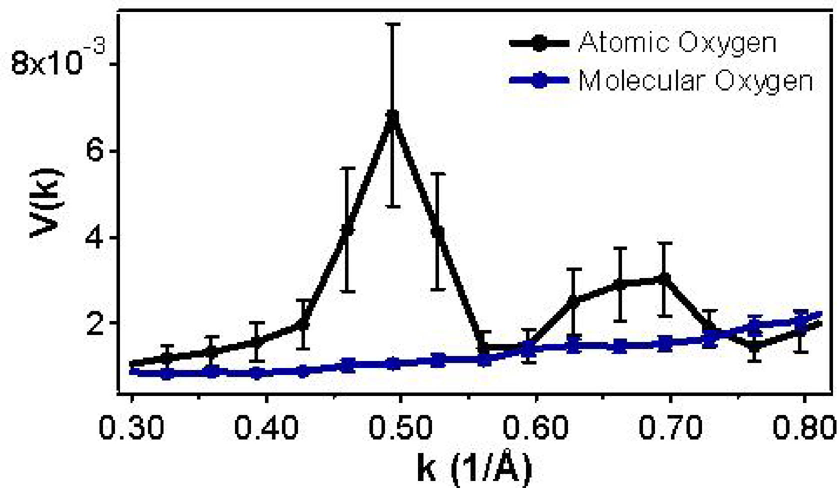


**Figure 35** Variance V(*k*) plots obtained from Si(100) oxidized by atomic (5eV) and MO.

An average of ten data sets from different areas of the sample is used to obtain the variance curve, with the error bars representing the standard deviation from the mean. The positions of the peaks correspond to the internal structure or type of MRO, while the intensity of the peaks reflects the degree of MRO order in the material [85]. The type of MRO (peak location) and degree of MRO (peak magnitude) for Si(100) oxidized by AO is dramatically different than that oxidized in MO. The variance curve for the 5eV AO oxidized sample shows

two distinct peak locations (type of MRO) with a higher magnitude (degree of MRO) compared to any feature in the curve for MO oxidized sample, demonstrating that the AO-formed silica, though amorphous, has a more ordered arrangement of Si and O atoms than the molecular-oxygen formed oxide.

Figure 36 shows an annular dark field image obtained from Si(100) oxidized by 5eV AO. $SiL_{2,3}$ edges are recorded as a spectrum image starting from the bulk Si, through $Si/SiO_2$ interface and bulk oxide.

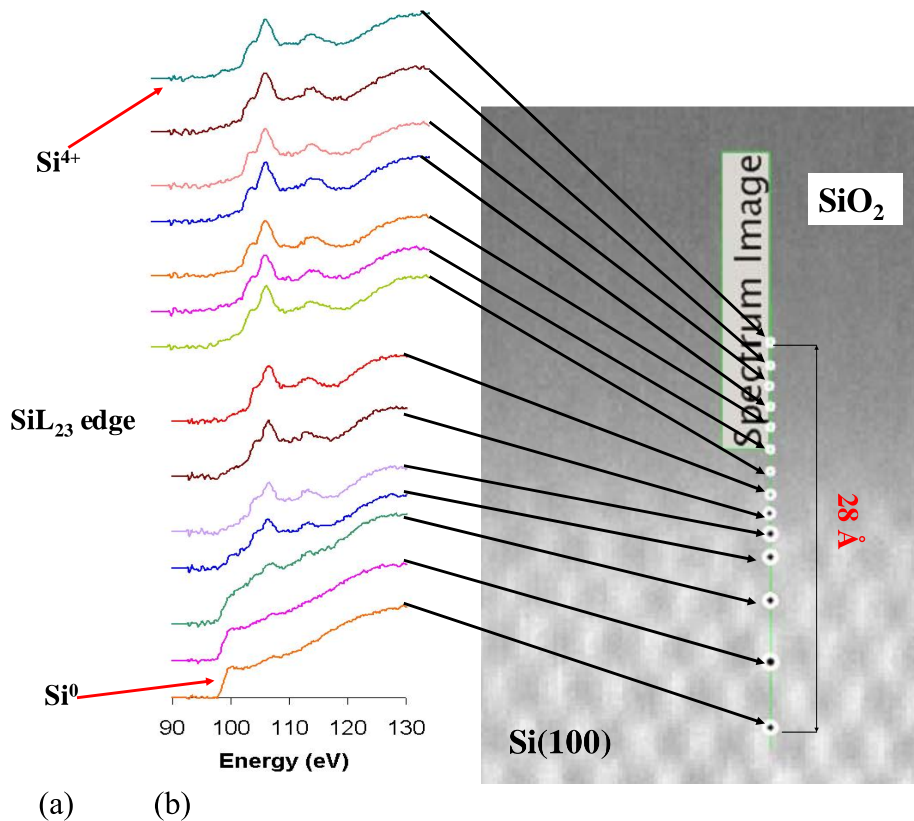


**Figure 36** Si(100) oxidized by 5eV AO (a) Annular dark field image (b) $SiL_{2,3}$ background stripped edge recorded in Si bulk, $Si/SiO_2$ interface and oxide bulk.

$SiL_{2,3}$ core-loss edges from Si(100) and Si(111) oxidized by the 5eV AO specie are superimposed on the $SiL_{2,3}$ edge Electron Loss Near Edge fine Structure (ELNES) for different forms of silica, obtained by Garvie et al.[108] (Figure 37). Generally, $SiL_{2,3}$ core-loss edges in

silica exhibit their onset at 103.5eV, characteristic larger peaks at 108eV, 115eV followed by delayed maxima at 130eV.

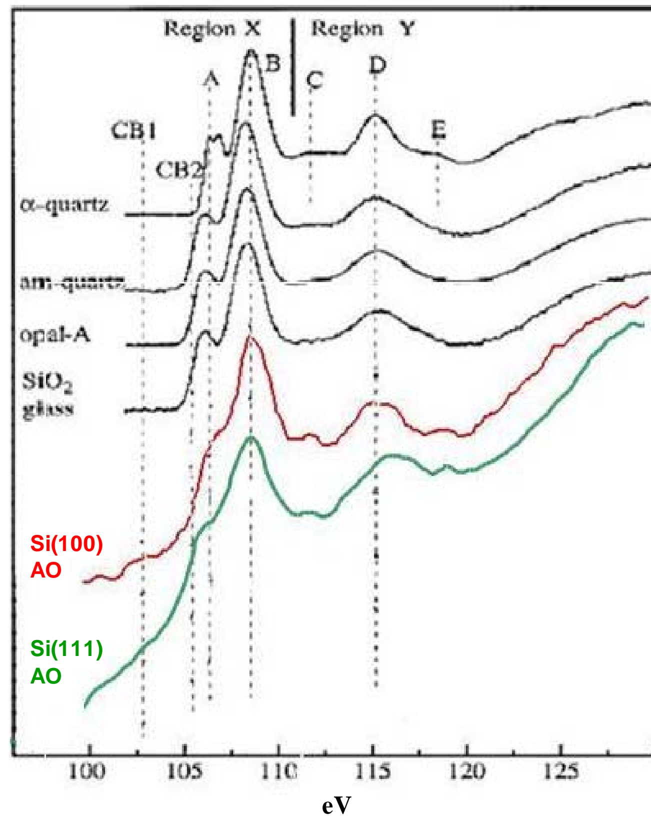


**Figure 37** ELNES comparison of $SiL_{2,3}$ edges of Si oxidized by 5eV AO with results of Garvie et al. (data acquired on $C_s$ corrected VG-HB501 STEM)

Garvie et al. found that it is possible to conclude whether the structure is crystalline or amorphous from the closer examination of peaks width and position (fingerprint method) [108]. The characteristic ELNES peaks/features are marked as A, B, C, D and E. Higher energy edge onset, sharper peaks and peak in position E are characteristic features that are present in the crystalline form of silica, alpha-quartz. Amorphous silica is found to have lower energy of the edge onset, broader peak maxima and lower energy ELNES maxima [5, 27]. I previously reported that $SiL_{2,3}$ edge in silicon oxide created by 5eV AO shows higher edge onset energy and

sharper peak B when compared to the $SiL_{2,3}$ edge obtained from silica layer formed by MO oxidation [5]. Also, small peak E around 118eV was noticeable for both for Si(100)and Si(111) oxidized by AO whereas such a peak is completely unresolved for amorphous silica formed by MO oxidation. It was concluded that oxidation of Si by hyperthermal AO produces more ordered silica structure, very similar to that of alpha-quartz while oxidation by MO created amorphous, non-ordered oxide [5, 27]. Here we confirm this conclusion on higher resolution level using $C_s$ corrected VG-HB501 STEM (0.5eV energy resolution), as shown in Figure 37. The presence of the peak E at 118eV is more obvious for both Si orientations, confirming less amorphous, quartz-like structure formed by the 5eV AO oxidation of Si, also supporting my previous SAED data.

## 6.2 EFFECTS OF ENERGETIC AO AND TEMPERATURE ON GERMANIUM OXIDATION

Structural characterizations of the Ge-oxide and Ge/$GeO_2$ interface were conducted in a similar manner as for Si samples. Oxide thickness, surface roughness and oxidation states were investigated in order to assess the differences in AO and MO formed structures on Ge substrate. Atomic oxygen beams with different energies were used to oxidize Ge, in order to determine how the oxide thickness and structure may depend on the AO translational energy. Oxidations at different temperatures were also performed to determine the effects, if any, of temperature.

### 6.2.1 $GeO_2$ increase in thickness due to increase in AO kinetic energy

The thickness of the oxide formed by 5eV AO and MO oxidation of Ge(100) single crystal at 200°C was determined by HRTEM (Figure 38).

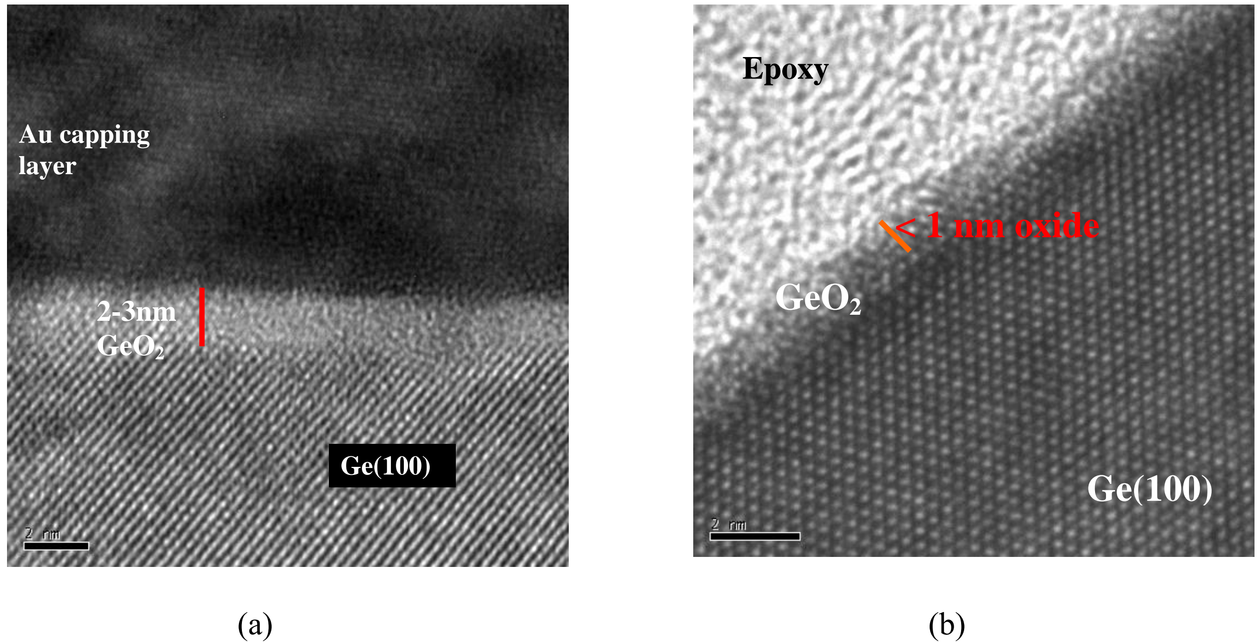


(a) (b)

**Figure 38** Cross-sectional HRTEM micrographs of the Ge oxide layer formed on Ge(100) oxidized by a) 5eV AO b) MO at 200°C, where the oxide thickness doubled due to AO exposure (2-3nm) as compared to MO (~1nm)

The Ge oxide created by 5eV AO at 200° C on Ge(100) has an average thickness of 2-3nm, while the passivated layer formed by MO was les than 1nm thick at the same temperature. A gold layer was deposited on the Ge oxide surface created by 5eV AO prior to X-TEM sample preparation in order to separate the $GeO_2$ from the epoxy.

Figure 39 shows that the Ge oxide created on Ge(100) by 5eV AO at room temperature also has an average thickness of 2-3 nm, thereby demonstrating that the temperature, within the T range in LEO, does not have noticeable effects on the oxide formation.

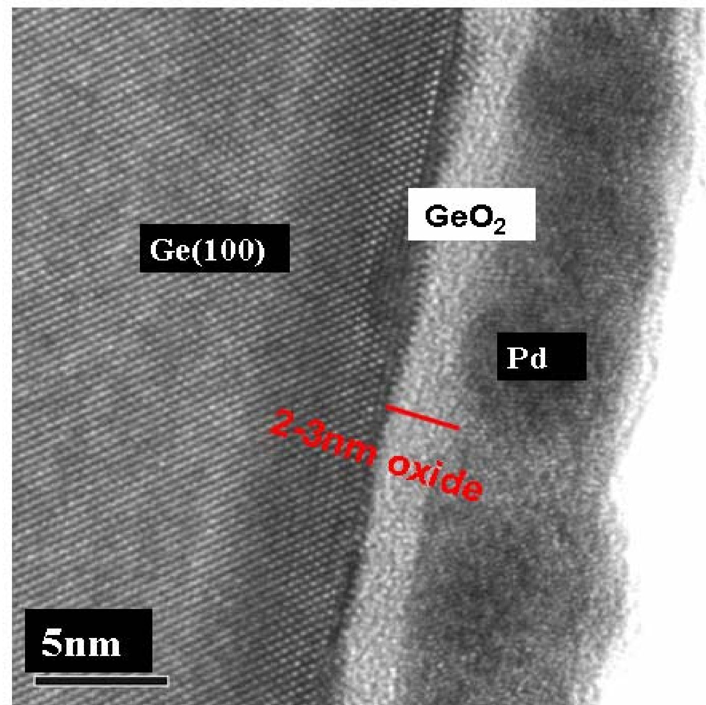


**Figure 39** Cross-sectional HRTEM micrograph of the 2-3nm Ge oxide layer formed on Ge(100) oxidized by 5eV AO at room temperature.

A Pd capping layer was deposited for a clear demarcation between Ge oxide and epoxy. 5eV AO forms the same oxide thickness at room temperature and at 200$^{o}$C. This observation is very interesting since it indicates that the oxide thickness is not dependent on the oxidation temperature in this temperature range (25-200$^{o}$C). This can be explained if the two oxidation steps, parabolic and linear, are considered separately. The factors responsible for the initial, rapid linear regime are inherent to substrate properties (dangling bonds, surface states, point defects, etc.) and the ability of AO to form Ge-O bonds. All of these factors might stay the same for the temperature between room T and 200$^{o}$C, which will result in the formation of similar oxide thickness. Once transport-limited proces take over, the diffusion is dependent mainly on AO kinetic energy. This energy can be transferred to the substrate and cause local heating (5eV is equivalent to ~58000$^{o}$C) which will promote diffusion of AO more efficiently than the change in

temperature in 25-200°C range. A thicker oxide layer formed on Ge when it was exposed to AO with higher kinetic energy, as seen from Figure 40. Figure 40-a and b are HRTEM micrographs taken from X-TEM samples of Ge oxidized by 9eV and 15eV AO, respectively.

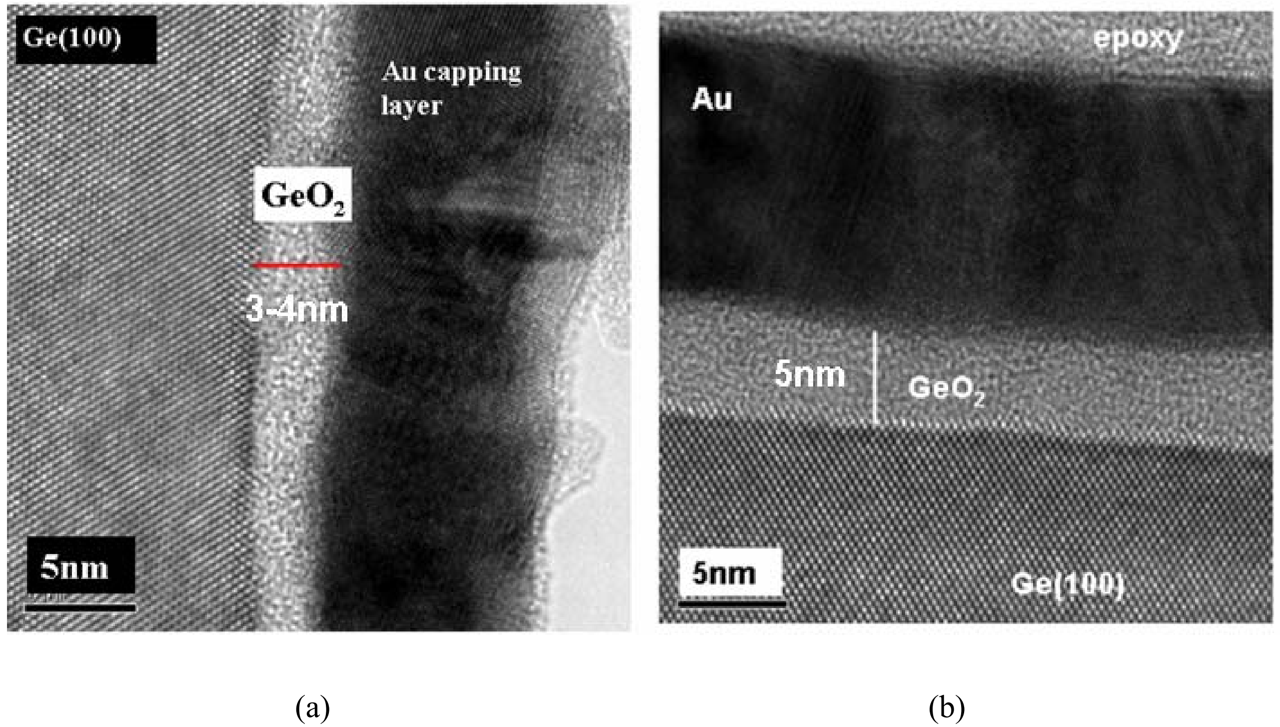


(a) (b)

**Figure 40** Cross-sectional HRTEM micrograph of the Ge oxide layer formed on Ge(100) oxidized by a) 9eV AO at 200°C (3-4nm) b) 15eV AO at 200°C (5nm)

It can be seen that the oxide formed by 9eV AO on Ge(100) is 3-4nm thick, while 15eV formed ~5nm thick oxide layer on the same substrate and temperature (200°C). The fluxes of 9eV and 15eV AO were comparable, of the same order of magnitude ($10^{14}$ at/cm$^2$sec), therefore it can be considered that the increase in oxide thickness occurred only due to the increase in AO kinetic energy.

### 6.2.2 Investigation of Ge/$GeO_2$ interface and oxidation states

Characteristic Ge $L_{2,3}$ and $L_1$ edges obtained from Ge(100) single crystal, oxidized at 200°C by 5eV AO, are shown in Figure 41.

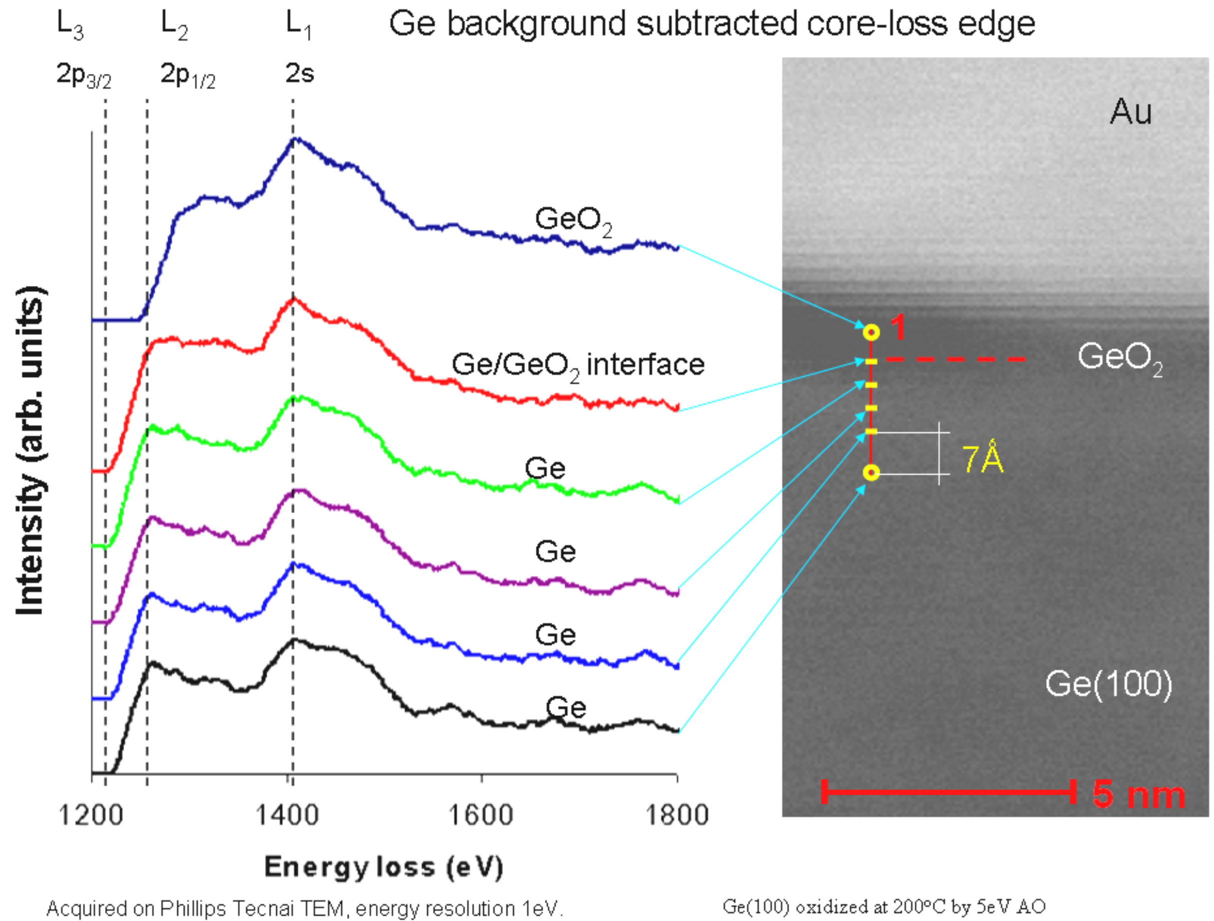


**Figure 41** Background subtracted Ge$L_{2,3}$ and Ge$L_1$ spectrum image of Ge(100) oxidized by 5eV AO, acquired on Philips Tecnai STEM (CMU).

A Philips Tecnai STEM, operating at 200kV, (spatial resolution 0.2nm, energy resolution 1eV), at CMU, was used to acquire the data from the X-TEM sample. The background subtraction was done using Hartree-Slater model embedded in the GATAN EELS software, in the similar way as it was done for EELS data taken at the Si/$SiO_2$ interface. The length of the

scan was 35 Å, and the distance between each spectrum was ~7 Å. The evolution of the GeL edge from the bulk silicon ($Ge^o$), across the $Ge/GeO_2$ interface to the germania bulk oxide suggests an abruptness of the $Ge/GeO_2$ interface formed by 5eV AO. The Ge $L_3$ edge has an onset at 1217 eV, followed by the characteristic peaks at 1248 and 1414 eV, for the $L_2$ and $L_1$ edge, respectively. The onset of the $GeL_3$ edge shifts, from $Ge^o$ (1217 eV) to higher energies, indicating a chemically abrupt interface. There is a lack of EELS data on the Ge and $GeO_2$ particularly, since mostly Si-Ge alloys, and not pure Ge, are used in the semiconductor industry, and therefore investigated more extensively. Only the Ge edge in pure Ge is available from EELS Atlas [88]; there is no available literature data for the Ge edge in $GeO_2$ [109].

We have seen from the HRTEM and EELS results, given in the background sections 2.4. (Figure 5) and 2.4.1 (Figure 10), respectively, that the oxidation of Si by MO at 220°C produced ~1nm thick interfacial layer. This interfacial roughness could be explained as being due to “steps and kinks” in the crystalline to amorphous transition as proposed by Helms [110]. The SAED results from my MS work showed that $SiO_2$ formed by MO oxidation is amorphous, thus supporting the idea of crystalline to amorphous transition at the interface (although no evidence of a second crystalline phase) (Figure 12-b). The reason for the possible formation of these non-uniform interface structures is the lower interfacial free energies, owing to the relaxation of the bonding constraints of a perfectly flat interface, as proposed by Helms [110].

On the other hand, $Si/SiO_2$ and $Ge/GeO_2$ interfaces are observed to be abrupt when formed by energetic AO. The EELS and SAED results of this thesis demonstrate that the oxide formed by AO on Si is more ordered than amorphous oxide formed by MO. A more ordered oxides can form an epitaxial oxide layers (with no bonding constrains) on the Si substrate, leading to low interfacial free energies. The SAED results reveiled that the smaller oxide grains

formed when Ge was exposed to the AO, as compared to the larger oxide grains formed by MO. Smaller oxide grains should form more abrupt interface on the Ge substrate than the larger ones, since the accommodation of the smaller grains should be easier, with less voids and defects in the interfacial layer. The surface roughness of the oxide layer formed by energetic AO is discussed later in section 6.2.3.

### 6.2.3 $GeO_2$ surface roughness

The AFM investigation was performed on a Dimension 3100 Digital instruments and images were acquired in the tapping mode. Atomic force microscope images of the surfaces of the Ge(100) oxidized by energetic AO and MO at 200°C are given in Figure 42, and the results are summarized in Table 4.

**Table 4** Summary of the mean square roughness (RMS) of the oxide surface formed by energetic AO on Ge substrate

| Sample | Roughness (RMS) (nm) |
|---|---|
| Ge $O_2$ 200°C | 1.49±0.15 |
| Ge native oxide | 0.48±0.11 |
| Ge 5eV AO room T | 1.93±0.13 |
| Ge 5eV AO 200°C | 2.26±0.18 |
| Ge 9eV AO 200°C | 2.37±0.15 |
| Ge 15eV AO 200°C | 5.25±0.26 |

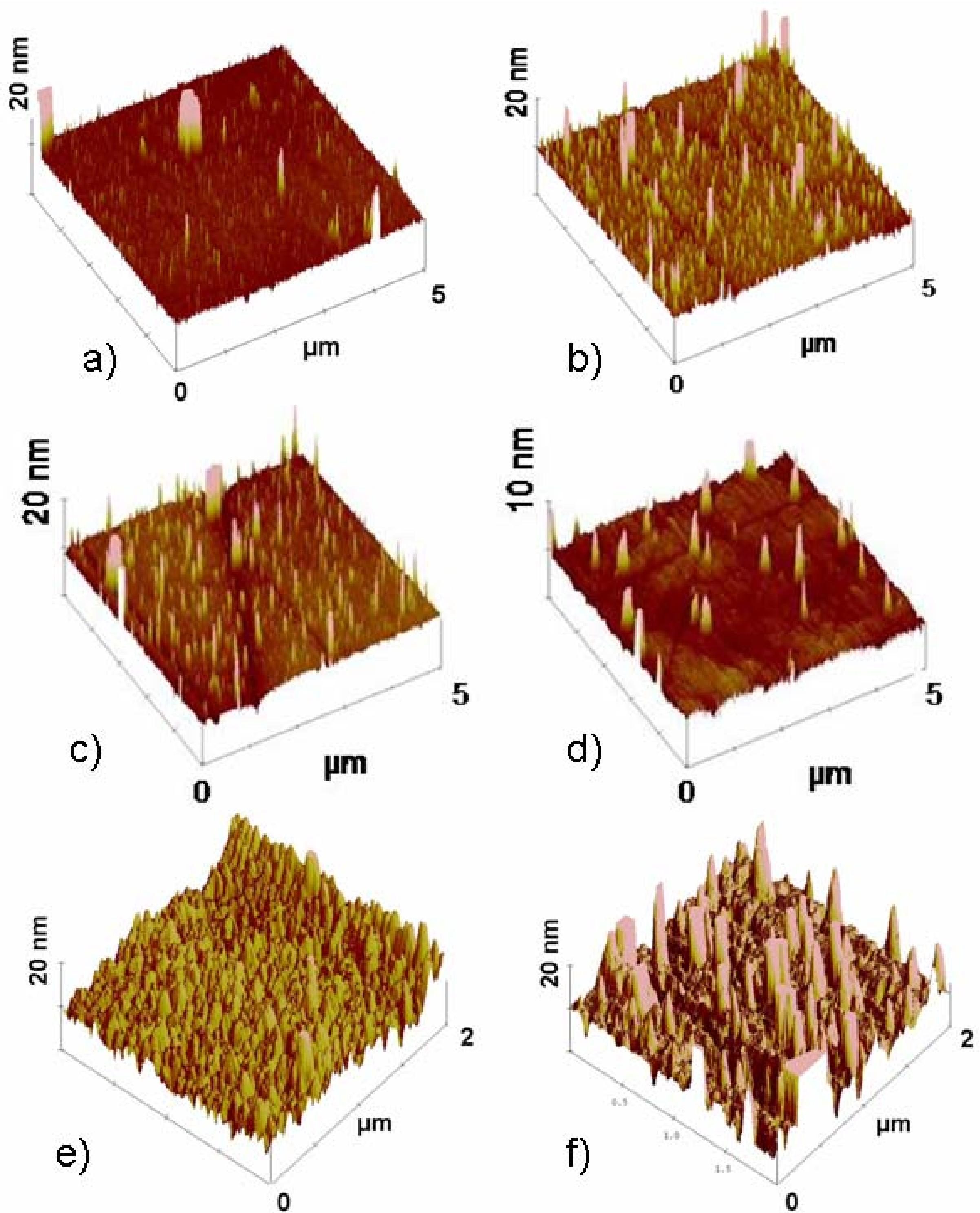


**Figure 42** AFM images of Ge(100) oxidized by a) 5eV AO at 200°C (RMS=2.26nm) b) MO at 200°C (RMS= 1.49nm) c) 5eV AO at 25°C (RMS=1.93nm), d) native oxide (RMS= 0.48nm), e) 9eV AO at 200°C (RMS=2.37nm) and f) 15eV AO at 200°C (RMS=5.25nm)

The surface roughness of the oxide formed by 5eV AO was 1.5 times higher than that formed by MO at 200$^{o}$C. The mean square roughness (RMS) is ~2.26nm (Figure 42-a) for the oxide created by AO, and ~1.49nm (Figure 42-b) for the oxide created by MO. This observation is similar to our AFM results on Si, where AO formed ~2 times rougher oxide layer than MO on the Si(100) substrate (Figure 8). The mean square roughness (RMS) is 1.93nm (Figure 42-c) for the oxide created by 5eV AO on Ge(100) at room temperature. AO forms ~4 times rougher oxide layer as compared to the native oxide layer at room temperature. There is an increase in the oxide surface roughness with the increase in AO kinetic energy, as one can see from the roughness results for 15eV AO compared to the results for lower energies of AO. 15eV formed on the surface roughest oxide, and RMS is ~2 times higher than for 5eV and 9eV AO formed oxides. On the other hand, only slight increase is noticed in the surface roughness for 9eV AO oxidized Ge as compared to 5eV AO oxidation at the same temperature. The increase in the oxide surface roughness is somewhat surprising, since a flat Si/$SiO_2$ and Ge/$GeO_2$ interfaces are observed, as shown by HRTEM and EELS results of this thesis work. This could be due to the high kinetic energy of the AO is causing surface damage during AO exposure.

Previous investigators have reported that the roughness features observed at the Si/$SiO_2$ interface also appear at the $SiO_2$ surface as well. Krivanek et al. observed by HRTEM the Si/$SiO_2$ interface and $SiO_2$ surface roughness for ultrathin (10-100Å) oxides grown on Si at 500$^{o}$C, in a dry, nitrogen-rich atmosphere. The results of these researchers showed the undulations at the oxide surface closely followed the Si/$SiO_2$ interface undulations (~8Å), so that the oxide thickness remains constant to within 5Å. It was deduced that the oxidation proceeded uniformly across the whole Si crystal, and that the roughness on the Si/$SiO_2$ interface originated from the initial roughness of the unoxidized Si wafer [84].

A possible reason for the enhanced surface roughness could be the disturbance of the oxide surface by the energetic AO; higher energy AO can break Si-O or Ge-O bonds causing surface roughness. There might also be erosion of the oxide surface by energetic AO, thereby enhancing surface roughness during oxidation.

## 6.3 KINETICS OF SI AND GE OXIDATION BY AO SPECIES

5eV energy was chosen for the QCM experiment since it represents actual AO energy in LEO environment, while 9eV energy was chosen to examine the effects of kinetic energy on oxidation kinetics. Although the FAST $^{TM}$ AO source is capable of producing 4 - 20eV AO, it has been optimized for 5eV energy. In order to examine the effects of lower kinetic energy, which were not obtainable on the UPitt's AO source but pertinent to LEO, a research grade QCM system was used to monitor changes of the mass with the time when Si and Ge were exposed to 5 or 9eV AO. The oxidation curves from Tagawa [18] were analyzed as well in order to examine a wider range of AO kinetic energies and fluxes.

It was found that all of the QCM and XPS data fit a power law. Reisman and Nicollian noted that a power law fits very well with many existing experimental data for dry oxidation by $O_2$ [65]. They used simple power law equation ($X_{OX}$=a $t^b$) to fit dry $O_2$ data published between 1968-1988. In this equation, $X_{ox}$ is the oxide thickness, t is the time and a and b are the coefficients dependent on the oxidation process. The experimental conditions for the data from the literature on which they performed the fit were as follows: the oxide thickness was in 4nm - 1μm range, the oxidation temperatures were 700-1000$^o$C, and the $O_2$ pressure was in $10^{-5}$ -20 atm range.

As inspired by Nicollian and Reisman, a model based on the oxide structure changing during oxidation is proposed in this work to explain the oxide thickness dependency on the AO kinetic energy, the power law kinetics, and the physical meaning of the a and b coefficients in the power law. The physical meaning and dependency on the AO energy will be discussed. Also, the efficiency to form Si-O and Ge-O bonds is ploted for different AO energies.

### 6.3.1 Oxidation curves obtained during 5eV and 9eV AO exposure of Si and Ge in QCM

Kinetics of 9eV AO oxidation was monitored using a QCM system in the FAST™ AO source at the University of Pittsburgh. Figure 43-a represents a plot of the mass gain versus time, where the upper curve corresponds to Si and the lower one to Ge. The mass gain (μgrams/cm$^2$) corresponding to Si and Ge oxide formed per unit area was converted to oxide thickness using the molar weights of $SiO_2$ and $GeO_2$ and their densities. The density values for bulk $SiO_2$ and $GeO_2$ were used, but it is possible that thin oxide films have densities that are different from the bulk values available in the literature. Figure 43-b shows the oxide thickness dependency on the 9eV AO fluence, where the AO flux is 1.88x10$^{13}$ at/cm$^2$sec.

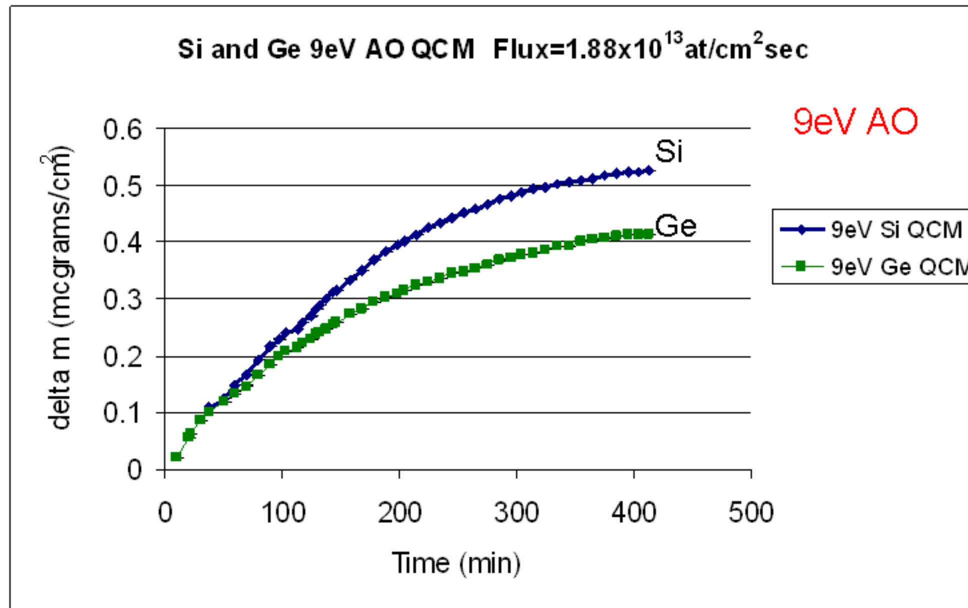


(a)

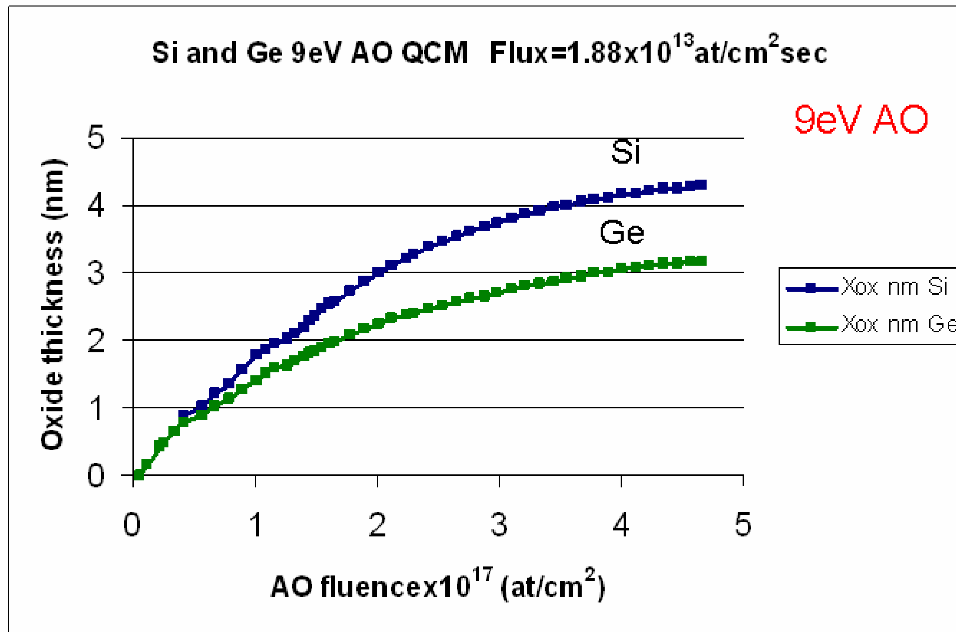


(b)

**Figure 43** Kinetic curves from QCM obtained for oxidation of amorphous Si and Ge by 9eV AO (Pitt) at T=297K and AO flux=1.88x$10^{13}$ at/cm$^2$sec. a) Oxide mass gain vs. oxidation time. b) Oxide thickness (calculated from the mass gain) vs. AO fluence. Error bars are not visible since they are smaller than the symbols used in the data points.

The uncertainty of mass measurements in QCM is 0.0005μgrams/cm$^2$ (since the smallest division is 0.001μgrams/cm$^2$). Due to such a high precision of the QCM device and very small error of the experimental measurements, the error bars are not visible in Figure 43 and 44 (they are actually smaller than the symbols used for the data points). The error analysis will be revisited in more detail in the next chapter. As shown in Figure 43, the oxide growth on both Si and Ge by 9eV AO appears to be parabolic and does not saturate even at a long oxidation time (~7hrs). The $SiO_2$ and $GeO_2$ thickness obtained after ~7hrs of exposure were 4.3 and 3.2nm, respectively. The plot of mass gain vs. oxidation time during the 5eV AO exposure of Si and Ge at room temperature in AO source is shown in Figure 44. Similar to the previous figure, the upper curve corresponds to Si and lower one to Ge. Again, Ge exibits a lower oxidation rate as

compared to Si. Figure 44-b shows the dependency of the oxide thickness on the 5eV AO fluence, with an AO flux of $1.75 \times 10^{14}$ at/cm$^2$sec.

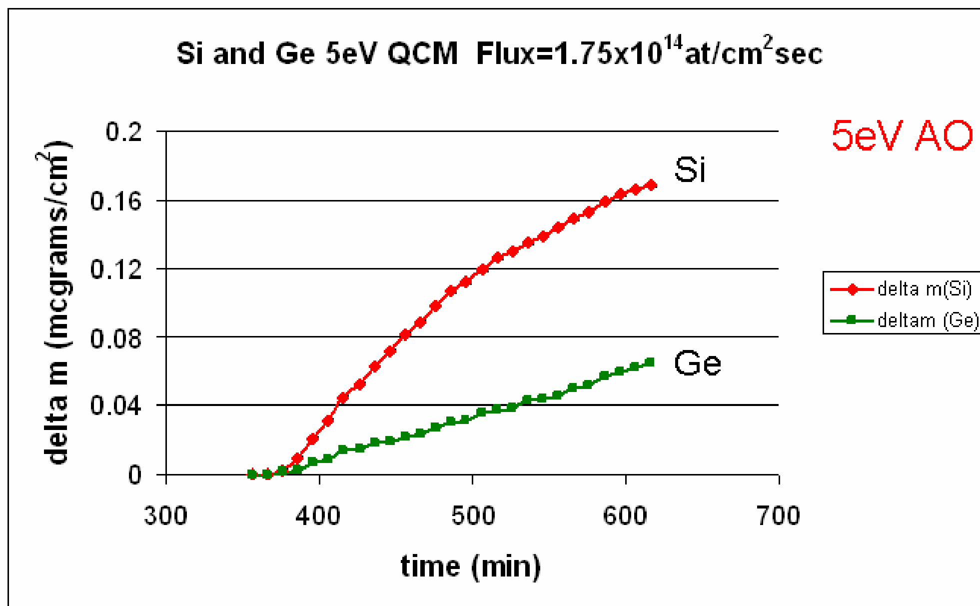


(a)

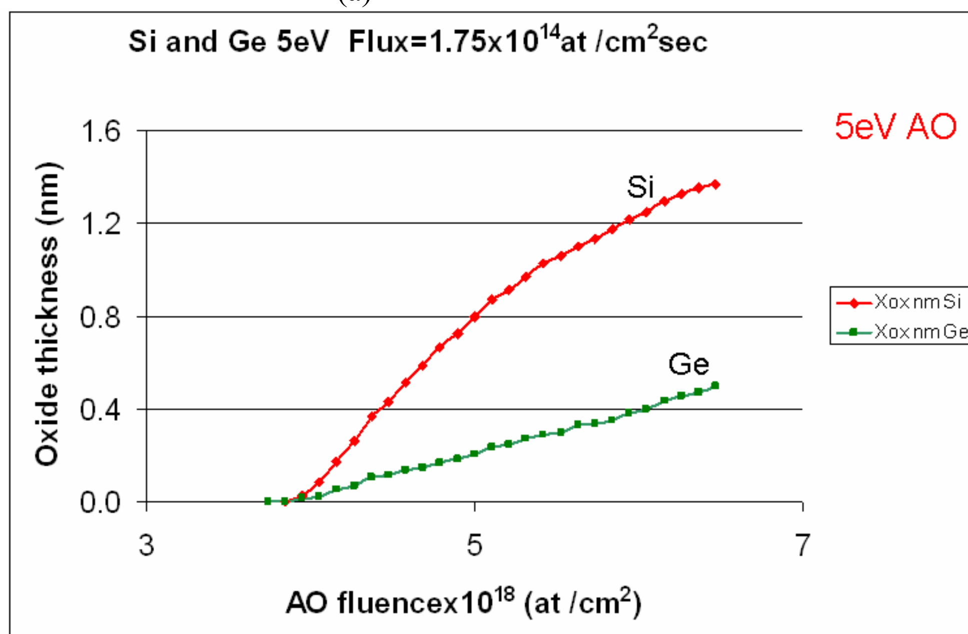


(b)

**Figure 44** Kinetic curves from QCM obtained for oxidation of amorphous Si and Ge by 5eV AO (Pitt) at T=297K and AO flux=$1.75 \times 10^{14}$ at/cm$^2$sec. a) Oxide mass gain vs. oxidation time. b) Oxide thickness (calculated from the mass gain) vs. AO fluence. Error bars are not visible since they are smaller than the symbols used in the data points.

During the later stages of oxidation, the dependence of the oxide growth vs. time follows a power law for Si, whereas it is linear for Ge. It should be noted that the mass gain and corresponding oxide thickness is shown for the later oxidation times (6-10hrs). Unfortunately, the data in the initial oxidation regime are not clear. The initial data are unreliable due to the initial out -gassing caused by the poor surface cleanliness, and were not used in this analyses. Therefore, the oxide thickness shown in Figure 44 corresponds to 6-10hrs of AO exposure. Hence, the absolute value of the overall oxide thickness cannot be calculated from this set of data, but the growth rates and coefficients *a* and *b* can be extracted.

It can be seen from Figure 43 and 44 that the oxidation rate of Ge by 5and 9eV AO is lower than the oxidation rate of Si. This observation is in agreement with the results of Mui et al. who used density functional theory to investigate the surface chemistry and initial oxidation stages of Ge(100) and Si(100) surfaces by water and hydrogen peroxide [113]. They defined the bridge-bonded O configuration as the most stable state, which leads to oxide formation. It was found that the desorption half-lives for bridge-bonded O species on Si(100) and Ge(100) surfaces at 900K are 92 days and 0.6s, respectively. This analyses suggests that $GeO_2$ readily undergoes reversible desorption from the Ge(100) surface, thus indicating that Ge/$GeO_2$ interface is thermodynamically unstable when compared to the Si/$SiO_2$ interface. For the AO assisted oxidation, where bridging O atoms are a likely precursors of the $GeO_2$ formation, it is expected that Ge oxidation will proceed with a lower rate than Si oxidation, as observed in my QCM experiments.

### 6.3.2 Oxide thickness dependency on the AO kinetic energy

The kinetic data shown in Figure 45 are for the lower energies of AO, namely 1.6, 3.6 and 4.6eV, which were obtained via XPS experiments by Tagawa [18]. The data were digitized and the oxide thickness was plotted versus the AO fluence. The oxidation curve for 9eV AO obtained using QCM in the FAST$^{TM}$ AO source at the University of Pittsburgh are superimposed on the same graph.

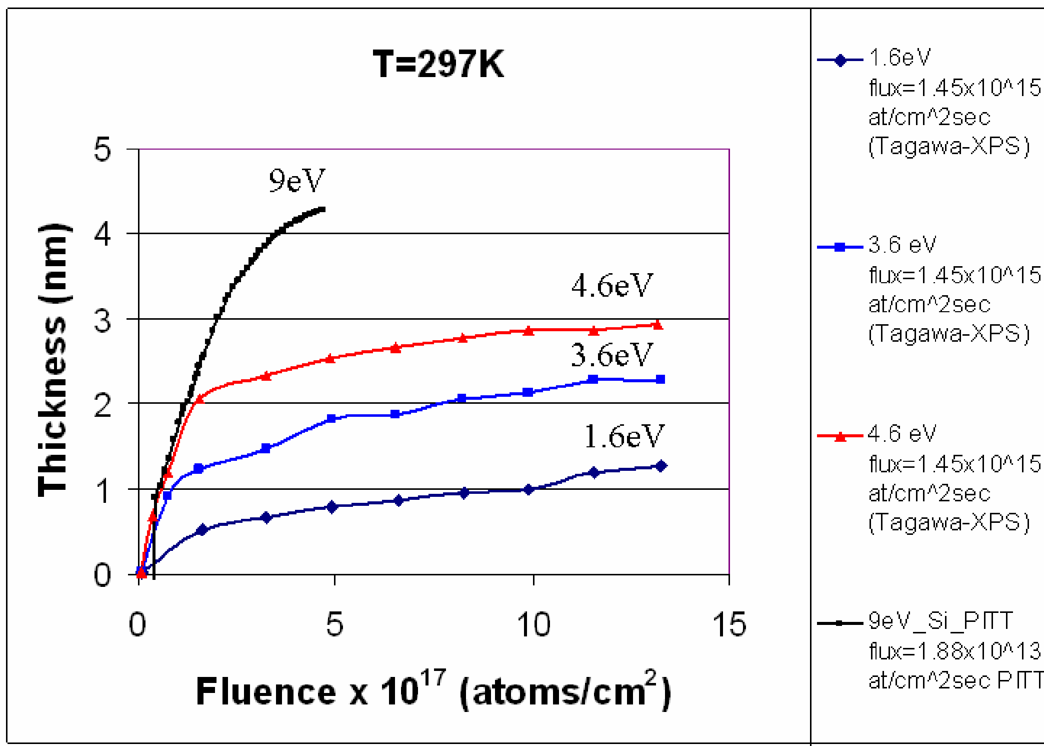


**Figure 45** Kinetic curves for the oxidation of H-terminated Si(100) by 1.6, 3.6, 4.6eV [**18**] AO (flux=$1.45\text{x}10^{15}$at/cm$^2$ sec), and oxidation curve for amorphous Si (native oxide covered) oxidized by 9eV AO (Pitt) (flux=$1.88\text{x}10^{13}$at/cm$^2$ sec), at T=297K.

The kinetic data for the oxidation of Si by 5eV AO in QCM are not shown in the upper graph, since these data were acquired from 6-10 hrs of exposure, and with the flux of AO of $1.75\text{x}10^{14}$at/cm$^2$ sec. These conditions gave a high fluence (3.7-6.5x$10^{18}$ at/cm$^2$) received in 6-10 hrs of oxidation time, while Tagawa's XPS data and Si 9eV AO data are in 0-15x$10^{17}$at/cm$^2$

range [18]. It should be noted that the total oxidation time was 7hrs for 9eV AO (PITT QCM), while for 1.6, 3.6 and 4.6eV AO it was only 15min. However, due to the 2 orders of magnitude difference in AO fluxes, the total fluence of AO received by these samples is of the same order of magnitude ($10^{17}$), and therefore, all 4 curves can be presented on the same plot. It is obvious that the high energy beam will promote oxidation and contribute to thicker oxide formation, even at room temperature. The increase in AO kinetic energy leads to an increase in the reaction yield of AO on Si. The hydrogen-terminated Si surface cannot be easily oxidized by $O_2$ at room temperature, but Engstrom et al. reported that the oxidation can occur with energetic AO (up to 0.16eV) [15, 17, 20]. A two-stage oxidation process is observed for AO fluences up to $2x10^{17}$at/cm$^2$, and this is most noticeable for 4.6eV AO. The fast, initial process might be due to the rapid oxidation of dangling bonds and the incorporation of oxygen into bridging sites in the uppermost surface layers [18]. 9eV AO forms the thickest oxide layer. The second slower oxidation stage is similar for all AO energies. It is most probably controlled by the diffusion of oxygen through the oxide scale. As determined by Tatsumura [118], AO diffuses by bond-breaking and forming, in contrast to $O_2$, which diffuses thru pores and pinholes in the amorphous silica [117].

"Paralinear process" should be discussed here, since it might explain the "flat" part of the oxidation curves for 1.6, 3.6 and 4.6eV AO (Tagawa's XPS data). This "flat" part is obvious for AO fluences larger than $2x10^{17}$at/cm$^2$. Basically, "paralinear kinetics" means that there exist two competing processes, one is oxide growth and another is the oxide removal. "Paralinear" oxidation kinetics is observed chromium at high T and high oxygen partial pressures. Under these conditions, there is evaporation of $Cr_2O_3$, which results in the continuous thinning of the $Cr_2O_3$ oxide scale, thus making diffusion transport through the scale rapid. The instantaneous

change in the oxide scale thickness is the sum of two contributions: thickening due to the diffusion and thinning due to volatilization. Initially, when the diffusion is rapid through the thin oxide scale, the effect of $Cr_2O_3$ volatilization is not significant. As the scale grows and becomes thicker, the rate of volatilization becomes comparable and eventually equal to the rate of diffusive growth. This results in a self- limiting oxide thickness, where the oxide growth rate is equal to zero [68].

This self- limiting oxide scale thickness is obtained when the rate of oxide removal becomes comparable to the rate of growth. Although the curves for 1.6, 3.6 and 4.6eV AO in Figure 45 are flat in the later stage, it can be observed that the oxidation curve for 9eV AO does not become flat. Also, the curves for Si oxidized by 5eV AO, and for Si and Ge oxidized by 9eV AO do not show a “flat” part (Figure 44 and Figure 43 respectively). Therefore, the simultaneous oxide growth and volatization of the oxide is not plausible for all of the cases in this study. The oxide surface could be eroded by energetic AO, as implied by our AFM results, but the rate of erosion is still significantly lower than the rate of oxidation, since it is observed that the limiting thickness is not reached and the oxide is still growing (Figure 43 and Figure 44). A general oxidation mechanism, that could be applied on each set of data, including Tagawa’s XPS data, should be considered, and this is discussed later in this section.

The oxide thickness vs kinetic energy of AO as measured by X-TEM (5, 9 and 15eV AO on Ge) and Tagawa’s XPS data (1.6, 3.6 and 4.6eV AO on Si) from ref. 18 are included on the same plot (Figure 46) in order to compare Si and Ge directly.

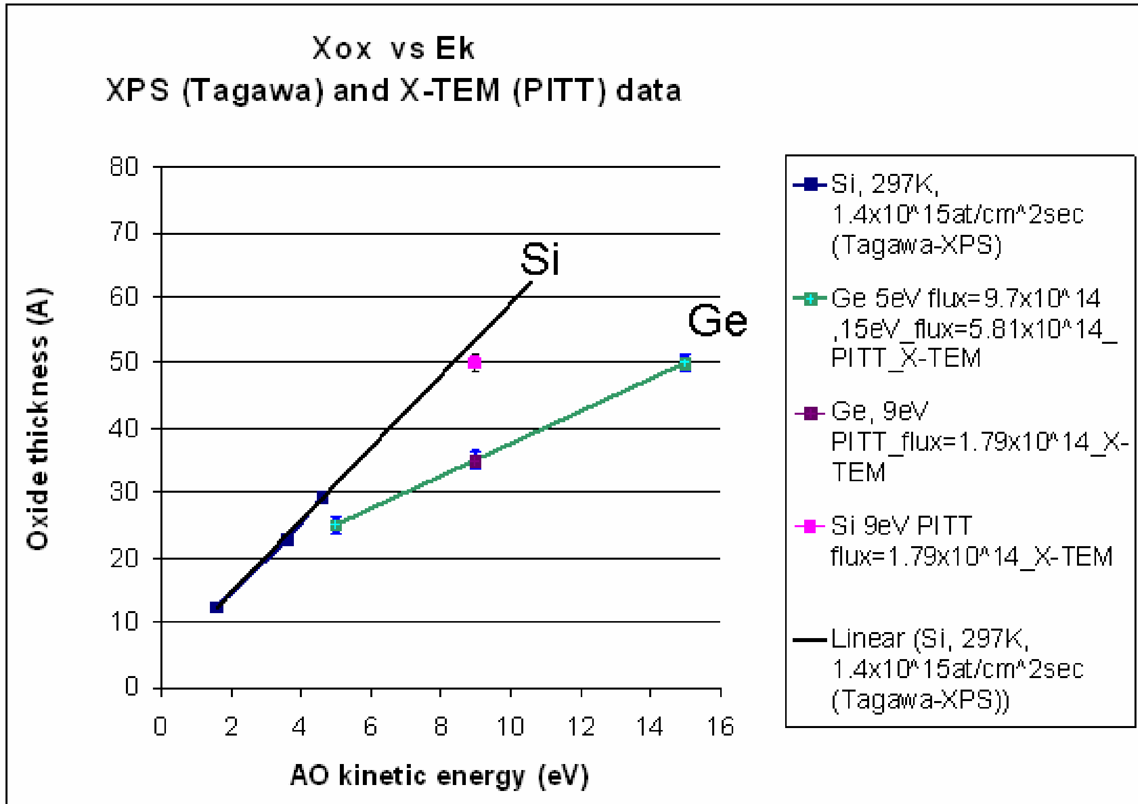


**Figure 46** Si and Ge oxide thickness dependence on the AO energy; combined data from X-TEM and XPS techniques from ref. 16.

The error bars are included for Ge samples where the oxide thickness was measured by X-HRTEM. The spatial resolution of the Tecnai TEM is 2.5Å, thus the uncertainty of the measurement can be estimated as 1.3Å. The explanation of this graph is not trivial since different AO fluxes are involved (although the same order of magnitude). If one wants to consider only the effect of AO energy on oxide thickness, all other factors should be fixed. Therefore, the plot above should be considered as an estimate. However, it can be seen that linearity of the oxide thickness vs. $E_k$ of AO is applicable for Ge (5, 9 and 15eV X-TEM data), as well as for 1.6, 3.6 and 4.6eV (Tagawa's data). It is noted that AO flux and fluence are kept constant for XPS set, while AO flux has the same order of magnitude for the X-TEM set mentioned above. The oxide

thickness formed by energetic AO, at room T, on Ge ranges from 2-5nm, as shown in Figure 46. This thickness is higher than 1.75nm oxide formed on Ge by $O_2$ for 3hrs at $400^oC$ [114].

At this point, it is useful to compare the oxide thickness measured by X-TEM, and by QCM, for the same AO energy. If the power law is extended for each set of data to the fluence that the ex situ samples received, the values for the oxide thicknesses is 2-3 times larger than observed by X-TEM. The reason for this discrepancy might be the different structure of the substrates used; Si-single crystals were used in HRTEM, while amorphous Si was used for QCM study. 2-3 times larger oxide thicknesses estimated by the extrapolation of our QCM data for the larger fluences (used in the HRTEM data) are in agreement with the 2.25 times larger value for the linear rate constant for amorphous compared to single-crystalline Si oxidation, as determined by Hellberg et al. for the oxidation in pyrogenic steam, at $800^oC$ [116]. The linear and parabolic rate constants dependency on the crystalline form of the Si substrate will be revisited in the next section.

The oxide thickness from X-TEM data for Si oxidized by 9eV AO is a good example on how the different combinations of the AO flux and energy can lead to approximately the same oxide thickness. This was observed before, when the oxide thickness was found to be predictable by controlling the AO energy, flux and impingement angle [11, 18].

The applicability of the Deal-Grove model to the experimental QCM kinetic data is presented in the following section of this chapter. The model of Deal and Grove has some constraints such as the assumption that the diffusion coefficient is not time-dependent. For this reason, it might not be possible for the Deal-Grove model to fit my experimental QCM data, since ex-situ TEM data reveiled more ordered oxide structure formed by AO species. However,

the idea of Reisman's model might be aplicable since it introduces time-dependent oxide changes to explain deviations from parabolic or linear kinetics.

### 6.3.3 The Deal-Grove model fit to the kinetic data

The experimentally obtained QCM kinetic data were first fitted to the Deal-Grove model since this model is the basic model for Si oxidation. The Deal-Grove linear-parabolic model is given by the following expression:

$$\frac{x^2 - x_i^2}{B} + \frac{x - x_i}{B/A} = t \qquad \text{(Equation 51)}$$

where x is the oxide thickness, $x_i$ accounts for any oxide present at the start of the oxidation, t is the oxidation time, B is the parabolic rate constant and B/A is the linear rate constant. An alternate way to express the Deal-Grove equation is:

$$\frac{x^2}{B} + \frac{x}{B/A} = t + \tau \qquad \text{(Equation 52)}$$

where $\tau$ is the initial time in which the initial oxide thickness, $x_i$, is formed:

$$\tau = \frac{x_i^{\ 2} + Ax_i}{B} \qquad \text{(Equation 53)}$$

If equation 53 is divided by x and multiplied by B, the following expression is obtained:

$$x = \frac{t + \tau}{x} B - A \qquad \text{(Equation 54)}$$

When the oxide thickness, x, is plotted against the inverse oxidation rate, $(t+\tau)/x$, the slope of the line gives the coefficient B while the intercept gives the coefficient A [29]. The procedure described above was used in order to extract coefficients A and B, and to calculate the

oxide thickness. The Deal-Grove model curves (solid lines) calculated using A and B coefficients are plotted in Figure 47. The A and B coefficients were determined from the slope (coefficient B) and intercept (coefficient A) when the oxide thickness is plotted versus the inverse oxidation rate. Symbols are experimental oxidation data points obtained for Si oxidized by 1.6, 3.6 and 4.6eV AO (XPS, Tagawa's data), Figure 47-a. The experimental data points for QCM (PITT) data for Si and Ge 9eV AO oxidized are represented by the symbols in Figure 47-b.

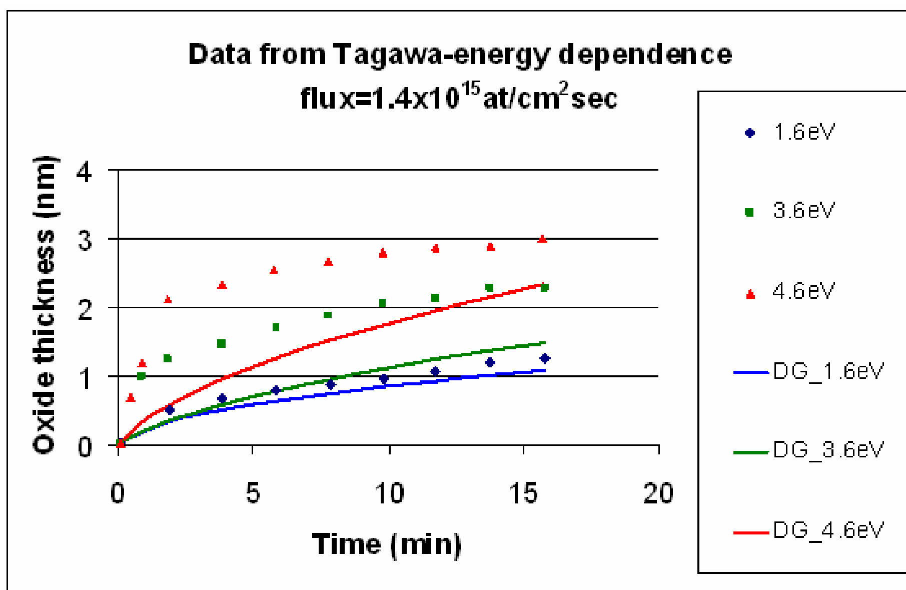


(a)

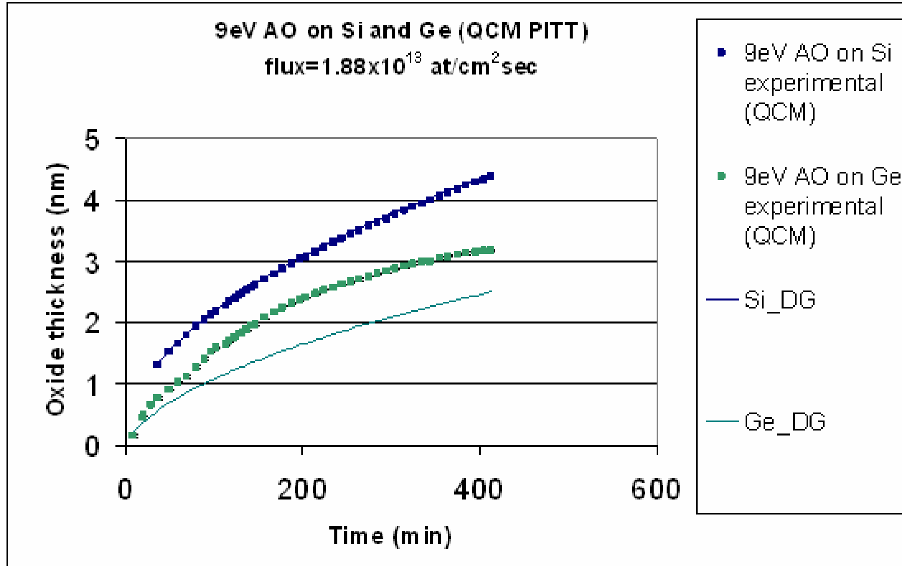


(b)

**Figure 47** The Deal-Grove linear-parabolic law model fit (solid curves) through the oxidation data points (symbols) for a) Si single-crystal oxidized by 1.6, 3.6 and 4.6eV AO at T=297K (Tagawa, XPS), AO flux=$1.4x10^{15}$ at/$cm^2$sec, b) amorphous Si and Ge oxidized by 9eV AO (QCM, Pitt), AO flux=$1.88x10^{13}$ at/$cm^2$sec, at T=297K. Error bars for QCM PITT data are within the symbols for the data points.

It is obvious from Figure 47-a that Tagawa's XPS data for 1.6, 3.6 and 4.6eV AO do not follow linear-parabolic oxidation kinetics represented by the Deal-Grove model. The higher energy AO beam (4.6eV) showed the greatest departure from the kinetics proposed by Deal and Grove.

Oxidation of Si in 9eV AO showed good agreement with the model of Deal and Grove, as represented with an excellent fit in Figure 47-b. It can be seen from the same figure that the oxidation of Ge in 9eV AO resulted in not so good fit. It was not possible to fit the data for 5eV AO oxidized Si and Ge using the Deal-Grove model, since negative slope was obtained.

It can be concluded that the Deal-Grove model cannot be used to explain the oxidation kinetics of Si and Ge in energetic AO, since it does not fit all of the experimental data sets. Also,

the Deal –Grove model assumes thermodynamic equilibrium, which is not the case here, hence, it is reasonable to assume that the Deal-Grove model is not applicable here. Another function, a power law is used, and the applicability of this model on the kinetic data is discussed next.

### 6.3.4 Reisman model and power law

The power law is given by dependency of oxide thickness, $X_{ox}$ with respect to time, t:

$X_{OX}$=a $t^b$ (Equation 55)

where coefficients a and b are given by equations 29 and 28, respectively in the background, section 2.7.2.2. In order to use a linear-fit to determine a and b, equation 55 is transformed into log form:

log $X_{ox}$=log a + b log t (Equation 56)

Coefficients a and b are found from the intercept and slope of the log $X_{ox}$ vs. log t plot respectively using a least squares method.

Error analyses

Table 5 gives values for intercepts, slopes, sum of squares and coefficient of determination ($R^2$) calculated for Tagawa's kinetic data [18], and for the oxidation data obtained using QCM device (PITT).

**Table 5** Statistic analyses and goodness of fit parameters of the least squares fit procedure

* XPS data from reference 18 used for calculation
**QCM kinetic data from PITT used (only 1 run)

| Sample | **AO Ek (eV)** | Intercept | Slope | SSR | SSE | SST | $R^2$ |
|---|---|---|---|---|---|---|---|
| Si(100) * | 1.6 | -0.46564 | 0.466584 | 0.057887 | 0.000803 | 0.05869 | 0.9863 |
| Si(100) * | 3.6 | 0.004436 | 0.304713 | 0.026295 | 0.000995 | 0.02729 | 0.9635 |
| Si (100) * | 4.6 | 0.276946 | 0.163108 | 0.007561 | 0.000158 | 0.00772 | 0.9795 |
| Si amorphous ** (6-10hrs) | 5 | -2.61908 | 1.217193 | 0.234287 | 0.002141 | 0.236428 | 0.9909 |
| | | -1.42061 | 0.648066 | 0.022571 | 4.38E-05 | 0.022615 | 0.9981 |
| Ge amorphous ** (6-10hrs) | 5 | -2.99127 | 1.110139 | 0.692157 | 0.002289 | 0.694445 | 0.9967 |
| Si amorphous ** | 9 | -0.66717 | 0.5 | 0.538769 | 2.56E-31 | 0.538769 | 1 |
| Ge amorphous ** | 9 | -1.30055 | 0.739024 | 0.82296 | 0.002755 | 0.825715 | 0.9967 |
| | | -0.57196 | 0.413472 | 0.051318 | 0.000347 | 0.051665 | 0.9933 |

SSR is known as unexplained variation or error sum of squares, SSE is explained variation or regression sum of squares (sum of squares due to error), and SST is the total sum of squares.

SSE statistic measures the total deviation of the response values from the fit to the response values. Value closer to zero indicates that the model has a smaller random error component, and that the fit will be more useful for prediction. Value $R^2$ is known as coefficient of determination, $R^2$=SSR/SST and determines usefulness of regression equation. This statistic measures how successful the fit is in explaining the variation of the data, R-square is the square of the correlation between the response values and the predicted response values. $R^2$ for all of the samples investigated is given in the last column of Table 5. It can be noted from Table 5. that there is an excellent agreement ($R^2$ =1) for the Si oxidized by 9eV AO , therefore we can consider fit for this set of data to be virtually error- free. In general, the result of the measurement is represented as:

$$(\text{measured value of } X) = X_{best} \pm \delta X \qquad \text{(Equation 57)}$$

where Xbest is the experimenter's best estimate for the quantity concerned, and δX represents the uncertainty, or error. Uncertainty in the instrumental measurements is usually defined as 20% or 50% of the smallest division [115]. It is possible to read 0.001 μg/cm$^2$ from the QCM device, resulting in uncertainty of 0.2 or 0.5ng/cm$^2$. When transformed into the oxide thickness, uncertainty of 0.0041nm is obtained (if 0.5 ng/cm$^2$ taken). The measurements of the time given on X-axis of the plots in Figure 43-a and Figure 44-a are considered to be error free (Δt ~ 0.1min), since the time reading was done at certain points (e.g. every 10 min exactly). The Y error bars are shown in the plot in Figure 43 and Figure 44, but they are not visible since the uncertainty of the experimental measurement is very small due to the high precision of the QCM device. Errors are uncertainty limits and following expressions were used for quantitative assessment of errors when calculating coefficients a and b in the power law. Errors in addition or subtraction were determined using the following equation:

If X=A+B-C:

$$\delta X = \sqrt{\delta A^2 + \delta B^2 + \delta C^2} \quad \text{(Equation 58)}$$

Error in multiplication or division was determined using:

If X=AB/C

$$\delta X = X * \sqrt{\left(\frac{\delta A}{A}\right)^2 + \left(\frac{\delta B}{B}\right)^2 + \left(\frac{\delta C}{C}\right)^2} \quad \text{(Equation 59)}$$

Error in logarithm:

If $X = \log_{10} A$ (Equation 60)

$$\delta X = 0.434 * \left(\frac{\delta A}{A}\right) \quad \text{(Equation 61)}$$

Error in antilog:

$$\delta X = 2.303 * X * \delta A \qquad \text{(Equation 62)}$$

*a* and *b* coefficients determination

Due to the availability of the data at longer oxidation times, coefficients *a* and *b* are determined for Si and Ge oxidation by 5 and 9eV AO (QCM), and for 1.6, 3.6 and 4.6eV AO (XPS) [18], and presented in Table 6.

**Table 6** *a* and *b* coefficients calculated from QCM and XPS-Tagawa [18] kinetic data at T=297K.

* XPS data from reference 18 (Tagawa) used for *a* and *b* coefficients calculation
**QCM kinetic data from PITT used (1 run)
$X_{OX}=a\ t^b$

| Sample | AO Ek (eV) | AO Flux ($at/cm^2 sec$) | B | a |
|---|---|---|---|---|
| Si(100) * | 1.6 | $1.45 \times 10^{15}$ | 0.467 ± 0.027 | 0.342±0.021 |
| Si(100) * | 3.6 | | 0.305±0.027 | 1.01±0.06 |
| Si (100) * | 4.6 | | 0.163±0.01 | 1.892±0.045 |
| Si amorphous ** (6-10hrs) | 5 | $1.75 \times 10^{14}$ | 1.217±0.044<br>0.648±0.01 | 0.0024±0.0005<br>0.038±0.002 |
| Ge amorphous ** (6-10hrs) | 5 | $1.75 \times 10^{14}$ | 1.110±0.015 | 1.02E-3±0.08E-3 |
| Si amorphous ** | 9 | $1.88 \times 10^{13}$ | 0.5±5.52E-17 | 0.215±6.32E-17 |
| Ge amorphous ** | 9 | $1.88 \times 10^{13}$ | 0.739±0.01<br>0.413±0.007 | 0.050±0.002<br>0.268±0.011 |

Two sets of coefficients a and b are shown in Table 6 for the amorphous Si oxidized by 5eV AO, and for the amorphous Ge oxidized by 9eV AO. While one set of a and b coefficients fits the data in the initial oxidation period very well, the another set must be used to obtain good fit for the later oxidation stage. Switching from one to another set of coefficients a and b implies

a break in the AO oxidation kinetics. The processes controlled by the interface reaction should be responsible in the initial period of the oxidation time, while oxidant transport processes should control the oxidation in longer time. This is discussed in more detail in the discussion section of this thesis. It can be noted from the Table 6 that the values of coefficient *b* decrease with increasing beam energy for fixed AO flux and temperature (Tagawa's data). The *b* value is less than 0.5 for all the data, except for one set, implies that the reaction at the $Si/SiO_2$ interface was limited by the diffusion of AO. For the one set of Si and Ge data set, the power law is around one, suggesting that these kinetics are controlled by the interfacial reaction.

Power curves (solid lines) based on a power law are plotted in Figure 48 using the a and b coefficients from Table 6. Symbols are experimental oxidation data points obtained in QCM for Si and Ge 5eV (Figure 44) and 9eV (Figure 43) AO oxidation. The equation corresponding to each curve is shown next to the curve, as well as the goodness of fit, $R^2$.

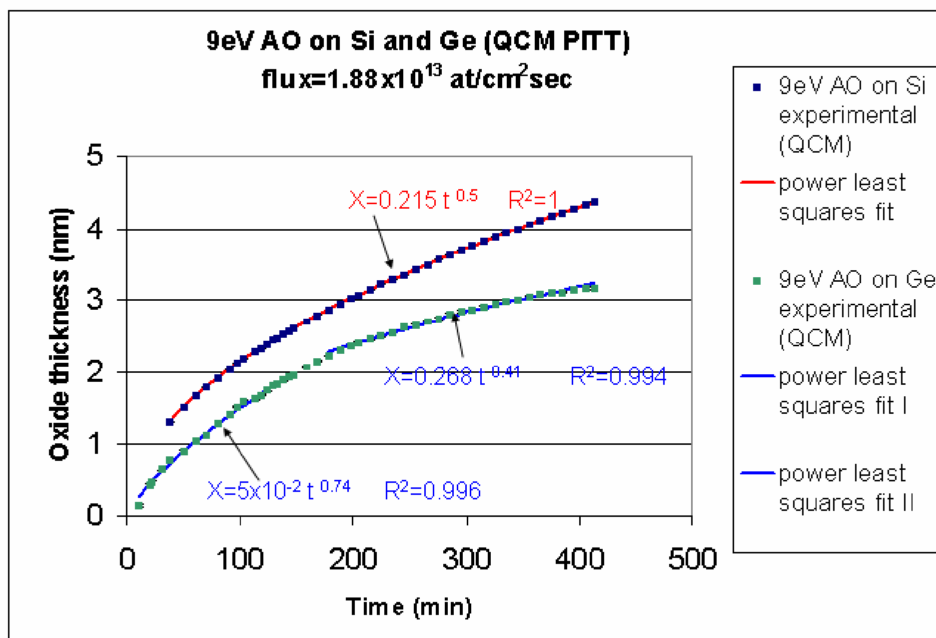


(a)

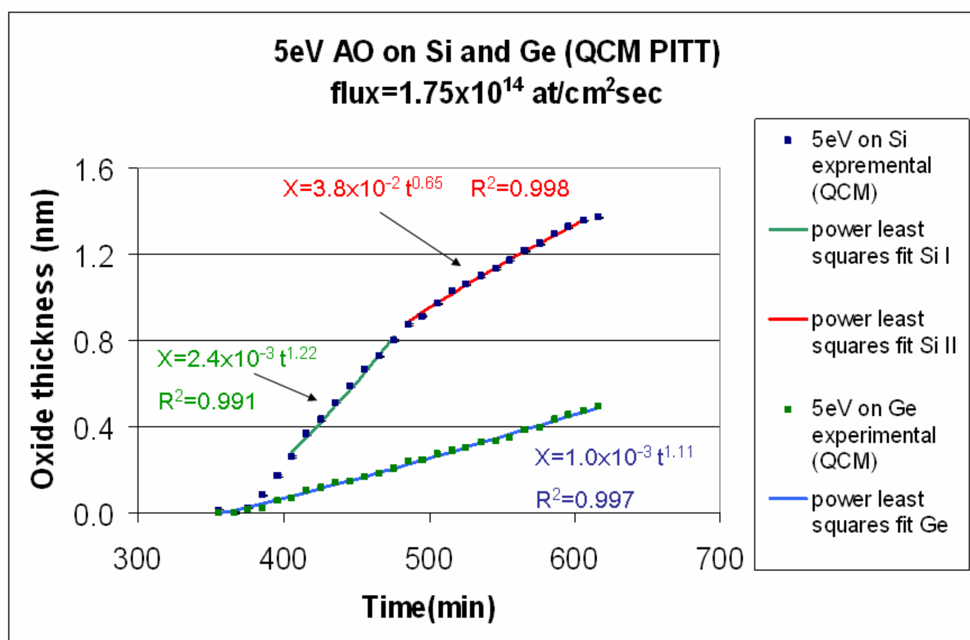


(b)

**Figure 48** Power law model fit (solid curves) through the oxidation data points (symbols) for Si and Ge oxidized by a) 9eV AO (Pitt) at T=297K, AO flux=**$1.88 \times 10^{13}$ at/cm$^2$sec** and b) 5eV AO (Pitt) at T=297K, AO flux=$1.75 \times 10^{14}$ at/cm$^2$sec. Two sets of coefficients for one curve indicate break in the AO kinetics.

It can be seen from Figure 48-a that the oxidation of Si in 9eV AO shows excellent agreement with the parabolic relationship ($R^2$=1) for the oxidation time up to 7hrs. It was not possible to obtain good fit for the experimental data for Ge oxidation by 9eV AO with single curve, using only 1 set of coefficients *a* and *b*. Therefore, the curve was fitted from two segments and coefficients *a* and *b* were obtained for each segment. Equations for the first and second parts were determined, and they are shown on the plot in Figure 48-a. It is interesting to note that the b coefficient for 9eV AO oxidized Si is equal to 0.5 exactly, therefore enabling us to calculate diffusion coefficient, D. Similar procedure for curve fitting from 2 segments was applied on the experimental data for Si oxidized by 5eV AO in QCM, shown in Figure 48-b by solid symbols. The experimental data in the first segment were fitted by the power law using coefficients b=1.217 and a=0.0024, while for the second part, b=0.648 and a=0.038 gave the best fit. Germanium oxidation by 5eV for longer times seems to be nearly linear, as represented in Figure 48-b. Tagawa's data fitted by the power law are given in Figure 49.

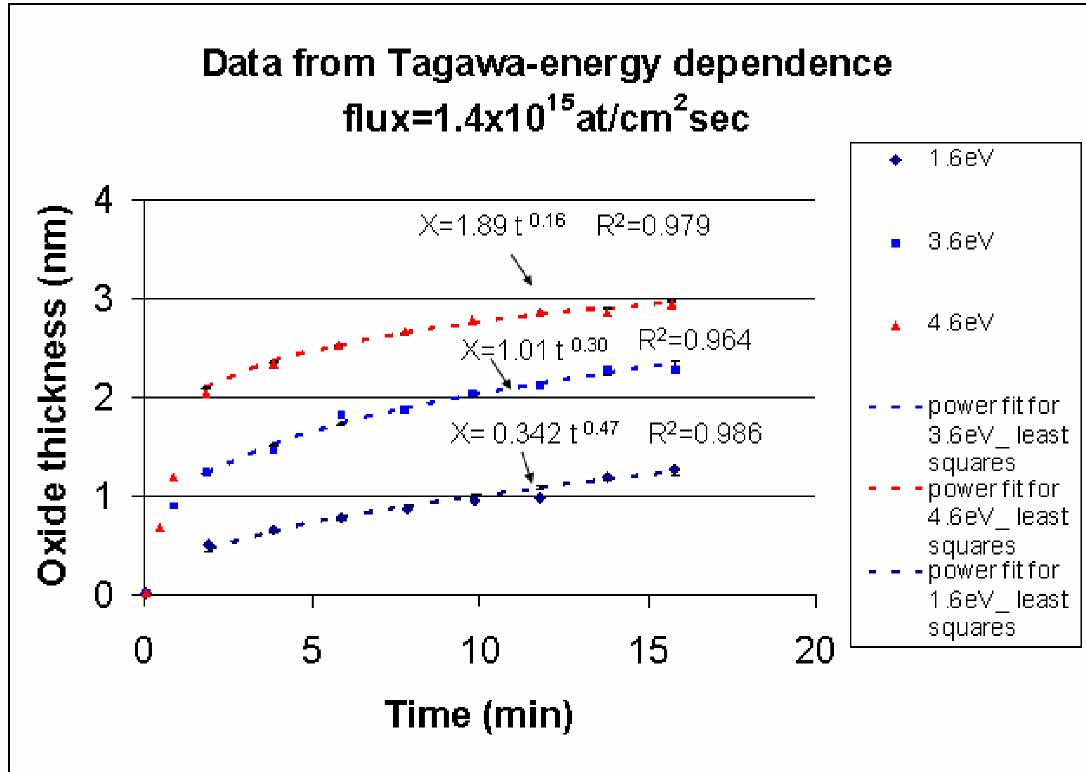


**Figure 49** Power law fit (dotted lines) through the oxidation data points (symbols) for Si oxidized by 1.6, 3.6 and 4.6eV AO at T=297K, AO flux=$1.4 \times 10^{15}$ at/$cm^2$sec (Tagawa's data, taken with XPS) [18].

### 6.3.5 Oxygen efficiency to form Si-O and Ge-O bonds

Since the oxide growth rate is known, the volume of $SiO_2$ or $GeO_2$ that is formed per second and per unit area can be calculated. Taking into account the molar weight of oxide, and its density, the number of the $SiO_2$ or $GeO_2$ molecules produced per $cm^2$ per second can be calculated, and from that, the fraction of incoming oxygen atoms incorporated into the oxide can be determined [119]. For example, for a growth rate of 14.5 Å/hr, a volume of about $4.04 \times 10^{11}$ $cm^3/cm^2$sec was formed, corresponding to $9.15 \times 10^{-11}$ g/$cm^2$sec (taking the density of $SiO_2$ to be 2.27 g/$cm^3$). With the molar weight of $SiO_2$ equal to 60g/mole and using Avogadro's number, the

number of $SiO_2$ entities produced is $9.2x10^{11}$ $SiO_2/cm^2sec$, or $1.84x10^{12}$ $O/cm^2sec$. With an average AO flux=$1.88x10^{13}$ $O/cm^2sec$, the efficiency of AO to form Si-O bond is 0.0979. Figure 50 is a plot of the calculated AO efficiency for Si-O and Ge-O bond formation vs. oxide thickness at room temperature. The data for the 1.6, 3.6 and 4.6eV AO efficiency are taken from ref. 18, while the data for the 9eV AO efficiency on Si and Ge oxidation were obtained from QCM (PITT).

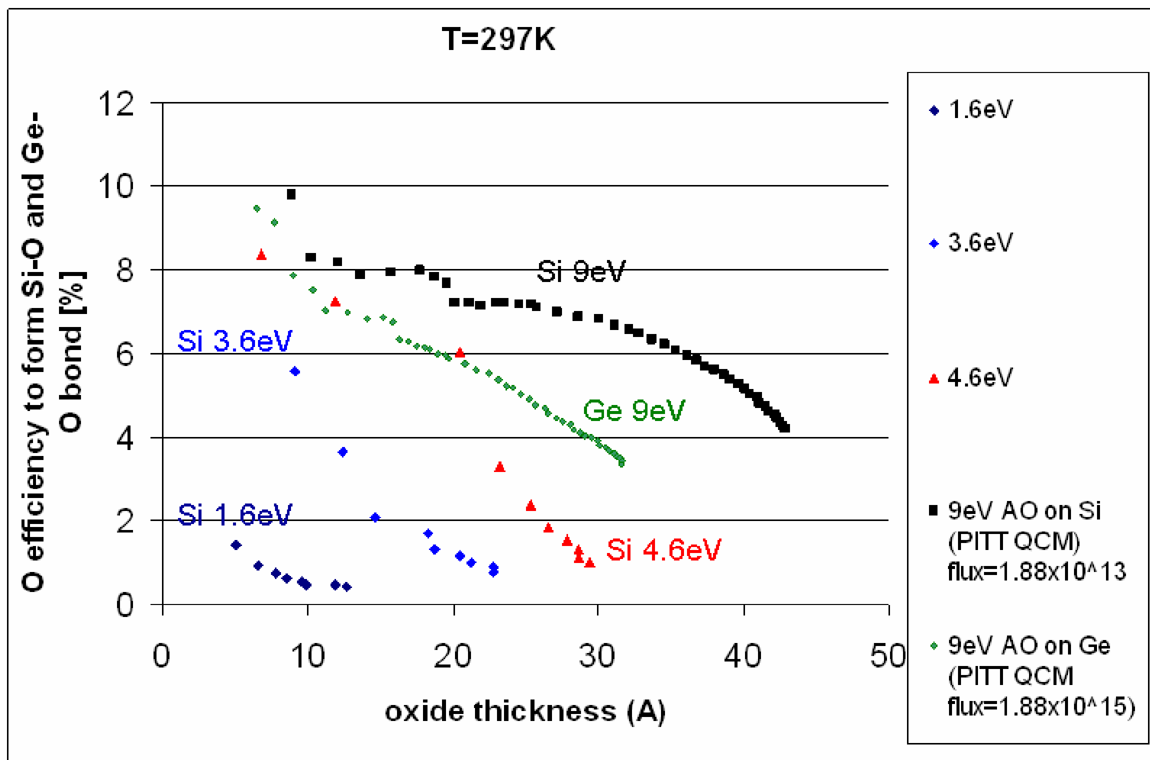


**Figure 50** Atomic oxygen efficiency (%) to form Si-O and G-O bonds; 9eV AO on Si and Ge (Pitt), flux=$1.88x10^{13}$ $at/cm^2sec$ and 1.6, 3.6 and 4.6eV AO on Si, from [18], flux=$1.4x10^{15}$ $at/cm^2sec$

As expected, the higher energy AO has larger efficiency to form bonds, as seen for 1.6, 3.6 4.6 and 9eV AO beams. The efficiency of 9eV AO to form Si-O bond is higher than its efficiency to form Ge-O bonds, except at the very beginning of oxidation. 9eV AO is able to

form ~4.5nm thick oxide on Si while the oxide thickness is only 3.2nm on Ge substrate. Figure 51 represents the dependency of the AO efficiency on time for different AO energies.

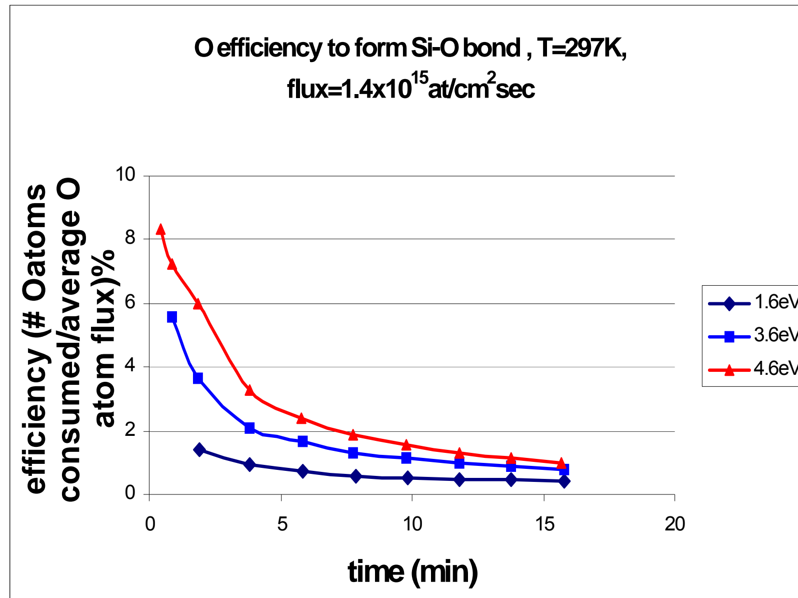


(a)

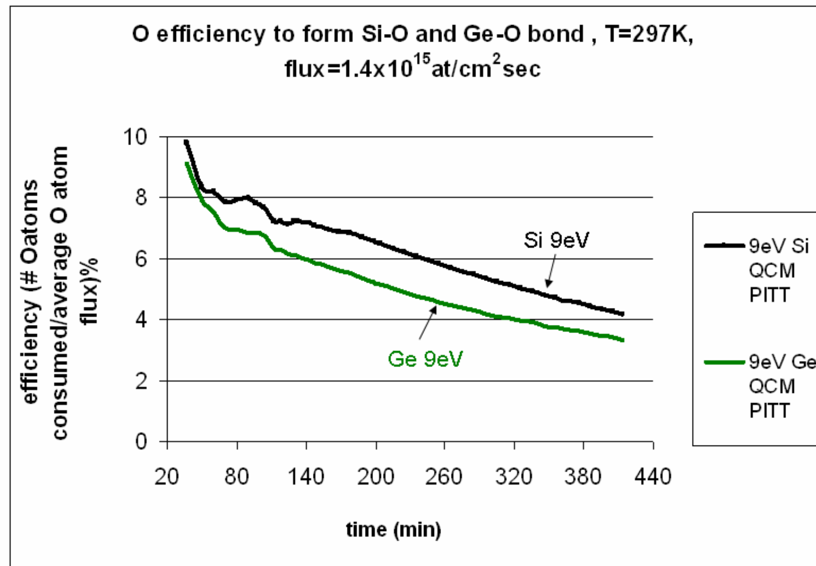


(b)

**Figure 51** Atomic oxygen beam efficiency (%) to form a) Si-O bond (1.6, 3.6 and 4.6eV AO) and b) Si-O and Ge-O bonds with 9eV AO

The efficiencies for 1.6, 3.6 and 4.6eV AO beams decrease from 1.85, 5.56 and 8.34%, to 0.44, 0.78 and 1%, respectively, during a 15 min time interval (Figure 51-a). On the other hand, 9eV AO beam is able to still form Si-O and Ge-O bonds even after 6 hrs of oxidation time (Figure 51-b). The loss of efficiency for 9eV beam is from 9.8 to 4.2% for Si and from 9.5 to 3.3% for Ge oxidation. The graph of average AO efficiency to form bonds vs. AO kinetic energy is given in Figure 52.

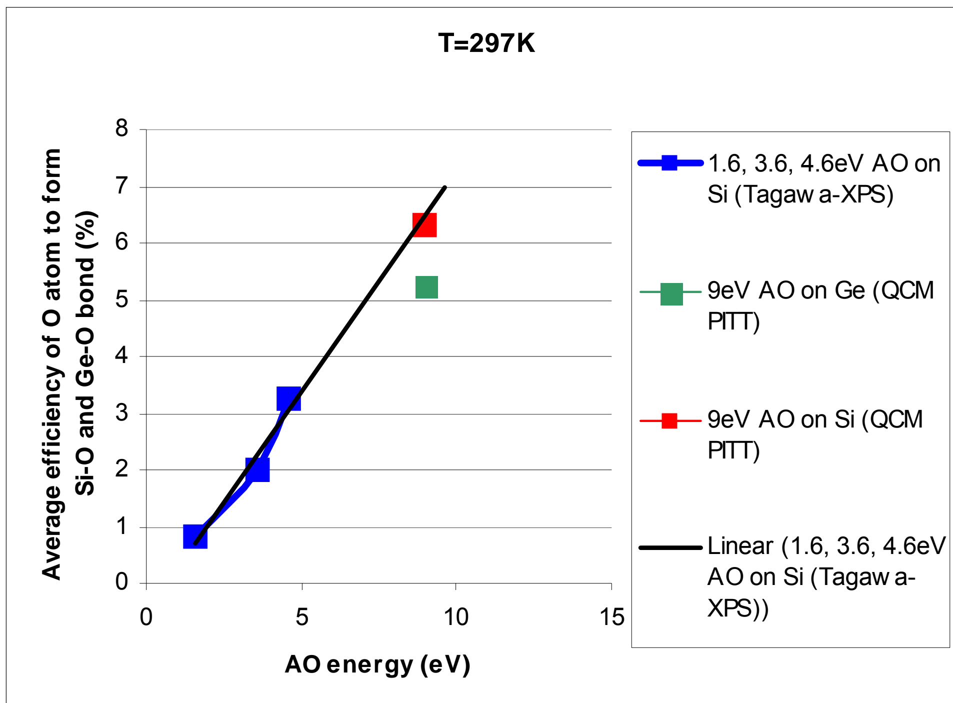


**Figure 52** Average AO efficiency for (1.6, 3.6 and 4.6eV AO) to form Si-O bond, and for 9eV AO to form Si-O and Ge-O bond.

It can be seen that the average efficiency of 9eV AO to from Si-O bond is approximately 2 times larger than the efficiency of 4.6eV beam. The straight line is fitted through the data for 1.6-4.6eV AO, calculated from [18], and it can be seen that the efficiency of 9eV AO lies on this line. This suggests that the efficiency can be predicted for certain AO energies, which would be

useful in design of protective coatings used in LEO. In general, the linear dependence of the sticking coefficient indicates that there is no desorption, while non-linearity in sticking coefficients suggest desorption processes. It should be noted that this data is not dependent on the flux, since the number of O atoms consumed to form the oxide is divided by the incoming AO flux to obtain efficiency. Therefore, the plots of AO efficiency on oxide thickness and oxidation time are dependent purely on AO kinetic energy.

# 7.0 DISCUSSION OF THE OXIDATION MECHANISMS BY HYPERTHERMAL AO ON SEMICONDUCTORS

**Interfacial abruptness due to AO directly inserting into Si back-bonds**

To understand the very initial reaction between the oxidant and Si or Ge surface, the initial steps of Si oxidation by $O_2$ in context of the back-bond insertion model should be considered [120]. The initial steps for the Si(100) oxidation by MO are given on the left-hand side of Figure 53, as originally proposed by Watanabe et al. [120].

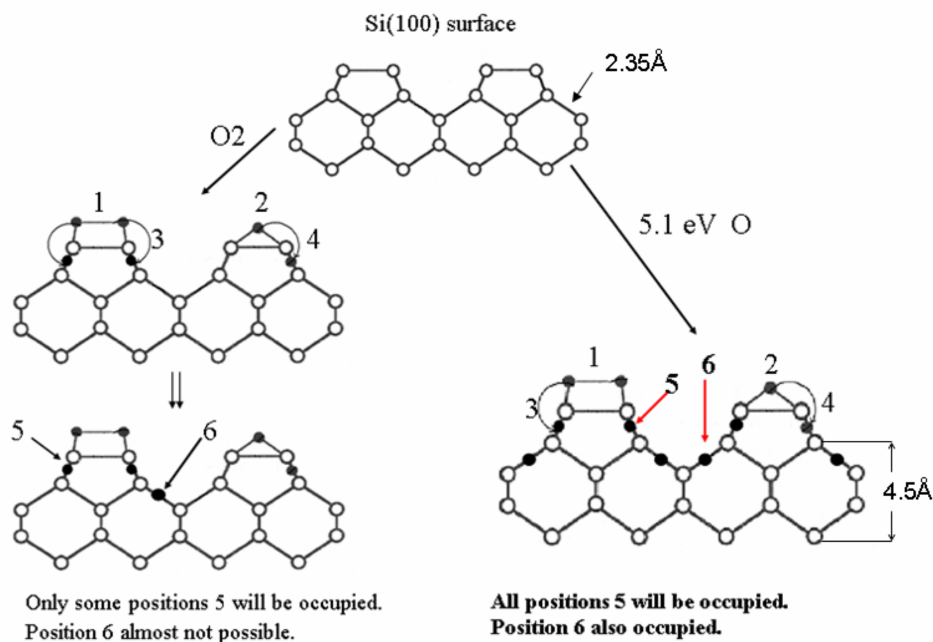


**Figure 53** Comparison of initial oxidation steps of Si(100) surface by MO and AO.

The first layer backbonds are available via O migration through the metastable surface state that provides the energy (2.96 eV for the top site, position 1, or 5.99 eV for the bridge site,

position 2) for the O atom to insert itself into the Si backbonds (positions 3, 4, 5, or 6) while direct O insertion into first or second layer backbond positions 5 or 6 requires energies of 1.0 or 2.4 eV, respectively.

To explain the interfacial abruptness observed experimentally, I proposed that AO could be directly inserted into the backbonds, leading to the observed abrupt interface. The possible steps for the Si(100) oxidation by AO are represented on the right-hand side in Figure 53 [5, 27]. The energetic AO has enough energy (5-15eV) (with no bonds that need to be broken), so it can directly attack backbonds in the first and even second subsurface layer of Si. Three monolayers can thus be oxidized by AO in the initial step, instead of only one by MO. The interface abruptness and suppression of suboxide states could be explained by the ability of energetic AO atoms to attack uppermost, first and second backbond layers [27]. Hence, the initial rate of oxidation would be increased, resulting in an abrupt interface, with fewer transitional states for AO as compared to MO, as observed by EELS. Typically, interfacial abruptness may worsen the interfacial adhesion, but no differences in the interfacial adhesion or spallation was noted neither after the oxidation nor due to cross-sectional TEM sample preparation, indicating a reasonably adherent scale.

**Increasing oxide thickness with increasing kinetic energy of AO**

According to the SRIM simulation results presented in the APPENDIX AI (Figure A II-3), 5eV AO impact on 4Å thick $SiO_2$ results in the 0.11% transmitted AO atoms. These transmitted atoms typically reach 4.5Å of $SiO_2$ layer depth, and have energy of 1-1.8eV. Tagawa's kinetic data for 4.6eV AO oxidation of Si have shown that the initial oxide thickness of ~2nm is formed in the linear regime. Since SRIM shown that 5eV AO can reach 4.5Å into the

oxide layer thickness, we speculate that there must be another mechanism following ballistic oxidation, which should be responsible for the extension of the linear regime up to 2nm observed for Si oxidation by 4.6eV AO.

This additional mechanism could be the enhanced electronic transfer from Si to $SiO_2$, or from Ge to $GeO_2$. Due to the amount of the energy transferred, thermionic emission of electrons from the semiconductor to the oxide can take place. The thermionic emission model for the oxidation by $O_2$, as well as modified thermionic emission model (part of my MS work) for the oxidation by energetic AO were described previously in the background section [5, 27]. Nevertheless, a brief description is given along following lines. The electron flux from Si to $SiO_2$ is assumed to be the rate-limiting step controlling the oxide growth rate [46, 47]. Irene proposed that the thermionic electron flux from Si to $SiO_2$ is proportional to the oxide growth rate and that the key step in the interface reaction is emission of electrons from Si to $SiO_2$. Thermionic emission helps electrons to overcome the energy barrier of a band gap and to transfer electrons from the Si to $SiO_2$ conduction band (could explain the observed extended linear regime, up to 2nm for 4.6eV AO oxidation of Si-Tagawa's data). While the process of the electron transfer appears to be very sluggish at low T, I speculated that the energy of AO helps electrons to overcome this energy barrier and transfer to the $SiO_2$ conduction band. The reasoning for the above mentioned enhanced electronic transfer is discussed next.

The temperature increase following the hyperthermal atom impact was found to be highly localized and very brief (<1 picosec, or $10^{-12}$sec) [112]. Although extremely short, this time is still longer than the typical time of electronic transfer (~ 1 femtosec, or $10^{-15}$sec).

**Reisman -inspired model to explain the later stages of oxidation and QCM data**

It can be seen that amongst the various effects described in background section, the one that comes closest to our experimental observations is Reisman's power-law model. The Deal-Grove linear–parabolic model cannot be used for AO oxidation, since this model assumes equilibrium and $O_2$ as a diffusing species. Also, Henry's law used in the Deal-Grove derivations would not be valid in the case of thin films, as already described in the background section 2.7.2.1.

From the QCM data, the oxidation kinetics of Si and Ge in energetic AO can be fitted to a power law, as originally proposed by Reisman. The power law is given by the equation $x= a\ t^b$ where x is the oxide thickness, t is the oxidation time and *a* and *b* are the coefficients dependent on the oxidation processes. Reisman assumed that the rate-limiting step is the conversion of Si to silica along the interface where viscous flow in the oxide accommodates the volume change as Si converts to silica. He proposed that deviations from linear growth is due to the changing average viscosity of the oxide scale during oxidation, which alters the ability of the oxide scale to accommodate the volume increase as Si converts to Si oxide. Here, I propose a modification of Reisman's model where instead of the average viscosity changes with time, the oxide structure changes with time. The deviations from linear growth is due changes in the raction rate constant of Si surface due to the stress between Si or Ge substrate and the oxide. The deviations from parabolic kinetics are due the changing oxide structure (the oxide becoming more ordered with time) that alters the oxygen diffusion coefficient as a function of oxidation time.

Whether the kinetics is interface reaction or diffusion limited depends on several factors including the specimen, kinetic energy of the AO and the oxidation time.

Interface-reaction controlled kinetics

For the case of interface-limited kinetics, the oxide growth rate is given by the following relationship:

$$\frac{dx}{dt} = \frac{F}{N_i} \qquad \text{Equation (63)}$$

where x is the oxide thickness, t is the oxidation time, F is the flux of oxidant species and $N_i$ is the number of the oxidant species per unit volume of the oxide. The flux, F, of the oxidant species at the interface is given by:

$F=k_sC_i$ Equation (64)

where $k_s$ is the surface reaction rate constant and $C_i$ is the oxidant concentration at the interface. Therefore, the following expression can be obtained:

$$\frac{dx}{dt} = \frac{k_s C_i}{N_i} \qquad \int dx = \int \frac{k_s C_i}{N_i} dt \qquad \text{Equation (65)}$$

Assuming that $k_s$, $C_i$ and $N_i$ are all independent of time, and solving the above differential equation:

$$x - x^o = k_s \frac{C_i}{N_i} t \qquad \text{Equation (66)}$$

where $x^o$ is the initial oxide thickness. The above equation 66 is linear with respect to time, i.e. $x = at^b$ where b=1. However, if $k_s$, $C_i$ or $N_i$ were not constants and changed during oxidation, then an additional time dependency would be introduced, and, thus, the power exponent, b, would deviate from "1". The ex situ SAED data suggests that the amorphous Si oxide is more ordered due to AO exposure. Hence, I speculate that the AO exposure could be increasing the amount of order in the oxide. Thus, any parameters that depend on structure will change with

time and affect "b", and parameters that are structure- independent are part of "a" in the power law equation.

For my QCM experiments where the Si is amorphous, as the oxide becomes more ordered, the lattice mismatch between the substrate and the oxide along the interface will increase. Due to this mismatch, Si-Si bonds in the Si substrate will be under stress (easier to break) and thus become more reactive, which will reflect in increasing $k_s$ and, hence, $b > 1$. Kobeda and Irene found that stress could influence oxidation rates significantly by affecting the Si surface reaction rates, which is in agreement with the above argument [121].

The number of oxidant species incorporated into the oxide unit volume, $N_i$, is structure-independent term, since the densities of amorphous silica and quartz (2.27 and 2.65 g/cm$^3$, respectively) are quite similar. It can be calculated that $N_i$ (amorphous silica) = 2.28 x $10^{22}$ ($O_2$ molecules/cm$^3$ $SiO_2$), and $N_i$ (quartz) = 2.66 x $10^{22}$ ($O_2$ molecules/cm$^3$ $SiO_2$). The oxidant concentration at the interface, $C_i$, is also structure -independent (contributes to $a$). The $C_i$ does not depend on structure since it is known that the sticking coefficient of AO is 1 [15]; hence all of the O atoms are incorporated into the oxide during the linear stage and $C_i$ is independent of the structure.

When the coefficient $b$ is close to 1, the oxidation process is considered reaction rate-limited. For the case when the oxidation process is reaction rate -limited, the oxide growth is controlled by the reaction rate constant $k_s$ at the Si/$SiO_2$ interface, which is influenced by the compressive stress at the Si/$SiO_2$ interface, as given in Figure 54 below.

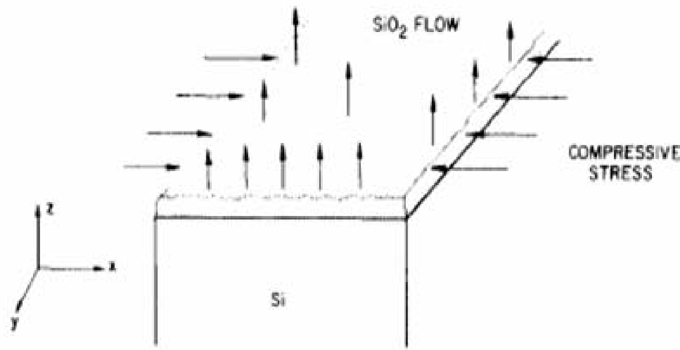


**Figure 54** The interface reaction controlled oxidation process

Whereas Reisman proposed viscous flow as the mechanism to accommodate the increased volume which is valid at higher temperatures that he studied (700-1000$^o$C), I propose for my low T oxidation study that the accommodation of the free volume could be achieved by the oxide network re-arrangement to a more ordered structure when AO diffuses thru the oxide scale via bond exchange. Other investigators also suggested that the network modification effect by AO (non-energetic) would be useful for relieving the intense stress near the Si/$SiO_2$ interface, consequently altering the reaction rate constant, $k_s$, and the oxide growth rate.

Diffusion-controlled kinetics

The transport of $O_2$ is generally believed to occur by the long-range $O_2$ migration through the disordered $SiO_2$ oxide during Si oxidation. Interstitial $O_2$ molecule diffusing through the disordered network was found to be the most energetically favorable species, as opposed to the not so favorable peroxyl and ozonyl linkages due to their higher formation energies [59]. This observation implied that diffusion process of $O_2$ occurs without giving rise to exchange process

with the oxide network atoms, as supported by the Rosencher's experiments [123]. In contrast, an X-ray diffraction study of the residual order peak emanating from the oxide shown that AO is incorporated into the $SiO_2$ network near the surface and diffuses toward the interface along with modifying it, through bond exchange [124]. These investigators concluded that the diffusion process of AO is via the incorporation into the oxide network, which may induce oxide modifications to the oxide network.

For the case of diffusion-limited process, the oxide thickness, x, is given by the general expression:

$$x^2=2kt \qquad \text{Equation (67)}$$

where $k=\Omega D[C_o-C_L]$, t is the time, $\Omega$ is the oxide volume formed, D is the diffusion coefficient, C is the concentration of oxidant species at interfaces O (oxide/gas interface ) and L (oxide/Si interface) [42]. The oxide thickness (x) can be re-written as:

$$x=\sqrt{2\Omega D\left[C_o-C_L\right]}t^{1/2} \qquad \text{Equation (68)}$$

The diffusion coefficient, D, of O atom can be represented as:

$$D_O=[\frac{1}{6}\alpha^2 z\nu\exp\frac{\Delta S_m}{R}]\exp\frac{-\Delta H_m}{RT} \quad \Delta G_m=\Delta H_m-T\Delta S_m \qquad \text{Equation (69)}$$

where α is a jump distance, z is the number of sites to which an O atom can jump, ν is vibrational frequency of the O atom in the Si-O bond, $\Delta H_m$ is the activation enthalpy for O atom migration, and $\Delta S_m$ activation entropy for atom migration, $\Delta G_m$ is the Gibbs free energy for atom migration, R is gas constant (8.314 J/molK), and T is the temperature in K. Now the oxide thickness can be written as:

$$x=\sqrt{2\Omega\frac{1}{6}\alpha^2 z\nu\exp\frac{\Delta S_m}{R}\exp\frac{-\Delta H_m}{RT}\left[C_o-C_L\right]}t^{1/2} \qquad \text{Equation (70)}$$

From the formula above, the parameters that should depend on the oxide structure include: $\alpha$ , z, $\Omega$ , ΔHm, ΔSm,. The factors independent of the oxide structure are: $\nu$ , $C_o$ and $C_L$. It is reasonable to assume that the vibrational frequency of the O atom in the Si-O bond, ν, mainly depends on the energy supplied to the O atom, thus the dependence on structure can be neglected. The thermal -spiking effect, discussed in the background section, is caused by the energy transfer from the incoming AO to the materials surface. Since this brief T increase causes lattice vibrations, it is possible that the O atom in the Si-O bond will vibrate at the higher frequency as compared to the non-energetic atom impact, when there is no T increase. Due to the increased vibrational frequency, the O atom will have a higher probability to jump into the neighboring Si-O bond. With higher AO energy, the jump probability of O atom is increased. The diffusion coefficient can also be written as

$$D_O = \frac{1}{6}\Gamma_O \alpha^2 \qquad \text{Equation (71)}$$

where $\Gamma_O$ is the number of jump attempts of the O atom from one to another Si-O bond per second. We speculate that the number of jump attempts, $\Gamma_O$, of energetic AO will increase for higher energy AO beam, due to the enhanced thermal spike of the O atom on the oxide. Increased $\Gamma_O$ consequently increases the probability that the O atom can interact with the oxide network. Since $\Gamma_O$ does not depend on the oxide structure much, then it will contribute the "a" in the power law expression. Hence, the coefficient *a* reflects the ability of AO to "hop" into the neighboring Si-O or Si-Si bonds.

Typically, *b*=0.5 for the oxidation process which is limited by the transport of oxidant. The altered "*b"* could be due to diffusion of AO changing with respect to time because of the changing structure of the oxide with respect to time. If one assumes that the oxide becomes more

ordered with time, then the ability of AO to insert into an oxide bond becomes more difficult and diffusion slows down with respect to time, giving *b* less than 0.5.

My model, as inspired by Reisman, in which the oxide growth is controlled by the time dependent transport of oxygen through the $SiO_2$ or $GeO_2$ scale, due to the structural modifications of the oxide with time is shown in Figure 55 below.

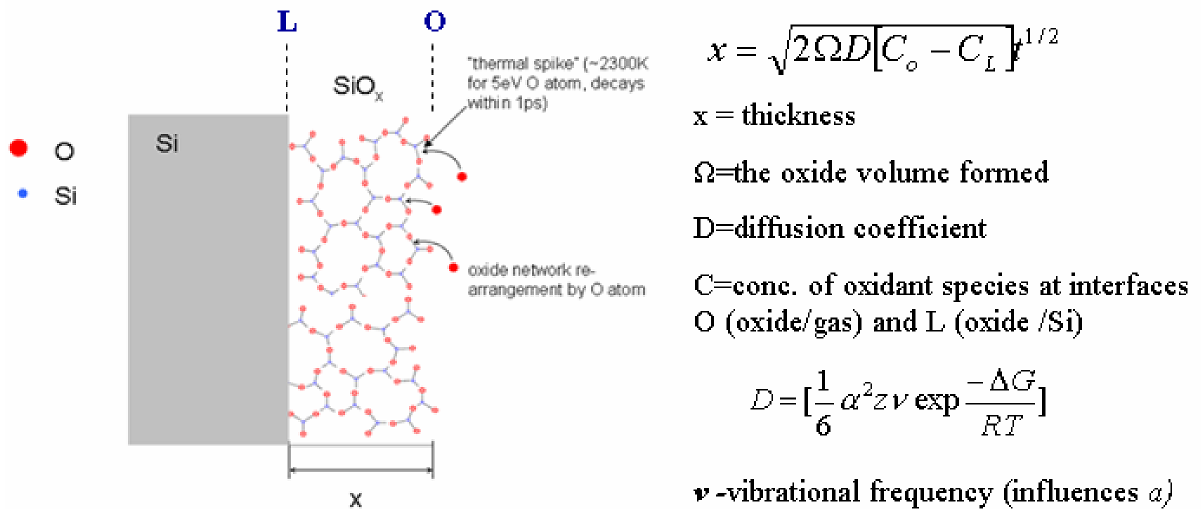


**Figure 55** Modified Reisman model –diffusion controlled oxidation process. $SiO_x$ is a growing oxide layer, with thickness x. The diffusion coefficient of oxygen, D(t), is time –dependent, due to the oxide structure changing with time. The thermal spike is brief (decays within 1ps) and localized (~6Å from the site of impact) but allows for structural re-arrangement of the oxide towards the more thermodynamically stable ordered quartz structure.

For the diffusion-limited oxidation process, there is one oxide phase whose structure changes with time due to the impact of energetic AO on the oxide surface. The thermal spiking at the surface of the oxide is caused by the energy transfer from the impacting O atom to the surrounding atoms. This energy transfer, although very brief and localized, promotes O atom hoping into the neighboring bonds, thereby enhances re-arrangement of the oxide network, and forming a more ordered oxide structure (thermodynamically favored oxide).

*Discussion of coefficients b and a and determination of the rate-limiting mechanism*

The coefficient *b* in the power law expression, $x = a\ t^b$, reflects the changing oxide structure, while "*a*" reflects the ability of O atom to "hop" into neighboring bonds. Table 7 is a tabulation of "*b*" and "*a*" values extracted from my experimental (QCM) data and Tagawa's XPS data, as described in the results section.

**Table 7** Determination of the rate-limiting mechanism of the oxidation process (interface reaction or diffusion-limited). Coefficients *b* and *a* were calculated from QCM and XPS (Tagawa) [18] kinetic data at T=297K; $b \sim 1$ for the oxidation process which is interface reaction-limited; $b \leq 0.5$ for diffusion-limited process.

* XPS data from Tagawa (reference 18) used for *b* and a coefficients calculation

**QCM kinetic data from PITT used

| Sample | **AO Ek (eV)** | **b** | **a** | **Oxidation process limited by** |
|---|---|---|---|---|
| Si(100) * | 1.6 | 0.467 ± 0.027 | 0.342±0.021 | Diffusion |
| Si(100) * | 3.6 | 0.305±0.027 | 1.01±0.06 | Diffusion |
| Si (100) * | 4.6 | 0.163±0.01 | 1.892±0.045 | Diffusion |
| Si amorphous ** (6-10hrs) | 5 | 1.217±0.044<br>0.648±0.01 | 0.0024±0.0005<br>0.038±0.002 | Interface reaction<br>Interface reaction to diffusion |
| Ge amorphous ** (6-10hrs) | 5 | 1.110±0.015 | 0.00102±0.08E-3 | Interface reaction |
| Si amorphous ** | 9 | 0.5±5.52E-17 | 0.215±6.32E-17 | Diffusion |
| Ge amorphous ** | 9 | 0.739±0.01<br>0.413±0.007 | 0.050±0.002<br>0.268±0.011 | Interface reaction<br>Diffusion |

My QCM kinetic results demonstrated that the oxidation rate of Ge by 5 and 9eV AO is lower than the oxidation rate of Si by the same species. This is in agreement with the surface chemistry study of the initial oxidation stages of Ge(100) and Si(100) surfaces which have shown that the desorption half-lives for bridge-bonded O species on Si(100) are several orders of

magnitude higher than for Ge(100) surfaces [113]. Hence, reversible desorption from the Ge(100) surface occurs much more rapidly than from Si(100), indicating that Ge/$GeO_2$ interface is thermodynamically unstable when compared to the Si/$SiO_2$ interface. If we assume that the precursor species for the oxide formation is also an O bridging atom, the high instability of this species and its desorption could contribute to the lower oxidation rate observed for Ge than for Si.

While the coefficient *b* reflects the oxide structural changing with time, coefficient *a* is assumed to reflect other effects than effect of AO on the oxide structure. Coefficient *a* is time-independent factor, and does not depend on oxide structure, but energy of AO. Coefficient *a* will be discussed in the context of atomic site-to site diffusion and the ability of O atom to "hop" into neighboring Si-Si or Si-O bonds.

For the linear regime (interface-reaction limited process), $x - x^o = k_s \frac{C_i}{N_i} t$ (equation 66).

The oxide structure dependent factor is reaction rate constant ,$k_s$, which affects coefficient b, while structure independent factors ($C_i$ and $N_i$) affect coefficient *a*. x is the oxide thickness, $x_o$ is the initial oxide thickness, $k_s$ is the surface reaction rate constant, $C_i$ is the oxidant concentration at the interface and $N_i$ is the number of the oxidant species per unit volume of the oxide. Coefficient *a* reflects $C_i$, which represents amount of AO incorporated into oxide.

For the diffusion-limited process, a large value of *a* implies high ability of AO to "hop" into Si-Si or Si-O bonds, and to form Si-O bonds, explaining the higher value of *a* found for the Si oxidized by 9eV AO, as compared to the oxidation by 5eV AO. Due to the increased vibrational frequency, higher energy O atom will "hop" into Si-Si bonds and form Si-O bonds at the higher rate than the lower energy atom.

Value of “b” close to 0.5 means diffusion –linited process, explaining the higher value of *b* found for the Si and Ge oxidized by 5eV AO, as compared to the oxidation by 9eV AO. Higher energy AO beam should cause ordering of the oxide structure at a higher rate.

The values of coefficients *b* and *a,* and their meaning in the light of modified Reisman model will be disused next for each set of QCM data.

*1.6, 3.6 and 4.6eV AO beams on Si (Tagawa's data)-coefficient b*

It can be seen from Table 7 that *b*<0.5 was found for all of Tagawa's XPS data. This observation suggests that the rate-limiting process for the oxidation by 1.6, 3.6 and 4.6eV AO is the diffusion of O through the oxide scale. The decrease of “*b*” from 0.5 means that the diffusion is slowing down with time than it would be if the diffusion coefficient were time-independent. The time-dependency of the diffusion coefficient could be explained by a changing oxide structure. The value of *b* is lowest (0.163) for the highest energy beam (4.6eV), indicating a faster rate of transformation of the oxide structure. Implication is that the oxide ordering for the higher energy (4.6eV) AO beam takes place faster than for the lower energy (1.6eV) beam. The oxide ordering with the time could cause more difficult O atom insertion into the oxide bonds, and O atom transport through the oxide, which will be reflected in *b* and *D* coefficients decrease.

Since all of the values of “b” are lower than 0.5 suggests that the oxidation kinetics are limited by diffusion. Interestingly, the values of “b” deviate further from “b” as the kinetic energy of the AO increases. According to my model, increasing kinetic energy causes a higher thermal spike on the oxide surface, thereby enhancing the modifications of the oxide network towards the more ordered oxide structure. As the oxide structure becomes more ordered, the ability for oxygen to diffuse via bond-insertion thru the oxide scale becomes increasingly

difficult because of the stronger Si-O bonds in the ordered oxide structure. Hence, with increasing kinetic energy of the AO, the ordering rate increases, and the rate of decreasing diffusion coefficient increases, leading to a greater suppression of "b", as was observed in Tagawa's XPS data.

*1.6, 3.6 and 4.6eV AO beams on Si (Tagawa's data)-coefficient a*

Table 7 shows that the value of coefficient *a* increases with the kinetic energy of the AO beam. 4.6eV AO beam causes more intensive thermal spike than the lower E beam. Although very brief, higher T increase due to the higher kinetic energy should cause more frequent lattice vibrations and increased number of jump attempts and jump probability of the O atom. As this probability is increased, more O atoms could jump into the neighboring Si-O or Si-Si bonds. This would reflect in the increase of coefficient *a*. My calculations of AO efficiency have shown that 4.6eV beam has ~4 times higher efficiency than 1.6eV AO beam to form Si-O bonds, at the beginning of the oxidation process.

*5eV AO beam on Si (QCM data) -coefficient b*

The value of *b* was calculated to be 1.217 and 0.648, thus suggesting interface-reaction limited process at the Si/$SiO_2$ interface. The observation of b>1 at the beginning could be explained by the increased reactivity (and increased $k_s$) of the Si oxidation along the interface due to the stress and lattice mismatch between the amorphous Si substrate and oxide layer formed. Due to the lattice mismatch, the Si-Si bonds in the Si substrate are stressed and easier to break, and thus more reactive, which could cause b>1. Departure of *b* from 1 and approaching to

0.5 in the second stage could be interpretated as the transition from linear to parabolic, diffusion-limited process, which would eventually take place as the oxide thickens.

*9eV AO beam on Si (QCM data) -coefficient b*

The value of *b* equals to 0.5 for Si oxidized by 9eV AO, clearly indicating that the oxidation process is diffusion-limited. Since *b*=0.5, it can be inferred that the diffusion coefficient is time-independent. The reaction-limited regime was not noted for Si oxidized by 9eV AO. This linear regime probably occurred during the first 40min of oxidation of Si in 9eV AO. As noted earlier, the initial QCM data was complicated by outgassing of the sample surface.

It is reasonable to expect that the oxidation in 9eV AO beam will be diffusion-limited, since *b* was approaching to 0.5 for 5eV AO oxidized Si, as discussed in the previous section. Higher energy beam (9eV) forms thicker oxide, therefore causing rate -limiting process to switch earlier to diffusion-limited. The thicker and at a higher rate structurally changing oxide is formed by higher energy AO beam and consequently oxidation process is diffusion-limited.

*5 and 9eV AO beams on Si (QCM data) -coefficient a*

A value of *a* equal to 0.215 was determined for Si oxidized by 9eV AO. This value is larger than a value for 5eV AO oxidized Si (0.0024 and 0.038, for the first and second part of the oxidation curve, respectively), and this is to expect since higher E beam should cause more intensive thermal spike and more frequent lattice vibrations. Higher E beam will cause more "hopping" of O atom into the Si-O bonds than lower E beam, thus the interaction of AO with the network will be enhanced with increase in eV.

The value of “a” for the later oxidation stage is higher as compared to the value of “a” in the beginning of 5eV AO oxidation of Si. Higher value of “a” for the later oxidation stage can be explained if more frequent lattice vibrations are assumed in the ordered oxide as compared to the less ordered oxide structure formed in the begining. The kinetic energy of impacting O atom causes thermal spike on the oxide surface, which results in the lattice vibrations. These vibrations are then transferred through the crystal affecting the number of jump attempts, $\Gamma_{O.}$ The number of jump attempts or “hops” of O atom increases with more frequent lattice vibrations since it should be easier for O atom to “hop” into the bonds which vibrate more frequently and in which the atoms are further from their equilibrium positions.

It is reasonable to assume that the lattice vibrations are attenuated faster and for shorter distances in less regular oxide structure (e.g. open amorphous structure, with wider rings), which leads to decrese in $\Gamma_{O,}$ and reflects in decrease of coefficient a. On the other hand, more regular or more ordered oxide structure (as formed later during the oxidation) should “conduct” lattice vibrations for a greater distances into the crystal, which leads to increase in $\Gamma_O$ and “a” (as determined for the second part of the oxidation process of Si by 5eV AO).

*5eV AO beam on Ge (QCM data) -coefficient b*

The value of coefficient *b* was found to be 1.110, indicating reaction-limited kinetics at the Ge/$GeO_2$ interface. It is interesting that Ge oxidized by 5eV AO follows linear oxidation kinetics for the total time of the QCM experiments (6-10hrs) while Si oxidized by 5eV for the same time shows a transition to diffusion-limited kinetics.

The observation of b>1 could be explained by the increased reactivity (and increased $k_s$) of the Ge oxidation along the interface due to the stress and lattice mismatch between the

amorphous Ge substrate and oxide layer formed. Due to the lattice mismatch, the Ge-Ge bonds in the Ge substrate are stressed and easier to break, and thus more reactive which could cause $b>1$.

*9eV AO beam on Ge (QCM data) -coefficient b*

The oxidation of Ge by 9eV AO beam resulted in two values of *b*, thus indicating a break in the kinetics. The larger value of *b* at the beginning of the oxidation (0.739) is to be expected, since the process is interface reaction –limited.

The value of $b>1$ would probably be determined for the very initial period of oxidation (first 10min), and b=0.739 was determined at a later stage where interface reaction-limited kinetics is transitioning to diffusion-limited kinetics. A value of *b* =0.413 in the second stage shows that the oxygen diffusion process has become the rate-limiting step, since $b<0.5$. As the oxide thickens, it will impose a barrier for the oxidant transport, and consequently the process becomes diffusion-limited.

*5 and 9eV AO beams on Ge (QCM data)-coefficient a*

It is shown in Table 7 that the value of coefficient *a* is lower (0.00102) for Ge oxidized by 5eV AO than for Ge oxidized by 9eV AO beam (*a*=0.05-in the 1st part and *a*=0.268-in the 2nd part). A larger value of “a” determined for 9eV AO is to be expected, since higher energy AO has higher ability of hopping along Ge-O bonds in $GeO_2$. Therefore, more AO will be incorporated into the oxide when higher energy AO beam is used, as compared to the AO beam with lower kinetic energy.

The larger value of "a" for the second as compared to the first oxidation stage was determined for Ge oxidation by 9eV AO. The explanation could be that more regular or more ordered oxide structure (as formed later during the oxidation) should "conduct" lattice vibrations for a greater distances into the crystal, which leads to increase in $\Gamma_O$ and "a" (as determined for the second part of the oxidation process of Ge by 9eV AO).

**Surface roughness explained by AO "implantation" damage**

Interestingly, AFM studies revealed that AO forms ~2 times rougher silica layer on Si(100) substrate at 220$^o$C. The Ge-oxide layer formed by AO at room temperature on Ge(100) is ~4 times rougher than the native oxide layer. Similar to Si oxidation, 5eV AO forms ~1.5 times rougher oxide on Ge at 200$^o$C. 15eV AO formed the roughest oxide on the surface, compared to 5eV and 9eV AO oxidized Ge.

While it was determined that oxide growth by molecular oxygen occurs at the Si/$SiO_2$ interface [117], recent investigations have shown AO incorporation into the oxide network at the surface of the oxide, network re-arrangement and structural oxide changing while progressing towards the interface [118]. In the same study, $O_2$ was shown not to react with the oxide network [118]. The impact of energetic AO can produce Si-O or Ge-O bond bending and breaking on the surface of already existing oxide. These effects of AO energy (e.g. surface damage due to AO bombardment) acting together with the exchange processes with the O network atoms and thermal -spiking at surface could lead to the rougher oxide surface observed. Thermal -spiking at the oxide surface can cause oxide network re-arrangement and increase in oxide surface roughness.

# 8.0 CONCLUDING REMARKS

Different oxidation mechanisms and the oxide structures formed by AO as compared to MO were expected due to AO energy and mono-atomic nature that could alter the oxidation kinetics. It was assumed that the energetic AO should form thicker oxide layer on Si due to its ability to oxidize more than one monolayer of Si substrate at once, and due to the easier transport through the oxide scale. It was shown within the results of this thesis that hyperthermal AO formed on Si and Ge thicker and on the surface rougher oxide layer than MO, as evidenced by ex-situ results of X- HRTEM and AFM studies, respectively. The effects of the kinetic energy and temperature of AO on oxidation of semi-conductor materials were investigated as well. In order to see whether the AO kinetic energy or the substrate T is more dominat factor, Ge samples were oxidized in 5eV AO at two different temperatures, 25 and 200$^{o}$C, both in LEO temperature range. It was determined by X- HRTEM that the same oxide thickness was produced on Ge when oxidized by 5eV AO at 200$^{o}$C and at room temperature. This is most probably due to the fact that 5eV energy corresponds to the ~58000K, thus making the temperature rise between 25 and 200$^{o}$C negligible compared to the dramatic effect of AO. Therefore, the kinetic energy of the AO is considered the primary factor causing the increase of the oxide thickness. More studies of the kinetic energy effect on the AO oxidation of Si and Ge were undertaken in order to prove the dependency of the oxide thickness on AO energy. The FAST$^{TM}$AO source at the University of Pittsburgh is capable of alternating AO beam in higher energy range, and the experiments were done using energy of 5-15eV. Ex-situ experiments of the oxide thickness determination by

HRTEM showed that the thickness of the oxide increases with the increase in AO kinetic energy, for similar AO fluxes applied. Germanium-oxides created by 5, 9 and 15eV AO were found to be 2.5, 3.5 and 5nm thick, respectively. Due to the 1 order of magnitude higher AO flux used to oxidize Si by 5eV AO when compared to the flux of 9eV AO beam, resulting $SiO_2$ layers were both ~5nm thick.

It was shown in the result section that energetic AO causes enhanced ordering of the amorphous $SiO_2$ structure [SAED, ELNES, FEM]. The $SiL_{2,3}$ edge ELNES obtained from Si(100) oxidized by 5eV AO showed similarities with the results of Garvie et al., suggesting that the oxide structure is similar to alpha-quartz while a more random arrangement of Si and O atoms are created by MO oxidation. Clearly resolvable diffraction rings in SAED, with the d-spacings corresponding to that of alpha-quartz for the AO formed oxide, are in agreement with the ELNES results. The SAED and EELS data on the silica created by hyperthermal AO agree well with previous studies of Si oxidation by ozone, which is reasonable since the ozone is a strong oxidant due to the decomposition on the AO and oxygen molecule [66-69]. It is reasonable to expect that AO should form less random and more ordered oxide microstructure due to the high kinetic energy of the oxygen atom, which would favor transformation to a thermodynamically stable ordered oxide. These results could be explained by the thermal spike (brief T increase) caused by energy of AO which allows the O adatom to hop and arrange nearby bonds toward the more thermodynamic (ordered) silica on the surface. Since this is a continuing oxidation process, the surface becomes part of the bulk, which explains why the oxide scale is so uniform and more ordered as compared to $O_2$ formed oxide.

It was assumed that AO should oxidize more than one monolayer at once, due to its ability to insert into the Si or Ge backbonds, therefore forming abrupt semiconductor/oxide

interfaces. As determined by EELS, the $Si/SiO_2$ interface formed by 5eV AO was found to be chemically abrupt, with the clear existence of only $Si^o$ and $Si^{4+}$ oxidation states, and the $Si/SiO_2$ interface abruptness was confirmed on higher resolution level, on $C_s$ corrected VG-HB501 STEM at ORNL with a spatial resolution below 1Å. The investigations of structural properties of Ge oxide and $Ge/GeO_2$ interface were conducted in the similar manner as for Si. The characterization of $Ge/GeO_2$ interface formed by AO revealed that abrupt interface is formed.

Atomic force microscopy results on both Ge and Si revealed that formation on the surface rougher oxide is assisted by higher energies of AO beam. 15 eV AO beam on Ge clearly formed the roughest oxide layer. Formation of the roughest surface oxide layer for higher energy AO beam could be caused by the oxide bond breaking and formation of the defect sites on the oxide surface due to the high energy atom impact. Higher energy AO beam has the higher ability to break Si-O and Ge-O bonds at the oxide surface and to increase surface roughness.

Initial, ballistic oxidation of Si and Ge by energetic AO was investigated using SRIM simulations, and the stopping ranges of energetic O atoms as well as their energies were calculated. Stopping range of ions in matter simulations done for 5eV AO impacting $SiO_2$ and $GeO_2$ targets revealed that energetic atom lost its energy before reaching 5Å of the target thickness. SRIM calculations indicated that only a small portion (up to 2%) of higher energy (15eV) O atoms was transmitted through the 5Å thick $SiO_2$ or $GeO_2$ layers. Higher energy O atoms (9 and 15eV) can be transmitted and reach target thickness of 7Å, at most. This result is in agreement with the kinetic data and hypothesis that the energy is transfered locally (first couple of Å from the impact site). It was concluded that there must be another mechanism responsible for the linear regime extension up to 2nm (observed for 4.6eV AO oxidation of Si-Tagawa's XPS data) following ballistic oxidation and this additional mechanism could be the enhanced

electronic transfer by thermionic emission from semiconductor to oxide. It is possible that the energy of AO promotes electron transfer over the energy barrier to the oxide conduction band

QCM kinetic experiments done in FAST$^{TM}$ AO source, using 5eV (on Ge) and 9eV AO (on Si and Ge) beams showed that Reisman-inspired model employing power -law can be used to explain the oxide growth kinetics in the later oxidation stage. Amongst many other models proposed by different researchers, this is the only model that considers the structural changes of oxide with time. While Reisman proposed that diffusion coefficient time-dependency is due to the average oxide viscosity changing with time, my model proposed within this thesis assumes that diffusion coefficient (and oxidation kinetics) changes with time due to the oxide structure continuously changing with time due to hyperthermal AO exposure. Ex-situ results of SAED and EELS studies showed that more ordered structure is formed by energetic AO, thus supporting the model of the oxide structure changing with time. It was shown that coefficient "b" (in power law) decreases with increasing eV, therefore implying that more energetic O species might increase the amount of order of the oxide scale or ordering rate. In-situ monitoring of the oxide structure evolution would be needed in order to investigate the oxide ordering with the time.

Although fundamental in its nature, the work performed is expected to have an impact on the design of the protective coatings used in LEO. One immediate application could be on the thickness of the coatings used to prevent AO diffusion and to protect underlying polymeric material. Abrupt Si/$SiO_2$ interfacial structure formed by AO could have an impact on the design, and performance of MOS devices. The current request to create only a few atomic layers thick $SiO_2$ in these devices without losing its inherent physical properties as an insulator could be satisfied using oxidation process involving energetic AO. Further measurements of capacitance are needed in order to determine electrical properties of the oxide and the interface formed by energetic AO.

# 9.0 FUTURE WORK

The research work presented in this thesis includes a number of interesting results such as increased thickness and surface roughness of the oxide scale due to the reactive AO, more ordered oxide structure, and a chemically abrupt semiconductor/oxide interface formed. The QCM kinetic experiments were performed at room T, but since this is not the most extreme temperature encountered in LEO, kinetic studies using higher T (e.g 200$^{o}$C) should be conducted. To underline, the oxidation process in our specific conditions depends on various experimental parameters, such as AO flux, sample structure and cleanness, pre-oxidation cleaning treatments and other ambient conditions. Since QCM experiment described above was preliminary in-situ oxidation study within the source, it is highly desirable to do more experiments in this field.

Finally, a comment about the reproducibility of the results reported in this thesis should be made at this point. The reader of this thesis should be aware that the exposures were not repeated. A total of 9 samples (3 Si and 6 Ge samples) were analyzed ex-situ mainly by TEM techniques, while 2 Si and 2 Ge samples were studied in-situ by QCM.

The reason for this is the fact that the LDS AO source was not readily available and actually exists at only few sites in the world. This type of source is unique due to its ability to produce hyperthermal AO with fluence comparable to the LEO conditions. No other source of AO comes as close as the PSI FAST$^{TM}$ source in simulating real LEO conditions. Fortunatelly, the FAST$^{TM}$ source arrived at the University of Pittsburgh, but the exposures of the samples were

not possible to do as soon as the source arrived. After the installation of the AO source, additional modifications needed to be done, such as heating stage and QCM systems addition. When the modifications were completed, (e.g. heating stage addition was completed in summer 2005), the exposures at highest T (200$^{o}$C) characteristic for LEO environment were possible. Since the system is now set up and readily available at the University of Pittsburgh, it is possible to address the reproducibility issues discussed above during the future research as a continuation of this thesis work. Many of the results represented within this thesis work are the first results acquired from this type of source and therefore contribute to new, fundamental knowledge of materials oxidation by energetic AO.

It would be very useful to establish the oxidation procedure and conditions under which specific factors can be isolated. For example, this thesis showed that sample cleanness is very important, especially for the initial oxidation regime where the kinetics of interface reaction is dominant. Single -crystalline samples should be used instead of amorphous ones, and one has to find the method to start the oxidation with the clean surface. Regarding this issue, the AO source needs to be modified in order to add sample preparation chamber. It is extremely important to conduct future experiments with the fixed AO flux, since we have seen that the change in flux leads to many ambiguities in the data interpretation. The change of AO flux influences the oxide network structural re-arrangement and might affect the solubility of oxygen in the oxide. Therefore, the effect of AO kinetic energy on the oxide thickness and structural ordering cannot be determined precisely unless the AO flux is kept fixed.

Work that has been done so far focused on the effect of AO energy on material oxidation. Other effects of LEO environment, such as VUV and thermal cycling acting either alone or in synergy with AO could change the corrosion behavior of semiconductors. Incident angle of AO

on the sample surface could be varied as well, only 90$^{o}$ AO impact was studied so far. In other words, more complete "picture" of the LEO factors on semiconductors oxidation should be created. While this thesis focused on ground-based simulation of LEO AO impact on Si and Ge, real space experiments would be very useful to compare ground-based experiments to LEO exposed samples. Currently, a space project, MISSE -7, is planned to be conducted. Semiconductors samples are to be sent in space amongst many other samples, and numbers of experiments, including dynamic ones are designed.

Additional experiments, such as in-situ TEM, are necessary to observe oxide formation in real time. For the realization of this work, FAST$^{TM}$AO source needs to be attached via interface to the VG HB501 STEM.

It would be interesting to determine the nature of diffusion coefficients in the thin films. For example, O tracer studies could be conducted in homogeneous oxide films formed by energetic AO. Sequential oxidation by AO and O isotope might be compared with the MO replacing AO.

# APPENDIX A

## FAST$^{TM}$ AO SOURCE AND MODIFICATIONS

The standard FAST$^{TM}$ AO source is rated for $10^{-7}$ Torr base vacuum. The AO source PSI constructed for the University of Pittsburgh is compatible with a base chamber vacuum of $10^{-9}$ Torr and capable of sub-monolayer exposure. At a 5Hz pulse rate, the AO source with a 7J/pulse pulsed $CO_2$ laser generates an 8km/sec AO beam with a flux of ~$5x10^{15}$ atoms/$cm^2$sec. The typical distance from the sample to the nozzle throat is fixed at 28cm for UPITT AO source. Since the laser energy is fixed at 7J/pulse, the number of AO atoms produced per pulse increases as the velocity is reduced. High vacuum pumping speed is needed to maintain base operational chamber vacuum of ~$10^{-5}$ Torr. There are 3 subsystems of the FAST$^{TM}$ AO source:

1. The AO source chamber subsystem consists of:

-a pulsed AO beam source valve/nozzle mounted on the top of the chamber

-a laser beam focusing and deflection system

-an optical radiometer system to monitor AO beam velocity (radiation is emitted during AO→$O_2$ recombination, and this radiation is measured by the two radiometers).

-helium cryopump, turbo pump and mechanical dry pump

2. The pulsed $CO_2$ laser subsystem utilizes Lumonics Hull Ltd. LT-7/300 pulsed $CO_2$ laser system delivering ~7J/pulse. The laser is key activated and connected to the laser control box.

3. The AO source subsystem control electronics consists of a digital oscilloscope, digital delay generator for triggering the laser after $O_2$ pulse, pulse beam valve controller, convection gauge and cold cathode gauge. These electronic instruments are manually operated.

## Heating stage design

According to the heating stage design given below, the parts are machined out from 316 stainless steel, in the chemistry machine shop. Rectangular Boralelectric heater (UHV compatible), supplied by GE Advanced Ceramics [108], was installed in the heater housing. This heating element has ultra-fast response and power outputs (>300wats/sq.inch), due to the combination of pyrolytic Boron Nitride (pBN) (dielectric ceramic material) with pyrolytic graphite (PG) (an electrical conductor). This electrically stable heating device can operate in temperatures up to 2000K. The heater cross-section is very thin (about 0.080"), resulting in a low thermal mass. UHV Heater kit was purchased from Tectra Company (Germany) [109]. This kit consists of: HC3500 heater controller, power supply, PID controller, current and thermocouple feedthrough, contact bolts and insulated thermocouple. AutoCAD drawings of the HTR1002 heater and photo of the UHV heater kit are given in Appendix. Several layers of Ta foil were used around the heater bottom and sides for thermal insulation.

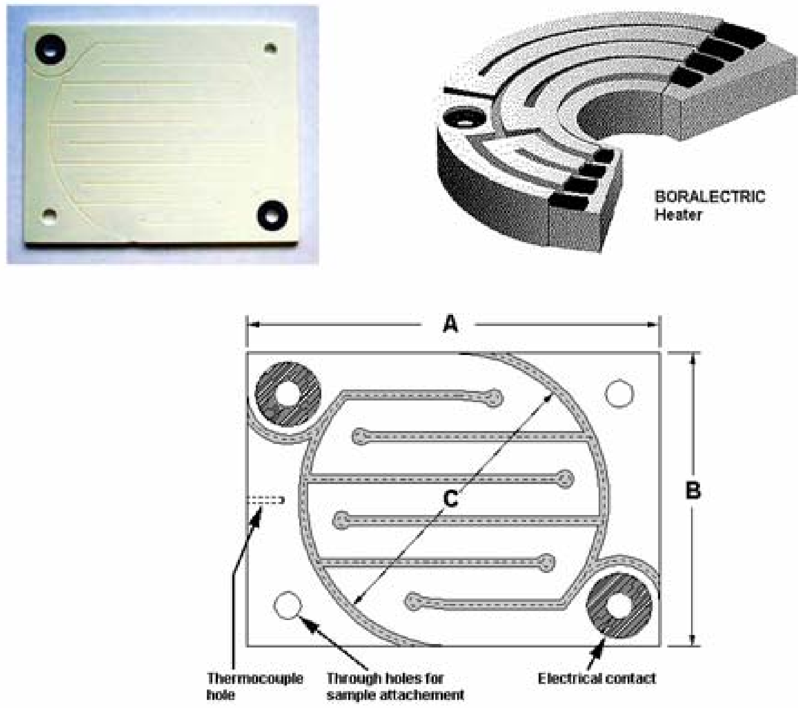


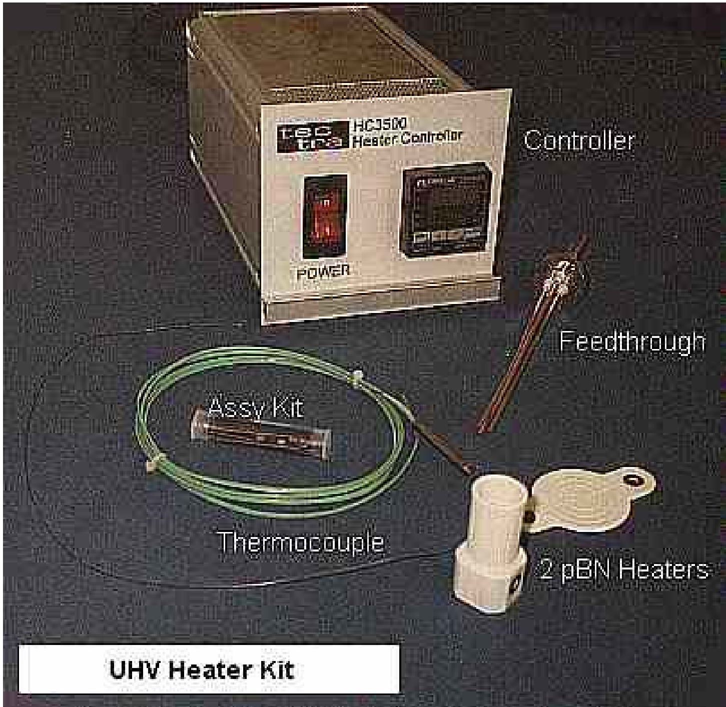


HTR 1002 Boraelectric heater,

supplied by GE Advanced Ceramics.

**Figure A I- 1** Boraelectric heating stage elements [126, 127]

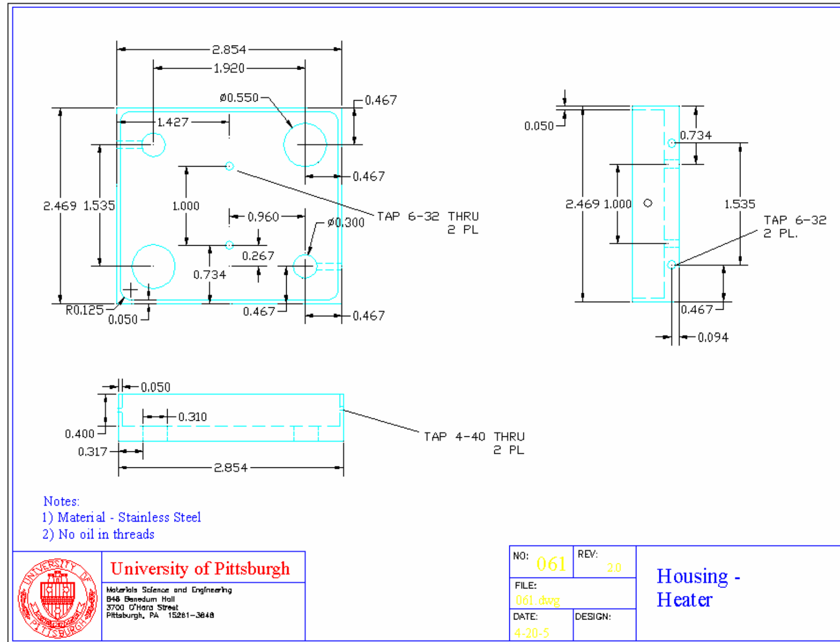


(a)

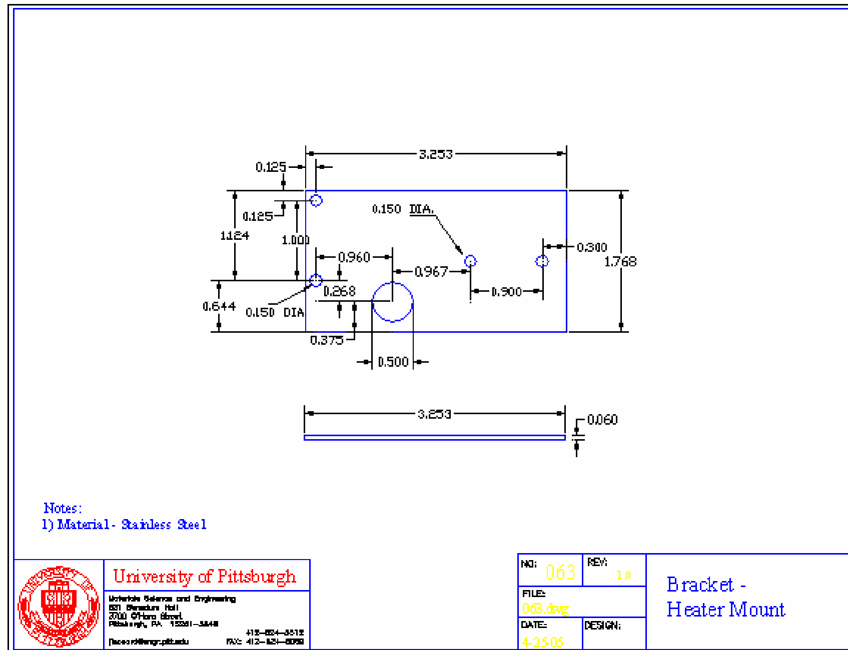


(b)

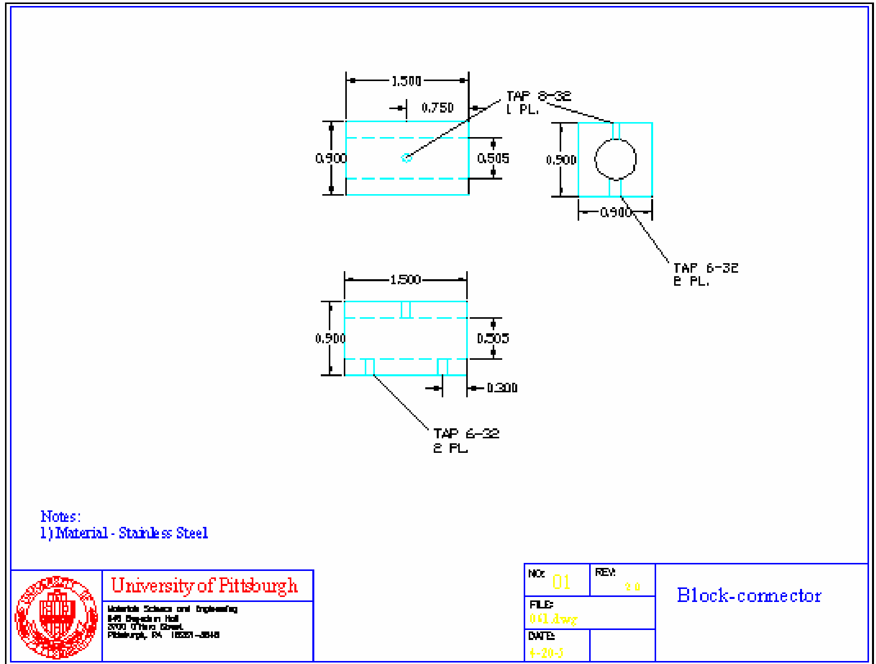


(c)

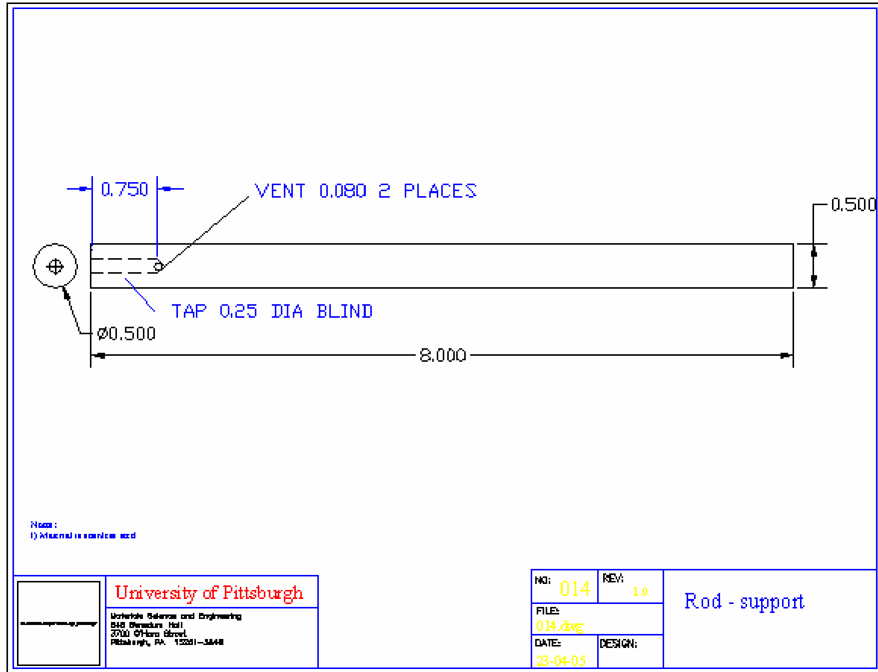


(d)

Figure A I- 2AutoCAD drawings of the heating stage elements a) heater housing b) heater mount c) block-connector and d) rod-support

Research quartz crystal microbalance (RQCM) system

A RQCM unit, ordered from Maxtek Inc., allows simultaneous monitoring of two sensors using two channels. The unit operates at ~6MHz, with a frequency resolution of 0.03Hz, giving a mass resolution of $0.4 ng/cm^2$. The figure below (Figure A II-3) shows the hardware of the RQCM system. The software uses the resonant crystal frequency to calculate mass gain (in $\mu g/cm^2$).

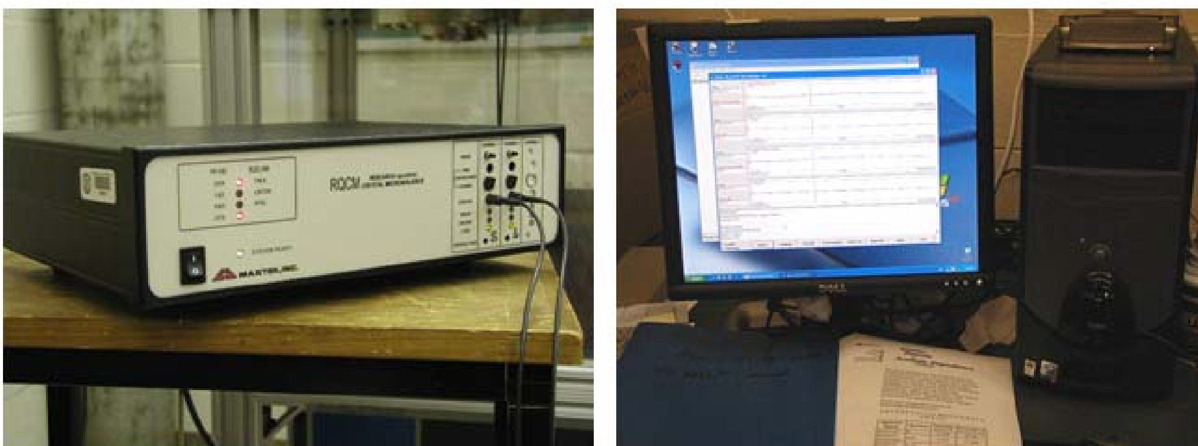


Figure A I- 3 Hardware of Research QCM (Maxtek Inc) system [105]

The view of the QCM unit inside the AO chamber is shown in Figure A I-4 (right), while the outside of the chamber is shown on the left side.

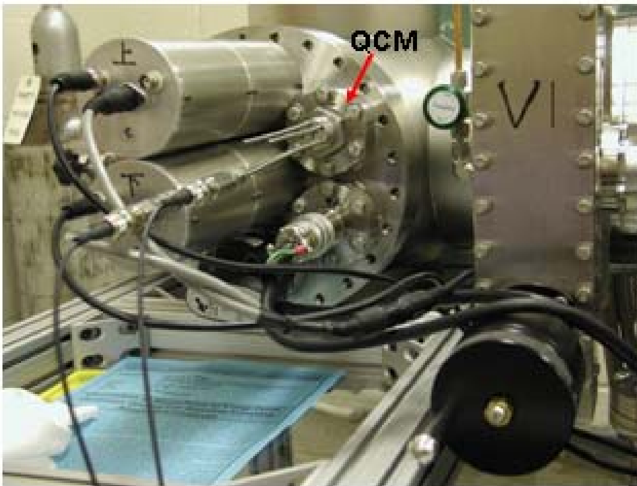


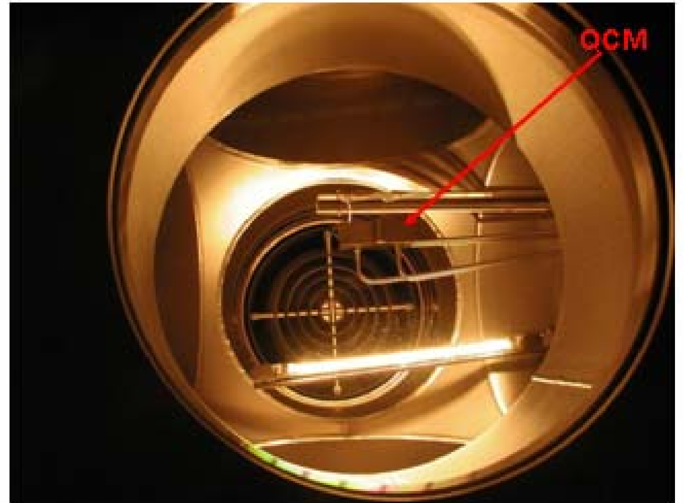


Figure A I- 4 The view of the QCM unit inside the AO chamber (right), and the outside of the chamber (left).

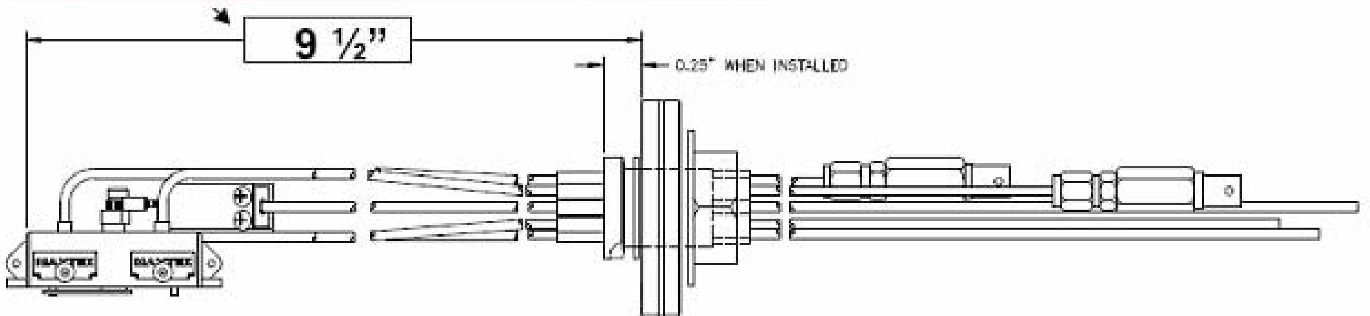


Figure A I- 5 Image and machine drawing of the RQCM unit (with the mounting flange)

VUV source

The top flange of the AO source was modified by Kurt Lesker Company in order to accommodate VUV lamp. The lamp is attached at 32.5cm with respect to the sample stage to achieve equivalent number of suns that will accurately simulate LEO conditions. Sample damage and disintegration is possible if 4 suns is exceeded. Deuterium VUV source (110-400nm wavelength), with $MgF_2$ window was purchased from Resonance Limited Company.

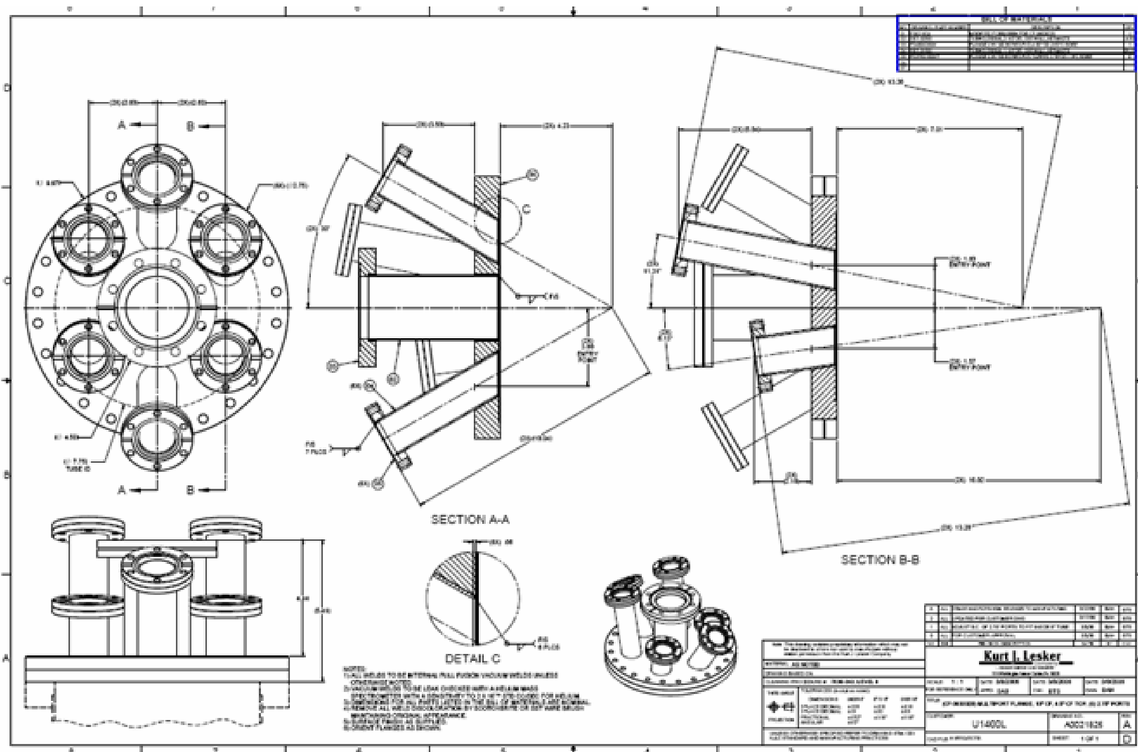

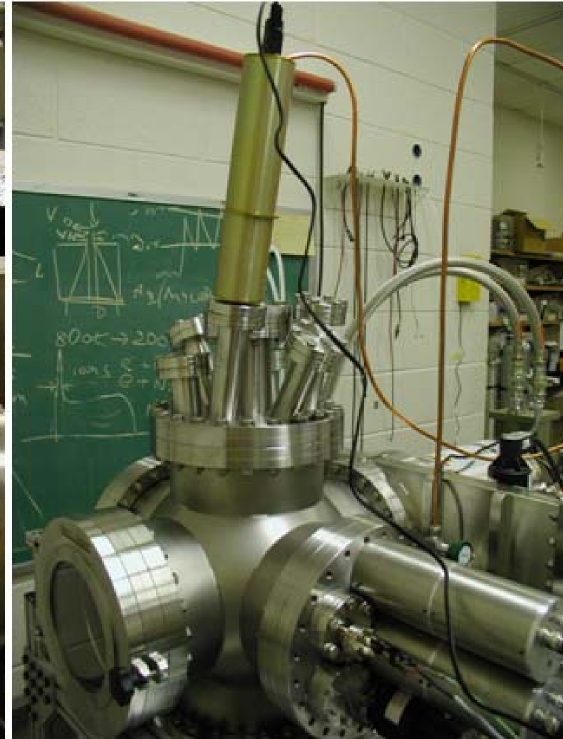


Figure A I- 6 Top flange modification

## D2ArCM-C Deuterium VUV Source 110 to 400 nm

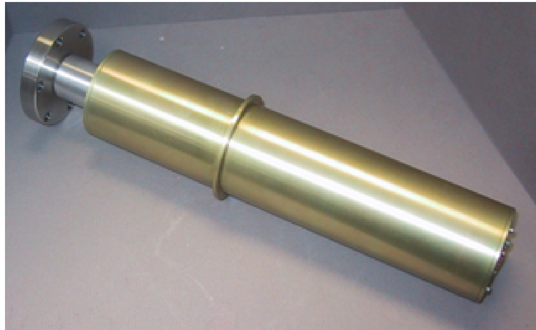

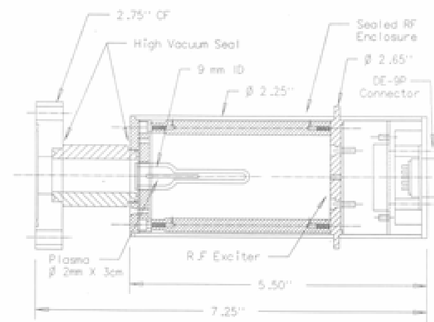


| Specification | Minimum | Typical | Maximum | units |
|---|---|---|---|---|
| Plasma Cavity | | 30 x 3 | | mm ID |
| Window Material | | MgF2 | | NA |
| Drift | | 0.2 | 1.0 | % per hour |
| Calibration | Absolute intensity determined by traceable NBS standard | | | |
| Testing | Test spectrum of entire UV spectral region performed | | | |
| Running Life | 1500 | >4000 | - | hours |
| Case Temperature | 0 | - | 55 | °C |
| Input Voltage | 8 | - | 35 | V |
| Input Power | 0.3 | - | 20 | Watts |
| Optional Pulsed Operation | - | - | 10 | kHz |

Resonance: http://www.resonance.on.ca/Continuum%20Sources%20Show.html

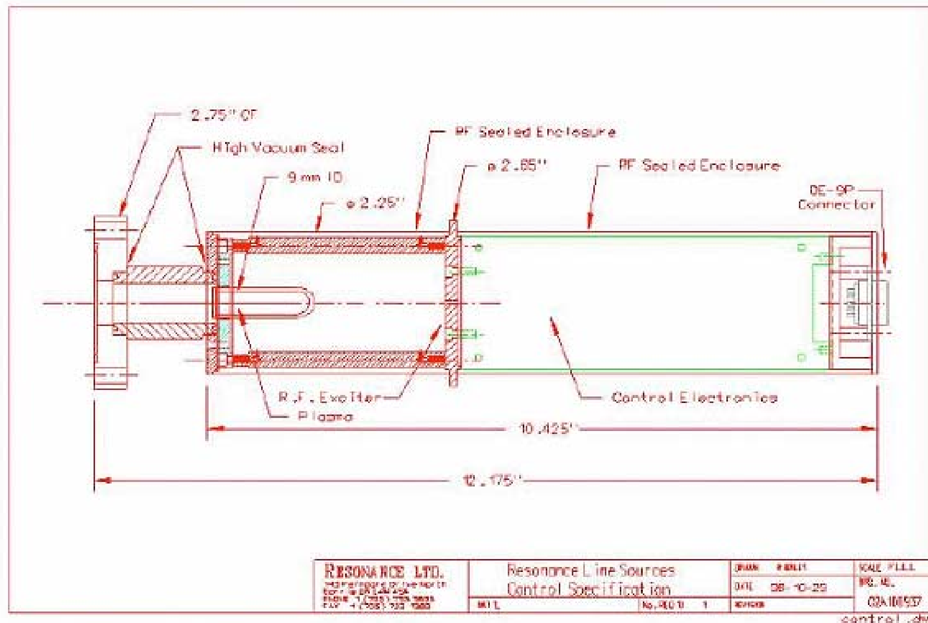


Figure A I- 7 Deuterium VUV source specifications and drawings (from Resonance Limited)

# APPENDIX B

# SRIM SIMULATION RESULTS

## Simulation using $SiO_2$ as a target material

In order to have an overview of the stopping range of energetic O atoms in $SiO_2$ and $GeO_2$ targets, a simulation program, SRIM (The Stopping and Range of Ions in Matter), based on the Monte Carlo method, was used. This Appendix contains results of SRIM calculations of the final distribution as well as the impinging atom's energy loss. The method used by this program is based to follow the "story" of each individual atom from the large number of incident atoms assigned. Each history starts with an incident atom with a well defined energy, position and direction. The incident O atom was assigned certain amount of energy (5, 9 and 15eV) in order to get as good correlation with the experiments as possible. Geometry in the AO source dictated the condition that the incident O atom hits the sample surface under the angle of 90o. The energy of the incident atom is decreased either by nuclear collisions (discrete reduction), or by electronic collision (continuous reduction). The principle of the code is to change incident atom direction when atom meets nucleus, while it keeps ion direction unchanged in case of interaction

with electrons. The mean free path of the atom between the nuclear collisions is defined by its energy, the higher energy atoms will have larger mean free path.

In the SRIM coordinate system, X-axis is defined as the target depth, and Y-axis and Z-axis are transverse coordinates.

The distribution of the O atoms with 5eV kinetic energy impinging $SiO_2$ layer under $90^o$ is given in Figure A II-1. The density of $SiO_2$ target materials was taken as $2.3 g/cm^3$.

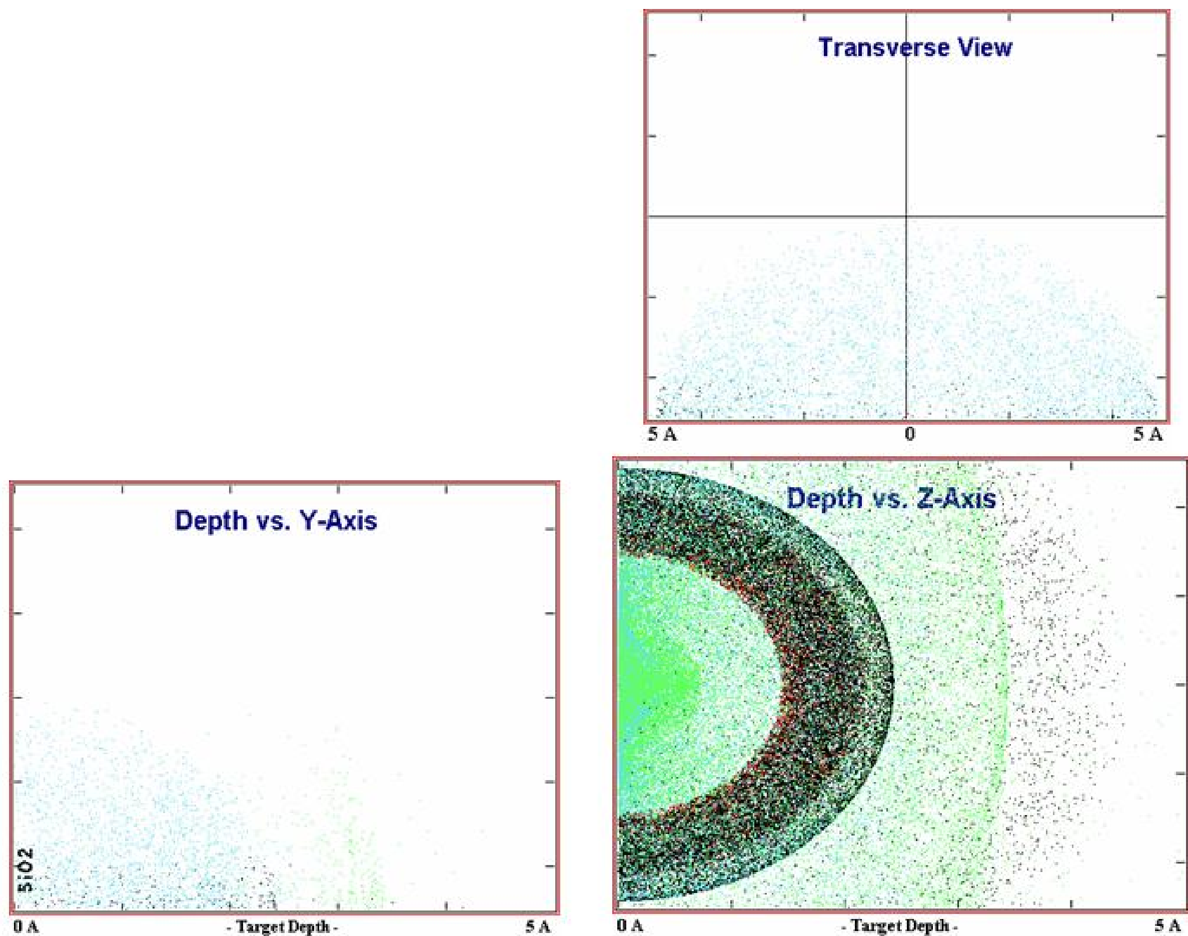


**Figure A II-** 1 SRIM simulation of 5eV AO impact (100 000 incident atoms) onto 5Å thick $SiO_2$ layer-no transmitted atoms.

It can be seen that all of the incident 5eV AO atoms (100 000 total) are stopped before they reach 5Å distance in the $SiO_2$ layer. The result of simulation showed that there were no transmitted atoms through the oxide scale of this thickness. In order to determine cut-off point or the exact distance at which all of the impacting 5eV AO atoms are stopped, SRIM simulation was carried out for the $SiO_2$ thickness of 3Å. Figure A II-2 represents the results of the SRIM calculation for 5eV AO impacting $SiO_2$ layer, 3Å thick.

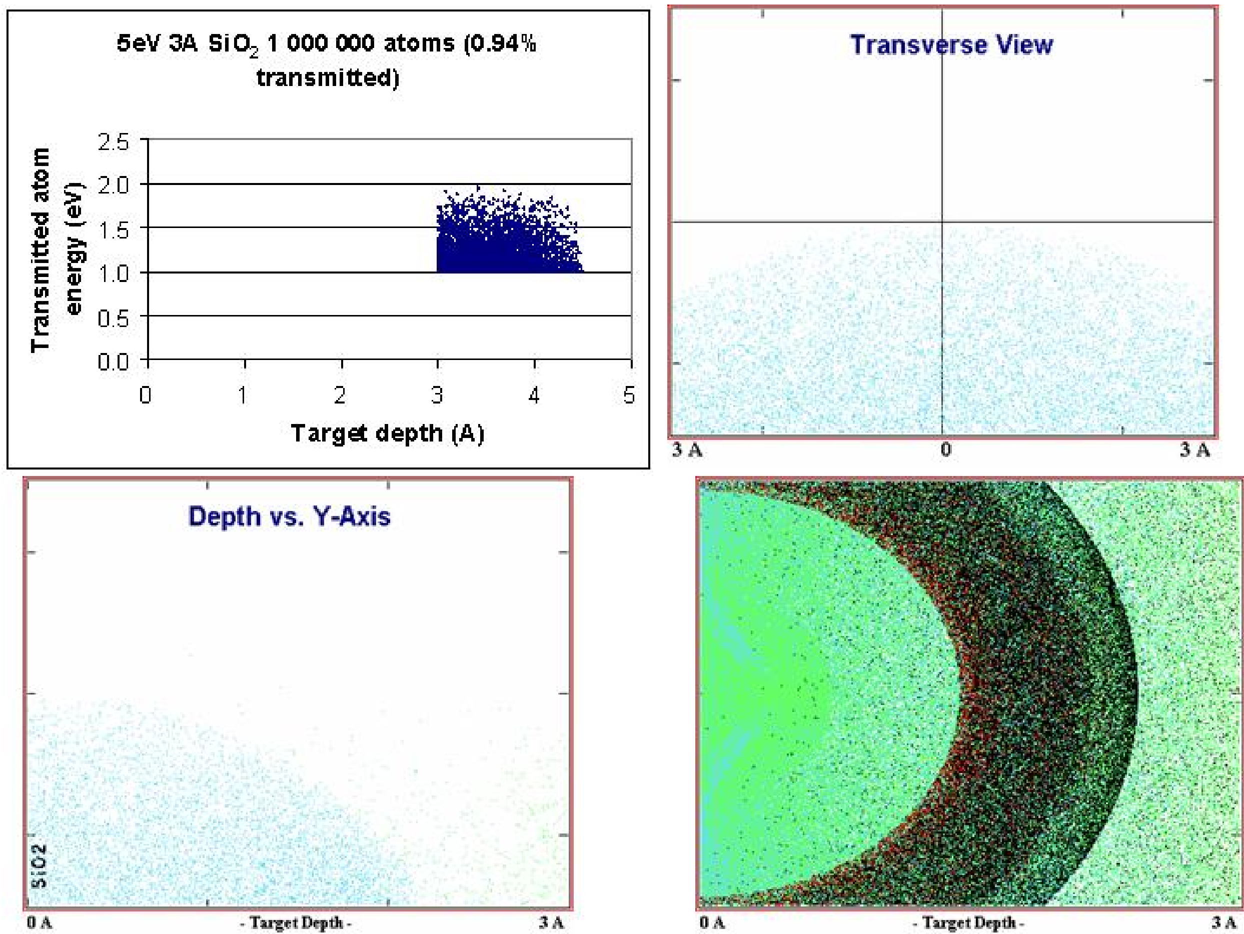


**Figure A II- 2** SRIM simulation of 5eV AO impact (1 000 000 incident atoms) onto 3Å thick $SiO_2$ layer-0.94% transmitted atoms

Opposed to the Figure A II-1, where no transmitted atoms were observed, it can be seen in Figure A II-2 that 0.94% of 1 million incident atoms was transmitted through the $SiO_2$ oxide

scale 3Å thick. The Transmitted ion file (TRANSMIT) is activated during the SRIM calculation and stores kinetics for every ion. The data about the ion energy, location and trajectory are contained within this file. Since this study is particularly interested in the distance of "how far" an atom with a certain amount of energy can travel through the target material, the data for the transmitted atom's energy at certain target depth were plotted. This is shown in the upper left corner of Figure A II-2. We can see that passing through the 3Å thick $SiO_2$ layer, 0.94% (~10000) atoms were stopped between 3-4.5 Å in target depth (denoted as X-direction in SRIM coordinate system). It can be also noted from Figure A II-2 that the energy of the transmitted atoms was in the range 1-2eV. To be even more precise and determine distribution of 5eV AO atoms and their energy, the impact was simulated for the oxide thickness of 4Å. Figure A II-3 shows SRIM simulation of 100 000 5eV AO atoms impacting 4Å thick $SiO_2$ layer.

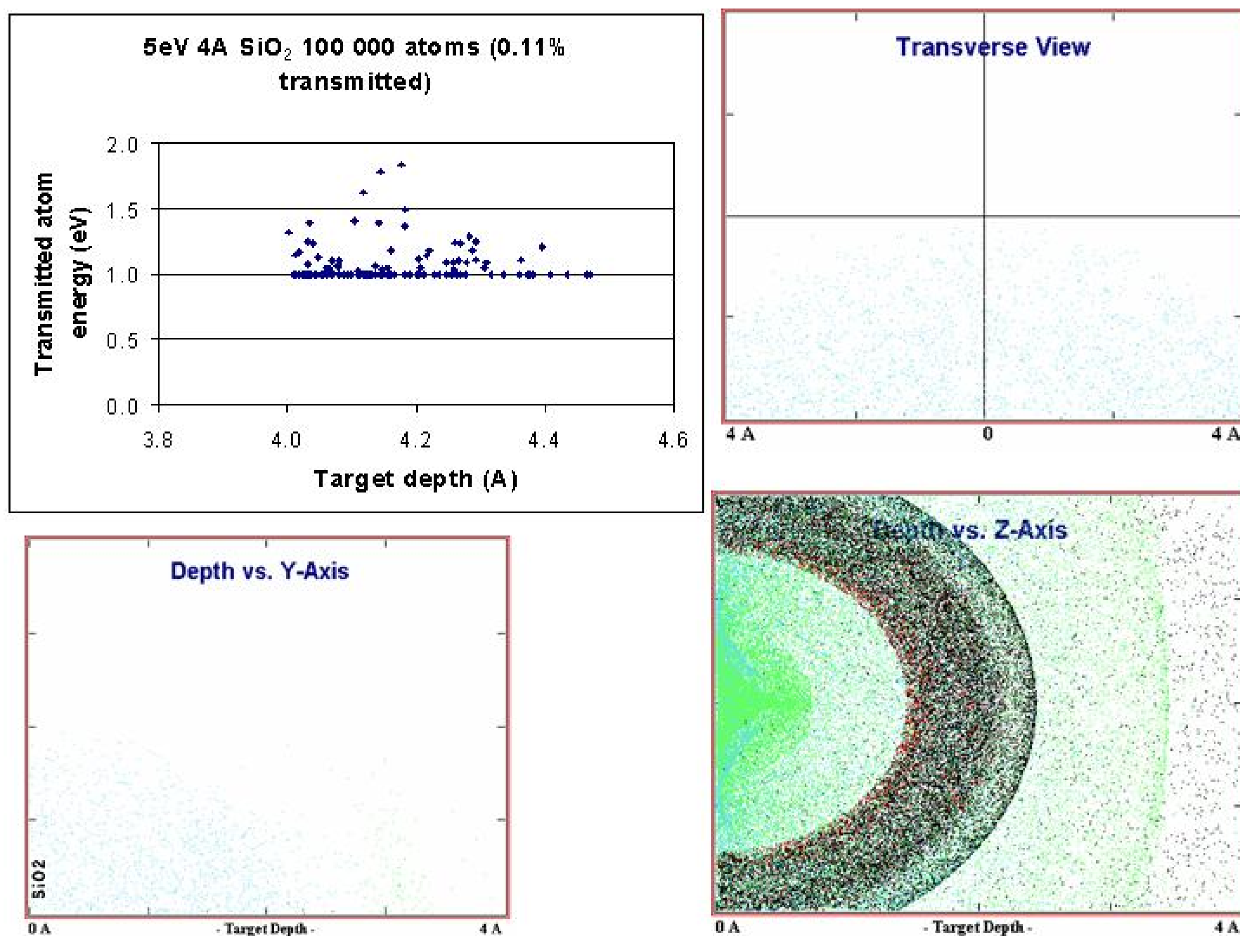


**Figure A II- 3** SRIM simulation of 5eV AO impact (100 000 incident atoms) onto 4Å thick $SiO_2$ layer-0.11% transmitted atoms

It can be seen that 0.11% of atoms is transmitted through this oxide thickness, with the final energy ranging from 1-2eV. However, the majority of transmitted atoms had the energy of 1eV and was stopped between 4-4.3 Å of target depth. Since we investigated experimentally the effect of different kinetic energies of AO on the oxidation of Si and Ge, 9eV and 15eV impacts were also simulated. Figure A II-4 shows SRIM simulation of 9eV AO impact on $SiO_2$ layer 5Å thick.

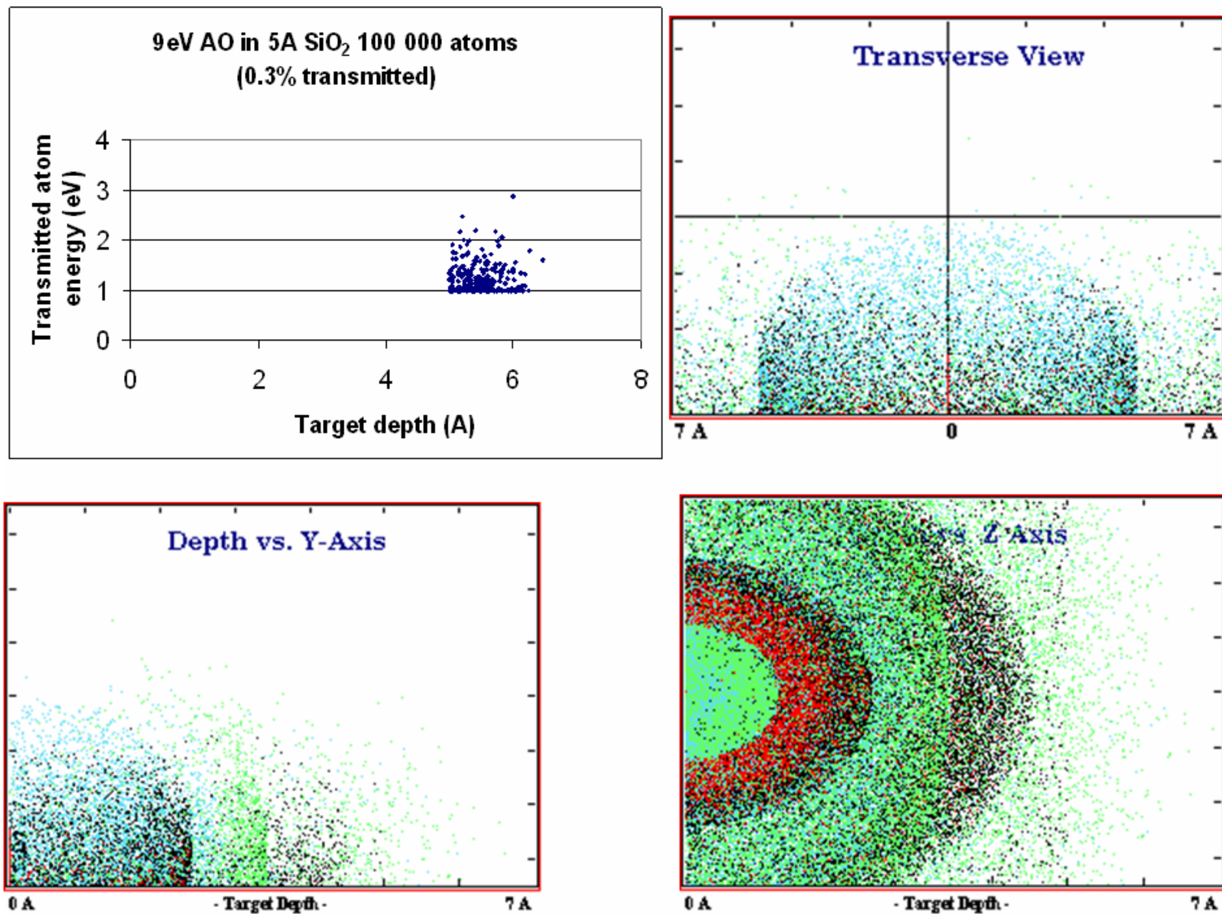


**Figure A II- 4** SRIM simulation of 9eV AO impact (100 000 incident atoms) onto 5Å thick $SiO_2$ layer-0.3% transmitted atoms

It can be seen that 0.3% (~330 atoms) is transmitted through this oxide thickness, with the final energy ranging from 1-2eV mostly. Only very few transmitted atoms had the energy higher than 2eV. However, the majority of transmitted atoms were stopped between 5-6 Å of target depth.

Figure A II-5 shows SRIM simulation of 15eV AO impact on $SiO_2$ layer 5Å thick.

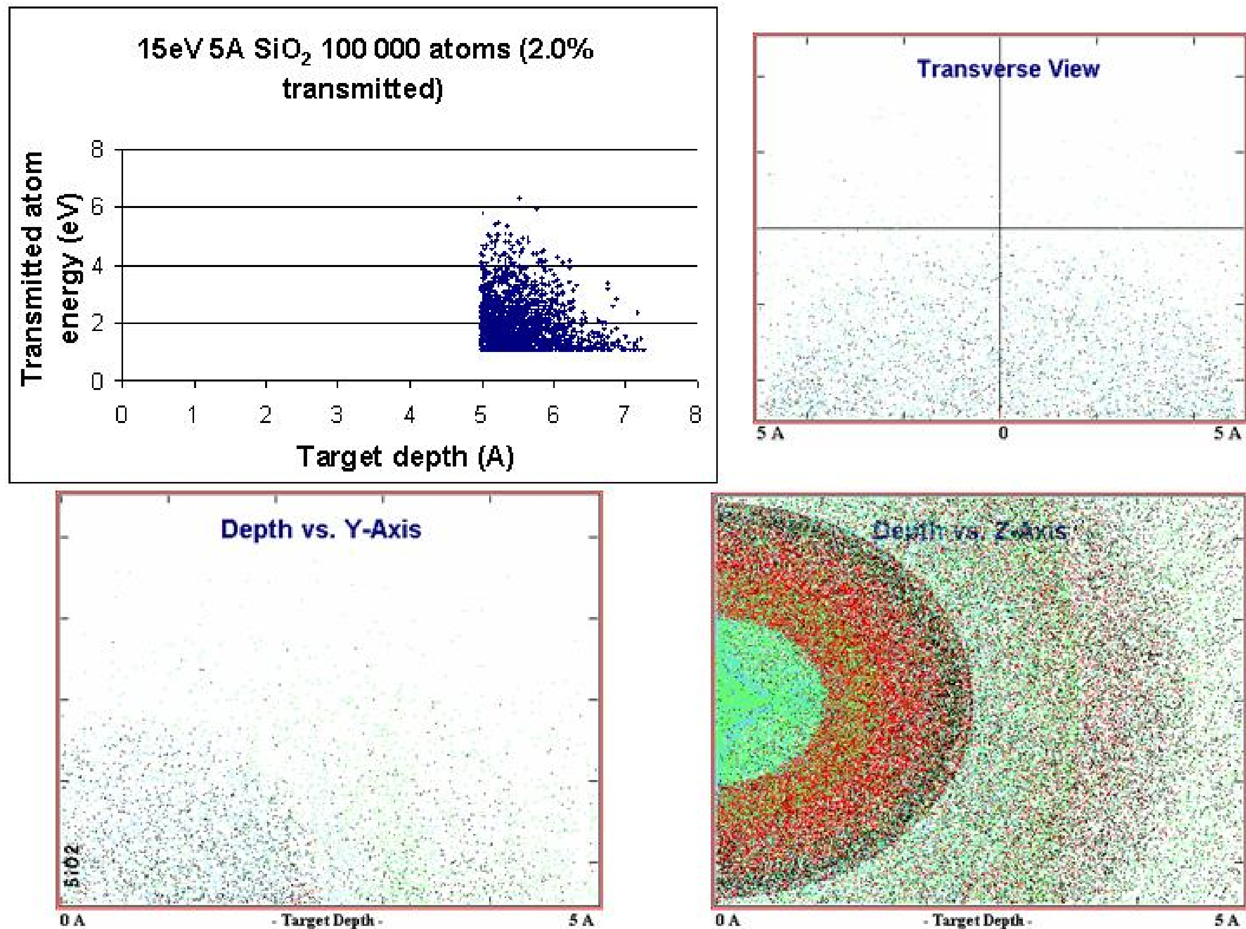


**Figure A II- 5** SRIM simulation of 15eV AO impact (100 000 incident atoms) onto 5Å thick $SiO_2$ layer-2% transmitted atoms

We can see that 2% (~2000 atoms) is transmitted through this oxide thickness, with the final energy ranging from 1-5eV mostly. Only very few transmitted atoms had the energy higher than 5eV. The majority of transmitted atoms were stopped between 5-7 Å of target depth. 15eV AO transmitted atoms still keep considerable amount of energy after the impact to the $SiO_2$ target material. The amount of this energy (up to 5eV) is significantly higher than the amount of energy associated with the transmitted atoms after the 9eV AO impact (up to ~2eV) for the same thickness of the target material.

## Simulation using $GeO_2$ as a target material

SRIM calculation was performed for 5, 9 and 15eV AO on a $GeO_2$ as a target material, in similar manner as for $SiO_2$ described above. The density of $GeO_2$ target materials was taken as 4.28g/cm$^3$, which corresponds to the quartz allotropic modification of $GeO_2$. Figure A II-6 shows SRIM simulation of 5eV AO impact on $GeO_2$ layer 5Å thick.

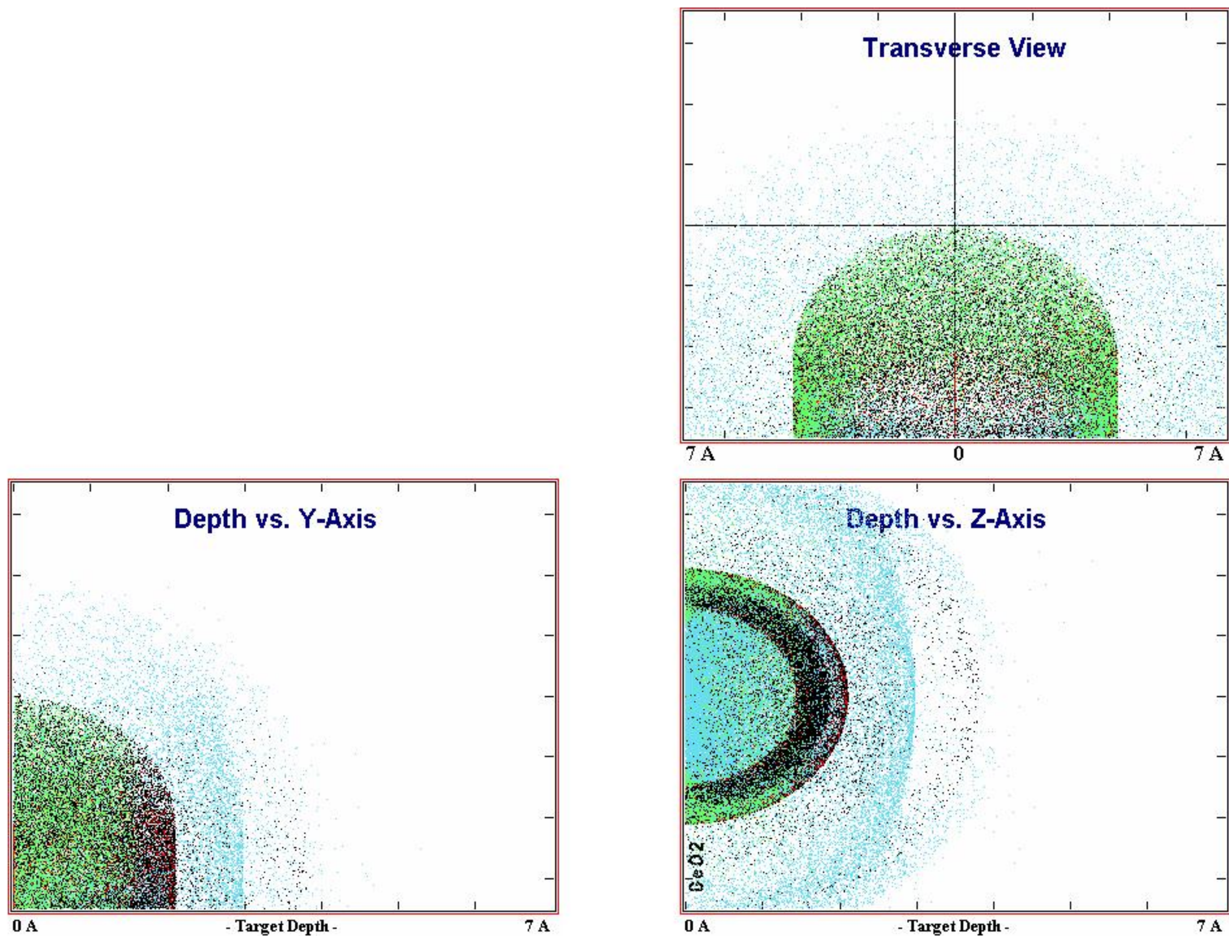


**Figure A II- 6** SRIM simulation of 5eV AO impact (100 000 incident atoms) onto 5Å thick $GeO_2$ layer-no transmitted atoms

Similarly to the result obtained for Si, it is noticeable that there were no transmitted atoms through the 5Å thick $GeO_2$ layer. Obviously, higher energy of impinging atom is needed

in order to transfer this atom through the oxide layer of this thickness. Figure A II-7 shows SRIM simulation of 9eV AO impact on $GeO_2$ layer 5Å thick.

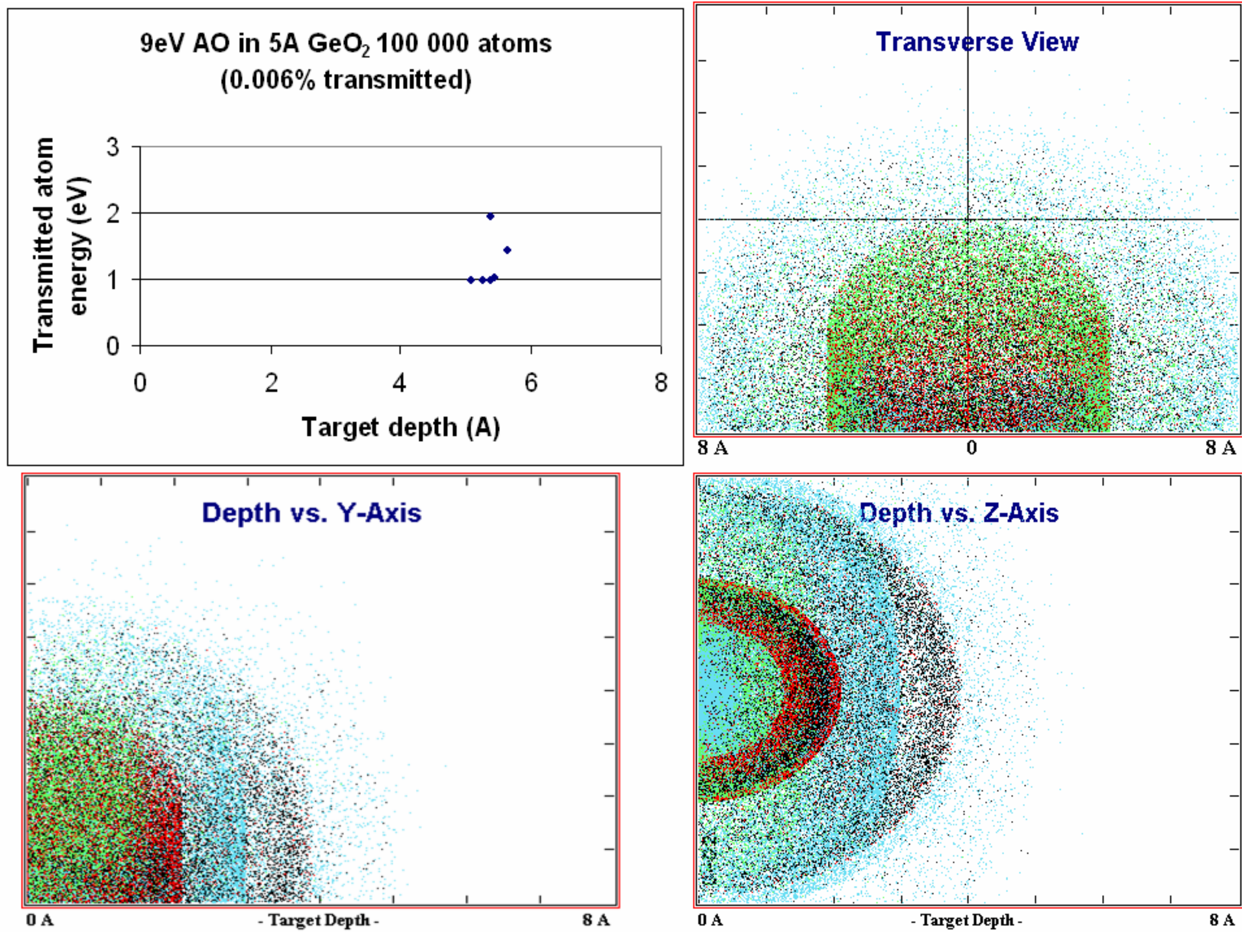


**Figure A II- 7** SRIM simulation of 9eV AO impact (100 000 incident atoms) onto 5Å thick $GeO_2$ layer-0.006% transmitted atoms**.**

Very few atoms were transmitted through the 5Å thick $GeO_2$ layer, and their energy ranged from 1-2eV. All transmitted ions (6 atoms total) were stopped between 5-6 Å. Figure A II-8 shows SRIM simulation of 15eV AO impact on $GeO_2$ layer 5Å thick, for 100 000 incident atoms.

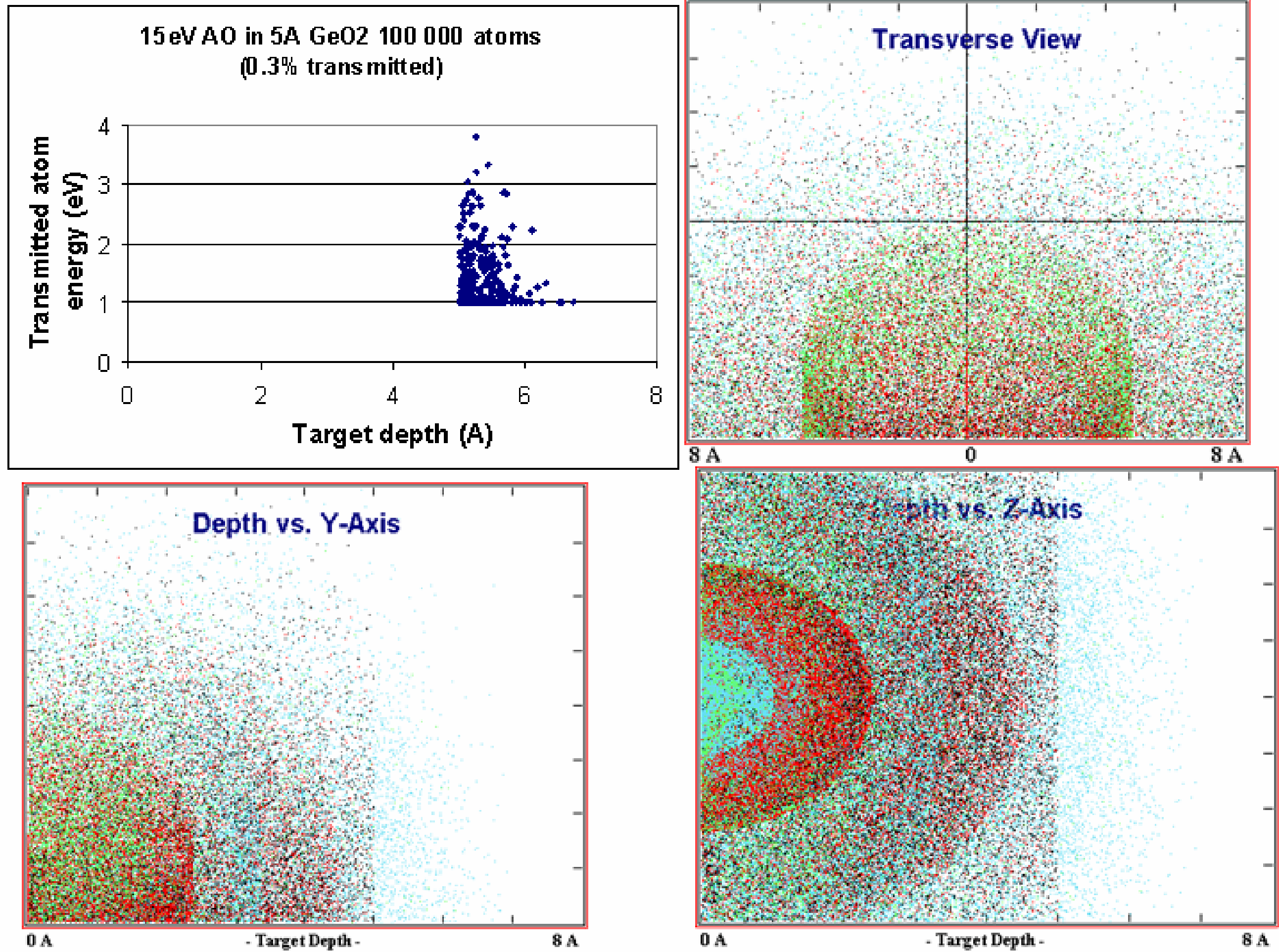


**Figure A II- 8** SRIM simulation of 15eV AO impact (100 000 incident atoms) onto 5Å thick $GeO_2$ layer-0.3% transmitted atoms.

It can be seen that higher energy of AO (15eV) caused more atoms to be transmitted compared to the lower energies impacts (5 and 9eV). 0.3% of atoms were transmitted and their energy ranged from 1-3eV. Only few of them had kinetic energy higher than 3eV, and the majority of the transmitted atoms can be found between 5 and 6 Å of target depth.

## APPENDIX C

## PHASE DIAGRAMS, OXIDATION PLOTS AND THERMODYNAMICAL PROPERTIES FOR SI-O AND GE-O SYSTEMS

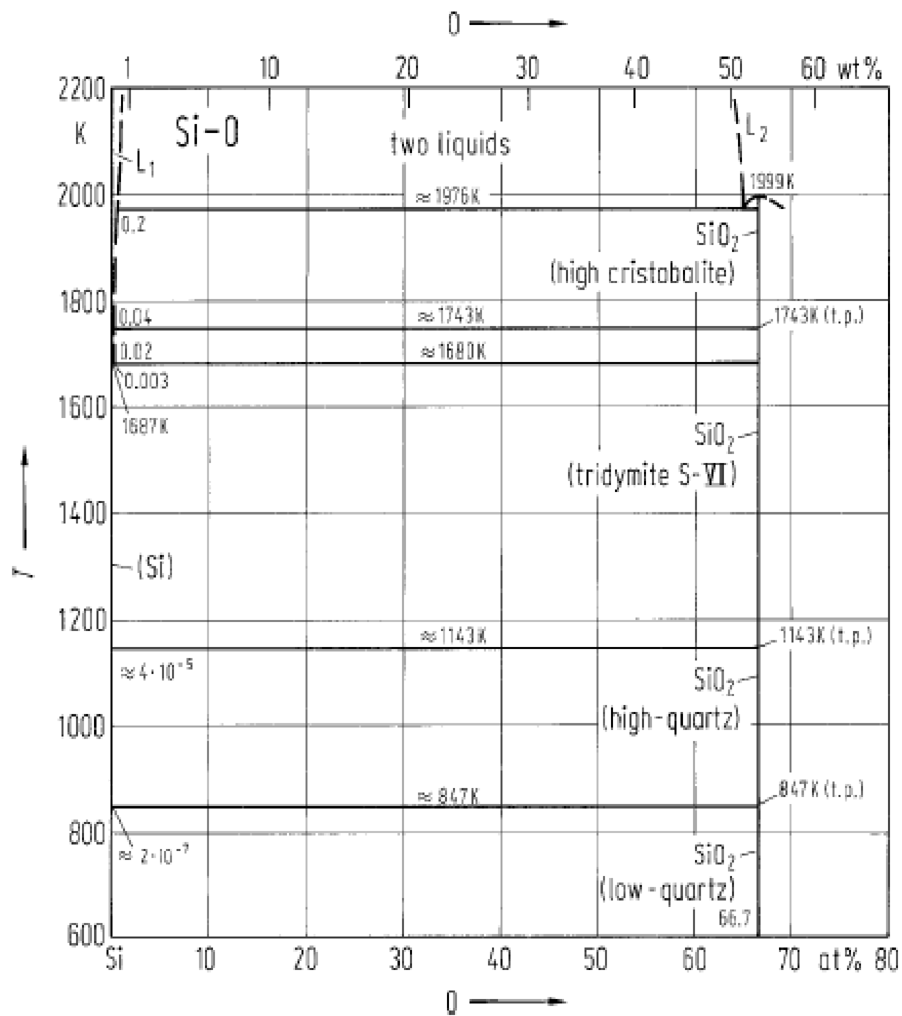


Figure A III- 1 Si-O phase diagram [128, 129]

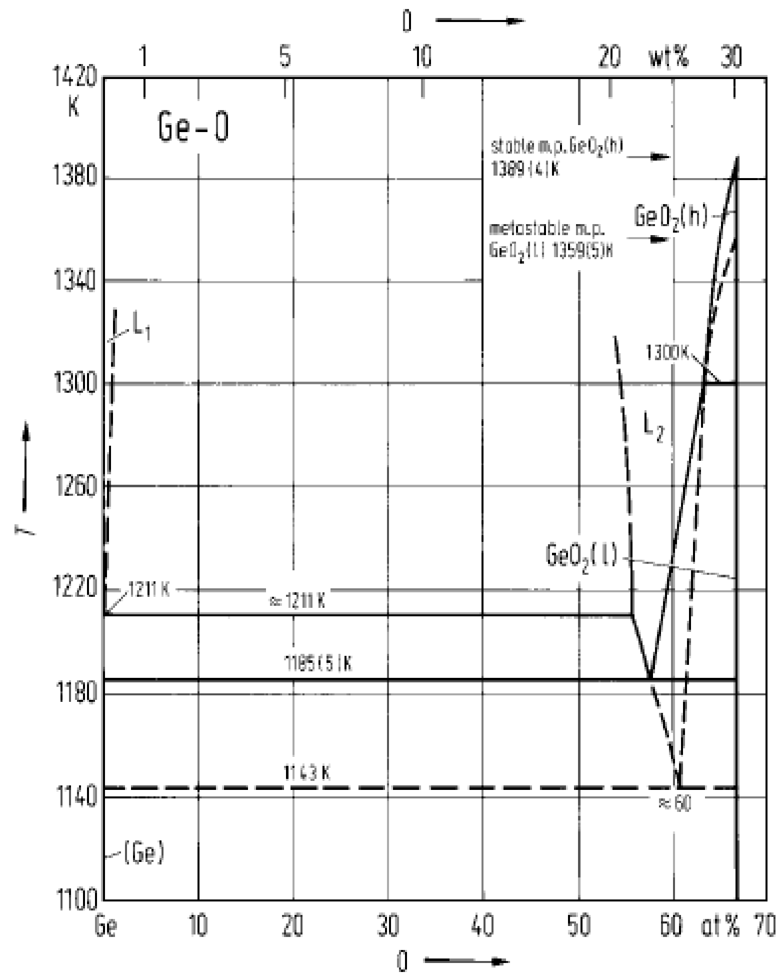


Figure A III-2 Ge-O phase diagram [128, 129]

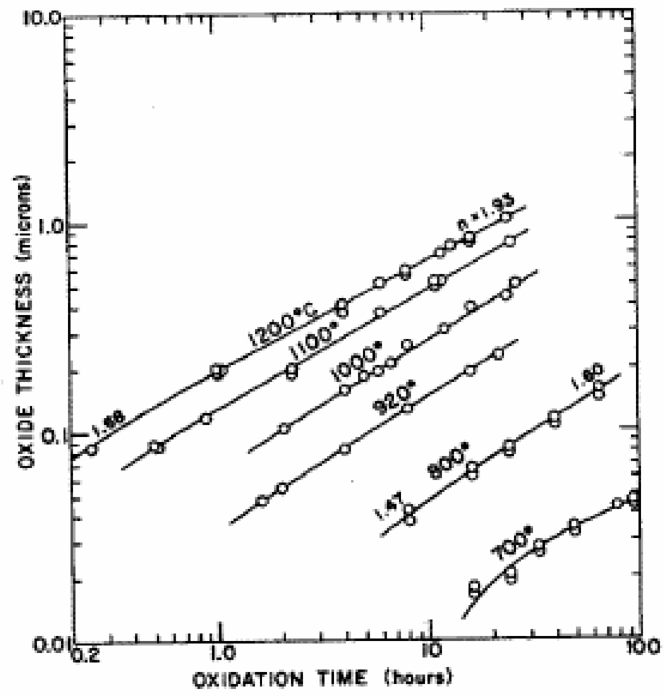


Figure A III-3 Oxidation of Si in dry $O_2$ [44]

Table A III- 1 Thermodynamical and electronic properties of Si, Ge, $SiO_2$ and $GeO_2$. Si-Si, Si-O, Ge-Ge and Ge-O bond strengths also given [130, 131]

| | Ge | $GeO_2$ (tetragonal) | | Si | Quartz | Cristobalite |
|---|---|---|---|---|---|---|
| | | | | | | |
| $T_m$ [C] | 938 | | | 1414 | 1427 | 1726 |
| ΔHf° cryst [kcal/mol] | 0 | –188.6 | | 0 | -217.6 | -216.9 |
| ΔHf° g [kcal/mol] | 88.9 | | | 108.9 | | |
| ΔHf° amor [kcal/mol] | / | | | 1 | | |
| ΔGf° (g) [kcal/mol] | 79.2 | | | 98.3 | | |
| ΔGf° [kcal/mol] | 0 | –124.6 | | 0 | | |
| S° [cal/degree mol] | 7.43 | 9.49 | | 4.5 | | |
| S° (g) [cal/degree mol] | 40.1 | | | 40.12 | | |
| Cp (c) [cal/degree mol] | 5.57 | 12.45 | | 4.78 | | |
| Cp (g) [cal/degree mol] | 7.38 | | | 5.32 | | |
| ΔHfus [kcal/mol] | 8.83 | | | 12.08 | 2.24 | 2.12 |
| ΔHvap [kcal/mol] | 79.8 | | | | | |
| Thermal conductivity @25°C [cal/sec/cm/°C] | 0.14 | | | 0.835 | | |
| Band gap (eV) | 0.6 | | | 1.1 | | |
| Electron mobility $m^2$/Vsec | 0.38 | | | 0.14 | | |
| Hole mobility $m^2$/Vsec | 0.18 | | | 0.05 | | |
| Si-Si or Ge-Ge single bond energy [kcal/mol] | 45 | | | 76 | | |
| Si-O or Ge-O single bond energy [kcal/mol] | | 108 | | | 106 | |

**Table A III- 2** Thermodynamic properties of $SiO_2$ and $GeO_2$ phase transformations [130, 131].

| | ΔH(kJ/mol) | ΔS(J/mol K) | ΔV ($cm^3$/mol) |
|---|---|---|---|
| quartz to coesite $SiO_2$ | 2.7±0.5 | -5±0.4 | -2.05 |
| coesite to stishovite $SiO_2$ | 49±1.7 | -4.2±1.7 | -6.63 |
| α to β quartz $SiO_2$ | 0.47 | 0.35 | 0.101 |
| β quartz to cristobalite $SiO_2$ | 2.94 | 1.93 | 0.318 |
| $GeO_2$ rutile-quartz | 5.6 | 4.0 | 11.51 |

## BIBLIOGRAPHY


1. Minton T. and Garton D. *Advanced series I physical chemistry*. ed. Dressler R. A. World Scientific. Singapore (2000)

2. Rutledge S. K. and Mihelcic J. A., in *Proceedings of a Symposium Sponsored by TMS-ASM Joint Corrosion and Environmental Effects Committee and the 199th Annual Meeting of the Minerals, Metals, and Materials Society* (Anaheim, CA, February 17-22, 1990).

3. Rutledge S. K. and Olle R. M., in *Proceedings from the 38th International SAMPE Symposium* (Anaheim, CA, May 10-13, 1993).

4. Brunsvold A. L., Minton T. K., Gouzman I., Grossman E., and Gonzalez R., High Perform. Polym. 16, 303 (2004).

5. Kisa M. Masters Thesis "Silicon Oxidation by Atomic and Molecular Oxygen", University of Pittsburgh, (2004)

6. Banks B. and LaMoreaux C. presented at the *24th International SAMPLE Technical Conference*, Toronto, Canada, October 20-22, (1992)

7. D. Kearns, D. Gillen, D. Voulot, R. McCullough and W. Thompson, Journ Vac. Sci. Technolog. A, 19(3) 2001, pg 993-997

8. Caledonia G.E. Krech R.H. and Green B.D. "High flux source of energetic oxygen atoms for material degradation studies" *AIAA J*. 25, 59-63 (1987).

9. Oakes D.B. Krech R.H. Upschuete B.L. and Caledonia G.E. *J.Appl. Phys*.77,2166-2172 (1995)

10. Banks B., Rutledge S., de Groh K. and Auer B. *NATO Advanced study institute conference* Pitlochry, Scotland, July 7-19 (1991)

11. Tagawa M., Yokota K., Ohmae N. and Kinoshita H. *High Perform Polym.*12, 53-63 (2000)

12. Banks B., Rutledge S. and Auer B. *119th TMS Annual Meeting* and Exhibit, Anaheim, February 18-22 (1990)

13. Zimcik D. and Wertheimer M. *J. Spacecraft,* Vol 28, No 6 (1991).

14. Schurig H., Kruer M., Levesque ,M. Gaddy E., and Andiario W. Proceedings of the thirty second Intersociety Energy Conversion Engineering Conference (IECEC), Honolulu, Hawai, (1997).

15. Engstrom J. and Engel T. *Physical Review B*, vol 41, 2, pg 1038-1041 (1989)

16. R. Krech, PSI FAST$^{TM}$ source manual, Physical Sciences Inc. 2004

17. Engstrom J. Nelson M. and Engel T *J.Vac.Sci.Technol*.A7(3), pg 1837-1840, (1988)

18. Tagawa M. Yokota K. Ohmae N. Kinoshita H. and Umeno M. *Jpn.J.Appl.Phys.Vol* 40, pg 6152-6156, (2001)

19. Nakazawa M. Nishioka Y. Sekiyama H. and Kawaze S. *J. Appl. Phys*. 65(10) 4019-4023 (1989)

20. Engstrom J. Bonser D. and Engel T. *Surf. Sci*. 268, pg 238-264 (1992)

21. Randjelovic M. and Yang J. C., *Materials at High. Temp. ,* vol. 20,281-285, (2003).

22. Gatan Inc. (2002) Digital Micrograph software

23. Gatan Inc. (2002) “Digital Micrograph EELS analyses user’s guide”

24. http://www.unb.ca/courses/geol21142/LEC-31.html (as retrived on 29. III 2007.)

25. Villars, P., Calvert, L.D.: "Pearson’s Handbook of Crystallographic Data for Intermetallic Phases", Second Edition, Vol. 4, Materials Information Soc., Materials Park, Ohio (1991)

26. PCPDF files

27. Kisa M., Minton T. K., and Yang J. C.*J.Appl. Phys.,* 97, (2005), 023520

28. M. Tagawa, T. Ema, H. Kinoshita, N. Ohmae, M. Umeno, and T. K. Minton*, Jpn. J. Appl. Phys.* 37, (1998), pp. L1455-L1457.

29. Judy Hoyt lectures MIT; http://web.mit.edu/6.774/www/lecture_6_rev.pdf

30. Wang Y., Hu Y. and Irene E. J. Vac. Sci. Technol. A, vol. 12, No. 4, (1994)

31. Craciun V, Appl. Phys. Lett. Vol 75 (9) 1261, (1999)

32. D. Kearns, D. Gillen, D. Voulot, R. McCullough and W. Thompson, Journ Vac. Sci. Technolog. A, 19(3) 2001, pg 993-997

33. O. Fukumasa and M. Matsumori, Review of Scientific Instruments, vol 71 (2), 935, Feb 2000

34. Revesz A. *Phys. Stat. Sol*. 19, 193 (1967)

35. Irene E. *J. Appl Phys.* 54, 5416, (1983)

36. Irene E., J. Vac. Sci. Technol. A, 4 (3), 916, (1986)

37. Doremus R. *Thin Solid Films*, 122, 191-196, (1984)

38. Fargeix A. *J. Appl. Phys*. 54, 2878, (1983)

39. Murali V. and Murarka S. *J. Appl. Phys*. 60, 2106, (1986)

40. Newman R., J. Phys.: Condens. Matter 12 (2000), R335-R365

41. Cabrera N. and Mott N. F. "Theory of the Oxidation of Metals" *Rept. Progr. Phys*. 12, 163, (1948)

42. Fehlner F. "Low Temperature Oxidation", *The Electrochemical Society, INC.* Pennington, New Jersey (1986)

43. D. Jiles, Electronic properties of materials, Chapman & Hall, 1984

44. J. Yang, B. Kolasa and J. Gibson and M. Yeadon, Appl. Phys. Lett. 73 (19), 2841, 1998

45. Fromhold A. T. "Theory of Metal Oxidation" Vol. I-Fundamentals, North Holland, (1976)

46. Irene E. *Applied surface science* 30(1987) 1-16

47. Irene E. *Appl. Phys Lett.*51(10) (1987)

48. Deal B. and Grove A. *Journal of Applied Physics* 36, 12, 3770-3778 (1965)

49. Helms C.R. and Deal B. "The Physics and Chemistry of $SiO_2$ and the Si-$SiO_2$ interface" Plenum Press, New York, (1988)

50. Massoud H. and Plummer J. J. Electrochem. Soc. 132, no7, 1745 (1985).

51. A. Athanassouli and S. Messoloros, Semicond. Sci. Technolog. 17 (2002) 65-76

52. Kim K. and Lee J., Semic, Sci Technol, 11, 1059 (1996)

53. Peng K., Journal of Vac, Sci Tech B, 14, 3316 (1996)

54. Tetelin, C. J. Appl. Phys. 83, 5 (1998).

55. Bongiorno A. and Pasquarello A., Phys. Rev. B 70, 195312 (2004)

56. Kosowsky S. and Roy P., Appl. Phys. Lett , 70, 3119 (1997)

57. K. Tatsumura, T. Shimura, Physical Review B 72, 045205 (2005)

58. Verdi and R. Kelly, Thin Solid films, 241, 383-387, (1994)

59. A. Bongiorno and A. Pasquarello, Phys. Rev. Lett. 88, 12, 125901 (2002)

60. E. Rosencher and G.Amsel, Appl. Phys. Lett. 34, 254 (1979)

61. Massoud H. Electrochem Soc, vol 132, no11, 2693, (1985)

62. G. W. Scherer, "Relaxation in Glasses and Composites", Wiley Interscience, New York, NY, 1986, Chapter 1

63. S. Brawer, "Relaxation in Viscous Liquids and Glasses" The American Ceramic Society, Inc., Columbus, Ohio, 1985, Chapter 11

64. T. Scopigno, G. Ruocco, F. Sette, and G. Monaco *Science* 31 October 2003 302: 849-852 (DOI: 10.1126/science.1089446)

65. Nicollian E. and Reisman A. J. Electronic Materials, 17, 4 (1988)

66. Kuznetsova A. , Zhou G. , Chen X. , Yang J., Yates J. T., Jr. *Langmuir*, (2001), 17, p. 2146-2152

67. Ichimura S. Kurokawa A. Nakamura K. Itoh H. Nonaka H. Koike K. *Thin Solid Films* 377-378. 518-524 (2000)

68. N. Birks, G. Meier, F. Petit, "Introduction to the high-temperature oxidation of metals", 2nd edition, Cambridge University press, 2005

69. Itoh H. Nakamura K. Kurokawa A. Ichimura S. *Surface Science* 482-485. 114-120 (2001)

70. http://www.mticrystal.com (as retrived on 29. III 2007.)

71. Trucks G.W. Raghavachari K. Higashi Y. and Chabal Y. *Physical review Letters,* vol. 65 (4) (504-507) (1990)

72. Eaglsham D. Higashi G. and Cerullo M.. *Appl. Phys. Let*t. 59(6) 685-687 (1991)

73. Nakazawa M. Nishioka Y. Sekiyama H. and Kawaze S. *J. Appl. Phys*. 65(10) 4019-4023 (1989)

74. Thompson P. Twigg M. Goodbey D. Hobart K. and Simons D. J. Vac. Sci. Technol. B 11(3) 1077-1082 (1993)

75. Higashi G. Becker R. Chabal Y. and Becker A. *Appl. Phys. Lett*. 58(15) 1656-1658 (1991)

76. http://www.universitywafer.com/ (as retrived on 29. III 2007.)

77. Reimer L. "Transmission Electron Microscopy" 4th edition, *Springer* (1997)

78. Williams D. and Carter B. “Transmission Electron Microscopy” Plenum Press, New York, (1996)

79. Fultz B. and Howe J. “Transmission Electron Microscopy and Diffractometry of Materials” Springer (2000)

80. W. Stratton, P. Voyles, Appl. Phys. Lett. **86**, 141910 (2005)

81. Elliot S. R., Physics of amorphous materials, pg 60, Longman Inc, New York, (1983)

82. personal communication with Dr. Xidong Chen, Cedarville University

83. Treacy M.M.J. and. Gibson J.M, *Acta Cryst. A*, 52(2), 212-220 (1996)

84. O. Krivanek and J. Mazur, Appl. Phys. Lett. Vol 37, No4, 392 (1980)

85. Voyles P.M., Gibson J.M., and Treacy M.M.J. *J. Electron Microsc*.49, 259-266 (2000)

86. Tanaka N. Yamasaki J. Usuda K and Ikarashi U. *Journal of electron Microscopy* (52) 69-73 (2000)

87. Egerton R.F. “Electron Energy loss Spectroscopy in the electron microscope” 2nd edn. Plenum Press, New York and London (1996)

88. Ahn C. and Krivanek O. “EELS Atlas” Gatan Inc. and ASU HREM Facility (1983)

89. Hofer F. and Golob P. *Ultramicroscopy* (21) 379-384 (1987)

90. Keast V. Scott A. and Brydson R. *Journal of Microscopy* 203(2) 135-175 (2001)

91. http://www.chem.qmul.ac.uk/surfaces/scc/scat5_3.htm (as retrived on 29. III 2007.)

92. http://www.eaglabs.com/en-US/services/esca.html (as retrived on 29. III 2007.)

93. Auchterlonie G. McKenzie D. and Cockayne D. *Ultramicroscopy* 31 217-222 (1989)

94. Garvie L. and Rez P. *American Mineralogist* , 85, 732-738 (2000)

95. Skiff W. Carpenter R. and Lin S. *J. Appl. Phys*. 58(9) 3463-3469 (1985)

96. Weng X. Rez P. and Batson P. *Solid State Communications*, Vol 74, No.9 1013-1015 (1990)

97. Batson P. *Physical Review B* 44 (15) 5556-5561

98. Li D. Bancroft G. and Feng X. *Solid State Communications* 87(7) 613-617 (1993)

99. Brundle R.(ed) “Encyclopedia of Materials CharacterizaFion” *Butterworth-Heinemann* (1992)

100. Cohen S. (ed) Atomic force microscopy/Scanning tunneling microscopy 2, Plenum Press, New York, (1997)

101. http://www.srim.org/ (as retrived on 29. III 2007.)

102. L Brügemann, R Blocht, W. Press and P. Gerlach, J. Phys.: Condens. Matter 2 (1990) 8869-8879

103. F. Ross and J. Gibson in "Fundamental Aspects of Silicon Oxidation, Yves.J. Chabal (editor) (2001), pg. 40

104. Bragg W. H. and Kleeman R., Philos. Mag., 10, 318 (1905)

105. www.maxtekinc.com (as retrived on 29. III 2007.)

106. Ohring M., The materials science of thin films, Academic Press limited, S. Diego, (1992)

107. Elliot S. R., *Physics of Amorphous Materials*, 2nd ed., Longman Inc. New York, (1983), Chap.3.2

108. Garvie L.A.J. and Buseck P.R. *American Mineralogist* 84, 946-964(1999)

109. personal communication with Dr. Ray Egerton, University of Alberta,. Edmonton, Canada

110. C. Helms in Materials Science Monographs 32, "The Si-SiO2 system", edited by P. Balk, Elsevier, 1988, page 77

111. Irene E. A., Microelectronics reliability, 40, 563-565 (2000)

112. Zhao C. and Irene E., Thin solid films, 313-314,pg 286-291, (1998)

113. Mui C. and Musgrave C., Langmuir 2004, 20, 7604-7609

114. Ligenza J.R. Bell , vol 64, pg 1017-1022, (1960).

115. Taylor J. R., An Introduction to error analysis, University Science books, Oxford University Press, 1982

116. Hellberg P, Petersson C., J. Appl. Phys.82 (11),pg 5773-5778 (1997)

117. Minton, M. Tagawa, Proc. 8th Int. Symp. Materials in Space Environment, June 2000, Arcachon, France, p.501

118. Zhou X.W., Wadley H.N., Surface Science 431,42-57 (1999)

119. Vickier C., J. Appl. Phys. Vol. 62, No4, 1450-1458 (1987)

120. Watanabe H. Kato K. Uda T. Fujita K. and Ichikawa M. *Phys. Rev. Lett.* 80, 345, (1998)

121. E. Kobeda and E. Irene, J. Vac. Sci. Tech. B 6 (2), 1988

122. Ohno S. and Yates J. T., J. Vac. Sci. Technol. A 23(3), May/Jun (2005)

123. Rosencher E and Amsel G., Appl. Phys. Lett. 34, 254 (1979)

124. K. Tatsumura and I. Ohdomari, Phys. Rev. B, 72, 045205 (2005)

125. Costello J. and Tressler R., J. Electrochem. Soc. 131, 1944 (1984), E. Gusev and E. Garfunkel, Phys. Rev. B 52, 1759 (1995)

126. http://www.advceramics.com/geac/ (as retrived on 29. III 2007.)

127. http://www.tectra.de/HTR.htm (as retrived on 29. III 2007.)

128. Wriedt, H.A., in: "Binary Alloy Phase Diagrams", Second Edition, Vol. 3, T.B. Massalski (editor-in-chief), Materials Information Soc., Materials Park, Ohio (1990)

129. Wriedt, H.A.: Bull. Alloy Phase Diagrams **11** (1990) 43

130. http://www.knovel.com/knovel2/Toc.jsp?BookID=1212 (as retrived on 29. III 2007.)

131. Patnaik P. Handbook of inorganic chemicals, McGraw-Hill, ISBN:0-07-049439-8